Physique quantique expérimentale à N corps dans des matrices d'atomes de Rydberg. Des modèles de spins à la matière topologique.

Vincent Lienhard

université PARIS-SACLAY

NNT : 2019SACLO022

INSTITUT d'OPTIQUE GRADUATE SCHOOL ParisTech

Experimental quantum many-body physics with arrays of Rydberg atoms

From spin models to topological matter

Thèse de doctorat de l'Université Paris-Saclay
préparée à l'Institut d'Optique Graduate School

École doctorale n°572 Ondes et Matière (EDOM)
Spécialité de doctorat: Physique

Thèse présentée et soutenue à Palaiseau, le 18 décembre 2019, par

Vincent Lienhard

Composition du Jury :

Jean-François Roch Professeur, UPS – LAC	Président
Leticia Tarruell Senior scientist, ICFO	Rapportrice
Jérôme Beugnon Maître de conférences, UPMC – LKB	Rapporteur
Bruno Laburthe-Tolra Chargé de recherche, CNRS – LPL	Examinateur
Thierry Lahaye Chargé de recherche, CNRS – LCF	Directeur de thèse
Antoine Browaeys Directeur de recherche, CNRS – LCF	Invité

Thèse de doctorat

Remerciements

Voilà, c'est fini. Après quatre belles années, riches en rencontres, rires, et en physique forcément. Après un millier de jours passés au sous-sol du laboratoire Charles Fabry à cliquer sur des écrans, quelques mois de rédaction, une oreille, quelques kilos en plus et quelques cheveux en moins (un jour je serai capable de faire l'inverse), une demi-douzaine de brioches aux pralines, une demi-tonne de frites du Magnan, un millier de cafés et quelques litres de bière, je regarde dans un mélange de joie, de fierté et de nostalgie tout ce à quoi j'ai pu contribuer lors de ma thèse. Je pense à tous ceux qui m'ont permis de réaliser ce travail, et qui m'ont accompagné durant ces années. Je leur dédie ces quelques pages de remerciements.

Tout d'abord, j'aimerais remercier mon jury de thèse, Leticia Tarruell, Jérôme Beugnon, Bruno Laburthe-Tolra et Jean-François Roch, pour le temps qu'ils ont consacré à mon travail, pour leur lecture attentive du manuscrit et la qualité de leurs rapports et des questions posées lors de la soutenance. Ce fut un plaisir de soutenir devant vous, d'autant plus en présenciel alors que des mouvements sociaux compliquaient un peu les déplacements à l'époque. J'aimerais pour cela vous exprimer toute ma gratitude.

Mes travaux de thèse sont le fruit d'un travail d'équipe, l'équipe CHADOQ, dirigée par Antoine Browaeys et Thierry Lahaye. Je remercie Antoine pour ses précieux conseils et éclaircissements en physique, et ces enrichissantes discussions, où l'on se pose des questions pour comprendre ensemble la dernière trouvaille d'un collègue théoricien, ou un concept obscur de physique des solides. Ces discussions étaient parfois lancées à l'heure fatidique de la fin de journée, quand on hésite entre prendre le dernier bus ou rester encore un peu, et bien qu'elles m'aient fait manquer quelques "happy hours", c'en était pas moins des heures heureuses à progresser en physique! Je tiens aussi à te remercier Antoine, pour le travail harrassant que tu as accompli pour obtenir des financements, ce qui nous a permis de travailler dans d'excellentes conditions ou partir en conférence par exemple. Lors de ces conférences, tu fais la publicité des posters des thésards de ton équipe, je tenais aussi à te remercier pour ça, et je garde un très bon souvenir de l'édition 2017 de ICOLS à Arcachon.

À la tête de notre équipe, je souhaite remercier aussi Thierry Lahaye, d'une part pour son rôle dans la promotion et gestion de l'équipe, ou dans l'obtention de financements, comme Antoine, mais aussi pour son rôle plus particulier de directeur de thèse. Déjà

avant la rédaction, j'ai pu profiter de tes conseils et connaissances, dont l'étendue et la profondeur donnent le vertige. Ensuite, ta patiente et attentive relecture, ainsi que tes critiques constructives m'ont permis de hausser le niveau de mon manuscrit de thèse. De manière générale, tu m'as formé au quotidien à l'art subtil de mener et présenter un travail scientifique, ce qui me servira pour toute ma vie, quelque soit mon futur métier. Je tiens à te remercier infiniment pour cela. Tu as été un soutien et un moteur dans mon travail de thèse, et aussi dans la recherche du jeu de mot le plus pourri (enfin, ce sont surtout les autres qui ne les apprécient pas). Ton humour, ton goût pour les contrepèteries et autres bonnes choses de la vie ont fait de cette thèse en Labex une expérience inoubliable!

J'ai eu la chance de travailler lors de ma thèse avec trois personnes exceptionnelles, en plus de nos chefs, qui sont bien plus que des collègues de travail mais des amis: notre post-doc indestructible Daniel Barredo, le redoutable Sylvain de Léséleuc et l'insaisissable Pascal Scholl. Grâce à toi Daniel, travailler devient un jeu, "a competition" comme tu aimes le dire, les petites galères du quotidien deviennent la source de "estories" hilarantes, l'ennuyeux trajet labo-RER devient la conclusion douce en voiture de journées bien remplies, et tout simplement un collègue devient un ami. J'ai appris tant de choses à tes côtés, poussé par ta formidable volonté de comprendre et de faire, que je ne te remercierai jamais assez. Les debriefs au coca de situations compliquées m'ont été salvateurs, et vont me manquer.

Sylvain, je te remercie, tout comme Daniel, pour m'avoir appris à travailler sur CHADOQ. Tu m'as toujours impressionné par ta vivacité d'esprit, quand tu synthétises en quelques idées un article que tu viens de découvrir, quand tu écris un code en quelques minutes, ou quand tu trouves la réplique cinglante en quelques dixièmes de secondes avec ton sens de la répartie implacable. Tu es en plus à l'origine d'escapades fondatrices pour la cohésion du groupe, comme notre virée à Durham voir Tom l'exilé, les rando-escalade-spa à Valence, ou la recherche de la pizza nocturne à Nice... Un énorme merci pour toutes ces heures passées ensemble, au labo ou ailleurs!

Enfin Pascal, qui nous a rejoint plus tard, mais que je connaissais déjà par la filière cachanno-niçoise. Cette connexion s'est muée en excellentes conditions de travail, où nous alignions la manip au son cosmique de l'Impératrice, ou sous la prose délicate de PNL... Je ne compte plus les bons moments et délires partagés, des balades dans la Canopée à l'ode au sandwich catalan! Tu as été d'un immense soutien sur la deuxième moitié de ma thèse, avec au-delà des blagues une rapide et grande implication sur la manip, et je te remercie infiniment pour ça.

La revue de l'équipe CHADOQ ne sera pas complète sans la mention de Hannah et

Kai, avec qui j'ai eu le plaisir de travailler sur la toute fin de mon temps à l'Institut, et aussi de Thomas Boulier, sur lequel nous avons pu compter un an. Sans oublier tous nos prédecesseurs, qui nous ont transmis une machine formidable : Aline Vernier, Lucas Béguin, Sylvain Ravets et Henning Labuhn. Qu'ils en soient chaleureusement remerciés ici. Je tiens une nouvelle fois à remercier toute mon équipe, pour m'avoir fait confiance et intégré sur la manip. Je suis encore bluffé par vos capacités, où chacun se complète pour former une grande équipe, et je repense aux éclairs de génie que l'un de nous a pu avoir pour faire avancer le problème un peu plus loin. C'était un immense plaisir de travailler avec vous, dans la bulle protectrice du sous-sol du laboratoire. Comme dirait Daniel "I like working with people smarter than me", je ne pourrai pas trouver mieux!

Notre équipe ne se limite pas à la manip CHADOQ, et je tiens à remercier ici tous ses autres membres, partenaires de la Sainte-Trinité des pauses cantine-café-goûter, pour tous ces bons moments et discussions variées partagés ensemble : Florence, Yvan, Igor, Eric, Nikola, Giovanni, Ludo, Tom et Toni. De bonnes conditions de travail viennent aussi de bonnes ententes entre les différentes équipes, insufflées par le tonitruant Martin, instigateur de tournois de coinche ou de chaleureux repas de Noël. Je repense à tous ces bons moments, notamment une performance remarquée au tournoi de foot, entre les groupes Optique Atomique et Naphel, en compagnie de Maumau, Guillaume, Anaïs, Clémence, Julien, Ilan, Émilie, Mauro, Max, Pierre, Maxime, Philip, Fred, Imam, Senka, Rajiv, Gros Gui, Julia et Martin. Ce dernier trio formait selon la légende "l'autre Dream Team", voisins de labo toujours partant pour un salut tout en grimace, pour nous voler du matos, ou pour braver les éléments pour rejoindre la capitale... Merci à tous pour ces super moments!

J'ai eu la chance lors de mon doctorat d'effectuer une mission d'enseignement au sein de l'Institut d'Optique, ce qui m'a permis de découvrir un peu plus ce métier, dans d'excellentes conditions. Je tiens à remercier l'ensemble de l'équipe pédagogique, pour leur soutien et leur disponibilité. J'en profite pour remercier l'ensemble du service administratif de l'Institut et du labo, ainsi que celui de l'école doctorale, pour leur efficacité et leur compréhension face à ma situation particulière. Je pense notamment à Patrick Georges, notre directeur toujours disponible. Ce tour de l'Institut enfin ne sera pas complet sans un clin d'œil à Hélène, chef des cafés, indissociable figure de mon aventure au labo.

Et puis, il y a les autres, en dehors des murs de l'Institut. Je me sens incroyablement chanceux de vous avoir eu à mes côtés, les mots me manquent pour vous remercier. Déjà au niveau des études, j'ai une pensée émue pour tous ceux qui m'ont guidé sur le

chemin du doctorat. Et puis les liens d'amitié qui se sont forgés et s'intensifient avec les années ont été un soutien primordial. Tous ces bons moments passés ensemble, entre foot, karaoké, concerts, ou tout simplement apéro, ont été autant de bulles d'oxygène pour oublier les tracas du quotidien et relâcher la pression. Elle a été particulièrement bien relâchée au Hurling Pub, théâtre de nos exploits parisiens dont cette mémorable soirée post-soutenance, qu'ils en soient remerciés ici. À défaut de pouvoir vous adresser à chacun un mot personnel, je tiens à vous témoigner ici ma profonde reconnaissance et joie de vous savoir parmi mes amis. Un grand merci à tous les membres de mon entourage qui ont pu venir à la soutenance, alors qu'encore une fois les conditions de transport ne le facilitaient pas, à ceux qui m'ont énormément aidé à l'organisation du pot, et à ceux qui ont assuré un service de gardes du corps jusque tard dans la nuit...

Mes plus anciens amis viennent de l'époque cannoise, Max, Djé, Titi, David, Nono, Meumeu et Antoine. Des deux Alpes à Barcelone en passant par la Corse, nos retrouvailles trop peu fréquentes sont de superbes souvenirs. Ensuite viennent les amis de prépa, Antoine (encore lui), Feufeu, Adrien, Ambre, Justine, Nico, Coralie et Omar, que j'ai encore le plaisir de retrouver sur Paris, ou à défaut à New York! Et puis il y a le cercle cachannais et les amitiés parisiennes, une tribu insolite aux multiples histoires que la pudeur m'empêche de dévoiler, dont voici la liste non-exhaustive : Beber, Dodo, Marion, Pascal, Hugues, Lucie, Bambouk, Édouard, Manel, Raphaël, Canal, Ayoub, Sophie, Marie, Mathilde, Verns, Gad, Fiona, Tim, Lucile, Matthow, Rbko, Chéché, Chatan, Nobod, Auriane, Tcho Hug, Stophe, Peau d'Ours, Lisa, Fred, Snach, Féfé, Richou, Doudou, Élise, Baptiste, Antoine, Castor, Clément, Philippe, Bourbon, Rouchon, Alice, Mégane, Baluche, Daphné, Pépette, Mathilde, Chloé, Vic, Mimine, Julie, Naom's, Eva et Simon. Un énorme merci pour tout ce chemin parcouru ensemble, et j'ai hâte de vivre la suite!

Je tiens à remercier le docteur Marchac et son équipe, ainsi que Brice Blanc pour m'avoir permis de rétablir la symétrie, ce qui est vital pour un physicien!

Enfin, je consacre la fin de ces remerciements à ma famille. Vous avez été d'un immense soutien tout au long de ma vie, et le retour aux sources en terres cannoises ou bourguignonnes m'a fait un bien incomparable. J'ai une pensée émue pour mes grands-parents maternels, qui n'ont pas pu voir ce manuscrit. Je tiens particulièrment à remercier mon frère et mes parents, mon noyau familial. À mon frère, merci notamment d'avoir été un coloc précieux, pour cette dernière année si particulière. Enfin, à mes parents, un immense merci pour votre infatigable soutien, et pour cette transmission, au-delà des mots, de cette envie de comprendre et de dćouvrir, qui ont été des cadeaux inestimables pour me conduire jusqu'à aujourd'hui.

Contents

Chapter 1

Introduction

Contents

For a few decades, many experimental research teams have been able to isolate and control individual quantum objects. These objects can be particles belonging to the field of AMO physics, where the trapping of atoms, molecules or ions has been successfully demonstrated. They can also be solid-state devices, where complex systems such as superconducting circuits, NV centers in diamond, quantum dots or semiconductor-based microcavities were proven to behave as individual multi-level systems, and consequently can be seen as "artificial atoms". On these different platforms, local high-fidelity state manipulations and long coherence times have been reported, so that single quantum objects are nowadays available at an exquisite level of control. After the demonstration of the isolation of single particles, the next major experimental breakthrough was the observation of entanglement between a few particles; for example, in the pioneering work of Aspect, Grangier, and Roger [1982] with correlated pairs of photons, or with two interacting ions [Schmidt-Kaler *et al.*, 2003].

These experimental demonstrations triggered a huge investigation effort in view of developing quantum technologies. They consist in using the coherent control of quantum objects, implementing genuine quantum features such as state superposition or entanglement, in view of outperforming their classical counterparts in a wide range of applications. For instance, at the single-particle level, the coherent manipulation of the isolated quantum objects allows for the local probing of external fields, leading to the development of the quantum sensors field [Kitching, Knappe, and Donley, 2011]. Along these lines, the measurement of magnetic fields on the nanometer scale with NV centers in diamond was reported [Rondin *et al.*, 2014]. For another application, quantum metrology, engineering highly entangled GHZ states enhances

the measurement sensitivity to reach the Heisenberg limit (one example with three entangled ions is reported in [Leibfried *et al.*, 2004]).

In most of these applications, a two-level system is encoded considering only two states of the controlled individual quantum object. This single two-level system, often called *qubit* for quantum logical bit, would be the elementary building block of a quantum computer. For this application also, taking advantage of state superpositions and entanglement would enable operations impossible with classical algorithms. The most famous example is the factoring problem, basis of most of the currently in-use encryption procedures, which could be solved with a quantum machine implementing Shor's algorithm [Shor, 1994]. The computation would be based on a sequence of one- and two-qubit logical operations, the latest being realized in practice using interactions between the single quantum objects. These quantum computing, or quantum information, tasks are hard, long-term applications, requiring the challenging increase of the number of quantum objects under control, with tailored interactions, and the implementation of fault-tolerant protocols [Barends *et al.*, 2014].

Controlling the interactions within an ensemble of qubits has another, mid-term, application. Hamiltonians of interest in condensed-matter physics or high-energy physics can in that way be implemented on an experimental platform in view of mimicking real-world matter with artificial systems. Simulating real matter with a controlled experimental quantum system is called *quantum simulation*, and was first proposed by Richard P. Feynman [1982]. Progress in the field was recently reviewed by Georgescu, Ashhab, and Nori [2014]. Quantum simulation is expected to be a reliable way to study quantum many-body dynamics as compared to numerical simulations. Indeed, due to the exponential growth of the Hilbert space with N the number of interacting particles, the current limit is $N \approx 40$ for the best classical computers, whereas it could be larger for quantum simulators (see the very recent experimental comparison, for a specific computational task, between a programmable superconducting quantum processor and a classical computer [Arute *et al.*, 2019]).

The aim of this manuscript is to report a few quantum simulation experiments realized during my Ph.D thesis. They were performed on a platform based on neutral ^{87}Rb atoms, trapped in a versatile configuration of micron-sized optical tweezers, and brought to highly-excited states known as Rydberg states. In this Introduction, I will first present a few exciting many-body phenomena, hosted by two types of model Hamiltonians, in condensed-matter physics. These two types of Hamiltonians have been both studied on our platform during my Ph.D thesis. Then, I will give a few examples of quantum simulation realized on different experimental platforms. Finally,

I will focus on Rydberg-based quantum simulators.

1.1 Quantum many-body phenomena in condensed-matter physics

One of the goal of condensed-matter physics is to explain the properties of (macroscopic) matter from one- and two-body operators acting at the particle (microscopic) level. Solid-state materials can be described as an ensemble of electrons (spin-1/2 particles) localized at the nodes of a crystalline structure, having the ability to hop between lattice sites, and with an on-site interaction energy. These two elementary processes, hopping and on-site interaction, results in the Fermi-Hubbard model, written

$$\hat{H} = -t \sum_{\langle i,j \rangle,\sigma} \left(\hat{c}_{i,\sigma} \hat{c}^{\dagger}_{j,\sigma} + \hat{c}^{\dagger}_{i,\sigma} \hat{c}_{j,\sigma} \right) + U \sum_{i} \hat{n}_{i,\downarrow} \hat{n}_{i,\uparrow} \tag{1.1}$$

where i, j are the indexes of the lattice sites (the brackets indicate that the sum runs over neighbouring lattice sites), σ the spin degree of freedom $\uparrow, \downarrow$, t the hopping amplitude, U the on-site interaction energy, $\hat{c}_{\sigma}$ and $\hat{c}^{\dagger}_{\sigma}$ the fermionic annihilation and creation operators, and $\hat{n}_{\sigma} = \hat{c}^{\dagger}_{\sigma} \hat{c}$ the number operator. Although this model is simple to write, it is extremely hard to solve. Then, the usual way to treat this model is to study the regimes where one of the two processes is the most prominent. For $t \ll U$, only the spin degree of freedom remains, and we can write spin Hamiltonians. On the contrary, for $U = 0$, we recover the tight-binding model. These two types of Hamiltonians, spin or hopping Hamiltonians, can be implemented with Rydberg atoms, as we shall see in this manuscript. Now, I describe a few interesting many-body phenomena associated to these Hamiltonians.

Spin Hamiltonians Spin Hamiltonians were proposed to understand the magnetic behaviour of matter, and are the central objects of study in the *quantum magnetism* field [Blundell, 2001]. The simplest models involve spins-1/2 localized on lattice sites. The quantum operators acting on spin-1/2 are usually written in terms of Pauli matrices, $\hat{\sigma}^x$, $\hat{\sigma}^y$, and $\hat{\sigma}^z$, with z the quantization axis. Then, the interaction between two spins localized on the lattice sites i and j is formally written as a product of Pauli matrices acting on both spins. Few examples of interacting models are: the Heisenberg Hamiltonian, where the interaction between two spins reads $J_{ij}\, \hat{\boldsymbol{\sigma}}_i \cdot \hat{\boldsymbol{\sigma}}_j$; the planar XY-model, where it is written $J_{ij} \left(\hat{\sigma}^x_i \hat{\sigma}^x_j + \hat{\sigma}^y_i \hat{\sigma}^y_j \right)$; or the uni-axial Ising model, written $J_{ij} \hat{\sigma}^z_i \hat{\sigma}^z_j$. The XY model, by the use of the spin raising $\hat{\sigma}^+$ and lowering $\hat{\sigma}^-$ operators, $\hat{\sigma}^+ = \hat{\sigma}^x + \mathrm{i}\hat{\sigma}^y$ and $\hat{\sigma}^- = \hat{\sigma}^x - \mathrm{i}\hat{\sigma}^y$, can also be written $J_{ij} \left(\hat{\sigma}^+_i \hat{\sigma}^-_j + \hat{\sigma}^-_i \hat{\sigma}^+_j \right)$.

I mention also the XXZ model, a combination of the Ising and the XY models, written $J_{ij}\left(\hat{\sigma}_i^x\hat{\sigma}_j^x + \hat{\sigma}_i^y\hat{\sigma}_j^y + \delta\hat{\sigma}_i^z\hat{\sigma}_j^z\right)$. When $\delta = 1$, we recover the Heisenberg model. In this manuscript, I will focus on the Ising and the XY models.

These simple microscopic spin models may have different physical origins. For example, when derived from the Fermi-Hubbard model (1.1), spin Hamiltonians originate from the combination of the Coulomb interaction and the Pauli exclusion principle. They can be interpreted classically as the tendency for spins, pictured as elementary magnets, to orient themselves with respect to each other to reduce the global energy of the system. Consequently, they explain the macroscopic spin-ordered magnetic phases of matter from the interaction at the particle level, which is the goal of quantum magnetism. The interplay between the lattice structure and the geometrical dependence of the interaction gives rise to a rich variety of phases, even if the interaction is simply written in terms of two-body operators. Some of these phases still lack a complete characterization, for example frustrated phases [Moessner and Ramirez, 2006], and are hot topics in condensed matter physics.

In the presence of a strong enough external magnetic field, all spins tend to align into its direction, constituting what is called a paramagnetic phase. A spin system will be in a paramagnetic phase rather than in the interacting spin-ordered phase as soon as the energy it gains due to the coupling to the magnetic field, given by the single-particle Hamiltonian $-(1/2)\,\mu_{\mathrm{B}}\,\hat{\boldsymbol{\sigma}}\cdot\mathbf{B}$, overcomes the energy gained due to the interaction. Varying the amplitude of the external field, the system undergoes a quantum phase transition, a phenomenon actively studied both theoretically and experimentally [Sachdev, 2011]. Other phenomena of interest originate from the out-of-equilibrium physics occurring in these systems while abruptly tuning external parameters, which can in some cases be seen as a dynamical quantum phase transition [Heyl, 2019].

Hard-core boson Hamiltonian Another important kind of Hamiltonians of interest in condensed-matter physics are hopping Hamiltonians (the tight-binding model is the limit $U = 0$ of the Fermi-Hubbard model). They capture most of the transport properties of materials, accounting for the distinction between conductors and insulators by computing the dispersion relation (band structure). Among insulators, new sort of phases are intensively being explored, topological insulators [Qi and Zhang, 2011], for their unique transport properties [Moore, 2010].

Rather than the Fermi-Hubbard model, I focus on the (spinless) Bose-Hubbard model, describing the hopping physics for bosons in a lattice. The quantum operators

acting on bosons are the creation $\hat{b}_i^\dagger$ and annihilation $\hat{b}_i$ operators. As in the fermionic case, the hopping of a boson from site i to j simply reads in terms of operators $\hat{b}_i\hat{b}_j^\dagger$, and the hopping term in the Bose-Hubbard Hamiltonian is written $J_{ij}\left(\hat{b}_i\hat{b}_j^\dagger + \hat{b}_i^\dagger\hat{b}_j\right)$, with J_{ij} the hopping amplitude. In addition to the hopping term, the Bose-Hubbard Hamiltonian takes into account the chemical potential μ and the on-site interaction U between bosons with the single-site term $-\mu\hat{n}_i$ and $U\hat{n}_i\left(\hat{n}_i - 1\right)$, with $\hat{n}_i = \hat{b}_i^\dagger\hat{b}_i$ gives the number of bosons on site i. This Hamiltonian is known to describe the transition between a superfluid and a Mott insulator. In the peculiar case of an infinite on-site interaction energy, each lattice site can host either zero or one boson, and the Bose-Hubbard model reduces to a hard-core boson Hamiltonian.

Actually, the XY and the hard-core boson Hamiltonians reduce to the same physical situation. Indeed, the XY interaction term acting on the pair state of spins $|\uparrow\downarrow\rangle$ transforms it into $|\downarrow\uparrow\rangle$, which means that the two spins have exchanged their states. This is why the XY Hamiltonian is sometimes referred to as a spin-exchange Hamiltonian. Rather than spins, we can see $|\uparrow\rangle$ as being a lattice site occupied by one particle and $|\downarrow\rangle$ as being an empty lattice site. The spin-exchange process is then equivalent to the hopping of one effective particle between the two sites. As there are only two levels involved, no state corresponds to a lattice site occupied by two or more particles, so two bosons cannot be on the same lattice site, they have infinite on-site interaction energy. As a consequence, implementing the XY Hamiltonian for spins allows also for the study of hopping hard-core bosons.

Finally, adding a magnetic field acting on these hopping particles extends even more the range of exotic phenomena potentially exhibited by this model, the most famous one being the quantum Hall effect [Klitzing, Dorda, and Pepper, 1980]. The action of the magnetic field can be taken into account directly in the hopping term, by writing complex hopping amplitudes. Then, having complex hopping amplitudes mimics the effect of an external magnetic field, even in the case of uncharged particles, and gives rise to an artificial gauge field [Aidelsburger, Nascimbène, and Goldman, 2018].

I have presented two types of Hamiltonian, enabling for the explanation of several many-body phenomena and promising the understanding of other exotic ones. I am now going to describe examples of their implementation on three different kinds of platforms, allowing for their study on a controlled artificial system.

1.2 A short overview of quantum simulation

In order to engineer the aforementioned Hamiltonians, a quantum simulator needs to fulfill several constraints. The first requirement is to have an ensemble of particles in a controlled geometrical configuration, mimicking the lattice structure. The ability for the particles to tunnel between lattice sites leads to the engineering of some hopping Hamiltonians. To mimic spin-1/2 physics, one should define a two-level system, i.e. a qubit, considering two quantum states of the particle. Then, if the interaction only involves the two considered states of the particles, the Hamiltonian of the controlled system can be mapped into a spin Hamiltonian. For the one-body operator of spin Hamiltonians, driving transitions between the two states of the qubit imitates the behavior of an external magnetic field on the effective spin-1/2. Indeed, both the driving of a qubit and the coupling of a spin-1/2 to a magnetic field can be formally written as rotations of the two-level system. Finally, to perform quantum simulations, the experimentalists must have access to the populations, for each qubit, in the two levels.

Quantum simulation then relies on rewriting the engineered interaction within the system under control in terms of spin or bosonic operators, in such a way that a mapping exists between the physical situation in the laboratory and the targeted model. To be more precise on the quantum simulation field, this is known as *analog* quantum simulations, where an artificial system, albeit physically quite different, obeys the same equation of evolution as the modeled system. In the experiments presented in this manuscript, we perform this kind of quantum simulation. Actually, it exists two other more abstract approaches, known as *digital* and *variational* quantum simulations.

Digital quantum simulation relies on the possible formal decomposition, referred to as the Trotter formula [Lloyd, 1996], of the evolution operator of a many-body system into a series of one- and two-body operators. The asset of this approach is that many different Hamiltonians can be studied that way, in a close correspondence to Richard Feynman's original idea. The drawback of this approach is that it requires the piling of a lot of quantum gates. Even if the single- and two-body operations show very high fidelity in ion- or superconductor-based platforms, the increasing complexity of the series of gates that must be performed would eventually be detrimental to the efficiency of this approach.

Another hybrid approach has been developed more recently, variational quantum simulation. It is expected to simulate as complex Hamiltonians as digital quantum

simulation but requiring less quantum operations. It is based on a feedback loop between an analog quantum simulator providing entangled trial wavefunctions and classical optimization algorithms to determine in an iterative way the solution to a given problem.

I now briefly explain how several experimental teams have succeeded in implementing the aforementioned Hamiltonians using degenerate quantum gases [Bloch, Dalibard, and Nascimbène, 2012; Tarruell and Sanchez-Palencia, 2018], trapped ions [Blatt and Roos, 2012] or superconducting circuits [Houck, Türeci, and Koch, 2012]. The few examples I describe are not an exhaustive list.

Ultracold quantum gases I start this short overview by the quantum simulators based on degenerate quantum gases. To get the particles in a controlled spatial configuration, experimental groups mostly use periodic trapping potential, coming from standing waves of off-resonant light, known as optical lattices [Bloch, 2005]. The lattice is filled by making the degenerate gas undergo the phase transition between a superfluid and a Mott insulator [Greiner *et al.*, 2002]. Using high-numerical aperture optics, some experimental groups are nowadays able to reach single-site resolution and locally probe the occupancy of each lattice site. These platforms are referred to as quantum gas microscopes [Bakr *et al.*, 2009]. They provide the largest controlled systems, as compared to the other platforms I will describe. The ability to perform local operations on the encoded qubits inside an optical lattice by using addressing light-shifts was demonstrated [Wang *et al.*, 2015].

By playing on the relative phase and amplitude of the beams generating the optical lattice, complex lattice structure can be engineered. Varying the lattice depth controls the tunneling amplitude of the particles between neighboring sites, resulting in tunable quantum simulators of hopping Hamiltonians. Based on the imaging of the quasi-momentum distribution, several groups have been able to measure characteristic properties of the implemented Hamiltonian. The group of Prof. Tilman Esslinger, for example, was able to produce a honeycomb lattice, and observe signatures of the Dirac points [Tarruell *et al.*, 2012], an emblematic feature of the band structure associated to this geometry. The group of Prof. Immanuel Bloch measured the Zak phase related to the band structure for a dimerized chain [Atala *et al.*, 2013]. The Zak phase, or in higher dimensions the Chern numbers, are topological invariants classifying the different phases with respect to their topological properties.

On these platforms, the interaction are mainly limited to the on-site range, whose amplitude can be easily tuned, for instance, via Feshbach resonances [Chin *et al.*, 2010].

This leads to the engineering of nearest-neighbour spin-spin interaction via a tunnelling assisted super-exchange process [Duan, Demler, and Lukin, 2003]. Nearest-neighbor spin-spin interaction can also be implemented using doublon-hole excitations of a Mott insulator in a tilted 1D optical lattice [Sachdev, Sengupta, and Girvin, 2002]. Following this approach, the group of Prof. Markus Greiner was able to observe 1D Ising antiferromagnets [Simon *et al.*, 2011]. Longer-range interaction may emerge using particles exhibiting a permanent dipole moment, such as magnetic atoms [Lepoutre *et al.*, 2019] or polar molecules [Gorshkov *et al.*, 2011; Goban *et al.*, 2018].

The platforms described so far rely on a "top-down" approach. Starting with a macroscopic, quantum degenerate assembly of indistinguishable particles, the system reduces to effective spins interacting on a lattice, or hopping particles. The loading of an optical lattice is necessary to imitate the Hamiltonians described in Section 1.1, but actually, other phenomena can be simulated without performing this experimental high-demanding task. For example, some groups have explored the propagation of matter waves in disordered potential [Billy *et al.*, 2008], or studied exotic phases of matter, such as the BEC-BCS crossover [Navon *et al.*, 2010; Ku *et al.*, 2012], quantum droplets [Ferrier-Barbut *et al.*, 2016; Cabrera *et al.*, 2018] or supersolids [Léonard *et al.*, 2017; Böttcher *et al.*, 2019; Chomaz *et al.*, 2019]. The advantage of this top-down approach is that it intrinsically provides a system with a large number of particles, in a thermal equilibrium. Using a quantum gas microscope leads to the control of the thermodynamic properties at an exquisite level. Indeed, the group of Prof. Markus Greiner succeeded in getting a higher fraction of the entropy on the edges of an optical lattice, in order to generate in the bulk of the lattice the largest antiferromagnetic correlations ever observed on a artificial state [Mazurenko *et al.*, 2017].

The two other platforms I am going to describe, and the platform I worked on during my Ph.D. are on the contrary based on a "bottom-up" approach. They consist in first controlling a single quantum object, and then adding more and more objects to have an assembly of interacting qubits. They involve fewer interacting particles than the quantum-gas platforms, but at a better level of single-particle control and a wider range of possible types of interactions.

Trapped ions I now turn to ion-based quantum simulators. Most of these platforms rely on ionic crystals in a linear Paul trap [Raizen *et al.*, 1992], exhibiting very high fidelity single- or two-qubit operations [Blatt and Wineland, 2008]. The largest systems are 1D chains of a few tens of qubits, but the extension to higher dimensions or to larger number of interacting particles is extremely challenging. The spin-spin

interactions are engineered using a laser coupling between the internal states of the ions and the collective vibrational modes of the ionic crystals [Cirac and Zoller, 1995; Porras and Cirac, 2004; Kim *et al.*, 2011]. They were shown to decay as $1/R^\alpha$, R being the inter-ion distance, where α can be tuned between 0 and 3, potentially leading to very long-range interactions.

The high fidelity of two-qubit operations on ion-based platforms allows the group of Prof. Rainer Blatt to perform digital [Lanyon *et al.*, 2011] or variational [Kokail *et al.*, 2019] quantum simulations.

Superconducting circuits Finally, I briefly mention the case of superconducting qubits. They triggered a lot of interest since they have been proved to behave as artificial atoms [Nakamura, Pashkin, and Tsai, 1999; You and Nori, 2005]. The technology has considerably improved so that nowadays, superconducting qubits are available at an excellent level of control [Paik *et al.*, 2011; Barends *et al.*, 2013]. Inter-qubit coupling have been implemented using either the exchange of microwave photons in cavity [Wallraff *et al.*, 2004; Dalmonte *et al.*, 2015] or the mutual inductance [Chen *et al.*, 2014]. On these solid-state devices, the interactions can be highly tunable as they do not rely on the geometrical arrangement of the qubits, but on the inter-connecting wiring. Nevertheless, tailoring these interactions for an increasing number of qubits while keeping the same level of control is quite challenging.

The performance of the superconductor- and ion-based platforms are then similar : they exhibit an outstanding fidelity for single- or two-qubit operations, but the scaling to larger number of qubits has not been proven yet. Their potential integrability and on-chip compactness makes them promising candidates for the future of quantum information [Devoret and Schoelkopf, 2013], and attracted world-leading companies such as Google or IBM to invest in this technology. On these platforms, some groups have already explored the digital quantum simulation of spin dynamics [Salathé *et al.*, 2015], the variational calculation of molecular energies [O'Malley *et al.*, 2016], or the analog quantum simulation of hopping Hamiltonians [Roushan *et al.*, 2017b].

Figure 1.1 compares the numbers of qubits involved in these different types of quantum simulators. The ones based on degenerate quantum gases provide the largest number of interacting particles whereas the two bottom-up approaches show the best fidelity for one- or two-qubit operations, and highly-tunable interaction at the single-particle level. Another criterion to compare these platforms is the cycling experimental time. For ultracold gases, the cycling experimental time is usually a

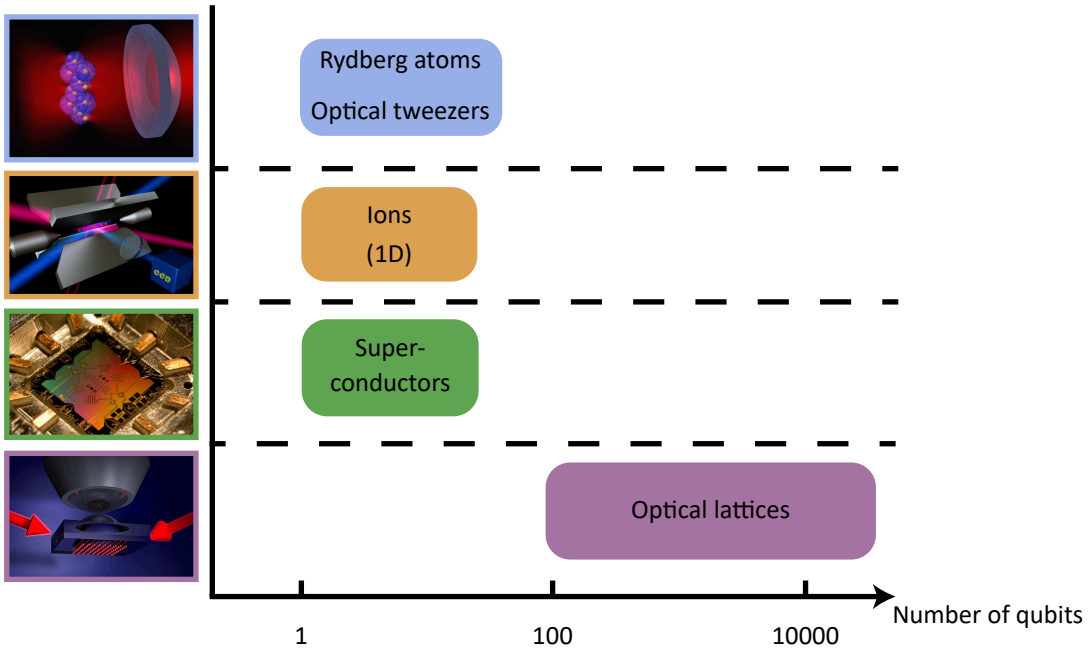

Figure 1.1: Experimental platforms for quantum simulation. The color patches indicate the typical number of qubits involved in different types of quantum simulators. The near-by images with an associated color frame are representative pictures of the platform. The purple one is a sketch of a quantum gas microscope[1]. The green one is a picture of a nine-superconducting-qubit device[2]. The yellow one is a sketch of an ion Paul trap[3]. The blue one represented sixteen atoms trapped in optical tweezers and excited to Rydberg states.

few tens of seconds. On the contrary, for ions, the time limiting factor comes from the read-out of the ion state, which can be as fast as a few milliseconds, leading to a cycling experimental rate close to 100 Hz. The cycling rate can even be higher for superconducting circuits.

1.3 Rydberg-based quantum simulators

I now turn to Rydberg-based platforms, the type of platform I worked on during my Ph. D. thesis. I will give a complete description of our experimental apparatus, one of the first Rydberg-based quantum simulators that have been built, in Chapter 2. In a few words, these platforms combine the trapping of several single neutral atoms in

[1]https://news.harvard.edu/gazette/story/2009/11/quantum-gas-microscope-created/
[2]https://web.physics.ucsb.edu/ martinisgroup/
[3]https://quantumoptics.at/en/research/quiqs.html

configurable arrays of optical tweezers and the coupling to Rydberg states. These states are highly excited states corresponding to a large principal quantum number $n \gtrsim 20$, exhibiting exaggerated properties [Gallagher, 1994]. In particular, their enhanced electric dipoles lead to large and tunable interactions, and their extended lifetimes ensure long coherence times.

Interacting Rydberg gases The first proposals aiming at performing quantum gates with Rydberg atoms relied on the Rydberg blockade [Jaksch *et al.*, 2000; Lukin *et al.*, 2001]. I will detail its mechanism in the beginning of Chapter 4. Its origin is the distance-dependent energy shift experienced by neighbouring interacting Rydberg atoms, which prevents the simultaneous excitation of several atoms to the Rydberg states, as one atom being in the Rydberg state brings its neighbours out of resonance. This results in the generation of entangled states with one Rydberg excitation shared among mesoscopic atomic assemblies. The first experiments were performed on dilute gases, and showed signatures of the Rydberg blockade by measuring a reduced number of excited atoms [Tong *et al.*, 2004; Singer *et al.*, 2004; Vogt *et al.*, 2006]. Then, some evidence of the coherence of the collective excited states were reported, still on dilute gases platforms [Heidemann *et al.*, 2007; Raitzsch *et al.*, 2008; Pritchard *et al.*, 2010]. A review on these studies of interacting Rydberg gases can be found in [Löw *et al.*, 2012].

Using optical tweezers In order to get a better control on the interaction, the team I joined for my Ph. D. chose to work with single atoms loaded in optical tweezers instead of dilute gases. Optical tweezers are tight confining optical dipole traps, and they were proven to be reliable single-atom sources in pioneering experiments performed at the Institut d'Optique, by the team of Prof. Philippe Grangier [Schlosser *et al.*, 2001]. Then, it is possible to control the interatomic distance, hence the interaction, between single atoms. This led the hosting team to observe the Rydberg blockade between two atoms [Gaëtan *et al.*, 2009], jointly with the group of Prof. Mark Saffman in a similar setup [Urban *et al.*, 2009]. The two groups then improved their control of this two-atom system, and reported the generation of entangled states [Wilk *et al.*, 2010], or the realization of the two-qubit C-NOT gate [Isenhower *et al.*, 2010].

Towards quantum simulation with Rydberg atoms Since these first experimental demonstrations, arrays of Rydberg atoms were considered as a promising platform for quantum simulation experiments [Weimer *et al.*, 2010]. The use of a versatile array of

optical tweezers enables for the engineering of any lattice geometry, whose lattice constant can be as small as a few microns. The interatomic distance is larger than in the case of optical lattices, which eases the single-site resolution of the lattice and local operations on the encoded qubits. Even for an interactomic distance of a few tens of microns, the interaction between Rydberg atoms can be on the MHz range, whereas their lifetimes is around a hundred of microseconds. Consequently, the typical timescale of the interacting dynamics is much smaller than the coherence time of the system, leading to its observation in a laboratory.

One of the advantages of using Rydberg atoms for quantum simulation purposes is that they can interact within different regimes, in such a way that they naturally implement different kinds of Hamiltonians. I refer to Appendix A for a detailed description of these regimes of interaction, and their links to the Hamiltonians presented in Section 1.1. In a few words, we have used in the experiments presented in this manuscript the van der Waals and the resonant dipole-dipole regimes. We can choose to work within one of the two regimes by encoding the qubit into a specific set of two atomic levels.

If the encoded qubit basis is $\{|g\rangle, |r\rangle\}$, with $|g\rangle$ the electronic ground state and $|r\rangle$ a Rydberg state, the atoms interact within the van der Waals regime. In that case, the interaction results in an energy shift of the doubly excited pair state $|rr\rangle$, which is at the origin of the Rydberg blockade mechanism I mentioned above. Then, the interaction between two atoms labeled i and j reads $U_{ij}\hat{n}_i\hat{n}_j$, with $\hat{n}_i = |r\rangle_i \langle r|_i$ the local projector on the Rydberg state, and U_{ij} is the van der Waals energy shift. Considering $|g\rangle = |\downarrow\rangle$ and $|r\rangle = |\uparrow\rangle$ leads to rewrite the interaction in terms of spin operators. As $\hat{n} = (1 + \hat{\sigma}^z)/2$, the interaction between two atoms is in the end $\propto \hat{\sigma}_i^z\hat{\sigma}_j^z$, implementing an Ising-like model. Combined with a laser field coupling the two qubit states $|g\rangle$ and $|r\rangle$, we can simulate an Ising-like model in the presence of effective transverse and longitudinal magnetic fields.

If the qubit is encoded into two dipole-coupled Rydberg states, for example a nS state and a $n'P$ one, the correct regime is in that case the resonant dipole-dipole interaction. Under the influence of this interaction, a pair of Rydberg atoms in the $|nS, n'P\rangle$ state will evolve back and forth between this state and the $|n'P, nS\rangle$ one [Barredo *et al.*, 2015], in the same kind of spin-exchange process I mentioned above (Section 1.1). This is why this interaction implements the XY model, or hard-core boson Hamiltonians. The use of a microwave field coupling $|nS\rangle$ and $|n'P\rangle$ imitates the behavior of a magnetic field in the context of spin Hamiltonians, or a chemical potential in that of hard-core boson Hamiltonians.

Our group first characterized the aforementioned different regimes of interaction between a few Rydberg atoms, resulting in several publications reviewed in [Browaeys, Barredo, and Lahaye, 2016]. Then, the team studied Hamiltonians involving a few tens of Rydberg atoms, with the implementation of an Ising-like model [Labuhn *et al.*, 2016]. The limitation at that time of Rydberg-based platforms was due to the stochastic loading of the optical tweezers by single atoms. I will come back to that point in Chapter 2. The basic idea is that our loading protocol of the optical tweezers implied that only half of them were randomly loaded by single atoms, preventing us to work with a targeted atomic configuration. We developed then an atom-by-atom assembling technique, consisting in moving the atoms in the array to fully load a targeted sub-array of optical tweezers [Barredo *et al.*, 2016]. A similar assembling process was developed at that time by the group of Prof. Mikhail Lukin [Endres *et al.*, 2016] and by the one of Prof. Jaewook Ahn [Kim *et al.*, 2016]. Very recently, a similar approach was implemented in the group of Prof. Gerhard Birkl [Ohl de Mello *et al.*, 2019].

Current Rydberg-based quantum simulators Figure 1.2 summarizes the basic ingredients used on Rydberg-based platforms to perform quantum simulation: defect-free atomic structures, one- and two-qubit operations and tunable interaction. The coherence and fidelity of the one- and two-qubit operations have considerably improved recently, as demonstrated by the group of Prof. Mikhail Lukin [Levine *et al.*, 2018, 2019], reaching a level of control closer and closer than those shown by ion- or superconductor-based platforms. It is now possible to generate entangled states involving up to 20 qubits [Omran *et al.*, 2019]. To compare these platforms to the other ones described in Section 1.2 (see Figure 1.1), they provide a similar number of qubits than ion- or superconductor-platforms, but in a more versatile configuration (we demonstrated the generation of 3D atomic structures [Barredo *et al.*, 2018]). The cycling experimental rate, limited by the necessary loading of the optical tweezers and the imaging time, is on the order of a few Hz.

The tunability of Rydberg-based platforms allowed us to study a bosonic version of the Su-Schrieffer-Heeger model and to observe signatures of a topological phase with interactions [de Léséleuc *et al.*, 2019], which would be extremely hard in other types of quantum simulators. This is why Rydberg-based experimental apparatuses are nowadays very attractive and competitive platforms to perform quantum simulation of many-body physics.

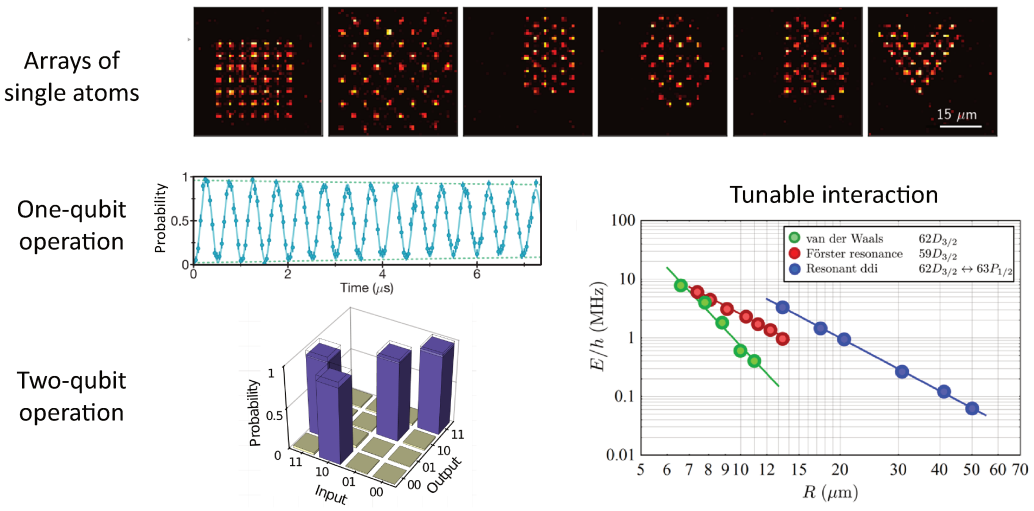

Figure 1.2: Quantum simulation with Rydberg atoms. Key ingredients to perform quantum simulation with Rydberg atoms. (Top) Single-shot fluorescence images of defect-free assemblies of single atoms [Barredo *et al.*, 2016]. (Left) High-fidelity one- and two-qubit operations. The one-qubit operation is a Rabi oscillation between the electronic ground state and a Rydberg state, showing high contrast and coherence [Levine *et al.*, 2018]. The two-qubit operation is the logical C-NOT gate [Levine *et al.*, 2019]. (Right) Interaction energies as a function of the distance between two Rydberg atoms, for different regimes [Browaeys, Barredo, and Lahaye, 2016]. The green disks correspond to the van der Waals regime, whereas the blue disks correspond to the resonant dipole-dipole one, the two regimes used in this manuscript.

Thesis outline During my time at the Institut d'Optique, I participated in a few projects which I will report in this manuscript. Some of them were dedicated to the improvement of our experimental apparatus (Part I). I will detail the assembling technique, extended to the generation of 3D atomic structures (Chapter 2). I will also report our ability to trap atoms excited to the Rydberg states in Chapter 3. The other projects concerned quantum simulation. In Part II, I will describe our observation of spin-ordered phases, in the Ising case (Chapter 4) and the XY one (Chapter 5). Finally, Part III is dedicated to the study of hopping Hamiltonians, and I will report our implementation of complex hopping amplitudes using the intrinsic spin-orbit coupling of the dipole-dipole interaction (Chapter 6), leading to the emergence of a gauge field.

Part I.

Arrays of single atoms

Chapter 2

Overview of the experimental apparatus

Contents

In the Introduction, arrays of Rydberg atoms were presented as one of the best platforms to perform quantum simulation. The aim of the present chapter is to describe the experimental procedures we follow to obtain the starting point of quantum simulation experiments, an assembly of qubits in a well-controlled initial state. Our experimental setup was built by Lucas Béguin and Aline Vernier, and then was upgraded by the following generations of Ph.D. students and post-doc : Sylvain Ravets, Henning Labuhn, Sylvain de Léséleuc and Daniel Barredo. I will briefly recall the working principles of the different steps of our experimental protocol, referring to their Ph.D. theses for further information. Most of the experimental results shown in this chapter were already presented in the thesis of Sylvain de Léséleuc [2018].

I will first describe in Section 2.1 the elementary building block of our experimental apparatus, the trapping of a single atom in an optical tweezers. Then, I will explain in Section 2.2 how we generate fully-loaded arrays of atoms. Finally, in Section 2.3, I will present the Rydberg excitation scheme in the single-atom regime, i.e. without taking into account interaction which will be the topic of the following chapters.

2.1 A single atom in an optical tweezers

One of the requirements for quantum simulation is to isolate and control one single quantum object. To do so, the tool we are using in our experiment is an optical tweezers [Ashkin *et al.*, 1986], to trap a single ^{87}Rb atom. Optical tweezers are now commonly used to trap various types of objects [Jones, Marag, and Volpe, 2015], and its application for single-atom trapping was first demonstrated in our lab, in a pioneering work of the team led by Philippe Grangier [Schlosser *et al.*, 2001]. In this section, I will first explain how we load and detect a single atom in an optical tweezers. Then, I will describe the different steps of the experimental sequence after loading, enabling the preparation of the atom in a specific hyperfine level of the electronic ground state. For this preparation we need to control the magnetic field inside the chamber. I will show in a third part how we measure the generated magnetic field using microwave manipulation of the electronic ground state.

2.1.1 Loading of an optical tweezers and single-atom imaging

The usual way to trap matter using light is to shine a far off-resonance red-detuned laser beam on particles. Indeed, light induces an electric dipole on the particle, which tends, to minimize its energy, to seek high-intensity regions. The trapping potential created that way U is such that $U \propto I/\Delta$, where I is the laser beam intensity and Δ is the (negative) detuning. When such a dipole trap is focused on a small volume, on the order of $\approx 1\,\mu\text{m}^3$, we create a so-called *optical tweezers*.

Tight focusing of a dipole trap beam In order to obtain an optical tweezers, one needs to focus light near the diffraction limit. Our group has been working on optical tweezers for about twenty years, and their generation has been successfully demonstrated with different techniques. At first, the careful design of a home-made microscope objective [Vigneron, 1998] allowed the team to achieve this goal in their

pioneering experimental setup, MIGOU. Then, the experimental effort was focused on simplifying the optical setup using a single large-numerical-aperture aspheric commercial lens [Sortais *et al.*, 2007; Fuhrmanek, 2011], in the second generation of the experimental platform, ASPHERIX. I have been working during my Ph.D. on the third setup generation, CHADOQ. Here, the light is also focused using a large-numerical-aperture aspheric lens (NA = 0.5, focal length $f = 10\,\mathrm{mm}$), which was designed by Lucas Béguin [2013]. From now on, I will only consider this experimental apparatus.

Describing it in a few words, the part under vacuum of the experimental setup is composed of two chambers connected by a Zeeman slower. The first one acts as an atom source. It contains solid Rubidium crystals heated up by an oven. A small aperture in one wall of the first chamber generates a directive atomic beam at room temperature inside the Zeeman slower. The Zeeman slower decelerates the atoms to a few mK, and the atoms arrive in the second, ultra-high vacuum, chamber. There, in addition to the aspheric lenses, the vacuum chamber contains coils and electrodes to control the magnetic and electric fields. The aspheric lenses are coated with a thin layer of ITO to avoid the accumulation of charges. In combination with the under-vacuum electrodes, these two ingredients allow for the cancellation of the electric field near the atoms, which was not the case in the previous experimental apparatuses. This significantly improved the coherent excitation of the atoms towards Rydberg states.

Loading of single atoms in an optical tweezers Now, I explain how our experimental setup enables the trapping of single atoms. The experimental setup is represented in a simplified way in Figure 2.1. A far off-resonance red-detuned 852-nm dipole trap beam (represented in red) is focused by the aspheric lens inside the vacuum chamber on a cloud of ^{87}Rb atoms at $\approx 100\,\mu$K, created thanks to the combination of a Magneto-Optical Trap (MOT) and a Zeeman slower (not shown in Figure 2.1 and along the y-axis on the experimental apparatus). The MOT light, consisting of six counterpropagating beams (represented in orange) slightly red-detuned from the D_2 line of the ^{87}Rb, slows down the atoms in the three directions of space via a resonant-light-induced friction force. As in most of the cold atoms experiments, the MOT light whose frequency is set on the cycling transition $\left|5S_{1/2}, F = 2\right\rangle \rightarrow \left|5P_{3/2}, F = 3\right\rangle$ comes along with a repumper light set on the transition $\left|5S_{1/2}, F = 1\right\rangle \rightarrow \left|5P_{3/2}, F = 2\right\rangle$. A pair of coils inside the vacuum chamber, in an anti-Helmholtz configuration, generates a magnetic field gradient. Outside the chamber, six compensation coils make it possible to adjust the position of the magnetic field zero, and are used to tune the position of

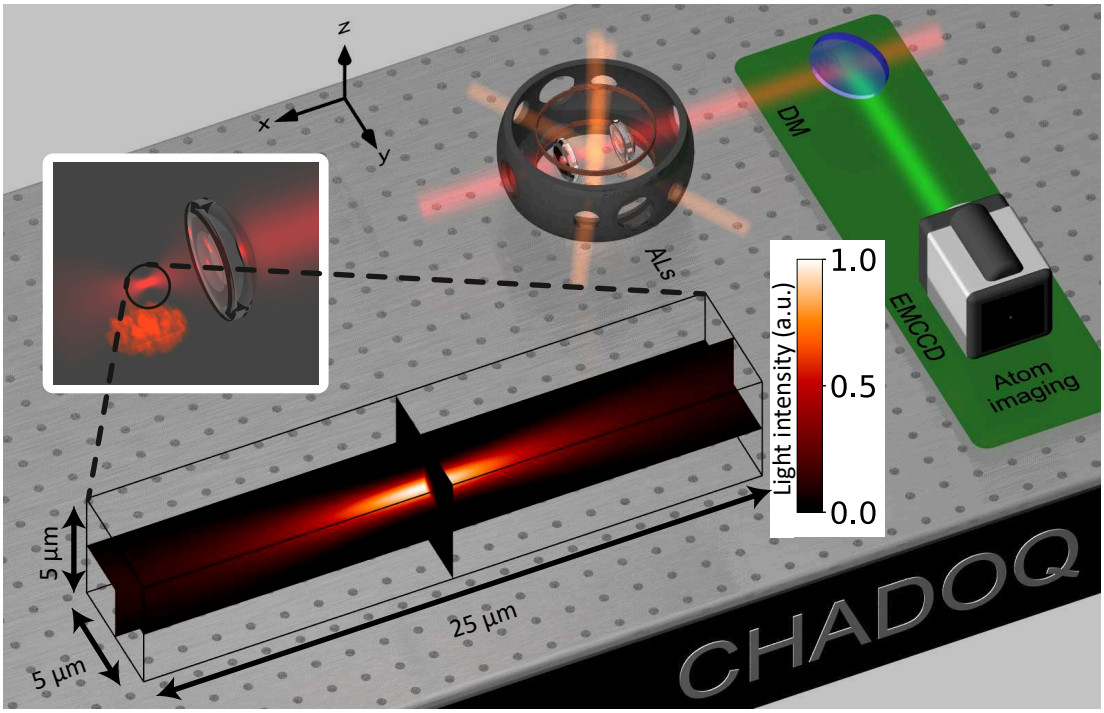

Figure 2.1: Trapping and imaging a single atom. The dipole trap beam at 852 nm (red) is focused inside a vacuum chamber using aspheric lenses (ALs). Six counterpropagating beams (orange) constitute the MOT light. The light scattered by the atom at 780 nm (green) is reflected by a dichroic mirror (DM) and imaged on the EMCCD camera. Top-left inset, zoom inside the vacuum chamber, where the tight focusing of the laser beam into an optical tweezers is shown. The orange cloud represents the atomic cloud. The 2D-cuts of the spatial intensity distribution of a Gaussian laser beam are shown in the bottom left corner. The spatial profile is Gaussian in the radial direction (yz plane), and is a Lorentz function in the longitudinal one (x direction).

the atomic cloud.

The dipole trap beam tight focusing results in an optical tweezers. The intensity profile is Gaussian, with a $1/e^2$ radius $w \approx 1\,\mu$m and Rayleigh length $z_R \approx 4\,\mu$m (see inset of Figure 2.1). Then, for about 5 mW of laser power, we obtain a trap depth $U_0/k_B \approx 1$ mK. Once the position of the atomic cloud is properly set near the optical tweezers, the atoms are cooled enough to fall in the dipole trap. The tight confinement resulting from the optical tweezers trapping potential, in addition to the MOT light shone on the atoms, make the system enter the *collisional blockade* regime, which prevents two atoms to be in the optical tweezers at the same time. Indeed, in this regime, two atoms inside one trap undergo fast inelastic light-assisted collisions, and the energy the atoms gain during this type of collisions is enough to expel both of

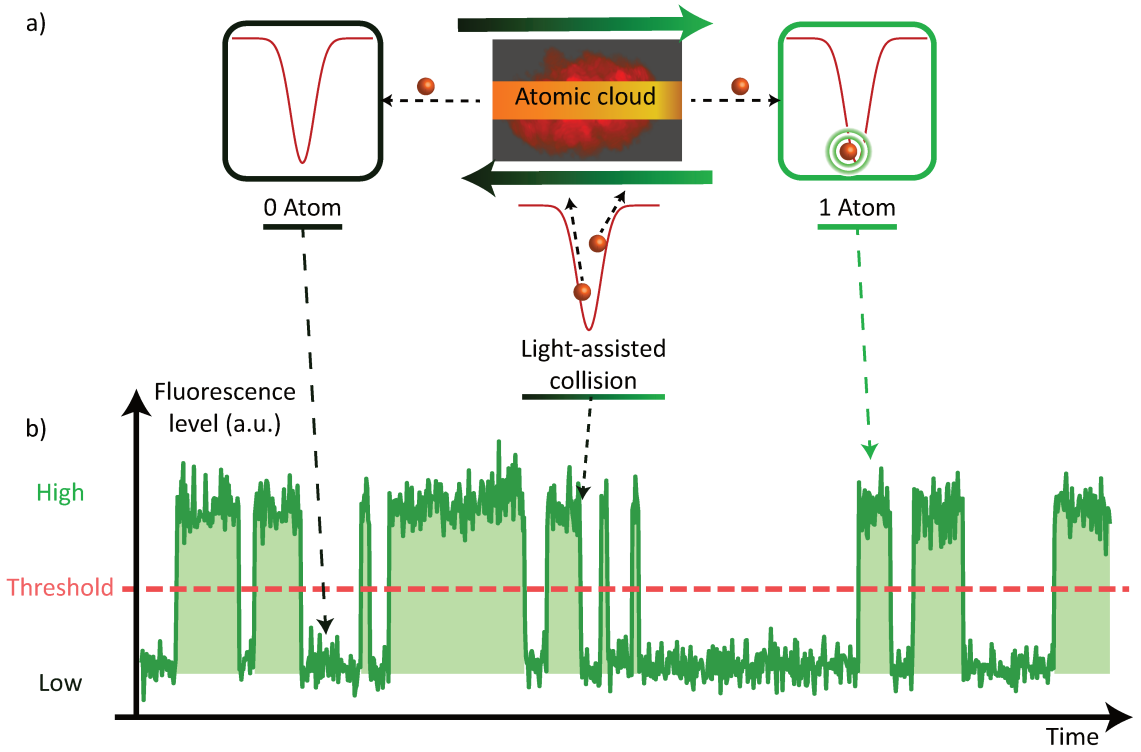

Figure 2.2: Stochastic loading of single atoms. (a) Two loading states of the optical tweezers: empty (dark frame) or occupied by one atom (green frame). The tweezers toggles between these two states due to the same phenomenon, an atom from the atomic cloud entering the trapping region. Once the atom is inside the optical tweezers, it scatters 780 nm fluorescence light (green circles). The two-body loss process due to light-assisted collisions is represented in a schematic way. (b) Fluorescence signal emitted from the optical tweezers area. The red line is a threshold allowing us to discriminate between the two loading states of the tweezers.

them out of the trap (see for example [Fuhrmanek *et al.*, 2012]). The loading of the optical tweezers then works as follows: When it is empty, an atom from the atomic cloud enters the trap and the tweezers becomes loaded by one atom; on the contrary, when the optical tweezers contains one atom, another atom from the atomic cloud can enter the trap and due to the inelastic collisions the tweezers becomes empty very quickly (see Figure 2.2(a)). Consequently, the optical tweezers only has two possible loading states, it holds zero or a single atom. As the same probabilistic event, an atom from the atomic cloud entering the optical tweezers, makes the optical tweezers toggle between its two possible loading states, both loading states are equally probable, or, in other words, the optical tweezers has a 50% chance to be loaded by a single atom. To sum up, the combination of the atomic cloud and the optical tweezers enables a

stochastic loading of the latest by single atoms.

Imaging of a single atom Once an atom is loaded in the optical tweezers, it scatters the MOT light in all directions. Part of this fluorescence light is collimated by the very same aspheric lens, separated from the dipole trap beam using a dichroic mirror, and imaged on an electron multiplying CCD camera (EMCCD Andor iXon Ultra 897). The fact that we are using the same optics for trapping and imaging is very convenient in terms of optical access, and was a strong constraint while designing the optics, which have to work at two different wavelengths, 852 nm and 780 nm [Béguin, 2013]. The imaging optical setup was designed in such a way that the radial size of one optical tweezers (about 1 μm) matches the size of one pixel of the Andor Camera (16 μm), to improve the signal to noise ratio. A typical fluorescence signal corresponding to the image of one optical tweezers (only a few pixels of the EMCCD camera were taken into account) is shown on Figure 2.2(b). We clearly see two levels of fluorescence, corresponding to the only two possible loading states of the optical tweezers: when the signal is low, the trap is empty, when it is high, the trap contains a single atom. The red line in Figure 2.2(b) corresponds to the threshold level, allowing us to discriminate between the two loading states by measuring the fluorescence signal. The fact that we cannot see a higher third level of fluorescence means that the optical tweezers cannot hold two atoms at the same time. In fact, the timescale of the light-assisted two-body losses (1 ms) is way shorter than the imaging exposure time (20 ms). Single atom loading in optical tweezers within this collisional blockade regime was demonstrated observing this typical two-level fluorescence signal [Schlosser *et al.*, 2001; Schlosser, Reymond, and Grangier, 2002].

Atomic motion inside an optical tweezers Due to its finite temperature T, which can be as low as a few tens of μK using additional cooling procedures described in the next subsection, the trapped atom oscillates around the peak intensity of the optical tweezers. As $k_B T \ll U_0$, the atom stays near the bottom of the trap. We can then approximate the trapping potential as a harmonic potential, characterized by two different frequencies, the radial $\omega_\perp/(2\pi)$ and longitudinal $\omega_\parallel/(2\pi)$ frequencies. The expressions of these frequencies can be written as a function of the trap depth U_0 and the typical length scales of the Gaussian beam profile, w and z_R

$$\omega_\perp = \sqrt{\frac{4U_0}{mw^2}} \quad \text{and} \quad \omega_\parallel = \sqrt{\frac{2U_0}{mz_R^2}} \tag{2.1}$$

where m is the mass of a ^{87}Rb atom.

The statistical distributions of positions and velocities of single atoms loaded in the tweezers follow a Maxwell-Boltzmann distribution. The standard deviation of the velocity distribution is $\sigma_v = \sqrt{k_B T/m}$, and in this harmonic approximation, the standard deviations of the distributions of the radial and longitudinal positions are $\sigma_{\perp,\parallel} = \sqrt{k_B T / \left(m\omega_{\perp,\parallel}^2\right)}$. As we shall see in the next subsection, this statistical description enables us to measure the temperature of the trapped single atoms via a release and recapture experiment (see [Tuchendler *et al.*, 2008]).

2.1.2 Typical experimental sequence

So far, I described the experimental apparatus in its steady state, an optical tweezers stochastically loaded by single atoms. I now present the successive manipulations we do in order to prepare our system in the right initial state to perform quantum simulation experiments, that is to say our typical experimental sequence. This will allow me to introduce the principle of the measurements we do, and to give the main characteristics of the trapped atom (lifetime, temperature, position dispersion inside the tweezers).

Overview of the experimental sequence Figure 2.3 sums up the different steps of the experimental sequence. We start by dispersing the atomic cloud, by turning off the magnetic field gradient shutting down the inner coils current, and switching off the MOT, repumper and Zeeman slower lights. Dispersing the atomic cloud stops the stochastic loading of the optical tweezers. We then take a first fluorescence image of the optical tweezers region in order to check on the presence of the atom. This is done in the same way as in the steady state regime, we shine MOT and repumper lights on the optical tweezers for 20 ms and look at the fluorescence signal on the EMCCD. The next step is the assembly of the atomic array, in the case where we are working with several optical tweezers. This step will be described in Section 2.2.

We then perform a first additional cooling procedure: after setting the values of the currents inside the compensation coils in order to cancel out the magnetic field, we increase the absolute value of the negative detuning of the MOT light to lower the limit temperature of the polarization gradient cooling process [Tuchendler *et al.*, 2008]. The detuning δ_{MOT} is ramped down from $\delta_{\mathrm{MOT}} = -5\Gamma$ to $\delta_{\mathrm{MOT}} = -8\Gamma$, with $2\pi \times \Gamma$ the natural linewidth of the MOT transition. After this first additional cooling

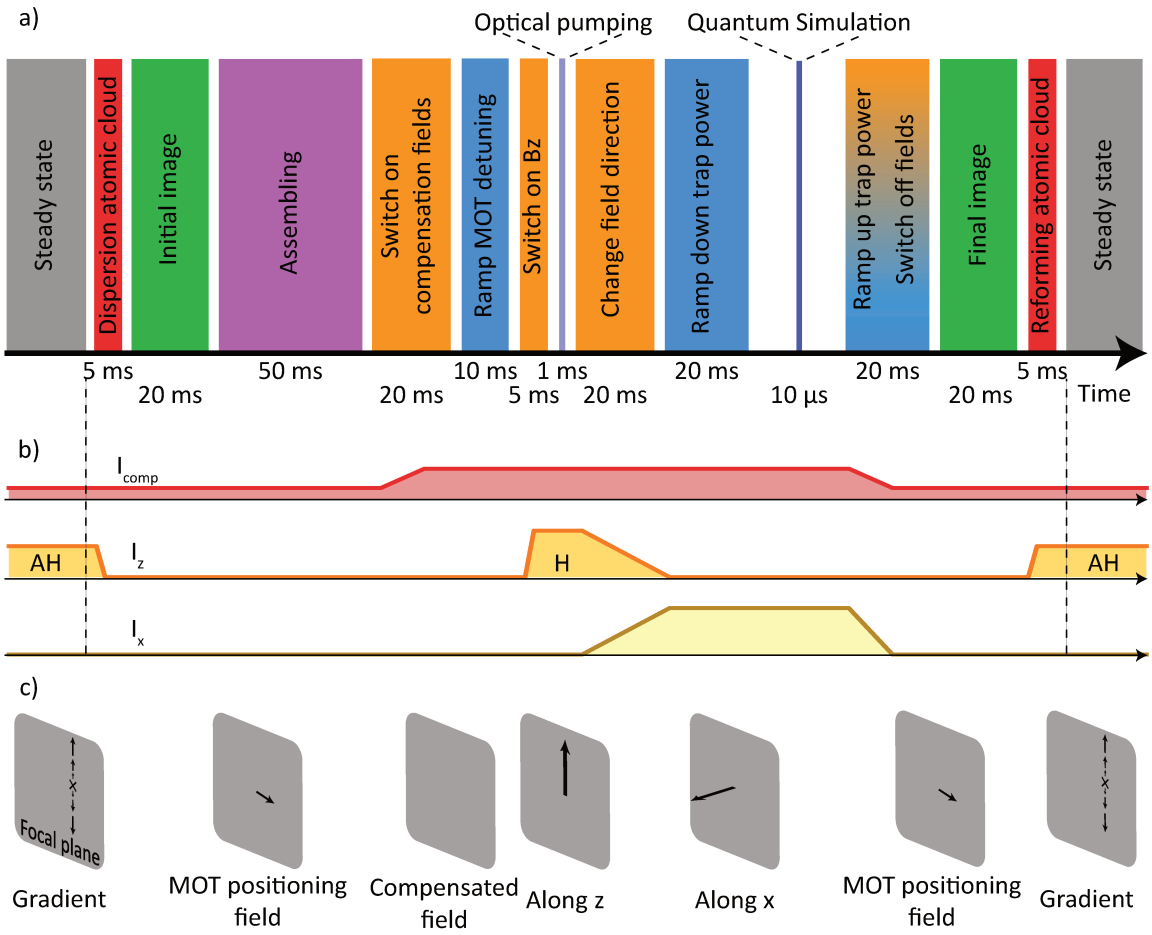

Figure 2.3: Experimental sequence. (a) Summary of the performed actions through the experimental sequence, with their respective durations. (b) Time evolution of the currents inside the different coils, compensation coils (I_{comp}), inner coils along z (I_z) and outer coils along x (I_x). We tune the currents in order to control the magnetic field inside the chamber. (c) Orientation of the magnetic field through the sequence.

step, we toggle the inner coils in a Helmholtz configuration in order to create a magnetic field along the vertical axis. This field, whose value ranges from a few Gauss up to 50 G, defines our quantization axis and lifts degeneracy between the Zeeman levels. Thanks to the defined quantization axis, we can optically pump the atom in a stretched Zeeman level of the $\left|5S_{1/2}, F = 2\right\rangle$ Zeeman manifold sending circular polarized light along the vertical direction. The optical pumping beam is resonant with the D_1 $\left|5S_{1/2}, F = 2\right\rangle \rightarrow \left|5P_{1/2}, F = 2\right\rangle$ transition. During optical pumping, repumper light is also shone on the atom to avoid letting it in one of the $\left|5S_{1/2}, F = 1\right\rangle$ Zeeman levels. In the latest chapter of this manuscript, it will be necessary to change the direction of the quantization axis along the aspheric lenses direction. We do it after

the optical pumping step, by simultaneously decreasing the current in the inner coils and increasing the current in another pair of coils outside the chamber, positioned along the x-axis. Therefore, the norm of the magnetic field stays different from zero and, the atom following adiabatically the orientation of the magnetic field, we do not lose its polarization. After optical pumping, we perform a second additional cooling process by adiabatically decreasing the trap power to a few percents of its initial value [Tuchendler *et al.*, 2008].

The previously described steps have two purposes: the additional cooling of the atoms and their preparation into the state $\left|5S_{1/2}, F = 2, m_F = \pm 2\right\rangle$. At this specific stage of the experimental sequence, we may perform quantum simulation experiments, where the atoms are excited to a Rydberg state (further described in the single-atom case in Section 2.3) and interaction between atoms may play a role. Nearly all the experiments described in the further chapters of this manuscript take place at this precise stage. At the end of the sequence, we take again an image of the atom fluorescence, to determine if the atom is still there. We end the sequence by reforming the atomic cloud and the experimental setup returns back to its steady state regime.

Working principle of the measurement The quantity we are measuring is the fluorescence light emitted from the optical tweezers area. Thanks to the threshold level introduced in Figure 2.2, by measuring the quantity of light we can check on the presence of the atom, at the beginning and at the end of the sequence (see Appendix A of Sylvain de Léséleuc [2018] thesis for more details). Repeating the sequence for a given number N of iterations allows us to measure the probability p for the atom to be recaptured. The error bar on this probability is the standard error on the mean (s.e.m), which is equal to $\sqrt{p\,(1-p)\,/N}$. The error is the biggest for $p = 0.5$. To reach the 5% level of error for this probability we need 100 iterations, and if we want to reach the 2% level of error we need more than 500 iterations. Hence the necessity to have a cycling experimental time as short as possible to be able to repeat a great number of times the experimental sequence and perform more precise measurements. Thanks to recent improvements of the experimental apparatus, we now reach a cycling rate of 3 to 4 Hz.

We can then measure the recapture probability as a function of a varying parameter of the experimental sequence. As we shall see in the next paragraph, this will allow us to measure some trapping characteristics, such as the single-atom lifetime and temperature, and the trapping frequencies. In the case where the recapture depends on the state of the atom, we infer the occupation of the different states via the recapture

probability measurement. For example, atoms in the Rydberg states are not trapped in the optical tweezers, so the probability to lose an atom is the probability to excite it to the Rydberg state. Therefore, our measurement protocol relies on a partial loss of the atoms, it is a destructive measurement. This is why we need to start again the stochastic loading of the optical tweezers at the end of each sequence iteration.

Measurement of the trapping characteristics using the recapture probability
The simplest experiment we can perform is to vary the total duration of the sequence, and measure the recapture probability as a function of this time. The lifetime of the single atom in the optical tweezers is inferred that way, it is measured to be around 20 s. The losses of the single atoms in that case are due to collisions with particles from the background gas at room temperature, and represent the ultimate limit for the possible duration of an experiment. This lifetime would considerably increase in a cryogenic environment, one of the major improvements expected from the next generation experimental apparatus currently developed in our team [Magnan, 2018].

Another quantity that can be inferred from recapture probability measurements is the trapping frequency, via a parametric heating experiment. Indeed, for a precise frequency of the modulation of the trap depth (twice the trapping frequency), we parametrically excite the atom out of the trap, and measure a drop of the recapture probability. Their values were found to be equal to $\omega_\perp/(2\pi) = 50.2\,(3)$ kHz and $\omega_\parallel/(2\pi) = 8.3\,(1)$ kHz. For the same trap, we measure spectroscopically its depth $U_0/h = 5.5\,(1)$ MHz (see Sylvain de Léséleuc [2018]'s thesis) and deduce from Equation (2.1) the dimensions of the Gaussian beam $w = 1.01\,(2)$ μm and $z_\mathrm{R} = 4.31\,(8)$ μm, which are on the expected order of magnitude.

Figure 2.4 shows how we can also determine the temperature of the single atoms using the measurement of the recapture probability in a release and recapture experiment. The experimental sequence is displayed in Figure 2.4(a): starting with an atom in the optical tweezers, we switch off the trap leaving the atom fly away due to its finite temperature (release); and switch on the trap again (recapture) after a time τ. An atom is still trapped in the optical tweezers after a flight of duration τ if the absolute value of the trapping potential at its final position is greater than its kinetic energy.

We measure the recapture probability as a function of the release time τ in three different cases (see Figure 2.4(b)). First (Exp 1), we do it without performing any additional cooling of the atoms. For Exp 2, we cool the atoms using the ramping of the trap power, and for Exp 3 we perform both additional cooling processes, the ramping of the trap power and MOT detuning. The cooler the atoms, the longer they stay around

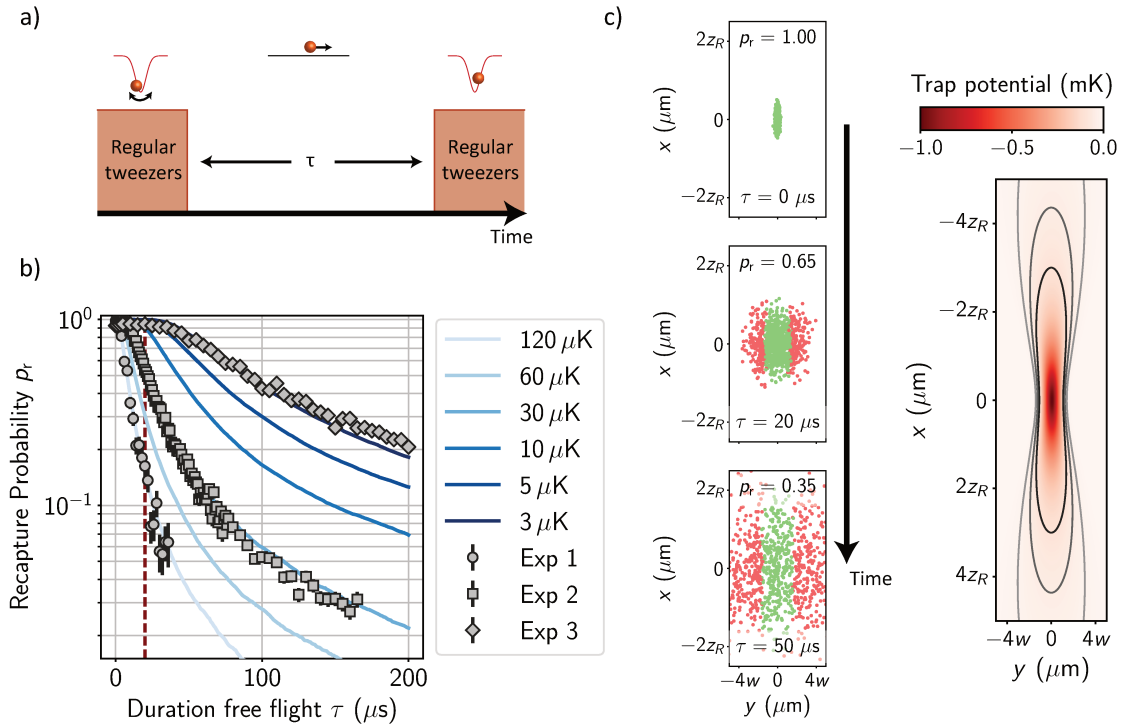

Figure 2.4: Measurement of the single-atom temperature. (a) Principle of the release and recapture experiment. The atom is in free flight for a duration τ. (b) Measured recapture probabilities as a function of τ (solid disks, squares or diamonds) for various cooling procedures. The experimental curves are compared with Monte Carlo simulations for different temperatures. The red dashed vertical line highlights the usual time of flight we use in order to quickly check the temperature of the atoms. (c) Snapshots of the ballistic evolution of atoms in free flight for 1000 different initial conditions (here, only the dynamics in the xy plane was taken into account). Atoms in green would be recaptured after a time of free flight τ, whereas atoms in red would be lost. Right, trapping potential of the optical tweezers in the xy plane, for $U_0/k_B = 1\,\mathrm{mK}$, $w = 1\,\mu\mathrm{m}$ and $z_R = 4\,\mu\mathrm{m}$. Solid lines are equipotential lines for 100, 50 and 20 μK (from black to grey).

the trapping region during their free flight, and the larger the recapture probability. These curves thus confirm the efficiency of our additional cooling procedures.

In order to be more quantitative, we infer from these curves the atomic temperature using Monte Carlo simulations. We compute the ballistic spreading of a set of atoms (see Figure 2.4(c)), whose initial conditions are chosen according to the temperature-dependent statistical distribution of the atomic position and velocity introduced before. We determine as a function of τ which fraction of the atoms are recaptured. If the atom is represented in green, its kinetic energy is lower than the absolute value of the local trapping potential and it is recaptured, otherwise it is represented in

red. Figure 2.4(c) also shows the spatial dependence of the trapping potential in the xy plane, and the equipotential lines corresponding to an energy of 100, 50 or 20 μK. We repeat this Monte Carlo simulation for different temperatures, and compare with the experimental results to infer the temperature of the atoms (Figure 2.4(b)). The temperature of the coolest atoms we can produce is 3 μK, whereas if we do not perform additional cooling procedures their temperature is on the order of 100 μK. We have improved the cooling by ramping down the MOT detuning in the very last months of my Ph.D. thesis, so in most of the experiments presented in this work, the atomic temperature was around 20 μK. In practice, when we check on a daily basis the temperature of the atoms, we measure the recapture probability for one given time, usually 20 μs (red dashed line in Figure 2.4(b)).

During the quantum simulation step, the atoms are in free flight. Indeed, the dipole trap is switched off in order to excite the atoms to a Rydberg state without any lightshift induced by the 852-nm laser beam. As all the recapture curves on Figure 2.4(c) start with a plateau at probability 1, we can perform this free flight for a given amount of time without losing too many atoms. Typically for $T \approx 20\,\mu$K, we only have a 3% probability to lose an atom for a 10-μs experiment.

The temperature of the atoms and the trapping frequencies allow us to estimate the statistical spreading in position around the peak intensity of the optical tweezers, $\sigma_{\perp,\parallel} = \sqrt{k_B T / \left(m\omega^2_{\perp,\parallel}\right)}$. These spreading are on the order of $\sigma_\perp \approx 100\,$nm and $\sigma_\parallel \approx 500\,$nm. They will be of interest further in this manuscript to understand in details the dynamics of interaction between Rydberg atoms, as the latest is affected by shot-to-shot fluctuations of the interatomic distance.

Control of the experimental sequence The experimental sequence reported above is realized in practice by sending a collection of TTL signals and analog voltages. They are generated by two National Instruments cards. At the time when I joined the team, a LabWindows interface was used to control the cards. My first task in the lab was to convert this program into a Python program. It was made possible thanks to a Python package dedicated to write on National Instruments cards, *PyDAQmx*, developed by Pierre Cladé. Since then, all the operating programs of our experimental setup are written in Python: the camera program acquiring the fluorescence images and triggering the experiments, the experiment control program writing the sequence, and the program analysing the images and computing the recapture probabilities. This uniformity of programming language will enable us to implement more easily in the near future some automatized optimization protocol [Caneva, Calarco, and

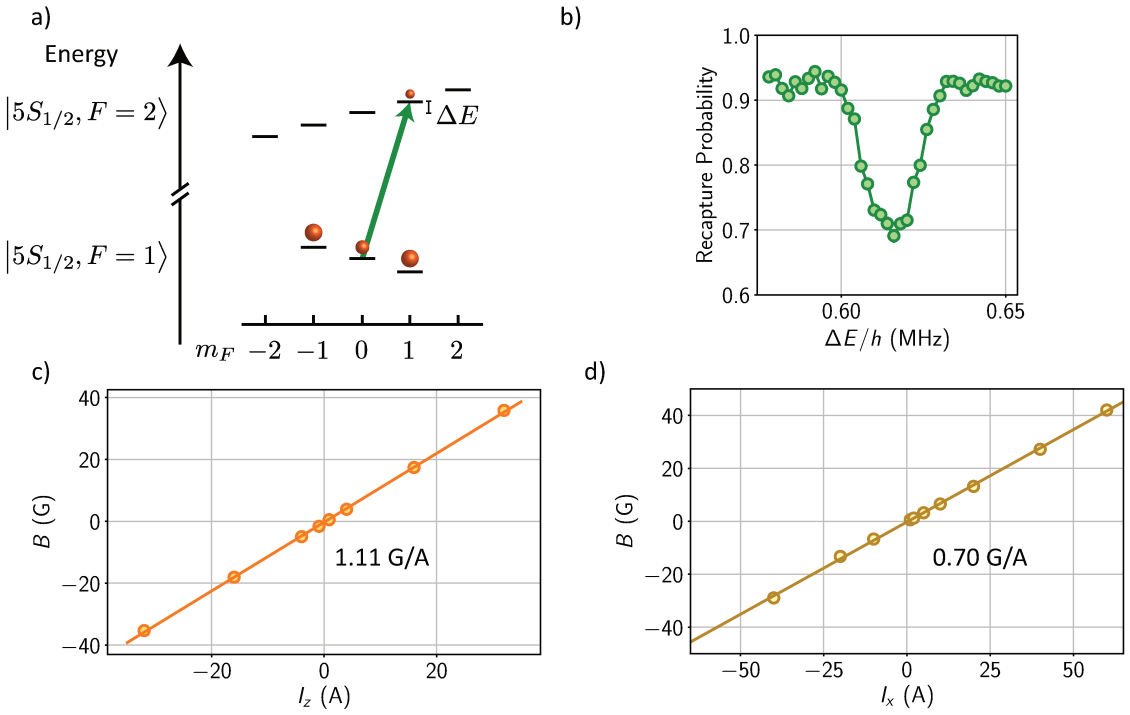

Figure 2.5: Measurement of the magnetic field using microwave spectroscopy. (a) Zeeman structure of the ground-state manifold. The transition we probe is indicated with a green arrow. (b) Typical spectroscopic signal, allowing us to point the position of the transition. (c) and (d) Magnitude of the magnetic field as a function of the current in the coils, along the z and x directions.

Montangero, 2011], where a master program could test a set of parameters, measure a figure of merit, and test a new set of parameters in view of improving it iteratively. We may use the same type of feedback loop protocols to implement variational quantum simulation [Kokail *et al.*, 2019] in the near future.

2.1.3 Ground-state microwave manipulation

In the previous subsection, I insisted on the required control of the magnetic field inside the vacuum chamber. We need it to be cancelled out during the polarization gradient cooling process, and to be along the z direction to define a quantization axis for optical pumping. Taking into account the Zeeman effect, measuring the transition frequencies between two levels of the two ground-state hyperfine states, $|5S_{1/2}, F = 1\rangle$ and $|5S_{1/2}, F = 2\rangle$, allows us to determine the value of the magnetic field.

Probing transitions in the electronic ground state The experiment consists in exciting the atom in the level $\left|5S_{1/2}, F = 1, m_F = 0\right\rangle$ to the level $\left|5S_{1/2}, F = 2, m_F = 1\right\rangle$, using a microwave field generated with an antenna outside the vacuum chamber (see Figure 2.5(a)). The difference $\Delta E/h$ between the frequency of this transition and the frequency of the clock transition insensitive to magnetic fields $\left|5S_{1/2}, F = 1, m_F = 0\right\rangle \rightarrow \left|5S_{1/2}, F = 2, m_F = 0\right\rangle$ is proportional to the magnetic field B, with a sensitivity 0.70 MHz/G [Steck, 2003].

The experiment then works as follows. We prepare the atom in the $\left|5S_{1/2}, F = 1\right\rangle$ state by shining some MOT light without any repumper light. We then send a microwave pulse at a controlled frequency and look at the atomic population in the $\left|5S_{1/2}, F = 2\right\rangle$ state. This alone would not allow us to determine in which hyperfine state an atom is because it would be recaptured in both cases. Therefore, we shine on the atom before the final image a "push-out" beam, set on the resonance $\left|5S_{1/2}, F = 2\right\rangle \rightarrow \left|5P_{3/2}, F = 3\right\rangle$, to expel the atom out of the trap if it is in the $\left|5S_{1/2}, F = 2\right\rangle$ state, whereas it will stay trapped if it is in the $\left|5S_{1/2}, F = 1\right\rangle$ state. Consequently, when the frequency of the microwave field matches the transition frequency, we observe a drop in the recapture probability (see Figure 2.5(b)), allowing us to determine the position of the line.

Calibration of the magnetic fields By measuring the frequency of the transition as a function of the current inside the coils, we calibrate the amplitude of the generated magnetic field. Figure 2.5 (c) and (d) show that the quantization field (along z or x) reach values on the order of 40 G. The larger the magnetic field, the larger the splitting of the Zeeman structure. This will be used to isolate two levels in the Rydberg manifolds for quantum simulation purposes, as we shall see later in this manuscript. Repeating the same measurement for the compensation coils enables us to find the current corresponding to the cancellation of the magnetic field, as already introduced in the previous subsection.

Time evolution of the generated magnetic fields When we switch on the current in a pair of coils outside the vacuum chamber, compared to a pair of coils inside, it will take longer for the generated magnetic field to reach its stationary value because it will have to overcome the induced eddy currents in the vacuum chamber. Using the spectroscopic experiment described above, we have estimated that we need to wait 20 ms for the quantization field along x to reach its final value, whereas 5 ms are enough in the case of the z direction, as in that case the magnetic field is generated

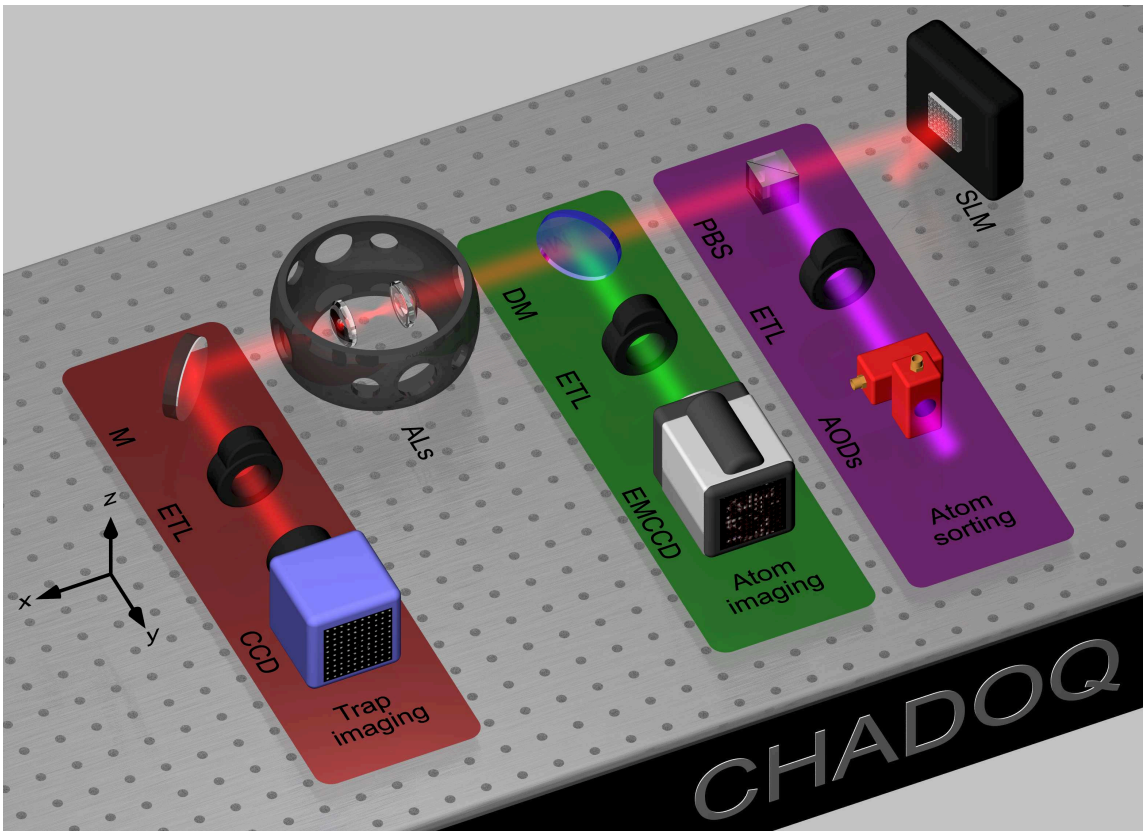

Figure 2.6: Trapping, sorting and imaging many atoms. Schematic representation of the experimental apparatus, where the devices required to go from a single atom to many were added. The Spatial Light Modulator (SLM) imprints a phase on the 852-nm beam, resulting in a controlled intensity pattern at the focus of the aspheric lens, imaged on the CCD camera. The purple beam is the moving optical tweezers beam, whose focus point in the focal plane is set using Acousto-Optic Deflectors (AODs). Three Electrically Tunable Lenses (ETL) enable the tuning of the focal plane of the different optical setups, in order to access the third dimension along the optical axis x.

with the coils inside vacuum. We have to take into account those different time scales when we change the direction of the quantization field to keep the value of its modulus different from zero.

2.2 Generation of fully-loaded arrays of atoms

So far, I presented how we can isolate a single atom in a confined region of space thanks to an optical tweezers. In this section, I will describe how we generalize this technique in order to obtain arrays of single atoms in a tunable configuration. This

requires a collection of devices represented in Figure 2.6. The roles of the Spatial Light Modulator (SLM) and the CCD camera will be reported in a first part, where I will explain how we generate a controlled pattern of many optical tweezers. Then, I will depict how we reach a targeted loading configuration from a random initial configuration via the atom sorting technique (purple optical path on the figure). Finally, I will describe how we improved our trapping and sorting protocol to extend it to three dimensions, using among other things Electrically Tunable Lenses (ETL).

The work briefly reported here are described in details in the original publications: [Barredo *et al.*, 2016] and [Barredo *et al.*, 2018].

2.2.1 Versatile trapping configuration using holographic techniques

The first requirement to fulfill to reach the generation of fully-loaded arrays of atoms is to multiply the number of optical tweezers, in a controlled geometry. This is realized using a Spatial Light Modulator (SLM). This device imprints a phase pattern on the dipole trap beam, resulting in an intensity pattern consisting of several optical tweezers in the focal plane of the aspheric lens via diffraction. Its first implementation on our experimental setup is reported in [Nogrette *et al.*, 2014] and in the thesis of Henning Labuhn [2016].

Computation of the phase pattern The algorithm we use to compute the required phase pattern to get a targeted lattice of optical tweezers is reported in [Leonardo, Ianni, and Ruocco, 2007], and its implementation is explained in the thesis of Sylvain de Léséleuc [2018]. It works in an iterative way, adapted from the Gerchberg-Saxton algorithm. The whole set of optical tweezers is considered as a collection of coherent point-like light sources, of uniform amplitudes and random phases. The propagation of the interfering light field, resulting from this collective emission and depending on the geometrical arrangement, is computed at the position of the SLM plane. We then take as a phase pattern for the SLM the phase of the interfering light field and compute at the positions of the optical tweezers the amplitude and phase of the light propagating from the SLM, i.e. in the reversed direction. The computed amplitudes are inhomogeneous. In order to compensate for that, we repeat the same procedure with the new computed distribution of phases, and, instead of considering a uniform distribution for the amplitudes of the traps, we choose a smaller amplitude for the stronger traps, and on the contrary, a larger amplitude for weaker ones. Moreover, to achieve a more homogeneous trap intensity distribution, we replace

the step consisting in calculating the amplitudes at the position of the optical tweezers by measuring using the CCD camera the actual intensities of each of the generated traps. That way, repeating this process for a few tens of iterations, we create the targeted configuration of traps with a standard deviation in their intensities smaller than 3%.

Global phase masks In addition to the phase pattern required to obtain the targeted intensity pattern, we can sum other phase masks that will have a global effect. A linear evolution of the phase modulo 2π is a blazed grating, acting as a mirror, so applying this kind of phase mask allows us to displace at will the trap pattern in the focal plane of the aspheric lens. A quadratic evolution of the phase modulo 2π is a (Fresnel) lens, so this kind of phase mask makes it possible to adjust the position of the trap pattern on the optical axis. Finally, the modifications of the wavefront induced by the SLM can be used to compensate the ones due to aberrations. By measuring the deformations of the wavefront due to aberrations with a Shack-Hartmann sensor, we are able to reduce them thanks to an adapted phase mask. Consequently, the three global phase masks described above allow us to tune in the three spatial dimensions the position of the array of optical tweezers, and to generate more confined optical tweezers by reducing aberrations.

Fluorescence imaging of the array of traps We follow the same procedure as the one reported in the single-atom case to take a fluorescence image of the trapped single atoms. As the radial size of an optical tweezers matches the size of one pixel of the EMCCD camera, and that two traps are not imaged on the same pixel, the fluorescence coming from each trap is spatially resolved. In Figure 2.7, the phase pattern on the SLM, the related trap intensity image and atom fluorescence image are displayed for two different configurations. Due to the collisional blockade regime, as an optical tweezers is loaded by a single atom half of the time, on average the array of optical tweezers is half loaded. As a consequence, we cannot work with a controlled atomic configuration, which is detrimental for quantum simulation purposes. I will explain in the next subsection how we overcome this drawback. Nevertheless, for single-atom measurements, working with partially loaded arrays of optical tweezers has already the advantage to decrease the s.e.m. using several atoms instead of one at each sequence iteration.

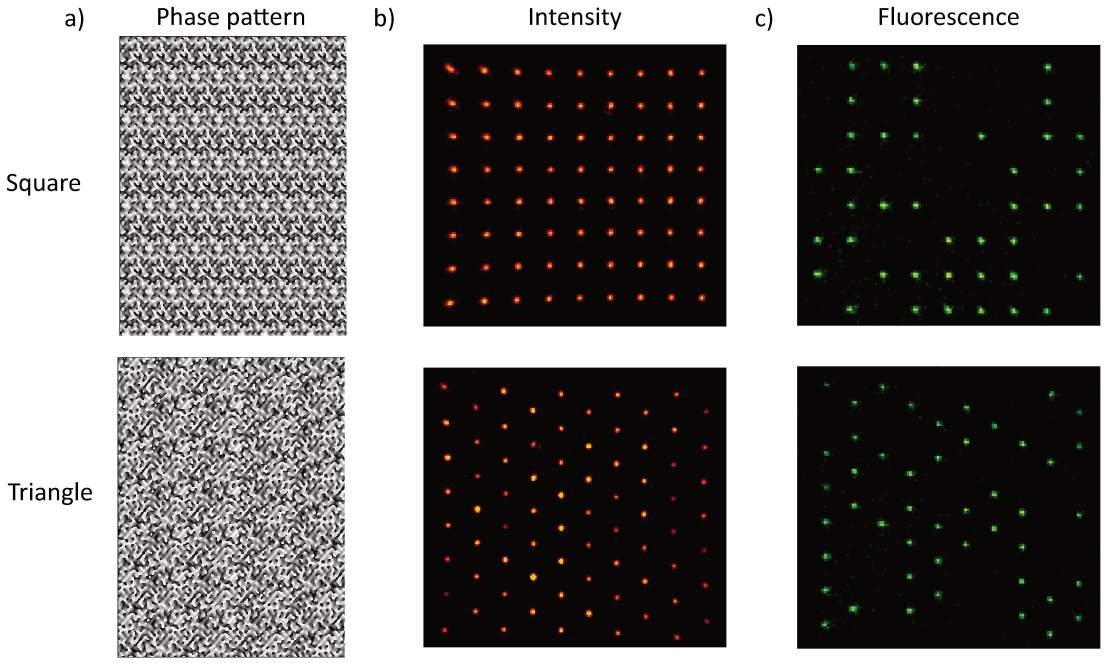

Figure 2.7: Tuning the lattice geometry using a SLM. (a) Computed phase pattern to generate a 8×9 square matrix of traps or a triangular lattice of 75 traps. The colormap represents the phase imprinted by the SLM, ranging from 0 (black) to 2π (white). (b) Intensity images of the array of traps. (c) Single-shot fluorescence images of the trapped atoms. The trap array is not fully-loaded, illustrating our stochastic loading protocol.

To conclude, a SLM-based holographic technique allows us to tune at will the geometry of the array of optical tweezers. The typical distance between traps in the focal plane in the experiments presented in this manuscript is $10\,\mu$m, and can be as small as $3\,\mu$m. The limitation in terms of number of generated traps comes from the total dipole trap beam power, we are able to generate up to about 150 traps; and ultimately, it comes from the total field of view of the aspheric lens, approximately $100 \times 100\,\mu\text{m}^2$.

2.2.2 The atom-by-atom assembler

As mentioned above, in the collisional blockade regime, the array of optical tweezers is on average half loaded with single atoms. As one optical tweezers has a probability $p = 0.5$ to be occupied by one single atom, the probability to get a fully loaded array of N optical tweezers is 0.5^N. We can still perform the stochastic loading of the trap array and wait for getting the fully loaded configuration, but this waiting time grows

exponentially with N. In practice, in our team, it was possible to perform experiments with up to $N = 9$ traps using the stochastic loading protocol. A possible solution would be to increase p, by tailoring the light-assisted inelastic collisions in view of expelling one atom instead of two after the collision [Grünzweig *et al.*, 2010; Lester *et al.*, 2015; Brown *et al.*, 2019]. This allowed some experimental research teams to reach up to $p \approx 0.9$, but in the end we still have to face the exponential growth with N of the required time to fully load the trap array.

In this subsection, I will describe the procedure we follow to get a controlled loading configuration. It consists in choosing an initial bigger array of $2N$ traps half loaded with single atoms, and then to move the atoms one by one to fill the traps we want to be occupied. That way, we generate a fully-loaded configuration of N optical tweezers. I will first explain how a single atom is transferred from one trap to another, and then I will depict the whole procedure to assemble a targeted sub-array of optical tweezers. This work was already reported in details in [Barredo *et al.*, 2016] and in the thesis of Sylvain de Léséleuc [2018].

Transferring one atom The idea is to use another optical tweezers (purple beam in Figure 2.6) whose position in the focal plane of the aspheric lens is dynamically changed using Acousto-Optic Deflectors (AODs). The moving optical tweezers is combined with the dipole trap static beam using a PBS, and imaged on the same CCD camera. We can then calibrate the position of the moving tweezers as a function of the frequencies of the RF signal feeding the AODs. These frequencies are set using Arduino Due controlled by the master computer program, so in the end, by analysing the image of the static traps and of the moving tweezers, the position of the moving tweezers can be automatically set to point to any of the traps, and to go from one trap to another. The depth of the moving optical tweezers is also tuned dynamically changing the amplitude of the RF signal feeding the AODs.

An atom stays trapped in the moving optical tweezers for slow enough motion, as previously demonstrated in our team [Beugnon *et al.*, 2007]. The transfer of one atom works as follows (Figure 2.8 (a)). The moving optical tweezers is pointed on an occupied trap with no power. Then, we gradually increase the depth of the moving tweezers U_{MT} in $300\,\mu$s to $U_{\mathrm{MT}}/\mathrm{k_B} = 10\,\mathrm{mK}$. The position of the moving tweezers is then shifted on an empty trap, steering the atom away, at a maximum speed of $10\,\mu$m/ms to avoid heating up the atom and lose it. The atom is then released in the empty static trap by decreasing the moving tweezers depth to zero in another $300\,\mu$s. We are able to realize that way the transfer of a single atom with a 99.3% efficiency in

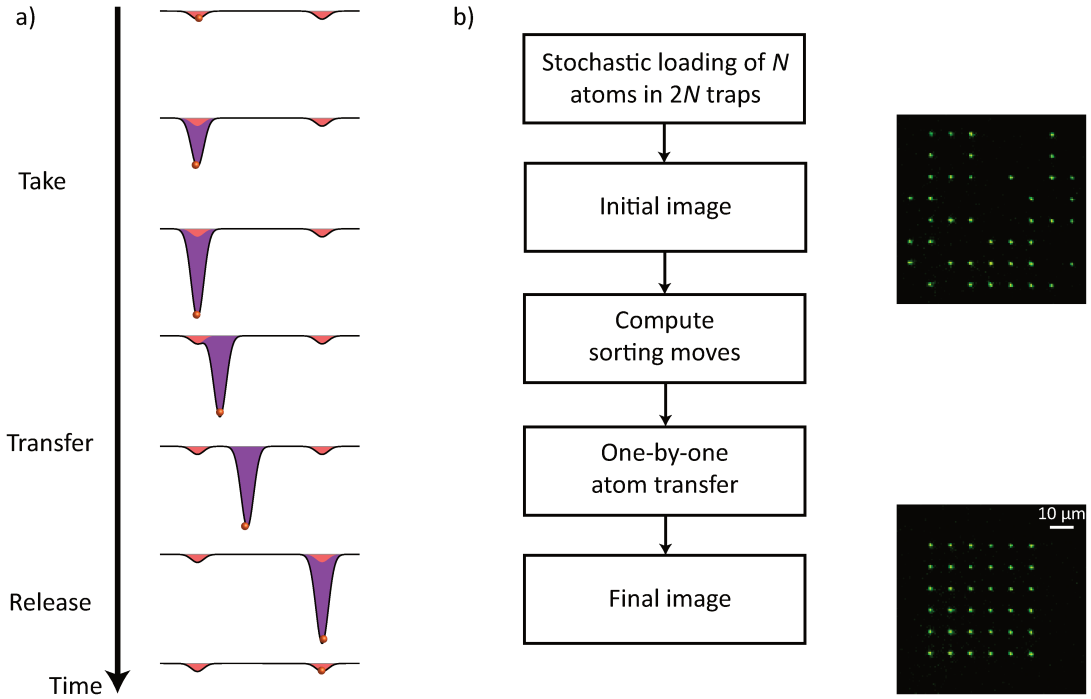

Figure 2.8: Atom-by-atom assembly. (a) Transfer of an atom from one trap to another. The trapping potentials of the static SLM traps are in red, whereas the one of the moving tweezers is in purple. (b) Overview of the sorting protocol. Single-shot fluorescence images are displayed, representing the initial random distribution of atoms in a 8×9 square matrix of traps, and the final targeted configuration of atoms ordered in a 6×6 square matrix.

approximately 1 ms.

Sorting of an array of atoms Repeating the described transfer of one atom allows us to get a targeted loading configuration from any initial random configuration, provided that there are enough atoms at the beginning. The sorting sequence, depicted on Figure 2.8 (b), works as follows. We take a first initial image to know which traps are occupied. Then, we compute on the fly which atoms we need to move in order to fully fill the targeted sub-array of traps. To find a suitable series of sorting moves, our algorithm computes the distances between an empty trap to fill and the available atoms, and chooses to move the atom corresponding to the smallest distance. Then, we perform the atomic transfer one after the other, and end the sorting sequence by taking another fluorescence image to check on the loading state of the trap array. This whole process is the assembling step on Figure 2.3.

Our assembling technique enables the generation of fully loaded configuration of up to $N = 50$ traps, with a 98% filling fraction. In practice, we produce one defect-free

7×7 square matrix of atoms every second sequence iteration, that is to say at a $1 - 2\,\mathrm{Hz}$ rate. As we take a fluorescence image after the assembling process, we can post-select the sequence iterations in order to consider only the ones where we had obtained a defect-free configuration.

2.2.3 Extension to 3D

The assembling technique presented before allowed us to explore quantum many-body physics in different 2D configurations (square, triangle, dimerized chain) as we shall see later in this manuscript. Extending this technique to the third space dimension would increase even more the complexity of the physical phenomena which could be studied in our experimental apparatus. I report in this subsection this latest improvement, which led to the publication [Barredo *et al.*, 2018]. I refer to the thesis of Sylvain de Léséleuc [2018] for more details.

Generation of 3D array of optical tweezers The advantage of the algorithm we use to compute the SLM phase pattern [Leonardo, Ianni, and Ruocco, 2007] is that it can be naturally extended to 3D configuration of traps. As already mentioned, the underlying idea to access the third dimension is to imprint a quadratic phase on the wavefront in order to mimic the propagation through a lens. This ability to pile up traps on the optical axis means that we can that way overcome the limitation of the number of generated traps coming from the finite field of view of our fluorescence imaging setup. The total available trapping volume is now of size $100 \times 100 \times 100\,\mu\mathrm{m}^3$.

Intensity and fluorescence imaging To image the intensity or the fluorescence of the whole 3D structure, one needs to change the object focal plane of both imaging optical setups in a controlled way. For that purpose, we use Electrically Tunable Lenses (ETL), whose focal lengths depend on applied control currents. We then take images for a range of focal lengths, and piling up this set of 2D images we reconstitute the 3D intensity or fluorescence distribution (Figure 2.9(a) and (b)). The Eiffel Tower array in Figure 2.9(b) looks fully loaded, as fluorescence light is emitted from every trap. Actually, it is not the case, we have performed the assembling only for multi-planar geometries (see next paragraph). Therefore, what is shown in Figure 2.9(b) is a stack of averaged fluorescence images.

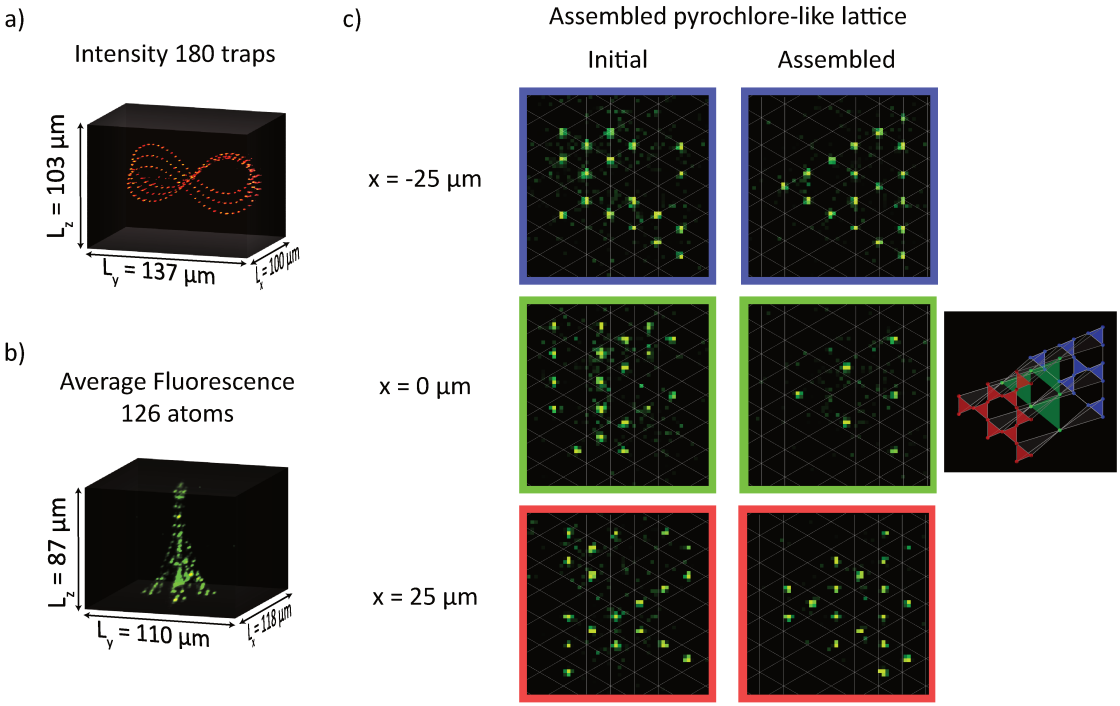

Figure 2.9: Imaging and sorting in three dimensions. (a) 3D reconstitution of the intensity of a Möbius strip composed of 180 traps. (b) Stack of the average fluorescence images for a 126-atom Eiffel Tower. (c) Assembly of a pyrochlore-like lattice (42 atoms). The displayed images are single-shot fluorescence images, for the three different planes of the lattice. The positions of each plane on the optical axis x are indicated. The inset is a sketch of the 3D structure, to help visualizing the pyrochlore geometry (sharing-corner tetrahedrons).

Assembly of multi-planar configurations The assembling technique can also be extended to 3D, by repeating the same sorting procedure for each plane of a multi-planar set of optical tweezers (Figure 2.9(c)). We need to change the focusing plane of the moving tweezers in order to do so. We then use another ETL for the moving tweezers optical setup. The 3D assembling procedure is as follows: we take one fluorescence image per plane to know the initial random atomic distribution in each plane. We then perform the sorting of each plane one after the other, changing the focus plane of the moving tweezers between two sorting processes. We finally take another set of fluorescence images to know the loading states of the traps. Our sorting procedure is for the moment limited to multi-planar geometries, and in order to avoid the moving tweezers to affect other planes while acting on a specific one, the distance between planes must be larger than 17 μm.

As a conclusion, I have reported in this section how we generate any 2D configurations of N atoms, and 3D configurations taking into account some constraints (multi-planar geometries and minimal inter-plane distance). I have thus described all the steps mentioned in Figure 2.3, except the quantum simulation one which will be the topic of the further chapters of this manuscript. At this stage, we have an assembly of qubits in a controlled initial state via optical pumping, and in a controlled spatial configuration. The necessary element which is still missing to perform quantum simulation experiments is interaction between atoms. We reach such an interacting regime by transferring the atoms to Rydberg states: highly excited orbitals with principal quantum number n ranging from 50 to 100. The aim of the next section, completing the overview of our experimental platform, is to describe how we transfer the atoms to this state.

2.3 Excitation to Rydberg states

Rydberg states are highly excited orbitals, whose exaggerated properties (enhanced dipole-dipole interactions and extended lifetimes) are of interest for quantum simulation purposes, as we shall see later in this manuscript. I will describe in this section how we excite an atom to a Rydberg state. After showing the two-photon transition we use, I will present the two regimes we have explored to prepare a Rydberg excitation.

2.3.1 Two-photon transition

For Rubidium, the frequency of the direct transition from the electronic ground state $|g\rangle$ to a Rydberg state $|r\rangle$ is in the UV range. As coherent sources at that wavelength are not easily available, it is more convenient to use a two-photon transition. The excitation to the Rydberg state then consists, in our case, in a first transition close to the D_1 line at 795 nm (red) coupling to the intermediate state $|e\rangle = \left|5P_{1/2}\right\rangle$, and a second transition around 475 nm (blue) coupling to the Rydberg state. Our two-photon scheme enables the preparation of a $nS_{1/2}$ or $nD_{3/2}$ excitation. After describing the different two-photon schemes used in this work, I will present the excitation lasers setup and explain how we detect the atom transfer to a Rydberg state.

Different excitation schemes Depending on the targeted state, or on the direction of the quantization axis, we have used different orientations and polarizations for the

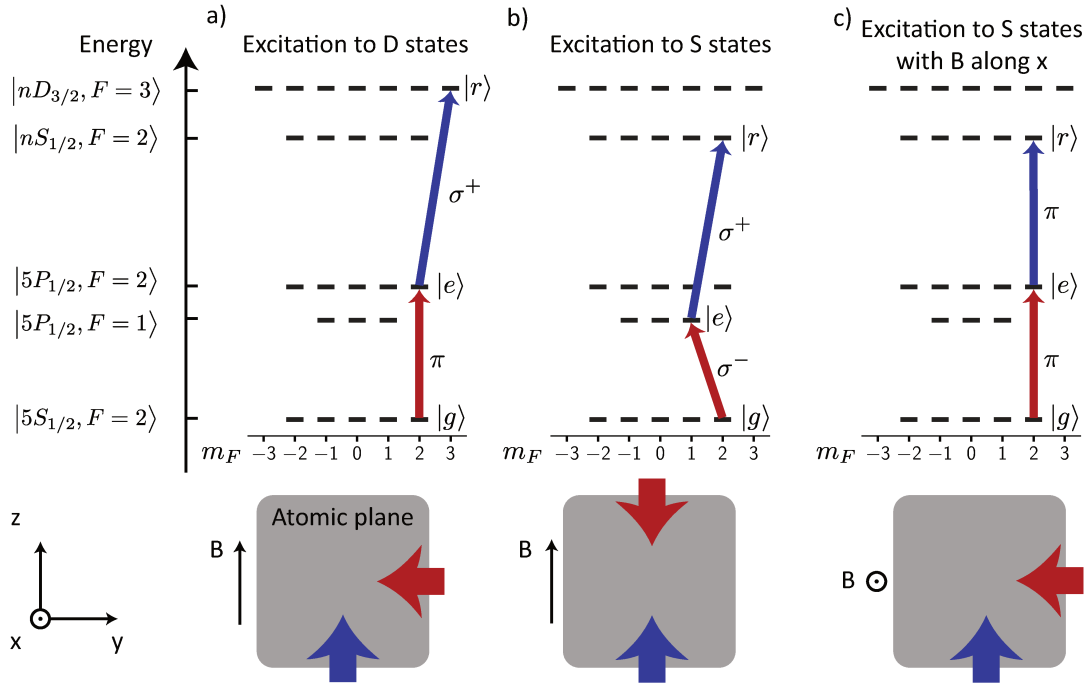

Figure 2.10: Two-photon excitation schemes used in this work. Quantum numbers of the states $|g\rangle$, $|e\rangle$ and $|r\rangle$. The hyperfine structure of the Rydberg states, although being indicated, cannot be resolved by spectroscopy, and in practice we consider only the fine structure for the Rydberg $|nS_{1/2}, m_J = 1/2\rangle$ and $|nD_{3/2}, m_J = 3/2\rangle$. In c), we cannot use circular polarized light because the excitation beams cannot be sent along the x axis. The sketches below the energy level structures show the orientation of the red and blue excitation beams with respect to the atomic plane (yz plane), and the quantization axis B.

excitation beams (Figure 2.10). We chose the excitation scheme in order to have the maximum Rabi frequencies for given red and blue laser powers. Consequently, we chose to use circular polarized light when it is possible, as the angular part of the electric dipole matrix element is the largest for transitions between Zeeman stretched states.

In addition to the dependence on the m_F of the states involved (angular part of the dipole matrix element), the blue Rabi frequency also depends on the principal quantum number n of the targeted Rydberg state (radial part), and decays as $n^{-3/2}$. In practice, as the dipole matrix element is much weaker for the transition $|e\rangle \to |r\rangle$ than it is for the transition $|g\rangle \to |e\rangle$, the blue laser power is the one limiting us to reach the largest coupling. For maximal power we obtain blue Rabi frequencies on the order of 50 MHz for the $60D_{3/2}$ state and on the order of 20 MHz for the $60S_{1/2}$ state.

Frequency locking of the excitation lasers Both excitation beams are generated by Toptica Diode Lasers. Sending a small portion of the excitation beams to a high finesse ultrastable cavity allows us to stabilize their frequencies using the Pound-Drever-Hall (PDH) technique. I refer to the thesis of Sylvain Ravets [2014] for further details. A careful analysis reported in the thesis of Sylvain de Léséleuc [2018] describes the origins of the laser phase noise when locked, which will be of interest to understand the damping of the laser-driven Rabi oscillations (see Subsection 2.3.2).

Optical setup for the excitation lasers In order to shape the time evolution of the amplitude and frequency of the excitation beams, we use an EOM and an AOM. The EOM allows us to switch on and off the excitation beams in a fast time scale (10 ns) to apply laser pulses as in the next subsection. The AOM, fed with a RF signal sent by an Arbitrary Waveform Generator (AWG), enables the generation of a tunable time profile for the amplitude or frequency of the excitation beams. For example, we use it to create a Gaussian amplitude time profile (Subsection 2.3.3), or to perform optical detuning sweeps (Chapter 4).

The experiments involving Rydberg excitations reported in this manuscript are limited to 2D configurations. In such a planar geometry, we can maximize the Rabi frequencies by focusing the excitation beams into sheets of light, using cylindrical lenses for the red laser, or the original ellipticity of the blue laser. For example in the excitation scheme on the left of Figure 2.10, the dimensions ($1/e^2$ radius) of the beams are: $w_x = 20\,\mu$m and $w_y = 50\,\mu$m for the blue laser; $w_x = 70\,\mu$m and $w_z = 230\,\mu$m for the red laser. Extending the waists of the exciting beams in the atomic plane direction allows us to reduce inhomogeneities of the Rabi frequencies over the atomic array.

Detection of a Rydberg atom To excite an atom to the Rydberg state, we first switch off the dipole trap to avoid the light-shift it induces, then send the red and blue laser pulses, and finally switch on the dipole trap again. If the atom is in $|g\rangle$ at the end of this sequence, it will be recaptured, if it is in $|r\rangle$, it will be lost. Indeed, Rydberg atoms are expelled from high-intensity regions via the ponderomotive force. We have used such a force to trap the Rydberg atoms in bottle beam traps, as we shall see in Chapter 3. Consequently, the final fluorescence image informs us on the state of the atom, and a high probability to excite an atom to the Rydberg state corresponds to a drop of the recapture probability.

In the experiments presented in this manuscript, we have used two different ways to excite an atom to a Rydberg state, depending on the Hamiltonian we want to simulate. Indeed, as stated in the Introduction, we must encode an effective spin-1/2 into the levels $|g\rangle$ and $|r\rangle$ to study the Ising model. In that case, the detuning Δ from the intermediate state $|e\rangle$ must be large to treat the atom as a two-level system $\{|g\rangle, |r\rangle\}$ while being driven by the two excitation lasers. This regime where we perform laser-driven Rabi oscillations is described in Subsection 2.3.2. On the contrary, in the XY-case, the spin-1/2 is encoded in the Rydberg manifold. Therefore, what only matters is to excite the atoms to the Rydberg state, and we do it using a stimulated Raman adiabatic passage in the small Δ regime (Subsection 2.3.3).

For both processes, using laser-driven Rabi oscillation or a stimulated Raman adiabatic passage, the intermediate state $|e\rangle$ must not be populated. Indeed, as it is short-lived (26 ns), populating it would induce spontaneous emission. In the following subsections, I will show how we succeed in avoiding this induced spontaneous emission in both cases.

2.3.2 Laser-driven Rabi oscillations

A common solution to avoid populating the intermediate state is to choose a detuning Δ from this state much larger than the red and blue Rabi frequencies Ω_r, Ω_b. In this subsection, I will first describe how we can restrict ourselves to the two-level system $|g\rangle$,$|r\rangle$ under this condition, and then I will present the typical spectrum and Rabi oscillation we obtain.

Reduction to a two-level system When $\Delta \gg \Omega_\mathrm{r}, \Omega_\mathrm{b}$, we can consider that the population in $|e\rangle$ is always zero. The time evolution of the population in the two-level system $|g\rangle$, $|r\rangle$ when the red and blue excitation laser beams are shone is then given by the effective Hamiltonian

$$\hat{H}_\mathrm{eff} = \frac{\hbar\Omega_\mathrm{eff}}{2}\left(|r\rangle\langle g| + |g\rangle\langle r|\right) + \delta_\mathrm{eff}\,|r\rangle\langle r| \tag{2.2}$$

where the effective Rabi frequency and detuning are

$$\Omega_\mathrm{eff} = \frac{\Omega_\mathrm{r}\Omega_\mathrm{b}}{2\Delta} \quad \text{and} \quad \delta_\mathrm{eff} = \delta + \frac{\Omega_\mathrm{r}^2 - \Omega_\mathrm{b}^2}{4\Delta} \tag{2.3}$$

with δ the detuning from the Rydberg state $|r\rangle$ (see Figure 2.11(a) for the three-level system scheme). The additional detuning appearing in δ_eff is the AC-Stark shift due

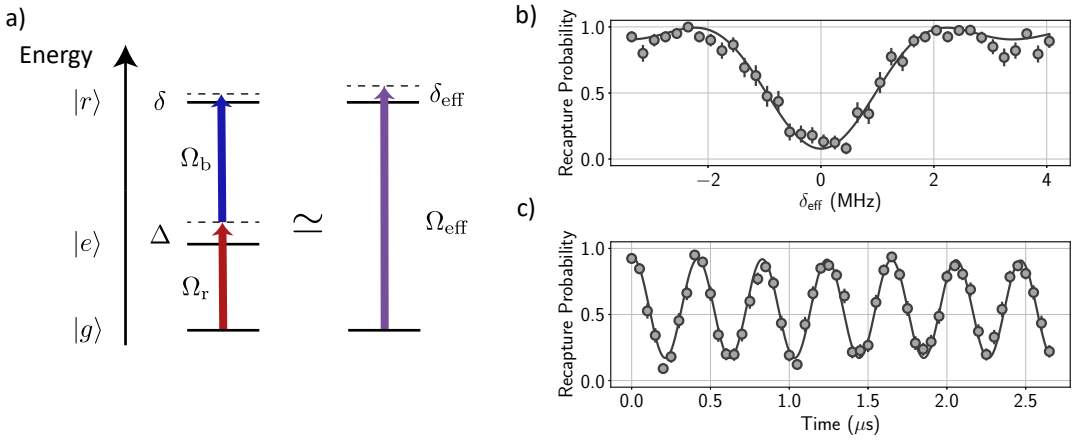

Figure 2.11: Optical Rabi oscillation. (a) Three-level system $\{|g\rangle, |e\rangle, |r\rangle\}$ showing the one-photon detuning Δ and the two-photon detuning δ, and its simplification to a two-level system when $\Delta \gg \Omega_r, \Omega_b$. (b) Typical spectroscopic signal obtained for a pulse duration of 200 ns, a Rabi frequency $\Omega/(2\pi) = 2.47\,\text{MHz}$, and $|r\rangle = |62D_{3/2}, m_J = 3/2\rangle$. The solid line is a fit to measure the position of the Rydberg line. (c) Typical Rabi oscillation measured for $\delta = 0$ and $|r\rangle = |62D_{3/2}, m_J = 3/2\rangle$. The solid line is a fitting damped sine allowing us to infer the value of the Rabi frequency $\Omega/(2\pi) = 2.47\,\text{MHz}$.

to the red and blue lasers. In practice, the blue power is set to its maximal value and we tune the value of Ω_{eff} by varying the red power. The intermediate detuning is $\Delta/(2\pi) = 740\,\text{MHz}$. We can then obtain an effective Rabi frequency up to about 5 MHz.

Our optical drive to the Rydberg state can then be seen as a two-level transition of Rabi frequency Ω_{eff} and detuning δ_{eff} which will be written from now on in a simplified way Ω and δ. This reduction to a two-level system will be mostly used in Chapter 4, about our study of an Ising-like model.

Spectroscopy of the Rydberg line Shining the laser beams for a duration $t_\pi = \pi/\Omega$ and at resonance $\delta = 0$ allows us to coherently excite an atom prepared in $|g\rangle$ to $|r\rangle$. Figure 2.11(b) shows the typical spectroscopic signal we obtain when we measure the recapture probability varying the detuning δ.

Pointing the position of the Rydberg line via spectroscopy for various power of the red laser enables the measurement of the light-shift induced by the latest. The estimation of this light-shift will be of interest in Chapter 4, and it is a way to measure the red Rabi frequency.

Due to their exaggerated polarizability, the Rydberg energy levels are quite sensitive to electric fields via the DC-Stark effect. As already presented in the very beginning

of this chapter, a combination of eight electrodes inside the vacuum chamber, in addition to an ITO coating on the aspheric lenses, allows us to cancel out the electric fields, which is crucial to have an efficient Rydberg excitation and a coherent driving. In practice, to compensate the electric fields, we scan the voltages on the different electrodes and choose the values that cancel out the measured DC-Stark shift.

Laser-driven Rabi oscillations When the detuning is set to $\delta = 0$, shining the laser beams for a varying duration coherently drives the system between the states $|g\rangle$ and $|r\rangle$. Figure 2.11(c) shows such a typical Rabi oscillation, fitted with a damped sine. The imperfections of the Rabi oscillation in terms of contrast and damping were carefully analysed in our publication [de Léséleuc *et al.*, 2018a]. I recall here its main results. The contrast is smaller than unity because of the detection errors ϵ and ϵ' (detailed in the paragraph below); and an imperfect initial preparation in the correct Zeeman sub-level during the optical pumping process. The damping mainly comes from the Doppler effect, the laser phase noise, and the still non-zero population in the intermediate state $|e\rangle$ resulting in spontaneous emission.

I give now more detail about the detection errors ϵ and ϵ'. I recall that our state detection protocol relies on the fact that ground-state atoms are recaptured whereas Rydberg atoms are not. Nevertheless, as we have seen in Figure 2.4, there is a (small) non zero probability to lose an atom during the experiment. In this unlikely case, an atom in the ground state will be mistaken as a Rydberg atom. We call the probability to make this detection error ϵ, and its typical value ranges between 2 and 5%, depending on the atom temperature and the total duration of the performed experiment. On the contrary, due to the limited lifetime of the Rydberg state, a Rydberg atom can decay back to the ground state before being expelled away from the trapping region, and then would be misleadingly considered as a ground-state atom. This detection error is called ϵ', and its typical value is also a few percent. More details on our detection errors can be found in the thesis of Sylvain de Léséleuc [2018].

2.3.3 Stimulated Raman adiabatic passage (STIRAP)

Another possible solution to avoid the spontaneous emission from the intermediate state is to use stimulated Raman adiabatic passages (STIRAP), a widely used solution recently reviewed in [Vitanov *et al.*, 2017]. Its working principle is the following. For $\Delta = 0$, in the presence of the two couplings Ω_r and Ω_b, one of the three eigenstates of the three-level system $|g\rangle$,$|e\rangle$, $|r\rangle$ has no projection on the short-lived state $|e\rangle$. This

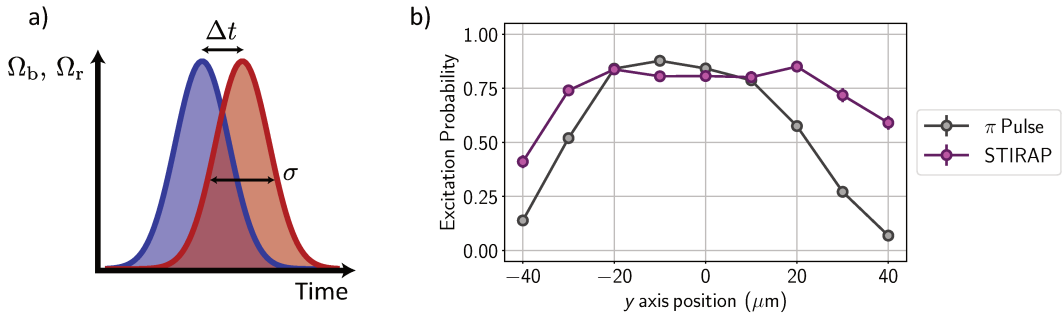

Figure 2.12: Rydberg excitation via STIRAP. (a) Gaussian time evolution of the red and blue Rabi frequencies. For an optimal excitation to the $|60S_{1/2}, m_J = 1/2\rangle$, we chose the following parameters: $\sigma = 360\,\text{ns}$, $\Delta t = 400\,\text{ns}$ and $\Omega_r = \Omega_b = 2\pi \times 20\,\text{MHz}$. (b) Comparison of the Rydberg transfer efficiency via the π-pulse (grey) or the STIRAP (purple) methods for different positions on the y axis.

eigenstate is equal to $|g\rangle$ for $\Omega_b \gg \Omega_r$, and is equal to $|r\rangle$ for $\Omega_b \ll \Omega_r$. The idea is then to sweep the parameters Ω_r and Ω_b between these two regimes, i.e. shining first the blue laser then the red one, to transfer the atom from $|g\rangle$ to $|r\rangle$ without populating $|e\rangle$. The variation of Ω_r and Ω_b must be slow enough to stay in the targeted eigenstate with no component in $|e\rangle$, which is the adiabatic condition to fulfill.

I will first describe in this subsection how we can measure the blue Rabi frequency by doing some manipulation at $\Delta = 0$. Then I will present the implementation of the STIRAP process on our experimental apparatus, and the opposite deexcitation protocol.

Autler-Townes splitting When it is in the $|e\rangle$ state, an atom can decay back to $|g\rangle$ or other Zeeman levels of the electronic ground state. In the end, shining the red laser at resonance $\Delta = 0$ depumps the atom from $|g\rangle$ to Zeeman levels of $|5S_{1/2}, F = 1\rangle$, which can be seen on the recapture probability using the push-out beam (see subsection 2.1.3). Shining at the same time the blue laser at resonance splits the line into two parts separated by Ω_b, via the Autler-Townes effect [Autler and Townes, 1955]. We will measure in that case a depumping in $|5S_{1/2}, F = 1\rangle$ at $\Delta = -\Omega_b/2$ and $\Delta = \Omega_b/2$, allowing us to infer the value of the blue Rabi frequency.

Implementation of STIRAP Figure 2.12(a) shows the Gaussian time evolution of the red and blue lasers amplitude. We optimize the value of the different parameters (delay between the two Gaussian pulses Δt, width of the pulses σ, amplitude of the

two lasers Ω_r, Ω_b) in order to have the most efficient Rydberg excitation. In practice, we set the blue laser power to its maximum value, and the red laser power in order to have $\Omega_b = \Omega_r$. After optimization, we reach a STIRAP transfer efficiency of about 90% for the $60S_{1/2}$ state in $2\,\mu$s.

The very valuable advantage of using STIRAP is that it stays efficient for a wide range of parameters. To illustrate that point, Figure 2.12(b) shows the measured Rydberg excitation probability as a function of the position on the y axis using the two different excitation protocols described in this section, a Rabi π-pulse (grey) or a STIRAP (purple). The STIRAP is more efficient in a wider region, this is why we will use it in Chapters 5 and 6 when we will want to initialize the atomic array in a Rydberg nS state.

Deexcitation protocol To transfer an atom in $|r\rangle$ back to $|g\rangle$, we could use an inverse STIRAP process (shining first a red pulse then a blue pulse). To perform the deexcitation faster, we shine instead a pulse of blue light at resonance to couple back the atom into $|e\rangle$, and then it will spontaneously decay back to the electronic ground state. This allows us to transfer back the atom in approximately 400 ns.

I have shown in this section that we can excite the atoms to a Rydberg state with an efficiency of $\approx 90\%$, depending on the targeted state. Our analysis conducted in [de Léséleuc *et al.*, 2018a] led us to conclude that the weak dipole matrix element between $|e\rangle$ and $|r\rangle$ is the limitation to achieve a better transfer efficiency. In order to improve it, our team plans to adopt the *inverted* scheme, successfully implemented in the group of Prof. M.D. Lukin [Bernien *et al.*, 2017; Levine *et al.*, 2018]. The idea is to choose the $\left|6P_{3/2}\right\rangle$ state as an intermediate state. Then, the wavelength of the transition from the intermediate state to the Rydberg state is around 1013 nm, for which we can use amplifying doped fibers to reach larger Rabi frequencies. Moreover, the new excitation laser setup the team plans to use is expected to exhibit a reduced phase noise, as it will involve Ti-sapphire lasers instead of diole lasers, resulting in an even more coherent laser-driven Rabi oscillations.

2.4 Conclusion

In this chapter, I presented our experimental platform: arrays of optical tweezers in a controllable configuration loaded by single atoms which can be excited to Rydberg states in order to implement some interaction. This presentation allowed me to

introduce the quantity we can measure, the recapture probability. As being recaptured depends on the state of the atom ($|g\rangle$ or $|r\rangle$), the occupation of these states can be inferred from this probability. More interestingly, as the fluorescence emitted from each trap can be resolved independently, we can measure spatial correlations of these occupations, which will be of interest in the second part of this manuscript.

I also showed in this chapter that most of the experimental parameters, such as the magnetic and electric fields, the red and blue Rabi frequencies, can be measured *in situ* using single atoms as probes. The generation of arrays of single atoms allows us to measure in parallel the spatial dependence of these parameters, eventually leading to a complete characterization of the experimental parameters.

The latest improvement of our experimental platform, the trapping of Rydberg atoms, will be described in the next chapter. The following chapters will be dedicated to the quantum many-body physics arising from the interaction between Rydberg atoms.

Chapter 3

Single Rydberg atoms in ponderomotive bottle beam traps

Contents

Rydberg arrays are an attractive platform to perform quantum simulation thanks to the exaggerated properties of Rydberg atoms, namely large interaction energies and extended lifetimes. These properties make them also suitable for more general quantum information tasks, and I already mentioned the realization of two-qubit logic gates using Rydberg atoms [Wilk *et al.*, 2010; Isenhower *et al.*, 2010; Jau *et al.*, 2016; Levine *et al.*, 2018]. Moreover, combining their strong interactions and the coupling to light fields, Rydberg atoms can be used to engineer non-trivial states of light and effective photon-photon interactions. Along those lines, the experimental realizations of strong optical non-linearities [Pritchard *et al.*, 2010], single-photon sources [Dudin and Kuzmich, 2012], attractive photon-photon interactions [Firstenberg *et al.*, 2013] and single-photon transistors [Tiarks *et al.*, 2014; Gorniaczyk *et al.*, 2014] have been demonstrated, extending the range of possible applications of Rydberg atoms in quantum technologies.

In order to improve the performance of Rydberg-based platforms, a missing ingredient so far is the trapping of single Rydberg atoms. Indeed, in the experimental demonstrations mentioned above, or in the quantum simulation experiments described in this manuscript, the Rydberg atoms are in free flight. As a consequence, due to their finite temperature or the mechanical forces induced by interactions, they slightly move during the experiments, which was proven to be a limitation for quantum gate fidelities [Saffman and Walker, 2005; Saffman, 2016] or to induce some dephasing processes in the evolution dynamics [Barredo *et al.*, 2015; de Léséleuc *et al.*, 2018a]. Moreover, trapping single Rydberg atoms would be necessary to perform precision measurements of fundamental constants using circular Rydberg states [Jentschura *et al.*, 2008; Ramos, Moore, and Raithel, 2017] or positronium [Cassidy, 2018].

To date, the three dimensional confinement of Rydberg atoms has been limited to the case of mesoscopic ensembles trapped in millimetre-size regions using static magnetic [Choi *et al.*, 2005] or electric fields [Hogan and Merkt, 2008]. To reach the tight confining regime required to generate traps for Rydberg atoms of micrometre-size, one should use the *ponderomotive* potential. It is the potential experienced by the weakly-bound Rydberg electron at position $\mathbf{r}$ in an AC electric field whose frequency is far from any internal transition frequency of the Rydberg atom, such as an infra-red laser-light field, for example. This potential is equal to the time-averaged kinetic energy of the electron oscillating in this field. It is then repulsive and proportional to the field intensity. The ponderomotive potential reads $V_P(\mathbf{r}) = e^2 I(\mathbf{r}) / (2 m_e \epsilon_0 c \omega_L^2)$, with e and m_e the charge and mass of the electron, respectively, and ω_L the angular frequency of the electric field. Consequently, ponderomotive potentials can be used to laser trap single Rydberg atoms in three dimensions, by creating a dark region surrounded by light in all directions.

Ponderomotive potentials have already been used to confine Rydberg atoms in optical lattices [Anderson, Younge, and Raithel, 2011; Li, Dudin, and Kuzmich, 2013], but only in one dimension so far. In this chapter, I will show how we trapped a single Rydberg atom in three dimensions, by transferring them from a regular Gaussian optical tweezers into a holographically generated bottle beam (BoB) trap, consisting in the required dark region surrounded by light. I will first describe how we create such traps and the experimental signature of single Rydberg atom trapping. Then, I will analyse in more detail the trapping potential and study our trapping efficiency, combining measurements and numerical simulations of the classical atomic motion inside the trap. Finally, I will show that these traps are compatible with the quantum simulation tasks we have already performed with Rydberg atoms in free flight, namely

microwave Rabi oscillations between neighbouring Rydberg levels and spin-exchange interaction. The results presented in this chapter led to the publication [Barredo *et al.*, 2019].

3.1 Upgraded apparatus for Rydberg trapping

To achieve the trapping of single Rydberg atoms via the ponderomotive potential, we need to create a dark region surrounded by light. This so-called bottle beam (BoB) trap can be generated with different techniques [Chaloupka *et al.*, 1997; Ozeri, Khaykovich, and Davidson, 1999; Zhang, Robicheaux, and Saffman, 2011]. Here we use holography, and I will describe how we adapted our experimental apparatus to do so in the first subsection. Then, I will show how we combine the ground-state optical tweezers with the BoB trap to obtain a single trapped Rydberg atom.

3.1.1 Holographic generation of bottle beam traps

I show in Figure 3.1 the required elements to trap single Rydberg atoms on our experimental platform. We use two laser beams at 852 nm, whose wavefronts are controlled by two Spatial Light Modulators (SLM). The red beam in Figure 3.1 creates optical tweezers at the focus of the aspheric lens, in the same way as explained in the previous chapter (see Subsection 2.1.1). It acts as a single ground-state atom source. On these tweezers we superimpose another beam, represented in blue in Figure 3.1. The second SLM imprints a π-phase offset on this beam, on a central disk of radius r_0, whereas the phase is not modified on the outer shell, see top-left inset of Figure 3.1. The total area of the beam, a disk of radius a, is controlled via an iris. The top-left inset illustrates how such a π-phase mask creates a BoB trap. The outer part of the beam, as it is wider, will create a tighter optical tweezers (in the radial and longitudinal directions) than the inner part of the beam. Since these two light fields are out of phase, they interfere destructively at the focus of the aspheric lens, and the subtraction of the two fields, shown on the left of the inset, is composed of a dark region surrounded by light. This is how we generate holographically a BoB trap. The simple argument used here does not lead to the correct intensity distribution near the focus of the aspheric lens. For this, one should solve the Fresnel diffraction integral [Chaloupka *et al.*, 1997; Ozeri, Khaykovich, and Davidson, 1999].

Figure 3.1 shows two-dimensional cuts of the measured light intensity distribution of

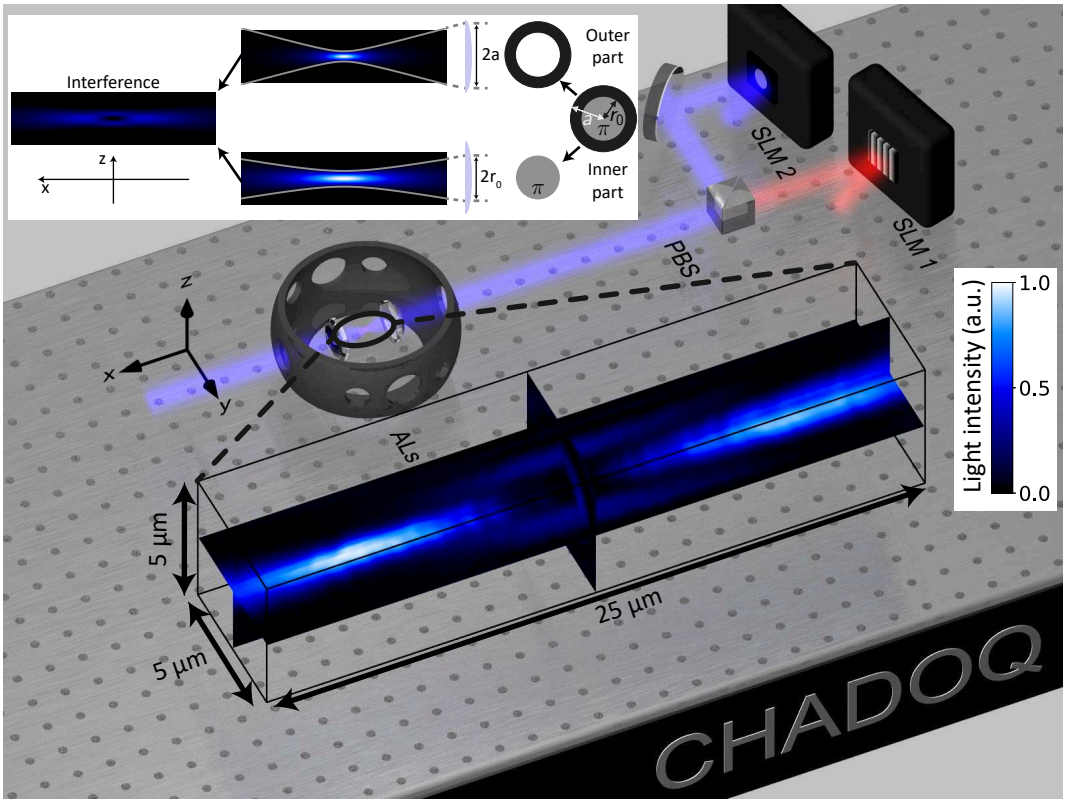

Figure 3.1: Simplified representation of the experimental apparatus for single Rydberg atom trapping. Two 852-nm laser beams are superimposed with a polarization beam splitter (PBS) to trap single Rydberg atoms. The red one creates the regular optical tweezers at the focus of the aspheric lens, as introduced in the previous chapter, and is a trap loaded by single ground-state atoms. A SLM (SLM1) imprints a phase on this beam to control the configuration of the array of optical tweezers. The beam represented in blue is reflected on another SLM (SLM2), which imprints a π phase on the inner part of the beam. This creates a BoB trap at the focus of the aspheric lens. The top-left inset illustrates the principle of the holographic generation of a BoB trap. Measured two-dimensional cuts of the light intensity distribution of the BoB trap are shown.

the BoB trap, indeed revealing a dark region surrounded by light. This measurement was performed using our trap imaging setup described in the previous chapter, with which we can record the light distribution on different planes perpendicular to the optical axis by electrically tuning the focal length of the imaging lens (see Subsection 2.2.3).

Figure 3.2 shows the phase pattern imprinted by the SLM and the associated intensity distribution in the xz plane. On the left, the phase pattern is the combination of a linear gradient of phase and a Fresnel lens, enabling for the control of the position

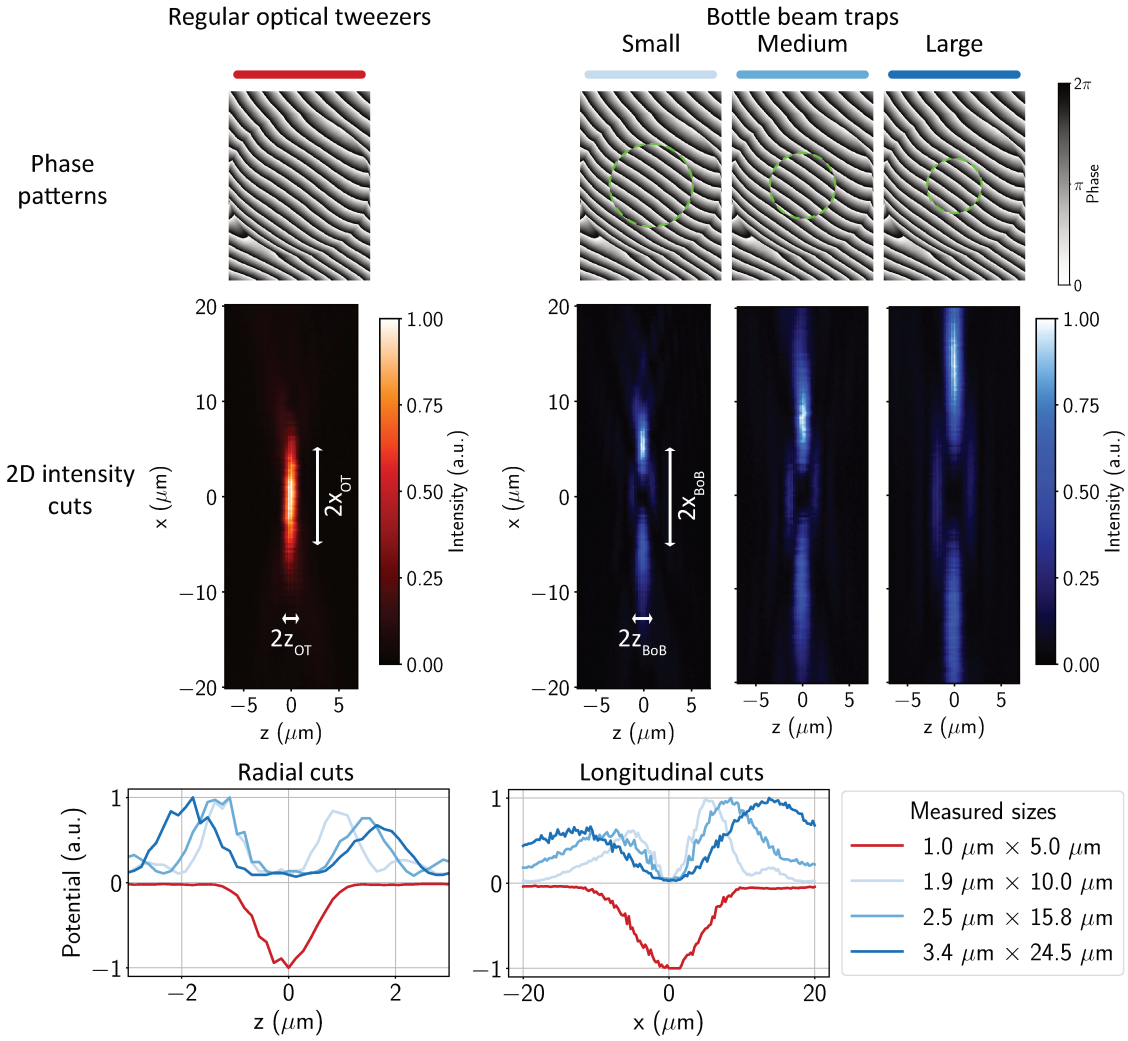

Figure 3.2: Creation of BoB traps. (Top) Phase patterns for regular optical tweezers or BoB traps. The dashed green circles indicate the border of the π-phase masks. (Middle) Intensity distribution in the xz plane associated to the different phase patterns. The typical radial and longitudinal dimensions are indicated. (Bottom) Trapping potentials along the radial (z) or longitudinal (x) directions.

of the optical tweezers. On the right, the phase patterns feature an added π-phase mask in a central disk of radius r_0, highlighted by a dashed green circle, leading to the generation of a BoB trap. The larger the beam impinging on SLM 2 (radius a), the smaller the BoB trap, and we have to adapt r_0 in order to always have a destructive interference condition at the focal point. On our range of parameters, this condition is $r_0^2 \approx 0.5\,a^2$, such that the central disk and the outer shell have approximately the same area. This is why the π-phase mask radius is the largest for the smallest BoB trap. All the maxima of intensity distributions are normalized to one.

The bottom of Figure 3.2 allows to compare the trapping volume of the regular optical tweezers (red, attractive potential normalized to -1) and the ones of BoB traps (blue, repulsive potential normalized to $+1$), both attractive and repulsive potentials being proportional to light intensities. The trapping regions have approximately the same size. The typical radial and longitudinal dimensions for the regular optical tweezers $z_{\mathrm{OT}} \times x_{\mathrm{OT}}$ are given by the $1/\mathrm{e}^2$ radius and the Rayleigh length, extracted from fits of the intensity spatial profile. We measured a trapping size $1.0\,\mu\mathrm{m} \times 5.0\,\mu\mathrm{m}$. For the BoB trap, we define the radial and longitudinal dimensions $z_{\mathrm{BoB}} \times x_{\mathrm{BoB}}$ as the distance between the two local maxima in the radial and longitudinal cuts of the intensity profile. These dimensions are indicated in the legend of Figure 3.2.

Since the regular optical tweezers and the BoB trap have approximately the same size, one way to trap a single Rydberg atom is the following: starting with a ground-state atom held in an optical tweezers, we release it and excite it to a Rydberg state while being in free flight, and then we trap it by shining the BoB trap. This transfer of the atom from one type of trap to the other is possible if the two traps are correctly overlapped, and if the atom does not move too far away while being in free flight. The two SLMs enable for the precise alignment of the traps with respect to one another, by tuning the direction of the imprinted linear gradient of phase.

3.1.2 Signature of Rydberg atom trapping

Once we have observed that we generate BoB traps, we should transfer single atoms excited to Rydberg states inside them and measure how long we are able to keep them. This experiment is described in Figure 3.3 (Exp 3). To confirm the trapping of single Rydberg atoms, we actually compare this experiment with two other ones, consisting in measuring the recapture probability after a varying time for a Rydberg atom in free flight (Exp 1) and for a ground-state atom in the presence of the BoB trap (Exp 2).

Exp 1 is the same kind of release and recapture experiment introduced in the

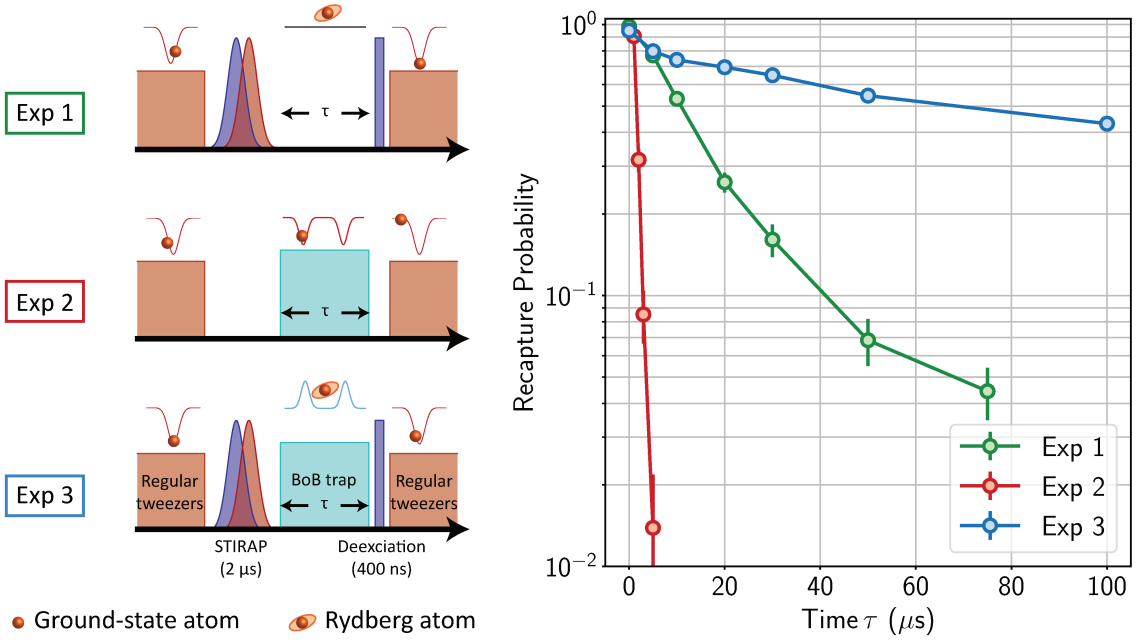

Figure 3.3: Trapping of single Rydberg atoms. Three kinds of experiment were performed to look for the signature of Rydberg trapping. The first one consists in letting a Rydberg atom in free flight for a varying time τ. The second one consists in shining for a duration τ the BoB trap on a ground-state atom. The third one is similar except that we shine the BoB trap on a Rydberg atom. For the tree experiments, the recapture probability as a function of τ is plotted.

previous chapter (see Figure 2.4) which allows us to infer the atomic temperature. Here, in addition to let the atoms in free flight for a varying duration τ, we excite them to a Rydberg state (in that case it was the $84S_{1/2}$ state) using a STIRAP process, and we deexcite them back to the electronic ground state with a blue pulse at the end of the free flight (see subsection 2.3.3 for more detail on the excitation/deexcitation protocols). Measuring the recapture probability as a function of the free flight duration (green disks in Figure 3.3), we infer an atomic temperature of 130 μK, and we have not noticed any heating due to the excitation to the Rydberg states.

In a second set of experiments, labelled as Exp 2, we let a ground-state atom in free flight and shine the BoB trap on it. For a ground-state atom, as the BoB trap is generated with an 852-nm light, i.e. a red-detuned light with respect to the transition to the first excited states, it will be attracted by high-intensity regions. As the high-intensity regions of the regular optical tweezers and the ones of the BoB trap do not overlap, the ground-state atom will be quickly attracted away from the final recapture region of the regular optical tweezers, and the recapture probability drops

drastically (red disks in Figure 3.3).

Finally, the third kind of experiment is the combination of the two previous one. It consists in exciting the atoms to a Rydberg state (still $84S_{1/2}$ in that case), shining the BoB trap for a varying duration τ, deexciting the atom to the ground state and recapturing it. The recapture probability of a Rydberg atom is enhanced thanks to the presence of the BoB trap (comparing the results of Exp 3 with the ones of Exp 1 in Figure 3.3), which is the signature of the trapping of single Rydberg atoms. Exp 2 allows us to confirm that the observed extended trapping time in Exp 3 is due to the excitation to Rydberg states, and not only the presence of the BoB trap. The measured signal in Exp 3 allows us to optimize the experimental parameters in order to obtain the best trapping. We vary the 852-nm laser power, the size of the BoB trap, and the position of the BoB trap with respect to the regular optical tweezers to have the largest recapture probability after 30 μs in the BoB trap. This led us to choose a laser power of 400 mW and the medium-sized BoB trap (see Figure 3.2). With these parameters, we observed an enhanced recapture probability if the principal quantum numbers of the Rydberg states involved is such that $60 < n < 90$. We will describe in more detail the trapping efficiency as a function of the principal quantum number in the next section.

I have shown here how transferring a single Rydberg atom inside a BoB trap allows us to recapture it for an extended time compared with the free flight case, demonstrating our ability to trap single Rydberg atoms. Although the trapping time is extended, the recapture probability in Exp 3 slightly decays. The aim of the next section is to understand the origins of this decay.

3.2 Trap characterization

Now that we have demonstrated our ability to trap single Rydberg atoms, we need to characterize quantitatively the BoB trapping features. I will first derive the expression of the trapping potential, leading to the computation of a minimal energy barrier which must be high enough to keep the Rydberg atoms trapped. Then, I will show that the characteristic lifetime inside a BoB trap depends on the principal quantum number n of the Rydberg state involved. More precisely, it is related to the Rydberg state lifetime in a 300 K environment. Finally, I will estimate the trapping frequencies in such traps.

3.2.1 Trapping potential

So far, I have only mentioned the ponderomotive potential $V_P(\mathbf{r})$ experienced by the nearly free Rydberg electron to explain the repulsive potential trapping the single Rydberg atom. I recall that it reads $V_P(r) = e^2 I(\mathbf{r}) / (2 m_e \epsilon_0 c \omega_L^2)$, with e and m_e the charge and mass of the electron, and ω_L the angular frequency of the 852-nm trapping laser. This potential is proportional to the light intensity $I(\mathbf{r})$, with $\mathbf{r}$ the position of the electron.

In fact, for the trapping potential experienced by a Rydberg atom at position $\mathbf{R}$, we must take into account the extension of the electronic wavefunction ψ_{nljm_j}. Then, in a Born-Oppenheimer-like approximation, the trapping potential for the Rydberg atom is given by the following convolution [Dutta *et al.*, 2000]

$$U_{nljm_j}(\mathbf{R}) = \int V_P(\mathbf{R}+\mathbf{r}) \left|\psi_{nljm_j}(\mathbf{r})\right|^2 \mathrm{d}^3 r. \tag{3.1}$$

For an hypothetical zero-extension Rydberg atom, $\left|\psi_{nljm_j}(\mathbf{r})\right|^2$ is the Dirac function, and the potential experienced by the Rydberg atom $U_{nljm_j}(\mathbf{R})$ reduces to the ponderomotive potential $V_P(\mathbf{R})$.

I will then present the result of a numerical calculation of convolution (3.1) in order to derive the value of $U_{nljm_j}(\mathbf{R})$. This will allow us to extract the minimum energy barrier confining the Rydberg atom.

Convolution with the Rydberg wavefunction Only Rydberg $nS_{1/2}$ were involved in the experiments described in this section. In that case, the electronic wavefunction depends on n and $r = |\mathbf{r}|$ (it is isotropic), which simplifies the treatment of equation (3.1). First, we focus on the relative effect of the convolution, we will be interested in the absolute value of the potential later. Therefore, we compare $U_{nS}(\mathbf{R})$ with the ponderomotive potential, represented in the xz plane in Figure 3.4(a). For this comparison, we compute the ratio $U_{nS}(\mathbf{R})/V_0$, where V_0 is the maximum value of the ponderomotive potential.

The effect of the convolution can be interpreted as the average of the ponderomotive potential over the spatial range of the radial density probability of the nS orbital $r^2 |\psi_{nS}(r)|^2$. This spatial range scales as n^2. These orbitals are plotted to scale in Figure 3.4(a). For $n \geq 100$, the spatial extent of the radial wavefunction is on the same order of magnitude as the typical length scale of the BoB intensity distribution, that is to say about $1\,\mu$m. Consequently, we expect that for such high principal quantum numbers the potential created by the BoB light will not be confining any more, the

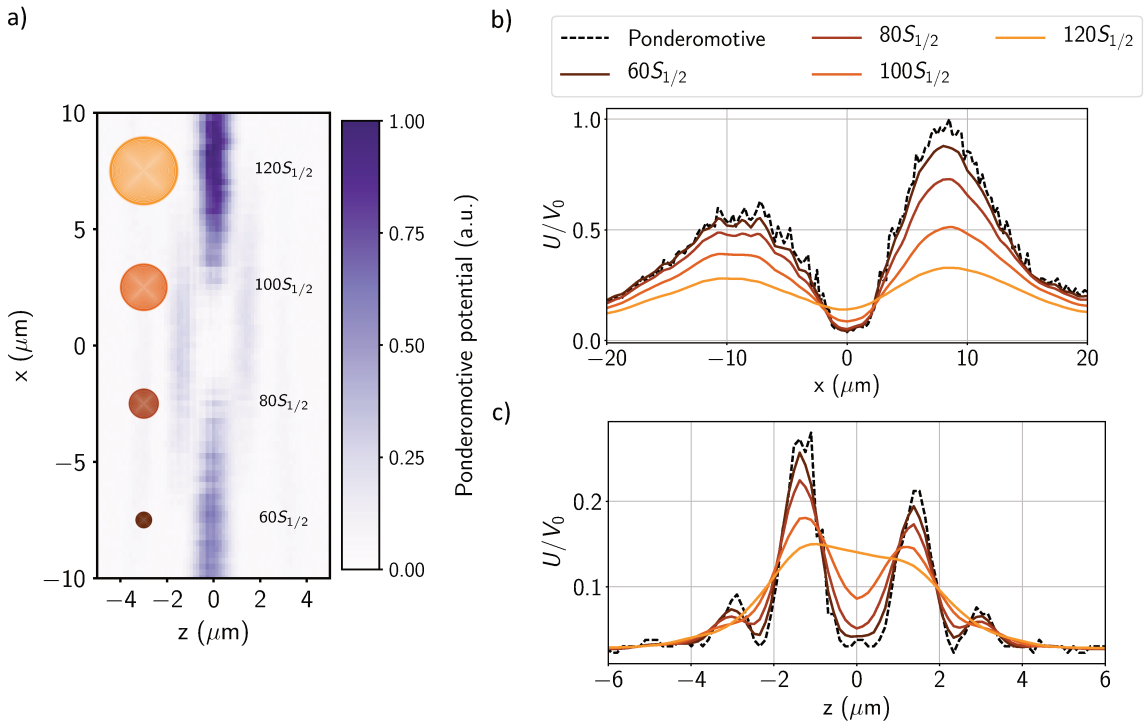

Figure 3.4: From the light intensity to the Rydberg trapping potential. (a) Ponderomotive potential in the xz plane. The size of the electronic Rydberg orbital is shown for different principal quantum numbers to be compared with the ponderomotive potential length scale. (b) and (c) Longitudinal and radial profiles of the trapping potentials for different principal quantum numbers, normalized to V_0, which is the maximum value of the ponderomotive potential for the same trapping laser power.

dark region surrounded by light will be totally averaged out.

This is indeed what is revealed by the result of the convolution, where the trapping potentials are plotted along the longitudinal (Figure 3.4(b)) and the radial (Figure 3.4(c)) directions. The larger n, the shallower the trapping potential, until the limit case of $n = 120$ where the potential is even anti-trapping in the radial direction.

Minimal energy barrier Now, we want to estimate the numerical value of the potential in order to retrieve the height of the potential barrier, to be compared with the trap depth of a regular optical tweezers. As the atom is confined in dark regions, it is repelled from the regions where it could experience the light-shift induced by the BoB trap light. Consequently, unlike the case of the regular optical tweezers, we cannot use spectroscopic measurements to deduce the BoB trapping potential energy. Then, to estimate this potential energy, we followed an indirect procedure. For the same incoming power of the 852-nm laser beam, we measured the strength

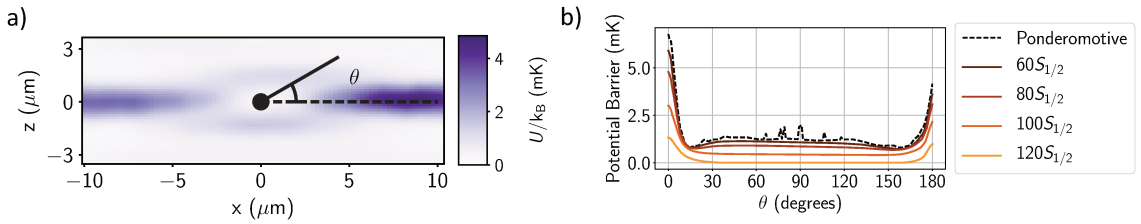

Figure 3.5: Potential barrier. (a) Trapping potential in the xz plane, for the $84S_{1/2}$ Rydberg state and 400 mW of laser power. (b) Potential barrier crossed when following a line with a given direction θ, for different principal quantum numbers and a 400 mW laser power.

of the signal on the CCD camera for trap imaging in the case where no π-phase mask is applied (regular optical tweezers), and when it is applied (BoB trap). For regular optical tweezers, we know from light-shift measurement that a laser power of 5 mW corresponds to a trap depth of 1 mK. Taking into account the ratio between the measured CCD signals in both cases, the ratio between the power used to generate the BoB trap and these calibration 5 mW, and the ratio between the polarizabilities of the Rydberg atom and the ground-state atom $\alpha = (\omega_0^2 - \omega_L^2)/\omega_L^2 \approx 0.17$, where ω_0 is the angular frequency of the transition between the ground state and the first excited state, we can estimate the value of the trapping potential.

This trapping potential is plotted in the xz plane in Figure 3.5(a) for an incoming laser power of 400 mW and for the $84S_{1/2}$ Rydberg state. The potential barrier around the central dark region of the BoB trap is not at the same height for all directions, as we could already expect from the intensity imaging (see Figure 3.2). It is the highest in the longitudinal direction, then it is approximately five times as small in the radial direction (for low enough Rydberg states $n < 90$) and finally it is even more reduced along a cone near the longitudinal direction.

In order to be more quantitative, we measure the maximum potential energy we cross while following a line from the center of the dark region and with a specific direction θ (see Figure 3.5(a)). This potential barrier is plotted in Figure 3.5(b), for different principal quantum numbers. For low enough n, the potential barrier is the smallest for a specific angle near the longitudinal direction $\theta \approx 15°$. For larger n, these spatial details of the BoB trapping potential are averaged out as explained above, and for $n = 120$, the potential barrier is zero in the radial direction, so the BoB potential is actually anti-trapping.

This study allows us to extract the minimal energy barrier seen by the atom while moving around the center of the dark region of the BoB trap. For a 400 mW laser

power and $n \leq 90$, this minimal barrier is about 1 mK, that is to say on the same order of magnitude as the trap depth of the regular optical tweezers for 5 mW. For a BoB trap, we then need a large laser power to generate high enough potential barriers in all directions to confine atoms at 130 μK. Decreasing the atomic temperature (we proved later that we can reach atomic temperature as low as a few μK), and using the smallest BoB trap, we have achieved to trap Rydberg atoms with 20 mW laser power, holding the promise for scalability. We may also work on more elaborate phase patterns to generate a more homogeneous surrounding potential barrier. In that case, we could use even less laser power per BoB trap.

3.2.2 Lifetime in the BoB trap

Now that we have understood in more detail the trapping potential, in terms of spatial dependence where we have seen the effect of the convolution by the Rydberg radial wavefunction, and in terms of minimal energy barrier, we can see for how long we can keep a Rydberg atom inside a BoB trap. To do so, we repeat Exp 3 introduced in Figure 3.3, still for a laser power of 400 mW and the medium-sized BoB trap, and for a varying principal quantum number of the Rydberg state involved.

Trapping lifetime Figure 3.6(a) shows the result of such an experiment (solid disks), for the four Rydberg states $60S_{1/2}$, $75S_{1/2}$, $84S_{1/2}$ and $92S_{1/2}$. The recapture probability decays roughly in an exponential manner, and the dashed lines are fit to extract the exponential mean lifetime. We compare the fitted lifetimes with the Rydberg state lifetimes in a 300 K environment [Beterov *et al.*, 2009; Archimi *et al.*, 2019] (see Figure 3.6(b)). The lattest are radiative lifetimes, computed in our case using the Alkali Rydberg Calculator (ARC) software [Šibalić *et al.*, 2016].

This radiative lifetime gives the mean duration before a Rydberg atom is transferred into another state. Either it spontaneously decays to low-lying states, either it transitions into neighbouring Rydberg states via black-body radiation from the environment. As shown in Figure 3.6(c), both types of radiative process lead to a loss of the atom. If the atom decays to a low-lying state, the atom is now attracted away, by the BoB light, from the final recapture region, and the recapture probability drastically drops as already explained for Figure 3.3 Exp 2. If the atom is transferred into a neighbouring Rydberg state, it stays trapped as it experiences almost the same trapping potential (its principal quantum number has only been changed by a few units). But the deexcitation pulse is not at resonance any more to transfer the Rydberg

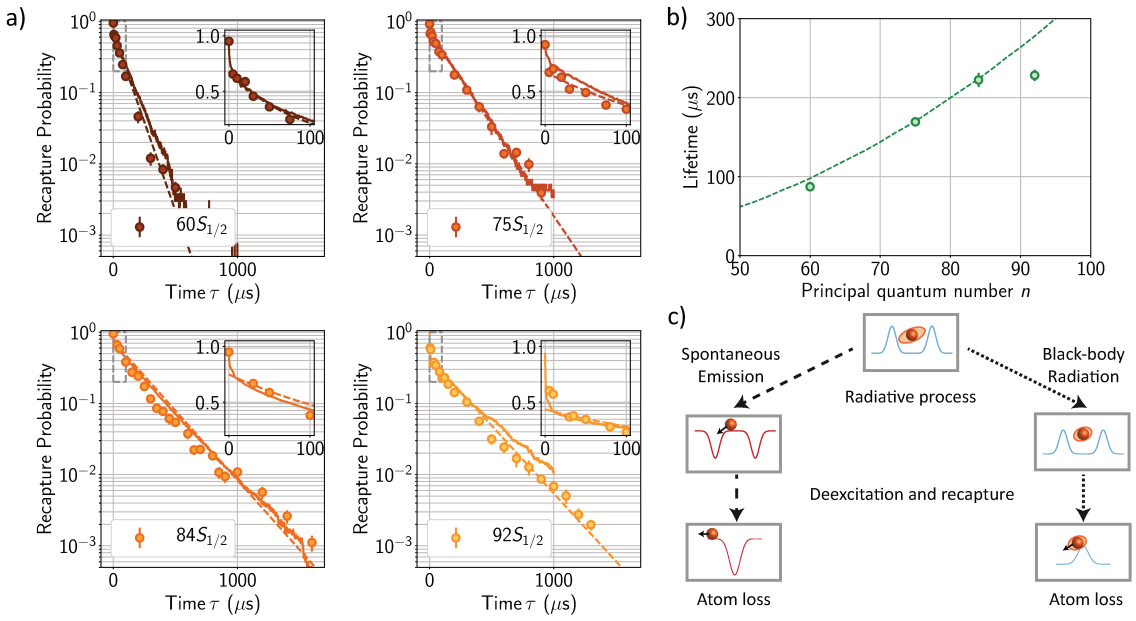

Figure 3.6: Measuring the lifetime in the BoB trap. (a) Recapture probability as a function of the time τ spent in the BoB trap (solid disks), for four different Rydberg levels. The dashed lines are fit to extract the mean lifetime of the exponential decay, and the solid lines are classical Monte-Carlo simulations. (b) Lifetimes extracted from the measured exponential decays (solid disks), to be compared with the radiative Rydberg lifetime in a 300 K environment (dashed line). (c) Scheme of the atomic loss mechanism due to radiative processes, if the atom spontaneously decays to a low-lying state (left) or is transferred into a neighbouring Rydberg state (right).

atom back in the electronic ground state, so the atom will be expelled by the regular optical tweezers as it is still in a Rydberg state. In the end, the atom is lost in both cases. This is why the lifetimes fitted on the measured recapture probabilities are in very good agreement with the computed radiative lifetimes in a 300 K environment. The agreement is less good for $n = 92$. It turns out that both lifetimes do not coincide for $n > 90$ due to additional losses called mechanical losses, which will be detailed below.

Classical Monte-Carlo simulations The insets on the plots in Figure 3.6(a) show a discrepancy at short times from this exponential decay behaviour. There, the decay is faster. To understand this point, we perform classical Monte-Carlo simulations, inspired by the ones we ran to infer the atomic temperature in release and recapture experiments (see Figure 2.4). These simulations consist in computing the atomic trajectory, with a set of initial conditions deduced from the thermal distributions in

position and velocity of the atoms at 130 μK inside the regular optical tweezers. After setting the initial conditions, we compute the motion first in free flight for the STIRAP duration, then inside the BoB trapping potential derived in the previous subsection for a time τ, and then again in free flight for the deexcitation duration. If the kinetic energy is larger than the potential trapping energy of the regular optical tweezers at the final position of the atom, the atom is not recaptured. In the end, repeating the same procedure one thousand times, we compute the recapture probability.

In addition to the atomic motion, we take into account the finite STIRAP excitation efficiency (about 10% of the atoms are not excited). If the STIRAP does not succeed, the atom stays in the electronic ground state. We also compute the atomic motion in that case, where the BoB potential is now attractive, which leads to a fast decay of the recapture probability as expected from Exp 2 in Figure 3.3.

Finally, the last ingredient we include in our classical computation of the atomic trajectory is the Rydberg lifetime in a 300 K environment. For each trajectory simulation, we pick up a time according to the exponential law whose time constant is the radiative lifetime introduced above. At this specific time, the atom is transferred to neighbouring Rydberg states or to low-lying states, and in both cases, the atom is lost (see Figure 3.6(c)). Therefore, for an easier numerical treatement of the Rydberg lifetime effect, we consider in our simulation that the atom is transferred back to the electronic ground state. Back in the ground state, the recapture probability drops, so in the end this simplification of the radiative loss mechanism leads to the same result.

The results of the simulations taking into account all the elements listed above are plotted as solid lines in Figure 3.6(a). The agreement with the measured recapture probabilities is good, especially, the simulation reproduces quite well the behaviour at short times (see insets). In our simulations, we do not take into account the photoionization effect (ionization of Rydberg atoms due to the absorption of trapping light photons), which leads to additional losses [Saffman and Walker, 2005; Zhang, Robicheaux, and Saffman, 2011].

Mechanical losses The advantage of our simulation is that we can artificially remove the effect of the Ryderg state decay to other states, to see only the effect of the trapping potential on the recapture probability. Indeed, as a function of the peculiar set of initial conditions, a Rydberg atom may escape the BoB trap. This results in a reduced recapture probability defined as mechanical losses. This is what is shown in Figure 3.7(a), where I computed the recapture probability as a function of τ for different Rydberg states, without taking into account any decay of the Rydberg state.

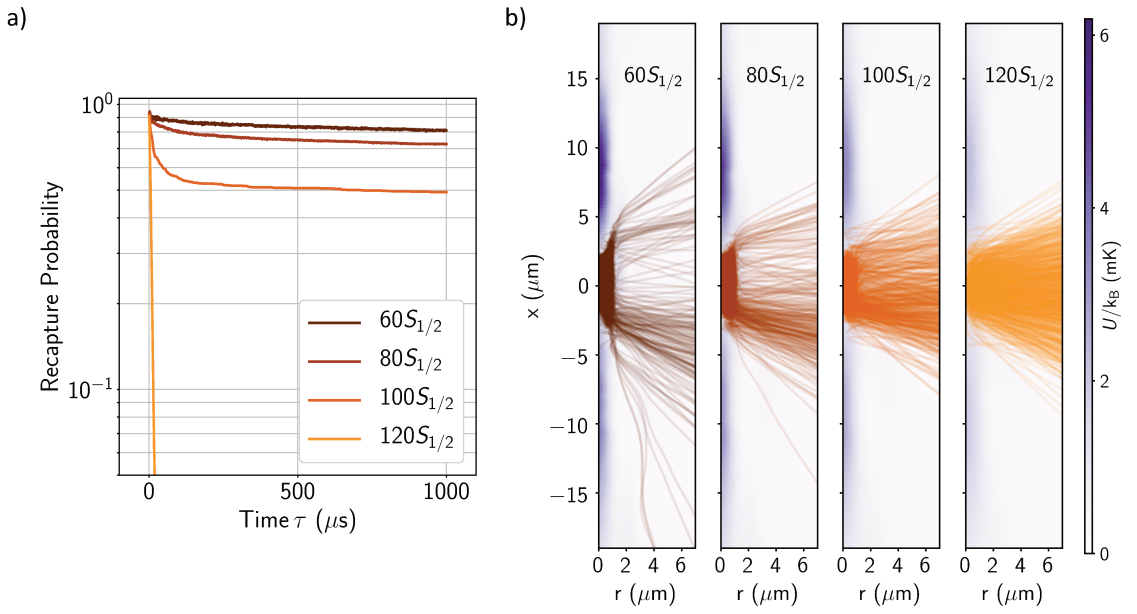

Figure 3.7: Dynamical leaking of the Rydberg atoms. (a) Computed recapture probabilities as a function of the time τ spent in the BoB trap if we neglect any radiative loss process, for different Rydberg states. (b) Atomic trajectories inside the BoB trap. They were computed in three dimensions $(x(t), y(t), z(t))$, and are represented here in two dimensions using a cylindrical system of coordinates $(x(t), r(t))$, with $r(t) = \sqrt{y^2(t) + z^2(t)}$. The colormap indicates the trapping potential in this plane.

For low n Rydberg states, most of the atoms stay trapped, and we only notice a slow decay in the recapture probability. For $n = 100$ a larger fraction of the atoms escape from the trap at short times, and for $n = 120$, all the atoms escape in a few tens of μs. This result could be anticipated thanks to our study of the effect of the convolution (Figures 3.4 and 3.5).

This numerical simulation neglecting the radiative decay allows us to understand why the measured trapping lifetime coincides with the radiative Rydberg lifetime only for $60 < n < 90$, by distinguishing between mechanical and radiative losses. For higher n, the losses due to the vanishing trapping potential are more important than the ones due to the radiative decay, and therefore completely explain the observed trapping lifetime.

The computed atomic trajectories, shown as solid lines in Figure 3.7(b), reveal the spatial dependence of the trapping potential we described in the previous subsection. For $n = 60$, most of the atoms stay trapped, and the ones escaping leak from the BoB trap through the minimal energy barrier at $\theta \approx 15°$ (see Figure 3.5(b)). For higher n, the atoms escape in the radial direction.

To sum up, we observed that the mean trapping lifetimes of Rydberg atoms in BoB traps coincide with their radiative lifetimes in a 300 K environment, for principal quantum numbers such that $60 < n < 90$. Classical Monte-Carlo simulations agree with the observed recapture probabilities, especially they show that the faster decay at short times is due to the quick loss of atoms which were not excited to Rydberg states, and to mechanical losses. In the end, these mechanical losses result in a finite trapping efficiency of Rydberg atoms. For low enough Rydberg states, $n < 90$, it saturates at $70 - 80\%$, and it vanishes for higher Rydberg states (see Figure 3.7(a)). According to the simulation, working with colder atoms would improve the trapping efficiency as it reduces the mechanical losses.

3.2.3 Trapping frequencies

Finally, the last trapping characterization lacking is the trapping frequency, already introduced in the previous chapter in the context of regular optical tweezers (see Subsection 2.1.1). In that case, these frequencies are derived using the approximation considering the light Gaussian profile as a harmonic profile, which is valid if the atom stays at the bottom of the trap. Here, the BoB light profile cannot be considered as a harmonic profile, it is quartic in the radial direction and harmonic only in the longitudinal one. Nevertheless, the convolution smoothes the quartic profile (see Figure 3.4(c)), and we are able to extract trapping frequencies.

Figure 3.8(a) describes the sequence we use to measure the trapping frequencies. It consists in exciting the breathing modes of the trapped atoms, as already explained in the thesis of Lucas Béguin [2013] in the context of regular optical tweezers. We first transfer the atoms in the BoB trap for 30 μs, in order to get rid of the hottest atoms. Then, we let them in free flight for 4 μs, shine the BoB trap for a varying duration τ, let them fly away for another 10 μs, and finally recapture them. For a harmonic trap of frequency ω, the recapture probability is expected to oscillate at 2ω.

Figure 3.8(b) shows the measured recapture probabilities for the medium-sized BoB trap and the $84S_{1/2}$ Rydberg state, for two different laser powers. The dashed lines are fitting damped sine to extract the trapping frequencies. The solid lines are the results of the same kind of Monte-Carlo simulations as the ones introduced in the previous subsection, taking into account the whole sequence of alternating free flight and trapping steps. They are in qualitative agreement with the measured recapture probabilities, especially at short times. The finite atomic temperature and the remaining anharmonicity of the BoB trap could explain the damping of the

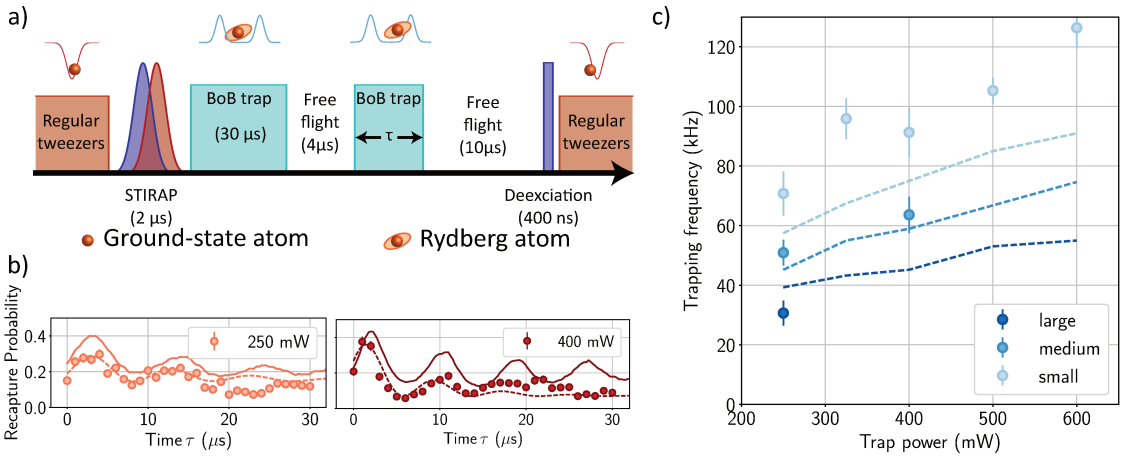

Figure 3.8: Trapping frequencies. (a) Experimental sequence used to excite the breathing modes of the trapped atoms and extract the trapping frequencies. (b) Measured oscillations in the recapture probability (solid disks). The dashed lines is a fitting damped sine to extract the trapping frequency, the solid line is a Monte-Carlo simulation with no adjustable parameters. (c) Measured trapping frequencies (solid disks) for different laser powers and sizes of the BoB trap. The dashed lines are the trapping frequencies extracted from the Monte-Carlo simulations.

observed oscillations.

Finally, we repeat the same kind of experiments for different sizes of the BoB trap, and different powers (Figure 3.8(c)). The measured trapping frequencies show the expected qualitative behaviour, the more power or the smaller the BoB trap, the larger the trapping frequency. The trapping frequencies extracted from Monte-Carlo simulations (dashed lines) is in a qualitative agreement with the measured ones. To generate a larger BoB trap, we have to clip a larger fraction of the laser beam in order to reduce a (see Figure 3.2). This is why we cannot probe the high power range with the largest BoB trap.

To conclude, I have demonstrated our ability to trap single Rydberg atoms. The trapping is efficient for Rydberg states such that $60 < n < 90$, and the trapping lifetime is in that case limited by the radiative Rydberg state lifetime in a 300 K environment. The numerical analysis of the trapping potential and the computation of the atomic trajectories allowed us to understand these trapping features. After these demonstrations at the single-particle level, we go one step further in the next section by studying the case of interacting Rydberg atoms while being trapped.

3.3 Rydberg trapping and quantum simulation

The aim of this last section is to demonstrate that the Rydberg trapping technique we have implemented is compatible with the quantum simulation tasks we usually perform while the Rydberg atoms are in free flight. I will even show that new phenomena are likely to emerge with the use of Rydberg trapping. In the Introduction, when I presented the quantum simulation projects we are able to perform on our platform, I insisted on the fact that depending on the Hamiltonian we want to mimic, the qubit must be encoded in different levels. The BoB trap we use is only suitable to confine Rydberg atoms and not ground-state atoms (see Figure 3.3 Exp 2), so using the Rydberg trapping technique described in this chapter, we can only perform quantum simulation of the XY Hamiltonian, where the qubit is encoded into two neighbouring Rydberg levels.

We are going to focus on two ingredients we use when studying the quantum simulation of the XY model: first, the microwave Rabi oscillation between the neighbouring Rydberg levels encoding the qubit, and second, the spin-exchange process. These two experiments, and their role with respect to the study of spin or hard-core boson Hamiltonians, will be described in more detail in the following of this manuscript (Chapter 5 for the microwave Rabi oscillation and Chapter 6 for the spin-exchange).

3.3.1 Microwave Rabi oscillations

Rabi oscillation The first experiment I describe is the microwave Rabi oscillation between neighbouring Rydberg levels. The Rydberg levels involved in the following are represented in Figure 3.9(a). Using two different excitation schemes (see Figure 2.10), we can prepare via STIRAP either $\left|82D_{3/2}, m_J = 3/2\right\rangle$ or $\left|84S_{1/2}, m_J = 1/2\right\rangle$. Then, applying a microwave pulse at the frequency of the transition (i) between $|\uparrow\rangle = \left|82D_{3/2}, m_J = 3/2\right\rangle$ and $|\downarrow\rangle = \left|83P_{1/2}, m_J = 1/2\right\rangle$ (around 3.87 GHz), we can induce a Rabi oscillation between the two encoded spin states $|\uparrow\rangle$ and $|\downarrow\rangle$. The experimental sequence we followed to observe this Rabi oscillation is shown in Figure 3.9(b). We transfer the Rydberg atom prepared in state $|\uparrow\rangle$ inside the BoB trap for a fixed duration of 50 μs, and apply while the atom is inside the BoB trap a microwave pulse at resonance of varying durations. When the BoB trap is switched off, if the atom is in $|\uparrow\rangle$, it will be deexcited back to the electronic ground state and then

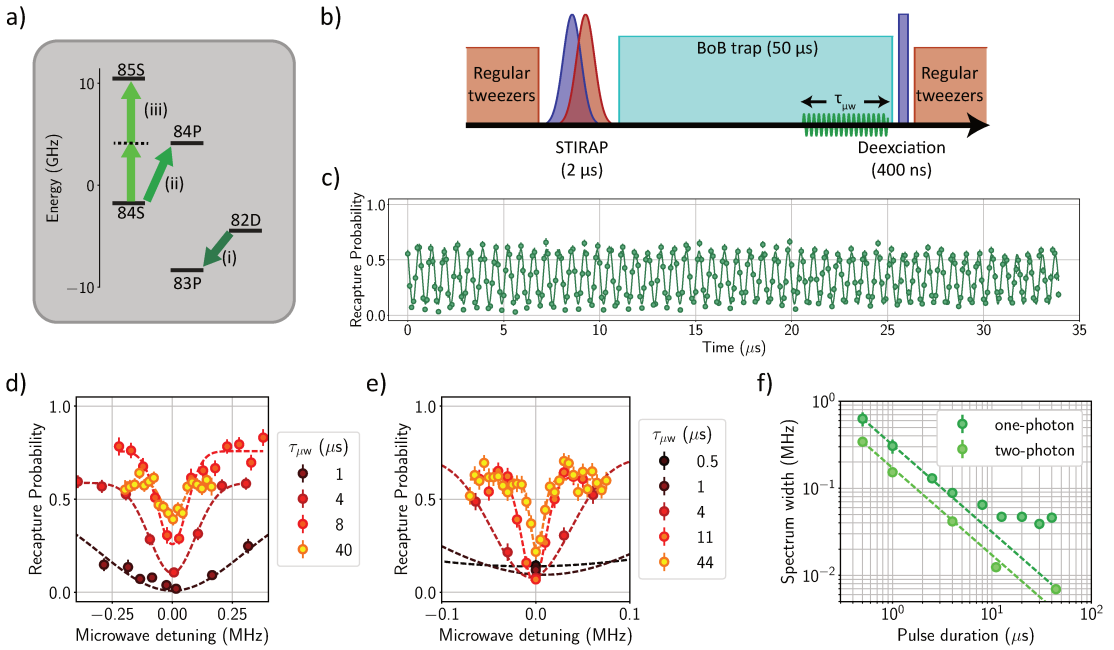

Figure 3.9: Microwave qubit driving. (a) Rydberg levels used in the following experiments. With our STIRAP protocol, we either prepare the Rydberg states $|82D_{3/2}, m_J = 3/2\rangle$ or $|84S_{1/2}, m_J = 1/2\rangle$, and we probe the transitions to (i) $|83P_{1/2}, m_J = 1/2\rangle$, (ii) $|84P_{1/2}, m_J = 1/2\rangle$ or (iii) $|85S_{1/2}, m_J = 1/2\rangle$ (two-photon transition). (b) Experimental sequence used to measure the Rabi oscillations. (c) Rabi oscillation between $|82D_{3/2}, m_J = 3/2\rangle$ and $|83P_{1/2}, m_J = 1/2\rangle$, corresponding to a Rabi frequency $2\pi \times 1.51\,\mathrm{MHz}$, deduced from the fitting damped sine (solid line). (d) Microwave spectroscopy of the single-photon transition (ii) for a varying pulse duration. Dashed lines are gaussian fits to extract the spectrum linewidth. (e) Same as (d) for the two-photon transition (iii). (f) Fitted spectrum linewidth as a function of the microwave pulse duration. The dashed lines indicate the expected narrowing as the inverse of the pulse duration.

will be recaptured, otherwise, it will stay in the Rydberg state $|\downarrow\rangle$ and will be lost. Measuring the recapture probability after the deexcitation pulse allows then to infer the population in the $|\uparrow\rangle$ and $|\downarrow\rangle$ states.

Figure 3.9(c) shows the measured recapture probability, indeed revealing a Rabi oscillation between the states $|\uparrow\rangle$ and $|\downarrow\rangle$. We chose to work with a constant total BoB trap duration not to induce any damping due to the mechanical losses of the hottest atoms, described in the previous section. Consequently, whatever the duration of the microwave pulse, we will have the same amount of mechanical losses, resulting in a reduced contrast (approximately 60%) but no induced damping. The fitting damped sine (solid line) gives a measured Rabi frequency of $2\pi \times 1.51\,\mathrm{MHz}$, for an almost

vanishing damping rate (4 kHz). As the BoB potentials seen by the two different Rydberg states are approximately the same (the principal quantum numbers only differ by one), and as the atom stays in the dark region at the center of the BoB trap, we are not able to measure any state-dependent light-shift induced by the BoB trap, whereas it was the case in an experiment performed in a ponderomotive optical lattice [Younge *et al.*, 2010]. The expected difference between the state-dependent light-shifts of two neighbouring Rydberg states is on the order of one percent of the ponderomotive potential.

Performing the same kind of experiment without any BoB trap, that is to say operating with a constant time of free flight and a varying microwave pulse duration, we would also observe an almost undamped Rabi oscillation (see Chapter 5), but with a reduced contrast (only 20% for atoms at 30 μK and for a 50 μs duration of free flight). The reason is the loss of atoms during free flight, they escape from the trapping region due to their finite temperature.

Long-duration spectroscopy Thanks to Rydberg trapping, we can then perform microwave manipulation of the Rydberg states for longer durations, with reasonable contrast with respect to the free-flight case. Consequently, we can probe spectroscopically transitions between Rydberg states for longer durations, that is to say with less microwave power. Then, the power broadening of the linewidth can be reduced to a few tens of kHz. This is what is shown at the bottom of Figure 3.9.

We first probe transition (ii) (see Figure 3.9(a)) with different microwave pulse durations. When increasing the pulse duration, we decrease its amplitude in order to always have the same pulse area. The resulting spectra are shown in Figure 3.9(d). The dashed lines are Gaussian fits to extract the spectrum linewidth. For the longest pulse durations, the linewidth stops decreasing. This is because the Zeeman shifts experienced by the $\left|84S_{1/2}, m_J = 1/2\right\rangle$ state and the $\left|84P_{1/2}, m_J = -1/2\right\rangle$ state are not the same, leading to a homogeneous broadening of the line proportional to the magnetic field fluctuations. This broadening is estimated to be approximately 40 kHz, as it is the minimal spectrum width we measured. Consequently, the shot-to-shot fluctuations of the magnetic field are about 30 mG. For an applied magnetic field of nearly 50 G, this means fluctuations below 0.1%, which is the expected order of magnitude.

We then probe the two-photon transition (iii) following the same procedure, and represent the different spectra in Figure 3.9(e). The fitted linewidth as a function of the pulse duration is plotted in Figure 3.9(f), while probing the one- or two-photon

transitions. In the two-photon case, the linewidth decreases as the inverse of the pulse duration (green dashed line) for longer pulse durations. The linewidth does not saturate in this case because the two-photon transition is insensitive to the magnetic field shot-to-shot fluctuations. Indeed, the Zeeman shifts experienced by the $\left|84S_{1/2}, m_J = 1/2\right\rangle$ state and the $\left|85S_{1/2}, m_J = 1/2\right\rangle$ state are the same, so there is no homogeneous broadening.

Consequently, I have shown that Rabi oscillations between neighbouring Rydberg states can be performed while the atom is trapped. This is the usual single-qubit operation required in quantum simulation experiments of the XY Hamiltonian. In the next subsection, we study a two-interacting-qubit process, the spin-exchange.

3.3.2 Spin-exchange

The spin-exchange process is a consequence of the resonant dipole-dipole interaction, as already described in the Introduction. Considering the two qubit states $|\uparrow\rangle = \left|82D_{3/2}, m_J = 3/2\right\rangle$ and $|\downarrow\rangle = \left|83P_{1/2}, m_J = 1/2\right\rangle$ and a minimal system of two atoms, the interaction Hamiltonian reads in the two-atom basis

$$\hat{H} = J\left(|\uparrow\downarrow\rangle\langle\downarrow\uparrow| + |\downarrow\uparrow\rangle\langle\uparrow\downarrow|\right).$$

Consequently, once the two-atom system is prepared in the state $|\uparrow\downarrow\rangle$, it will oscillate between the two states $|\uparrow\downarrow\rangle$ and $|\downarrow\uparrow\rangle$ at a frequency $2J/h$, as represented schematically in Figure 6.5(a). For the Rydberg states involved, the interaction energy for two atoms at $40\,\mu$m is such that $J/h = 0.36\,$MHz.

Experimental sequence To observe such a phenomenon, we must prepare the state $|\uparrow\downarrow\rangle$, which means that we must change the state of one of the atoms while the other stays in the same state. As the microwave driving has a global effect on the two atoms, we use an additional laser beam, called an addressing beam, focused on one of the two atoms to shift the resonance frequency of this atom. Then, the two atoms do not have the same resonance frequency and we can change the state of one atom without affecting the other one. I will come back on this addressing technique in Chapter 6.

Once $|\uparrow\downarrow\rangle$ is prepared, we let the system evolve for a varying duration, see the experimental sequence in Figure 6.5(b). We perform the microwave preparation and this evolution while the two Rydberg atoms are inside the BoB traps. At the end of

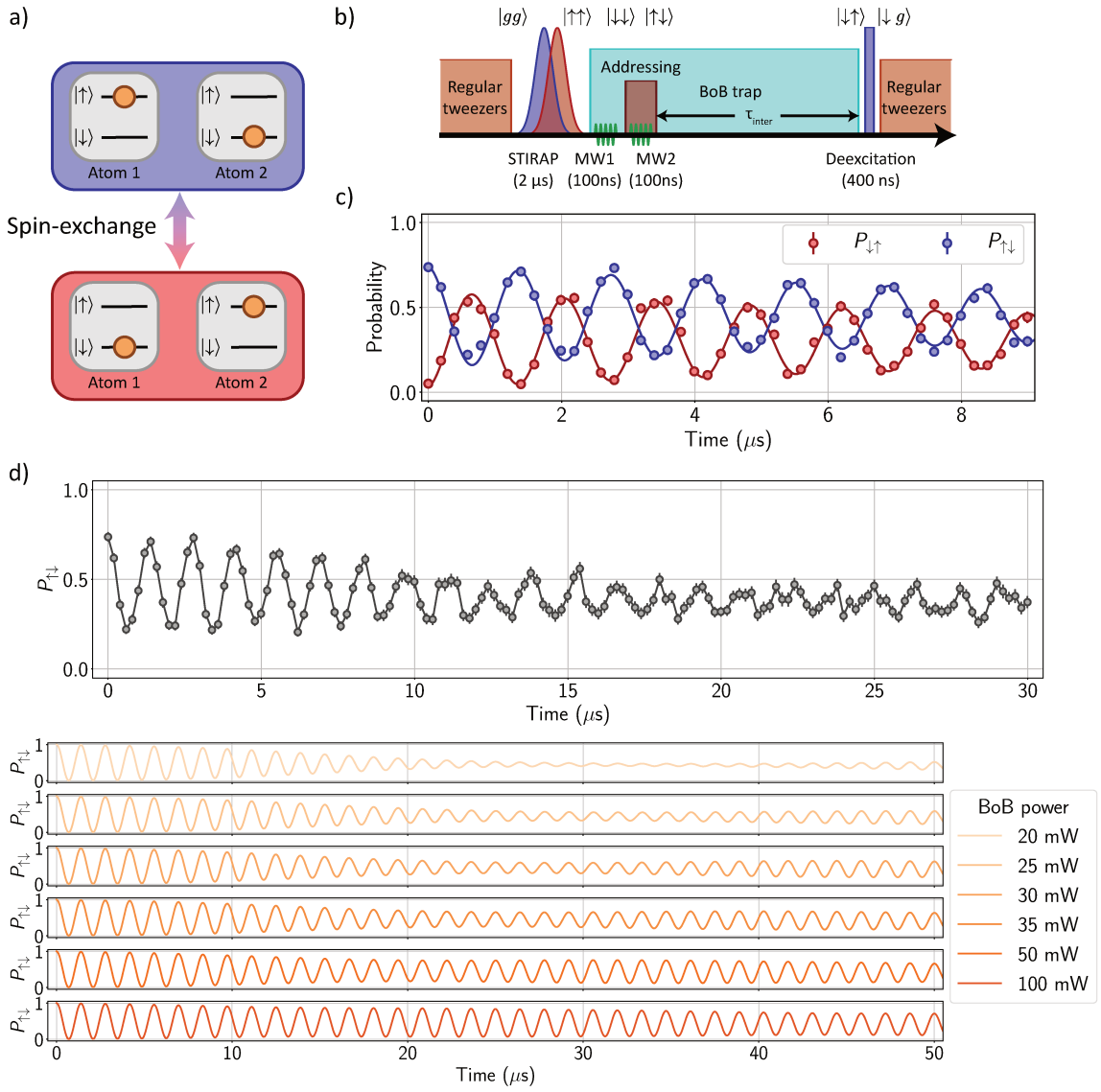

Figure 3.10: Spin-exchange in BoB traps. (a) Schematic representation of the spin-exchange process, where the system oscillates between the state $|\uparrow\downarrow\rangle$ (blue) and the state $|\downarrow\uparrow\rangle$ (red). (b) Experimental sequence used to prepare the state $|\uparrow\downarrow\rangle$ and observe the spin-exchange. (c) Measured probabilities of the states $|\uparrow\downarrow\rangle$ (blue) and $|\downarrow\uparrow\rangle$ (red), fitted by damping sines. (d) Measured probabilities to obtain $|\uparrow\downarrow\rangle$ (black disks), as a function of the interaction time, to be compared with the computed probabilities while varying the laser power generating the BoB trap (orange lines) .

the evolution, we deexcite the atoms. As in the previous subsection, if the atom is in $|\uparrow\rangle$, it is transferred back to the electronic ground state and recaptured, whereas if it is in $|\downarrow\rangle$, it will stay in the Rydberg state and will be lost.

Measured spin-exchange The sequence above allows us to observe the spin-exchange process, shown in Figure 6.5(c). We indeed measure an oscillatory behaviour, where $|\uparrow\downarrow\rangle$ and $|\downarrow\uparrow\rangle$ become successively the most probable states. The spin-exchange process, observed here while the Rydberg atoms are trapped, exhibits the same features as in its original demonstration realized in free flight [Barredo *et al.*, 2015].

Study of the damping Again, the advantage of observing the spin-exchange process while the Rydberg atoms are being trapped is that we can study it for extended durations. In Figure 6.5(d), I show the full time evolution of the probability to be in the state $|\uparrow\downarrow\rangle$ during the spin-exchange process, and I will focus on the damping of the oscillation. The global decrease of the amplitude of the oscillation is due to shot-to-shot fluctuations of the interatomic distance, since they result in fluctuations of the frequency of the spin-exchange oscillation. A possibly more interesting behaviour is the slight increase of the amplitude around $15\,\mu$s. We propose in the following an explanation for such a behaviour by studying the interplay between the atomic motion of the Rydberg atoms inside the traps, and the spin-exchange interaction.

To do so, we perform the same kind of classical Monte-Carlo simulation as before. We pick up a set of initial conditions deduced from the thermal distributions in position and velocity (in this specific experiment, the atomic temperature was reduced to $3\,\mu$K), and compute the atomic motion inside the BoB trap. We use the medium-sized BoB trapping potential already derived for the Rydberg state $\left|84S_{1/2}, m_J = 1/2\right\rangle$. The trapping potential for the involved Rydberg states here should be different because of their different orbital quantum numbers. We compute the atomic motion inside the trap, without taking into account any radiative decay of the Rydberg state or the imperfect preparation. This gives us a time-dependent distance between the two atoms. We plug this time-dependent distance into the Schrödinger equation and solve it.

Averaging over many trajectories, we obtain the damped spin-exchange curves displayed at the bottom of Figure 6.5(d), for different laser powers generating the BoB trap. For low powers, we observe beating in the spin-exchange oscillations, due to the harmonic part of the motion of the Rydberg atoms inside the BoB traps. The time when the amplitude of the oscillation increases, or the power needed to observe

such a beating behaviour, do not correspond with the experimental ones, which may be because in our simulation we do not derive the potential for the correct Rydberg states.

Nevertheless, taking into account the motion inside the BoB trap leads to the same kind of beating in the spin-exchange amplitude, so what we observed may be a hint of the interplay between the spin-exchange interaction and the atomic motion. The correct way to treat this problem would be to include in the Schrödinger equation the atomic motion, and we could expect to observe effect of the entanglement between the atomic motion and the spin-exchange if the atoms are cooled down to the vibrational ground state of the trap, which is not the case for now. It was recently proposed to use this entanglement to engineer exotic interactions [Gambetta *et al.*, 2019]. These interactions have the same origin as the effective spin-spin interactions arising between trapped ions.

3.4 Conclusion

I have shown that we are able to trap single Rydberg atoms with high efficiencies for low enough $n \leq 90$ principal quantum numbers, using holographically generated BoB trap. We have demonstrated that these traps are compatible with usual quantum simulation tasks performed in the Rydberg manifold. The following steps could consist in improving the trapping efficiency by cooling down the atom and using more elaborate phase masks, while generating the BoB trap with less power.

Actually, the same kind of holographically generated BoB traps can be used to trap single atoms in the electronic ground state [Xu *et al.*, 2010], if the BoB traps are created with a blue-detuned light with respect to the transitions to first excited states. Indeed, for blue-detuned light, the potential induced by light is repulsive, in the same way as the ponderomotive potential, and the atom will seek low-intensity regions.

We could aim in the future at implementing such a blue-detuned BoB trap, for several reasons. First, trapped in a dark region, a ground-state atom experiences a smaller light-shift than the one it sees trapped in a regular optical tweezers. Therefore, such blue-detuned optical traps enable for a more coherent laser-manipulation of trapped atoms. Second, for a specific wavelength of the trapping laser beam, the so-called "magic" wavelength, the repulsive potentials experienced by an atom in the ground state and in the Rydberg state will be equal [Zhang, Robicheaux, and Saffman, 2011]. In that case, the excitation to Rydberg states can be achieved without any induced light-shift while being trapped, and the atom is trapped whatever its state,

opening the way to long duration quantum simulation of the Ising model.

Part II.

Spin-ordered phases

Chapter 4

Growth of antiferromagnetic correlations in an Ising-like magnet

Contents

In the Introduction, I have shown how Rydberg atoms interacting in the van der Waals regime can be used to implement an Ising-like Hamiltonian (see Hamiltonian (A.1)). When no external fields are applied, the canonical form of the Ising Hamiltonian simply reads :

$$\hat{H}_{\text{Ising}} = U \sum_{\langle i,j \rangle} \hat{\sigma}_i^z \hat{\sigma}_j^z,$$

where U, the nearest-neighbour coupling, is the only coupling taken into account. From this model, we deduce the existence of two spin-ordered phases. Indeed, if $U < 0$,

two neighbouring spins will tend to align to decrease the total energy of the system. Then, the ground state will be such that every spin points into the same direction, giving rise to a macroscopic magnetic moment. This is the so-called ferromagnetic phase. On the contrary, when $U > 0$, two neighbouring spins will tend to anti-align. Consequently, on an infinite square lattice, the ground state corresponds also to a spin-ordered phase: a staggered pattern of spins up and down (a spin up only has spins down as nearest neighbours and vice versa), with a zero global magnetization. This is known as an antiferromagnetic or Néel phase. It is characterized by the alternating sign of the spin-spin correlation function when scanning the inter-spin distance, as a positive (negative) correlation means that the two spins point into the same (opposite) direction.

The topic of the present chapter is the observation of these antiferromagnetic correlations in a system of Rydberg atoms. More precisely, I will show how we generated antiferromagnetic-like correlations in an assembly of single atoms, initialized in a product state, by a dynamical tuning of the parameters of Hamiltonian (A.1). This work, done in collaboration with Michael Schuler, Louis-Paul Henry and Prof. Andreas M. Läuchli, a theory team from the University of Innsbruck, led to the publication [Lienhard *et al.*, 2018].

4.1 Introduction to Rydberg-based Ising antiferromagnets

Before describing our work in detail, I will address two points. First, I will emphasize the link between Ising antiferromagnets and Rydberg atoms interacting in the van der Waals regime while being coherently driven at resonance. Second, since the approach we follow in this chapter, i.e., the dynamical tuning of the Hamiltonian, is a very general protocol implemented on several quantum simulators, I will present its principle and application to the study of spin Hamiltonians.

4.1.1 Rydberg blockade and antiferromagnetic ordering

The connection between interacting Rydberg atoms and Ising antiferromagnets is done in Appendix A by rewriting Hamiltonian (A.1) defined in the qubit-basis $\{|r\rangle, |g\rangle\}$ in terms of spin operators. This results in an interacting term proportional to $\hat{\sigma}_i^z \hat{\sigma}_j^z$, hence the mapping to an Ising-like model. I will show here that this mapping can be easily understood referring to a characteristic feature of interacting Rydberg atoms,

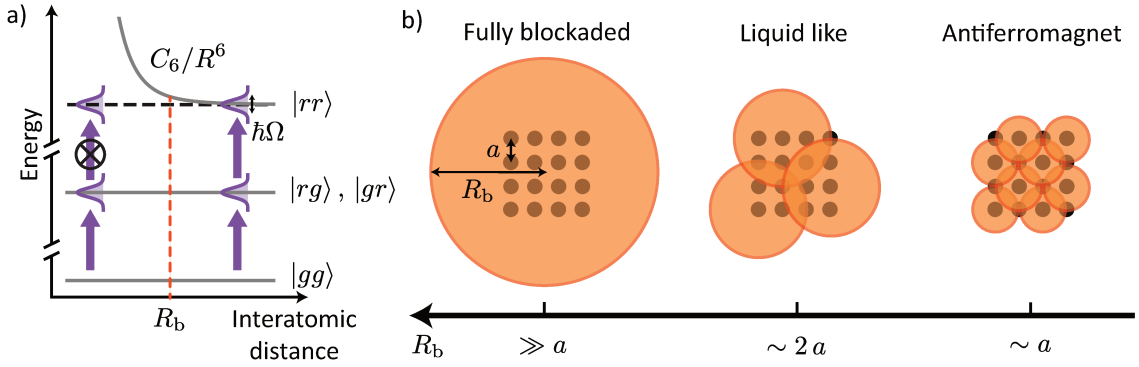

Figure 4.1: From the van der Waals interaction to an Ising antiferromagnet. (a) Energy diagram of a two-atom system in the qubit basis $\{|r\rangle, |g\rangle\}$, interacting in the van der Waals regime. When the system is driven at the qubit resonance with a Rabi frequency $\Omega/(2\pi)$ (purple arrows) and the interatomic distance is smaller than R_b, the coupling to the doubly excited state $|rr\rangle$ is inhibited due to the van der Waals energy shift. (b) Expected spatial configurations of the Rydberg excitations on a square array of lattice constant a as a function of R_b. When $R_b \sim a$, the system enters a solid-like regime with one Rydberg excitation every second lattice site.

the Rydberg blockade.

Let us consider two atoms in the qubit basis $\{|r\rangle, |g\rangle\}$, coherently driven at resonance by a Rabi coupling Ω between $|g\rangle$ and $|r\rangle$, see Figure 4.1(a). The van der Waals interaction results in an energy shift $U = C_6/R^6$ of the doubly-excited state $|rr\rangle$. For small enough distances, the doubly-excited state becomes off resonant with the laser excitation, which prevents two Rydberg excitations to be close by. This is known as the Rydberg blockade. It occurs for distances smaller than the blockade radius $R_b = (C_6/(\hbar\Omega))^{1/6}$, where the driving strength matches the interaction energy.

This blockade mechanism results in a saturation of the fraction of Rydberg atoms while the system is driven at resonance. More interestingly, the saturated Rydberg fraction for a disordered ensemble of atoms was predicted to follow a universal scaling law [Weimer *et al.*, 2008], whose value of the critical exponent was confirmed experimentally [Löw *et al.*, 2009]. The blockade mechanism also leads to correlations of the positions of the Rydberg excitations, as they will tend to maximize their relative distance to minimize the total energy. These correlations were predicted by Robicheaux and Hernández [2005] and observed in a disordered atomic ensemble in a dipole trap [Schwarzkopf *et al.*, 2013].

We now consider an array of atoms with a lattice constant a coherently driven to the Rydberg state. Depending on the ratio between a and R_b, the Rydberg excitations

will order themselves in different spatial configurations (Figure 4.1(b)). If R_b is much larger than the size of the array, there will be one single Rydberg excitation shared among the atomic ensemble. When R_b is on the order of a few a, blockade disks containing a dozen of atoms will pave the array. In this regime, explored in a quantum-gas-microscope platform [Schauß *et al.*, 2012], although Rydberg density correlations can be observed, the precise arrangement of the lattice is not yet relevant, they are liquid-like correlations. Decreasing the interaction strength to $R_b \sim a$ makes the system enter a strongly correlated regime, with one Rydberg excitation every second lattice site on a square array. Since the lattice structure is relevant in this regime to explain the spatial dependence of the correlations, this is a solid-like regime. This corresponds to an antiferromagnetic phase when applying the spin-1/2 mapping $|r\rangle = |\uparrow\rangle$ and $|g\rangle = |\downarrow\rangle$.

Consequently, driving an array of atoms at resonance with interactions tuned such that $R_b \sim a$ enables for the observation of antiferromagnetic correlations. This sudden switch on of the driving is called a quench, as it abruptly brings the system out of equilibrium. Quenching an array of Rydberg atoms was explored in our platform [Labuhn *et al.*, 2016], where the team were able to study three different regimes by tuning the interaction energy: the fully blockaded regime $R_b \gg a$, the correlated regime $R_b \sim a$ and the independent regime $R_b \ll a$. Quench experiments were also recently studied by the group of Prof. Jaewook Ahn [Kim *et al.*, 2018], where their careful analysis of the many-body relaxation dynamics following a quench led them to observe signatures of thermalization in a closed quantum system.

4.1.2 Adiabatic sweeps and phase transition

The contrast of the antiferromagnetic correlations generated by a quench depends on time, since quenching a system is an out-of-equilibrium process. In this chapter, we focus instead on the equilibrium properties of the system, described in terms of thermodynamic phase. This is why we have used another approach to generate antiferromagnetic correlations in an array of Rydberg atoms, which is a very general approach to engineer non-trivial targeted states. Instead of applying a quench, it consists in changing the Hamiltonian slowly enough so that the system follows an adiabatic evolution and stays in the same instantaneous energy level of the time-dependent Hamiltonian (Figure 4.2(a)). Then, tuning the Hamiltonian in such a way that the initial prepared state is an eigenstate of the initial Hamiltonian (for example the one with the lowest energy), and that the targeted state is the eigenstate of the

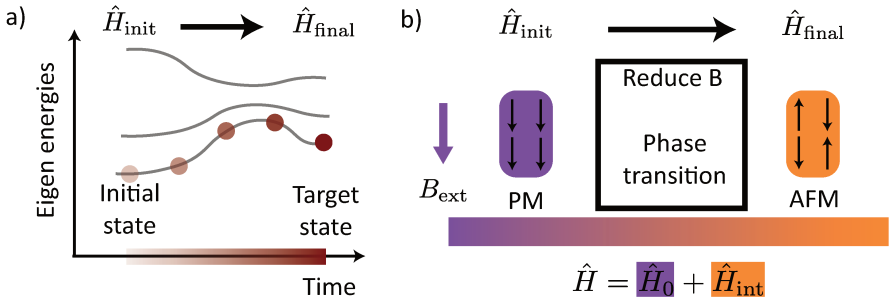

Figure 4.2: Principle of the state-preparation protocols. (a) Scheme of the energy levels of a time-dependent Hamiltonian, where the disks encode as a function of time the projection of the system on the instantaneous eigenstates. When the initial state is the ground state of the initial Hamiltonian $\hat{H}_{\text{init}}$, and the targeted state the ground state of the final one $\hat{H}_{\text{final}}$, following an adiabatic evolution ensures the generation of the targeted state. (b) Exploring the phase transition with an artificial spin system. At the beginning, the external field B_{ext} is large and the ground state of the system corresponds to the paramagnetic (PM) phase, a state easy to prepare. Reducing the external field makes the interacting term of the Hamiltonian the largest, so that the ground state is an antiferromagnetic (AFM) phase.

final Hamiltonian corresponding to the same ranking in energy (so it would be the ground state of the final Hamiltonian in our example), ensures the generation of this targeted state.

Following an adiabatic evolution when the initially prepared state is the ground state of the initial Hamiltonian enables for the search of the ground state of Hamiltonians of interest. This is the principle of quantum annealing. It consists in reaching the ground state of a Hamiltonian by first artificially generating important quantum fluctuations and then adiabatically decreasing them [Battaglia and Stella, 2006]. In the presence of the added quantum fluctuations, the ground state of the system is an easily prepared trivial product state. Preparing this state and decreasing the fluctuations lead to the preparation of the ground state of the Hamiltonian of interest. For example, the D-Wave company has implemented quantum annealing protocols using superconducting circuits to study the Ising Hamiltonian [King *et al.*, 2018].

This approach can be used in the context of spin Hamiltonians (Figure 4.2(b)). Spin Hamiltonians are usually divided into two terms, one containing single-spin operators taking into account the effect of the external field (purple term $\hat{H}_0$ in Figure 4.2(b)), and the other one containing two-spin operators for the interaction (orange term $\hat{H}_{\text{int}}$). When the external field is stronger than the interaction, the ground state of the

system is a trivial product state with all spins aligned in the same direction, it is a paramagnetic phase. Adiabatically decreasing the external field makes the system going from a paramagnetic phase to a correlated phase, the ground state of $\hat{H}_{\text{int}}$. In our case of the Ising Hamiltonian, this correlated state is the targeted antiferromagnetic phase. It turns out that the initial paramagnetic phase can be easily generated with artificial systems. After preparing such an initial state, several experimental teams were able to study the phase transition between a paramagnet and an antiferromagnet, by slowly reducing the amplitude of the effective external field, proportional to the Rabi frequency of the qubit driving. For example, the group of Prof. Christopher Monroe studied it on its quantum simulator based on trapped ions [Edwards *et al.*, 2010; Islam *et al.*, 2013].

Similar adiabatic protocols were proposed in the context of interacting Rydberg atoms to observe crystalline structure of the excitations [Pohl, Demler, and Lukin, 2010; Schachenmayer *et al.*, 2010; van Bijnen *et al.*, 2011], and were implemented in the quantum-gas-microscope platform of Prof. Immanuel Bloch [Schauß *et al.*, 2015]. This motivated our work, and I will report here our observation of the many-body dynamics during a sweep of the external field, for different 2D geometries, in view of engineering the antiferromagnetic state of the Ising model. At the same time, a similar correlated state was observed in the quantum-gas-microscope platform of Prof. Waseem Bakr's team [Guardado-Sanchez *et al.*, 2018], involving Li atoms excited to low-lying Rydberg states. These correlations were also intensively studied by the group of Prof. Mikhail Lukin on their optical-tweezers platform. They observed Z_2, Z_3 and Z_4 phases in a chain of trapped atoms [Bernien *et al.*, 2017]. A Z_n phase corresponds to an ensemble of blockaded sub-chains containing n atoms, the Z_2 phase corresponds then to the antiferromagnetic phase we are focused on. They also measured more recently the critical exponent of the phase transition [Keesling *et al.*, 2019].

For all of these adiabatic protocols to succeed, the evolution of the Hamiltonian must be slow enough for the system to stay in the instantaneous ground state. If not, the system could be excited to higher-energy states via Landau-Zener transitions. The smaller the energy gap between the ground state and the excited states, and the stronger the coupling to excited states, the more likely the Landau-Zener transitions. This results in a limiting speed for the dynamical tuning of the Hamiltonian, known as the adiabaticity criterion. Since the energy gaps decrease at the phase transition, and as imperfections of our laser-driving reduce the coherence time of the evolution, I will show here that we are not able to adiabatically reach the antiferromagnetic ground state.

We decided then to address the reversed question, which is, considering a given time evolution of the parameters of the Hamiltonian, what is the amount of correlations we can expect, and how do they spread in the system? The speed of spreading of correlations is limited theoretically by the Lieb-Robinson bounds [Lieb and Robinson, 1972], an important concept in quantum information. These bounds were explored in the context of quenches where a light-cone-like spreading of correlations was observed in an optical lattice [Cheneau *et al.*, 2012] or with trapped ions [Jurcevic *et al.*, 2014]. Our work extends this study to the context of slow sweeps.

In this chapter, I will first present in more detail the procedure we have followed to get our system of interacting Rydberg atoms close to an antiferromagnetic state. Then, I will describe the two types of sweeps we have performed, revealing the antiferromagnetic region in the phase diagram, and a time limit for a coherent evolution. Finally, I will analyse the time- and space-dependence of the build-up of correlations, allowing us to observe their finite speed of spreading, and a growth mechanism well captured by a short-time expansion of the evolution operator.

4.2 Reaching the antiferromagnetic phase

As mentioned before, we want to reach an antiferromagnetic state with Rydberg atoms by dynamically tuning the parameters of the Hamiltonian. Restricting ourselves to the nearest-neighbour (NN) interaction $U = C_6/a^6$ with a the lattice constant, and taking into account the laser-coupling between the two-qubit states $\{|r\rangle, |g\rangle\} = \{|\uparrow\rangle, |\downarrow\rangle\}$ described in subsection 2.3.2, the Hamiltonian reads, in terms of spin operators and in the rotating wave approximation

$$\hat{H} = \sum_i \left(\frac{\hbar\Omega}{2} \hat{\sigma}_i^x - \hbar\delta\, \hat{n}_i \right) + U \sum_{\langle i,j \rangle} \hat{n}_i \hat{n}_j \tag{4.1}$$

with $\hat{n} = (1 + \hat{\sigma}^z)/2$, Ω the Rabi frequency and δ the detuning from resonance. We can restrict ourselves to the NN interactions because we will operate in the regime $R_\mathrm{b} \sim a$. This will make the description of the phase diagram associated to $\hat{H}$ easier. Nevertheless, in the numerical simulations presented in this chapter, the full $1/R^6$ dependence of the interaction was taken into account.

For this work the qubit is encoded in the two states $|\downarrow\rangle = \left|5S_{1/2}, F = 2, m_F = 2\right\rangle$ and $|\uparrow\rangle = \left|64D_{3/2}, m_J = 3/2\right\rangle$. As we shall see below, the choice of a Rydberg D state instead of a Rydberg S state makes the mapping to a spin-1/2 Hamiltonian more difficult, but on the other hand, we take advantage of the increased laser coupling

towards D states, which justifies in the end its use. The lattice constant is tuned between 9 and 7.5 μm, leading to a NN interaction $|U|/\mathrm{h} \sim 1 - 3\,\mathrm{MHz}$. Before describing the phase diagram as a function of δ and Ω for a square and a triangular array, and the specific time evolution of these parameters we have investigated to reach an antiferromagnetic state, I will insist on the special care we needed to take in order to involve only the two levels of the qubit basis in the many-body dynamics of the system.

4.2.1 Accurate mapping to a spin-1/2 Hamiltonian

In Appendix A, I showed that the energy shift experienced by the doubly-excited state $|rr\rangle$ comes from a second-order perturbation theory, the perturbation being the dipole-dipole interaction between pairs of Rydberg states. In this perturbative regime, the eigenstate of the two-atom system has a large overlap with the unperturbed $|rr\rangle$ state, and its potential curve follows the expected asymptotic behaviour in C_6/R^6. In that case, a mapping to a spin-1/2 Hamiltonian is possible, and the Rydberg blockade mechanism is valid.

It turns out that the situation can be much more complicated depending on the precise Rydberg state involved and this simple asymptotic behaviour does not apply systematically for the distances explored in our experiments. This could lead to failures of the Rydberg blockade, and to deviations from the Ising-like model we want to implement, as the team observed in one of its previous work [Labuhn *et al.*, 2016]. To understand those deviations, in collaboration with Prof. Hans-Peter Büchler and Sebastian Weber from the University of Stuttgart, we analysed the potential curve of the pair state after a numerical diagonalization of the dipole-dipole interaction Hamiltonian, and indeed, we found discrepancies from the asymptotic behaviour. We also found a convenient value for the magnetic field defining the quantization axis allowing us to reduce these deviations, implementing correctly the Ising-like model. This accurate mapping into a spin-1/2 Hamiltonian was reported in [de Léséleuc *et al.*, 2018b]. I will briefly describe this study here, and I refer to this publication or to the thesis of Sylvain de Léséleuc [2018] (Chapter 6) for more details.

Dipole-dipole interactions with $nD_{3/2}$ state The treatment of the dipole-dipole interaction is more complicated with $nD_{3/2}$ states for several reasons. First, the fine splitting are narrower for nD states, which reduces the energy separation between pair of Rydberg states and makes the effect of the perturbation stronger.

Moreover, a $\left|nD_{3/2}, nD_{3/2}\right\rangle$ pair state can be almost at the same energy as a $\left|(n+2)\ P_{1/2}, (n-2)\ F_{5/2}\right\rangle$ state. This accidental quasi-degeneracy is called a Förster resonance. In this peculiar interaction regime, explored by our team in [Ravets *et al.*, 2014], when the two pair states are exactly at resonance, the eigenstate of the system has only a 50% overlap with the unperturbed state $\left|nD_{3/2}, nD_{3/2}\right\rangle$, and the system oscillates back and forth between the two pair states $\left|nD_{3/2}, nD_{3/2}\right\rangle$ and $\left|n+2\,P_{1/2}, n-2\,F_{5/2}\right\rangle$. Consequently, close to these kind of resonances, the dipole-dipole interaction does not result in a mere energy shift of the pair state, which is detrimental for our implementation of the Ising model.

In addition to Förster resonances, coupling to other pair states must be taken into account when the internuclear axis is tilted with respect to the quantization axis. Indeed, the dipole-dipole interaction can couple pair states with a different total magnetic number (the sum of the m_J of the two atoms) in that case, thus involving a larger part of the Zeeman manifold in the dipole-dipole interaction. As the Zeeman manifold is more extended for nD states than it is for nS, the possible number of pair states that must be taken into account in the treatment of the dipole-dipole interaction increases. Finally, an additional electric field could mix the different Rydberg states, extending even more the number of possibly coupled pair states.

For all these reasons, an analytical treatment of the effect of the dipole-dipole interaction is intractable, and we need to perform the numerical diagonalization of the pair interacting Hamiltonian.

Deviations from the spin-1/2 model Figure 4.3(a) shows the result of such a diagonalization as a function of the interatomic distance, where $|r\rangle = \left|61D_{3/2}, m_J = 3/2\right\rangle$ and the interacting angle $\theta = 78°$, in the presence of a magnetic field (quantization axis) $B_z = 6.9\,\mathrm{G}$ and an electric field $E_z = 20\,\mathrm{mV/cm}$. I intentionnaly chose those parameters because they realize the worst-case scenario for the treatement of the dipole-dipole interaction. This numerical treatment was possible thanks to the open-source software *pairinteraction*, developed by Sebastian Weber *et al.* [2017]. The potential curve of the pair state $|rr\rangle$ is far from being as simple as the asymptotic behaviour in C_6/R^6, and the eigenstate of the two-atom system is projected onto many different unperturbed Rydberg pair states. This would lead to deviations from the spin-1/2 model we want to implement.

To illustrate that point, I show in Figure 4.3(b) the result of a quench experiment, in the same spirit of the ones performed in [Labuhn *et al.*, 2016]. The magnetic field was set to the value $B_z = 6.9\,\mathrm{G}$, but the electric field was not as high as in Figure 4.3(a).

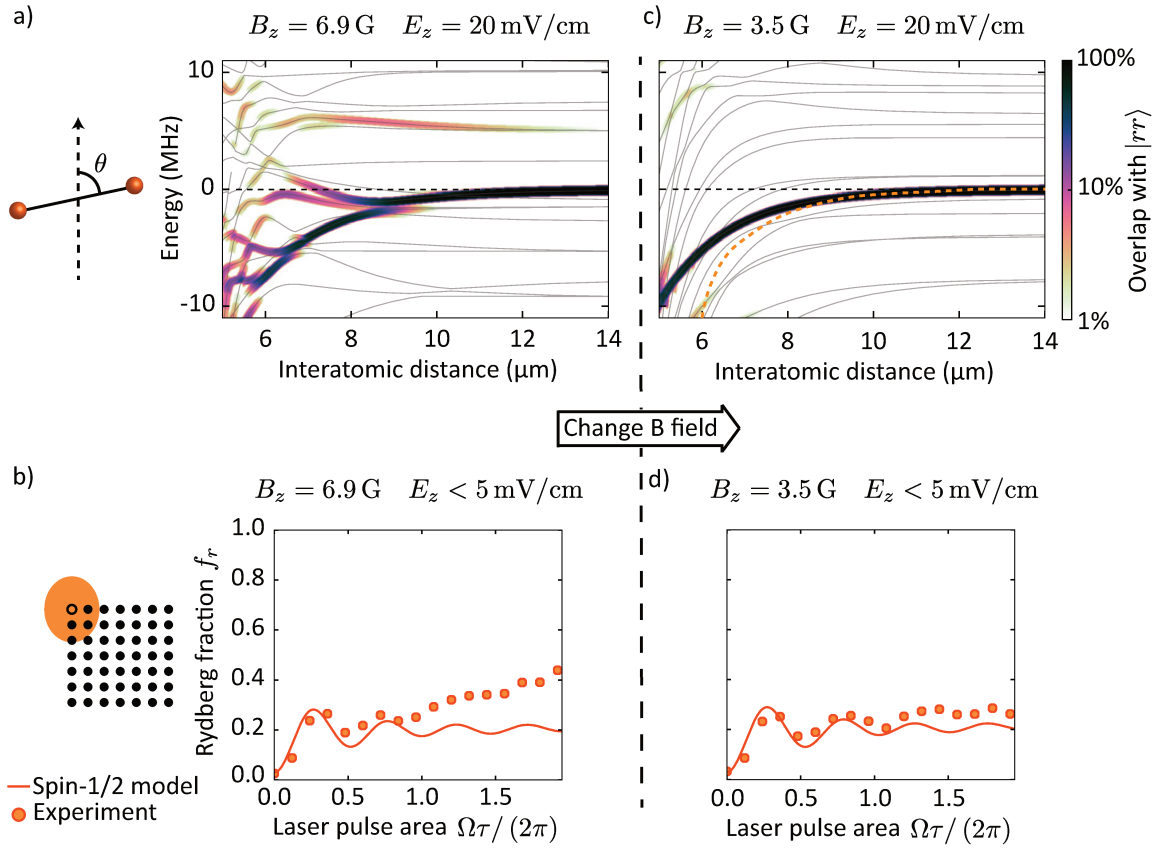

Figure 4.3: Accurate mapping into a spin-1/2 model. (a) Full diagonalization of the pair interacting Hamiltonian, as a function of the interatomic distance, in presence of a magnetic and an electric field. The angle between the quantization axis and the internuclear one is $\theta = 78°$. (b) Rydberg fraction as a function of the laser pulse area. The sketch on the left shows the relative size of the blockade sphere (orange) compared to the lattice constant. The measured Rydberg fraction (disks) does not match the prediction of a spin-1/2 model (solid line) at long times. (c) Same calculation as in (a) for a smaller magnetic field $B_z = 3.5\,\mathrm{G}$. The dashed orange line is the asymptotic behaviour C_6/R^6. (d) Same experiment as in (b) but for a reduced magnetic field.

We have compensated the electric fields in order to have them smaller than 5 mV/cm. The experiment consists in abruptly driving at resonance a 7×7 square array of atoms prepared in $|g\rangle$, and measuring as a function of the illuminating time τ the fraction f_r of atoms in $|r\rangle$. Due to the Rydberg blockade, the Rydberg fraction is expected to saturate, as shown by the simulation based on the spin-1/2 model (solid line). On the contrary, the measured many-body dynamics (disks) shows a clear increase of f_r at long time, suggesting a breakdown of the Rydberg blockade and an incorrect mapping on the Ising-like model.

Systematic search for an accurate mapping The *pairinteraction* software allows us to look for a set of experimental parameters for which we retrieve the C_6/R^6 behaviour. It turns out that another value for the magnetic field, $B_z = 3.5\,\mathrm{G}$, leads to a much simpler potential curve for the doubly-excited state $|rr\rangle$, as shown in Figure 4.3(c). The eigenstate of the two-atom system is mostly projected onto $|rr\rangle$, and the C_6/R^6 behaviour (dashed lines) is a valid approximation, as long as the interatomic distance is larger than about $8\,\mu$m, i.e. for the distances of interest in our experiments. This results in an accurate mapping into our spin-1/2 model, as observed in the experiment (Figure 4.3(d)), where the increase of f_r is no longer visible and the experimental data are in very good agreement with the spin-1/2 model. This is, to date, the quantum simulation experiment involving the largest number of spins (49) we have performed on our platform.

To conclude, I emphasized on the careful analysis of the dipole-dipole interaction we needed to perform in view of accurately implementing an Ising-like model with $nD_{3/2}$ Rydberg atoms. This careful treatment was possible thanks to the development of the *pairinteraction* software. The situation would be simpler using $nS_{1/2}$ states, as the Zeeman manifold would be reduced to two levels and there are no Förster resonances. But as the laser-coupling to Rydberg S states is less efficient, we decided to keep working with $nD_{3/2}$ states, having with this study the tools to determine the good parameters for an accurate mapping.

4.2.2 Phase diagram of an Ising-like model

Now that we have ensured that Hamiltonian (4.1) correctly describes the many-body dynamics occurring in our atomic array, I will present the phase diagram associated to this Hamiltonian for two different geometries, a square and a triangular array (Figure 4.4). A phase diagram is built by evaluating, as a function of the parameters

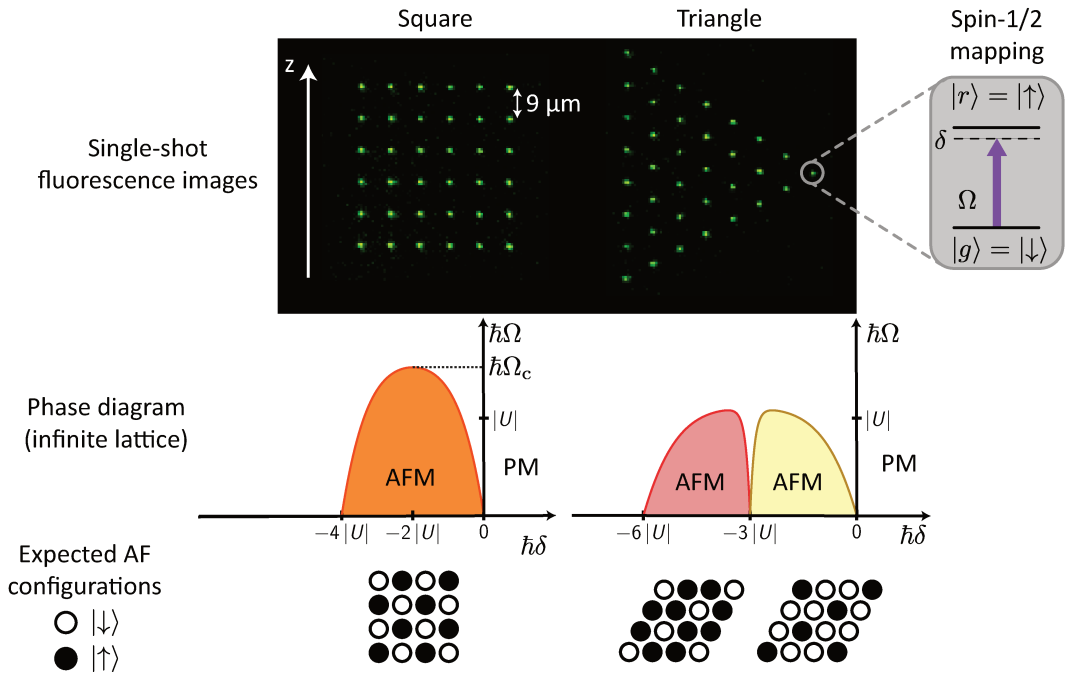

Figure 4.4: Phase diagram of an Ising-like model. (Top) For a square (left) and a triangular (right) array, single-shot fluorescence images of defect-free atomic arrays obtained after our assembling process (Subsection 2.2.2). Each atom is initialized in $|g\rangle$, and is coupled to $|r\rangle$ with a Rabi frequency $\Omega/(2\pi)$ and a detuning from resonance δ. (Middle) Phase diagrams as a function of (δ, Ω) for both geometries. The coloured patches indicate the antiferromagnetic (AFM) regions, surrounded by the paramagnetic (PM) region. (Bottom) Expected spatial configurations of the Rydberg excitations for the antiferromagnetic states.

(δ, Ω), the ground state of Hamiltonian (4.1). The atomic patterns used here are obviously finite-size systems, whose edges slightly modify the phase diagram obtained for infinite lattices. Nevertheless, we will neglect these finite-size effects for the present discussion, as anyway the size of the antiferromagnetic domains we will be able to generate on our platform is smaller than the size of the atomic array.

Anisotropy of the van der Waals interaction On top of Figure 4.4, the displayed atomic pattern are slightly stretched in the vertical direction. This is to compensate for the dependence of the van der Waals interaction on the angle between the quantization axis and the internuclear axis. We have checked spectroscopically that the residual anisotropy of the interaction is below 10%. For that we measured the position of the doubly-excited line to infer the interaction energy for various angles between the quantization axis and the internuclear axis.

Phase diagram of $-\hat{H}$ One can notice in Figure 4.3(c) that the potential curve is shifted downwards with respect to the unperturbed pair state, which means that the van der Waals shift $U < 0$. This is the case for most of the $nD_{3/2}$ states, including the one used in this work $\left|64D_{3/2}, m_J = 3/2\right\rangle$. Consequently, for the Rydberg state involved, the previously described antiferromagnetic state is in fact the most excited state of $\hat{H}$, or stated otherwise, the ground state of $-\hat{H}$. I will then describe this most excited state, but the fundamental concept of phase diagram still holds if we consider $-\hat{H}$ instead of $\hat{H}$. In our context of adiabatic state-preparation protocols, for an isolated quantum system, what matters is to stay on the same energy level, but this level does not have to be the lowest one. To be in the lowest energy level is only important when temperature and equilibrium with a thermal bath play a role, which is not the case for our platform.

Trivial phase In Hamiltonian 4.1, when δ or Ω is way larger than $|U|/\hbar$, the most excited state is only determined by the single-spin operators, and therefore is a trivial product state, every atom being in the same state. When δ is large and positive, this state corresponds to every atom in $|g\rangle$, when it is large and negative, it corresponds to every atom in $|r\rangle$, and finally when Ω is large, it corresponds to every atom in the superposition $-\left(|g\rangle + |r\rangle\right)/\sqrt{2}$. Using again our mapping into a spin-1/2 system, this state corresponds to all spins aligned in the opposite direction of the effective external magnetic field, of transverse (longitudinal) component proportional to Ω (δ). It can be then considered as the aforementioned paramagnetic phase of $-\hat{H}$. This phase is present in both phase diagrams.

Antiferromagnetic phase for a square lattice The interesting region of the phase diagram is where the effective external field competes with the interaction, delimiting the boundaries of the antiferromagnetic phase. The boundaries in δ for $\Omega = 0$ are $\delta = 0$ and $\delta = -4\,|U|/\hbar$. The detuning δ must be negative for the most excited state to host Rydberg excitations, and smaller in absolute value than $4\,|U|/\hbar$, proportional to the energy gain of having a spin aligned with its four nearest neighbours. The number of nearest neighbours, or coordination number, $z = 4$, plays an important role in those phase boundaries in condensed matter physics. Finally, the boundary in Ω for $\delta = -2\,|U|/\hbar$ is known to high precision from Monte Carlo simulations $\hbar\Omega_c/|U| = 1.52219\,(1)$ [Blöte and Deng, 2002].

Interacting phase for a triangular lattice On a triangle, it is impossible for all bonds to fulfil the anti-aligned condition at the same time. This prevents an antiferromagnetic ordering, which is called geometrical frustration. It results in a macroscopic degeneracy of the ground state, revealed by a non-vanishing entropy near zero temperature, as measured in a frustrated condensed matter system [Ramirez *et al.*, 1999]. In a quantum system, some "order by disorder" processes can occur in these frustrated phases [Moessner and Sondhi, 2001].

In a triangular lattice, the coordination number is $z = 6$, and due to this frustrated geometry the phase diagram is richer. A first phase with one Rydberg atom every third lattice site appears in the region $\Omega = 0$, $-z/2\,|U| < \hbar\delta < 0$. The conjugated crystal (a Rydberg atom becomes a ground state atom and vice versa) is the most excited state in the region $\Omega = 0$, $-z\,|U| < \hbar\delta < -z/2\,|U|$. The order by disorder process occurs on the line $\hbar\delta = -z/2\,|U|$ for low Ω. As we shall see, some technical imperfections prevents us from studying these frustrated phases, because of a limited duration of a coherent evolution. Nevertheless, observing the growth of the correlations in the triangular case, we will infer some signatures of geometrical frustration (Subsection 4.4.3).

4.2.3 Sweep towards the antiferromagnetic phase

Now that we have identified the ground state of $-\hat{H}$ for different regions of the parameters space (Ω, δ), we can choose a time profile for the tuning of these parameters to reach the antiferromagnetic state in a square array following an adiabatic evolution. These time profiles, and the associated trajectories in the phase diagram, are plotted in Figure 4.5(a). Before showing in the next section the result we have obtained with the presented sweeps, I will numerically demonstrate that they can generate an antiferromagnetic state for the simple case of a 2×2 matrix. I will also explain how we realize in practice these sweeps on our experimental setup. Finally, as the generation of antiferromagnetic correlations relies on adiabatic evolutions, I will show how we can experimentally probe the adiabaticity on an ensemble of non-interacting qubits.

A three-step sweep At the beginning of the experimental sequence, all the atoms, in a defect-free structure, are in $|g\rangle$. This is the starting point of our quantum simulation step described in Figure 2.3. This corresponds to the paramagnetic phase in the region $\delta > 0$ and $\Omega = 0$ in the phase diagram. In order to prepare adiabatically an antiferromagnetic state, we then choose to start the dynamical tuning of the parameters in this region, with $\delta_{\text{init}} > 0$ and $\Omega = 0$ (step 1 in Figure 4.5(a)). Then, we

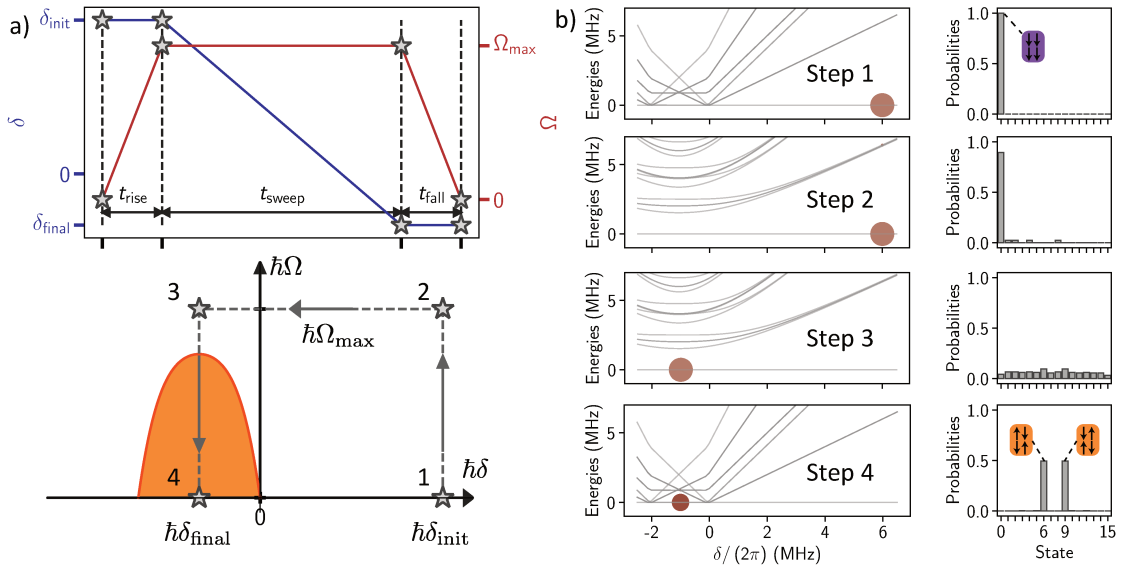

Figure 4.5: Dynamical tuning of the external field for an antiferromagnetic state generation. (a) Time evolution of the two parameters δ and Ω, and the associated trajectory in the phase diagram. The four steps mentioned in the main text are indicated by grey stars. (b) Resolution of the time-dependent Schrödinger equation for the three-step sweep presented. (Left) Energy levels of the time-dependent Hamiltonian as a function of the detuning, for four different times during the evolution. The area of the red disks encodes the projection of the system onto the instantaneous eigenstates (see text). (Right) Probabilities to find the 2^4 states defined in the N-qubit basis, for the same specific times of the evolution.

gradually increase the qubit coupling Ω for a duration t_{rise} to reach the maximum value $\Omega_{\max}$ with a constant detuning δ_{init} (step 2). The next step consists in sweeping the detuning from δ_{init} to δ_{final} for a duration t_{sweep} at constant Rabi frequency (step 3). Finally, we linearly decrease the Rabi coupling to zero in t_{fall} (step 4). This last step corresponds to the decrease of the external field described in Figure 4.2(b). Staying in the instantaneous ground state of $-\hat{H}$ while following this trajectory in the phase diagram would ensure the preparation of the antiferromagnetic state if δ_{final} lies in the antiferromagnetic region $-z\,|U| < \hbar\delta_{\text{final}} < 0$.

Example with a 2×2 square array To illustrate that point, I numerically solved the time-dependent Schrödinger equation for Hamiltonian (4.1), in the case of a 2×2 square array, with the following parameters: $|U|/h = 1.0\,\text{MHz}$, $\Omega_{\max} = 2\pi \times 2.0\,\text{MHz}$, $\delta_{\text{init}} = 2\pi \times 6.0\,\text{MHz}$, $\delta_{\text{final}} = -2\pi \times 1.0\,\text{MHz}$, $t_{\text{rise}} = 0.25\,\mu\text{s}$, $t_{\text{sweep}} = 3.0\,\mu\text{s}$ and $t_{\text{fall}} = 5.0\,\mu\text{s}$. I plot in Figure 4.5(b), for the four different time-steps described before,

the eigen-energies of $\epsilon_0(t) - \hat{H}(t)$ as a function of the detuning. The energy $\epsilon_0(t)$ is the one of the most excited state, in order to always have on these plots the energy level of the targeted state on the zero energy line. I add on these plots the projection of the quantum system onto the instantaneous eigenstates of $\hat{H}(t)$, encoded in the area of the dark red disks. I also plot for these different times the probability to find the 2^4 states defined in the N-qubit basis, see the bar plots on the right of Figure 4.5(b). The leftmost probability is the one to find $\left|\begin{smallmatrix}\downarrow & \downarrow \\ \downarrow & \downarrow\end{smallmatrix}\right\rangle$ and the rightmost one $\left|\begin{smallmatrix}\uparrow & \uparrow \\ \uparrow & \uparrow\end{smallmatrix}\right\rangle$. The columns 6 and 9 correspond to the two antiferromagnetic configurations $\left|\begin{smallmatrix}\uparrow & \downarrow \\ \downarrow & \uparrow\end{smallmatrix}\right\rangle$ and $\left|\begin{smallmatrix}\downarrow & \uparrow \\ \uparrow & \downarrow\end{smallmatrix}\right\rangle$.

At the beginning (step 1), the system is in the $\left|\begin{smallmatrix}\downarrow & \downarrow \\ \downarrow & \downarrow\end{smallmatrix}\right\rangle$ state, which indeed corresponds to the most excited state (the system in on the zero energy line). When we increase Ω, a necessary ingredient as it enables for the appearance of some Rydberg excitations, the energy separation between the most excited state and the other states increases, while the system stays in the instantaneous most excited state. Then, the system can go through the avoided crossing with a reduced probability for the aforementioned Landau-Zener transitions to occur (from step 2 to step 3). In the end (step 4), the system has stayed on the same energy level and is therefore an antiferromagnetic state, as it can be seen on the probability bar plot. Indeed, the system is in an equal superposition of the two antiferromagnetic configurations. These two configurations correspond to the two degenerate most excited eigenstates of the system in the antiferromagnetic region. Therefore, the system is not mostly projected onto one eigenstate but equally projected onto two degenerate ones. This is why the area of the red disk encoding the projection is smaller for the final step, in fact there are two superimposed red disks for the two degenerate eigenstates.

The role of the Rabi frequency is therefore to enlarge the excitation gap for an easier adiabatic evolution. As $\hat{\sigma}^x$ does not commute with $\hat{\sigma}^z$, the transverse field term can be seen as the generator of quantum fluctuations appearing in quantum annealing protocols. This transverse field can even be considered as a "quantum catalysis" for the phase transition [Richerme *et al.*, 2013].

The numerical simulation carried out in the case of a 2×2 square array shows that we must tune the effective magnetic field for about $8\,\mu$s to generate a quasi perfect antiferromagnet. As already stated, the suitable duration to reach the targeted state depends on the energy gap Δ_E between the instantaneous eigenstates. More precisely, the suitable duration scales as $1/\Delta_E^2$ [Das and Chakrabarti, 2008]. For finite-size systems, Δ_E was proven to scale as $1/\sqrt{N}$ for a square array, and to be exponentially reduced with N for a triangular array, with N the number of spins. Therefore, the larger the system, the smaller the energy gap, and the longer it takes to follow an

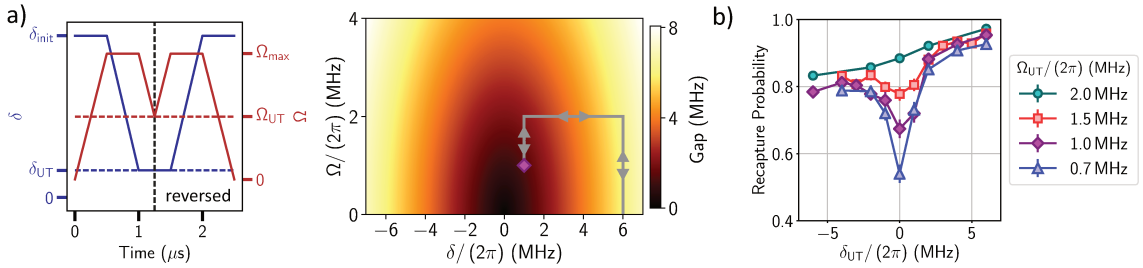

Figure 4.6: Probing the adiabaticity via round-trip sweeps. (a) Time profiles of $(\delta(t), \Omega(t))$ and associated trajectory in the (δ, Ω) plane. The colormap indicates the energy gap for the two-level system, and the purple diamond shows the coordinates $(\delta_{\text{UT}}, \Omega_{\text{UT}})$ of the U-turn point. (b) Recapture probabilities measured after a round trip for different U-turn points. The different lines corresponds to different values for Ω_{UT}.

adiabatic preparation. On our platform, as we studied large systems of $N = 36$ spins, we anticipate that the sweep duration for an adiabatic evolution is not accessible.

Experimental realization of the sweeps In practice, to realize the parameters sweep presented in this chapter, we dynamically tune the amplitude (to tune Ω) and the frequency (to tune δ) of the RF signal feeding the Acousto-Optic-Modulator (AOM) diffracting the red laser excitation beam. The time-dependent RF signal is generated with an Arbitrary Waveform Generator (AWG) (central frequency around 30 MHz) mixed with a carrier frequency at 80 MHz.

As we are using a two-photon transition to couple $|g\rangle$ and $|r\rangle$ (see Subsection 2.3.2), varying Ω_{r} changes the detuning to the Rydberg state due to the AC-Stark shift on the intermediate level (see Equation (2.3)). We measure spectroscopically the induced light-shift as a function of the red power and we compensate for this change of detuning by modifying the frequency ramp accordingly.

Signature of adiabaticity We can already experimentally probe the adiabaticity of our dynamical tuning of the external field on an assembly of non-interacting atoms. In that case of a simple two-level system, the transition between $|g\rangle$ and $|r\rangle$ occurs at $\delta = 0$ on the $\Omega = 0$ line, and the energy gap between the two eigenstates is $\hbar\sqrt{\Omega^2 + \delta^2}$. The evolution is adiabatic if, when performing a sweep of parameters followed by the inverted sweep, that is to say performing a "round-trip" sweep in the phase diagram, the system returns to the initial state. Figure 4.6 shows the result of such an experiment. The sweep used here consists in, starting with atoms in $|g\rangle$ and $\delta_{\text{init}} = 2\pi \times 6.0\,\text{MHz}$, increasing $\Omega/(2\pi)$ to 2.0 MHz in 0.5 μs, sweeping δ to different

final values at a constant speed $10\,\mathrm{MHz}/\mu\mathrm{s}$, decreasing Ω to different values in another $0.5\,\mu\mathrm{s}$, and then applying the reverted sequence (Figure 4.6(a)). The coordinates of the U-turn point $(\delta_{\mathrm{UT}}, \Omega_{\mathrm{UT}})$, and the energy gap in the (δ, Ω) plane, are indicated in Figure 4.6(a). We measure the probability to be in $|g\rangle$ at the end of the round-trip sweep for different coordinates of the U-turn point (Figure 4.6(b)). The drop in the recapture probability for U-turn points near the vanishing gap region $\delta = 0$, $\Omega = 0$ illustrates our loss of adiabaticity.

4.3 Following different trajectories in the phase diagram

So far, I have presented and justified the experimental protocol we followed to reach an antiferromagnetic phase with arrays of Rydberg atoms. In this section, I will describe our investigation of the most suitable time profiles for $\delta(t)$ and $\Omega(t)$ in order to generate the largest antiferromagnetic correlations in a 6×6 square array of atoms, all initialized in $|g\rangle$. To quantify the amount of antiferromagnetic correlations, we evaluate the Rydberg-Rydberg density correlation function, defined in the next subsection. It is based on the measurement of one- and two-atom recapture probabilities, that we infer from the analysis of the final fluorescence images as explained in Section 2.3: at the end of the parameter sweep, if the atom is recaptured, it will be considered as a $|g\rangle = |\downarrow\rangle$, if not, it will be considered as a $|r\rangle = |\uparrow\rangle$. In order to be accurate in the evaluation of these statistical quantities, we repeat the same parameter sweep for a few hundred times.

Our first optimization stage consists in looking for the most suitable final detuning, which is expected to be between $-4\,|U|\,/\hbar$ and zero. To do so, we perform the dynamical tuning of the external field shone in Figure 4.5(a), for a varying final detuning, and a constant ramping speed of the detuning. As we want to be as close as possible to adiabaticity for a large range of detuning, we set the parameters of the system in order to have $\Omega_{\mathrm{max}} > \Omega_{\mathrm{c}}$, where Ω_{c} is the boundary in Rabi frequency of the antiferromagnetic region (see Figure 4.4). Indeed, proceeding that way, we reach the paramagnetic region $\delta < 0$ without intersecting the antiferromagnetic one where the excitation gaps would be smaller.

Once we have found an optimal value for the final detuning, we vary the ramping speed while crossing the phase boundary. Consequently, the parameters of the system are in that case such that $\Omega_{\mathrm{max}} < \Omega_{\mathrm{c}}$. This leads us to find an optimized value for t_{sweep}.

Our detailed analysis of the laser-driving of a single atom in the qubit basis $\{|g\rangle, |r\rangle\}$

showed that the driving is the most coherent when $\Omega/(2\pi)$ ranges between 1 and 3 MHz [de Léséleuc *et al.*, 2018a]. Consequently, we have chosen to work with $\Omega_{\max}/(2\pi)$ around 2 MHz. To realize the two kinds of sweeps described above ($\Omega_{\max} > \Omega_c$ and $\Omega_{\max} < \Omega_c$), we therefore tune Ω_c via a change of the lattice constant (resulting in a change of U), rather than varying $\Omega_{\max}$.

4.3.1 Probing the phase boundaries in detuning

In this subsection, I will present the results we obtain after performing the set of sweeps where we vary the final detuning (Figure 4.7(a)). The precise fixed parameters for the time profiles are: $|U|/h = 1.0$ MHz, $\Omega_{\max} = 2\pi \times 2.3$ MHz, $\delta_{\text{init}} = 2\pi \times 6.0$ MHz, $t_{\text{rise}} = 0.25\,\mu$s and $t_{\text{fall}} = 0.50\,\mu$s. The final detuning $\delta_{\text{final}}/(2\pi)$ is scanned between -6 and 2 MHz, and as we operate at constant detuning ramping speed, the duration of the detuning sweep step is such that $t_{\text{sweep}} = (\delta_{\text{init}} - \delta_{\text{final}}) / \{2\pi \cdot 10\,(\text{MHz})\}$ μs. Since $|U|/h = 1.0$ MHz, $\Omega_{\max} > \Omega_c$ (the Ω_c value is highlighted with a red dotted line in Figure 4.7(a)), and we explore the paramagnetic region $\delta < 0$ without intersecting the antiferromagnetic one.

Rydberg fraction A first observable we may think about to make the distinction between the paramagnetic and the antiferromagnetic phase is the mean density of Rydberg atoms $\langle \hat{n} \rangle$, also called the Rydberg fraction. Indeed, in the $\Omega = 0$ case, $\langle \hat{n} \rangle = 0$ or $\langle \hat{n} \rangle = 1$ for the paramagnetic phase (for $\delta > 0$ or $\delta < -4\,|U|/h$), whereas $\langle \hat{n} \rangle = 1/2$ for the antiferromagnetic phase. This quantity is expected to jump abruptly at the phase transition, which would allow us to observe the boundaries in detuning of the antiferromagnetic phase.

I plot in Figure 4.7(b) the measured Rydberg fraction as a function of the final detuning of the sweep. We observe a smooth transition when probing the antiferromagnetic region between two regimes, where $\langle \hat{n} \rangle$ is close to 0 or close to 1, rather than the expected plateau at 1/2. This smoothing of the staircase-function (green dashed line in Figure 4.7(b)), which should have been obtained if we were preparing the most excited state of Hamiltonian 4.1 when $\Omega = 0$, means that we cannot probe adiabatically this region. I will come back in the next chapter to these experiments consisting in observing steps in the Rydberg density.

Spin-spin correlations Consequently, we need another observable to probe the phase boundaries. The mean density of Rydberg atoms, in the analogy to spin-1/2 physics,

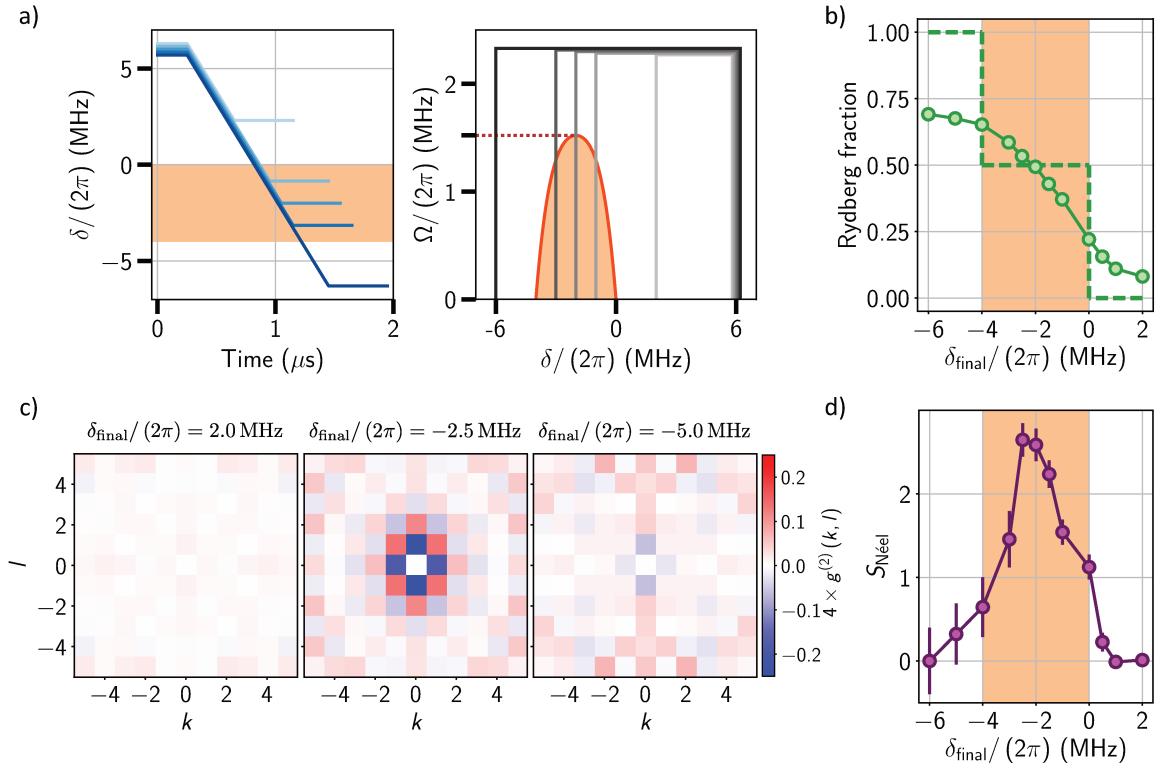

Figure 4.7: Revealing the antiferromagnetic region. (a) Time profiles $\delta(t)$ and associated trajectories in the phase diagram, for the set of sweeps used here to probe the phase boundaries in detuning of the antiferromagnetic region. This region is highlighted with an orange color patch (b) Measured Rydberg fraction as a function of the final detuning. The orange color patch still indicates the boundaries in detuning of the antiferromagnetic phase. (c) Measured correlation function for different final detuning. (d) Néel factor, computed from the correlation functions, as a function of the final detuning. Here also the boundaries in detuning of the antiferromagnetic region are indicated.

is the mean magnetization. It is an easily measurable quantity, as it is the average of a single-particle operator. But one of the assets of our apparatus is that we can independently determine the recapture of each atom (so its final state $|g\rangle$ or $|r\rangle$) for each experimental shot. This means that we can measure the site-dependent average of two-body operators. Therefore, we are going to choose as an observable to probe the engineered antiferromagnetic state the connected Rydberg-Rydberg density correlation function, defined as

$$g^{(2)}(k,l) = \frac{1}{N_{k,l}} \sum_{(i,j)} \{\langle \hat{n}_i \hat{n}_j \rangle - \langle \hat{n}_i \rangle \langle \hat{n}_j \rangle\} \tag{4.2}$$

where the sum runs over atom pairs (i,j) whose separation $\mathbf{R}_i - \mathbf{R}_j$ corresponds to a

jump of k lattice sites in the horizontal direction and l lattice sites in the vertical one, and $N_{k,l}$ the number of such atom pairs in the array. By definition, the correlations are such that $g^{(2)}(k,l) = g^{(2)}(-k,-l)$. In order to improve the statistics, we symmetrize the data for a given (k,l) over the four quadrants $(\pm k, \pm l)$. Since these operations are symmetries of the setup, the symmetrization does not alter genuine features in the experimental data. Following our connection to spin-1/2 physics, this function is an equivalent of the spin-spin correlation function mentioned in the introduction to this chapter. For a perfect Néel state, $g^{(2)}(k,l) = \pm 1/4$ for $|k| + |l|$ even or odd, so we indeed retrieve this characteristic feature of the alternating sign of the correlations when scanning the distance between two atoms.

I show in Figure 4.7(c) the measured correlation functions, and as expected we see alternating sign correlations when δ lies in the antiferromagnetic region. We can extract two numbers from $g^{(2)}(k,l)$ in order to get more quantitative. The amplitude of the correlations decreases with distance, and we can fit this decay with an exponential function, $g^{(2)}(k,l) \propto (-1)^{|k|+|l|} \exp\{-(|k| + |l|)/\xi\}$. The correlation length ξ (given in number of lattice sites) is the first number we can extract. Second, we can compute the Néel factor, written as

$$S_{\text{Néel}} = 4 \times \sum_{k,l} (-1)^{|k|+|l|} g^{(2)}(k,l). \tag{4.3}$$

This factor is an estimator of the mean number of spins antiferromagnetically correlated with a given spin, so the average size in number of spins of the antiferromagnetic domains in our 6×6 square array. This quantity can therefore be associated with the correlation length in lattice sites, $S_{\text{Néel}} \propto \xi^2$, for short-ranged enough correlations. As we get less statistics to evaluate the correlations for long distances, we restrict ourselves to the indexes k, l such as $|k| + |l| \leq 4$ to compute the Néel factor. Figure 4.7(d) shows the measured Néel factor, which is significantly different from zero only inside the boundaries of the antiferromagnetic phase. This is why the measurement of this quantity allowed us to identify the phase boundaries in detuning.

Statistical and detection errors I have already presented in Chapter 2 the statistical error on the recapture probability, the standard error on the mean (s.e.m). This allows us to compute the error on the Rydberg fraction. For the error on the correlations, and consequently on the Néel factor, our theory collaborators estimated the error (error bars on Figure 4.7(d)) via bootstrapping techniques, consisting in re-sampling the original set of data.

I also presented in Subsection 2.3.1 the detection errors: ϵ is the probability to misleadingly see a ground state atom as a Rydberg one, while ϵ' is the probability to make the inverted detection error. Due to these errors, the ratio between the measured correlations and the one which would have been obtained without any error is $(1-\epsilon-\epsilon')^2$. None of the experimental results presented here (and in general in all this manuscript) are corrected for these detection errors. We rather include the detection errors in numerical simulations to get a better agreement with the experimental data.

4.3.2 An optimal sweep duration

We have now determined the most suitable final detuning to observe the most extended antiferromagnetic correlations. We can in a following optimization stage vary the value of t_{sweep} (Figure 4.8(a)). The precise fixed parameters for the time profiles are in that case: $|U|/h = 2.7\,\text{MHz}$, $\Omega_{\text{max}} = 2\pi \times 1.8\,\text{MHz}$, $\delta_{\text{init}} = 2\pi \times 6.0\,\text{MHz}$, $\delta_{\text{final}} = -2\pi \times 4.5\,\text{MHz}$, $t_{\text{rise}} = 0.25\,\mu\text{s}$, $t_{\text{fall}} = 0.25\,\mu\text{s}$. For these parameters, as $|U|/h = 2.7\,\text{MHz}$, we are in the regime $\Omega_{\text{max}} < \Omega_{\text{c}}$, and we cross the phase boundary while sweeping the detuning. We sweep it for a varying duration t_{sweep} ranging from 0.1 to $1.3\,\mu\text{s}$. Considering the adiabaticity criterion, we expect that t_{sweep} should be large to have the most correlated state.

Figure 4.8 summarizes the results obtained when varying t_{sweep}. The best correlations are obtained for $t_{\text{sweep}} = 0.7\,\mu\text{s}$, corresponding to a measured correlation length in lattice sites $\xi = 1.35 \pm 0.09$ (Figure 4.8(c)). Although the correlation length is smaller than two sites, the correlations have the expected sign up to $|k| + |l| = 5$, that is to say for almost the whole array. The successive shells corresponding to a constant $m = |k| + |l|$ are called Manhattan shells, I will describe in more detail the correlations inside a shell in the last section of this chapter.

Figure 4.8(d) shows the Néel factor as a function of t_{sweep}. This factor first increases while increasing t_{sweep} as expected from the adiabatic theorem, but then it saturates and finally decreases. In order to understand this behaviour, our theory collaborators performed several numerical simulations. First, they resolved the time-dependent Schrödinger equation. As the Hilbert space size grows as 2^N with N the number of interacting atoms, tackling this numerical resolution in our case $N = 36$ is hardly achievable without any truncation of the Hilbert space. Since the correlations in our system remain relatively short-range, they chose to solve the equation for smaller systems, 4×4 or 5×5 atomic arrays, taking into account the full Hilbert space. The

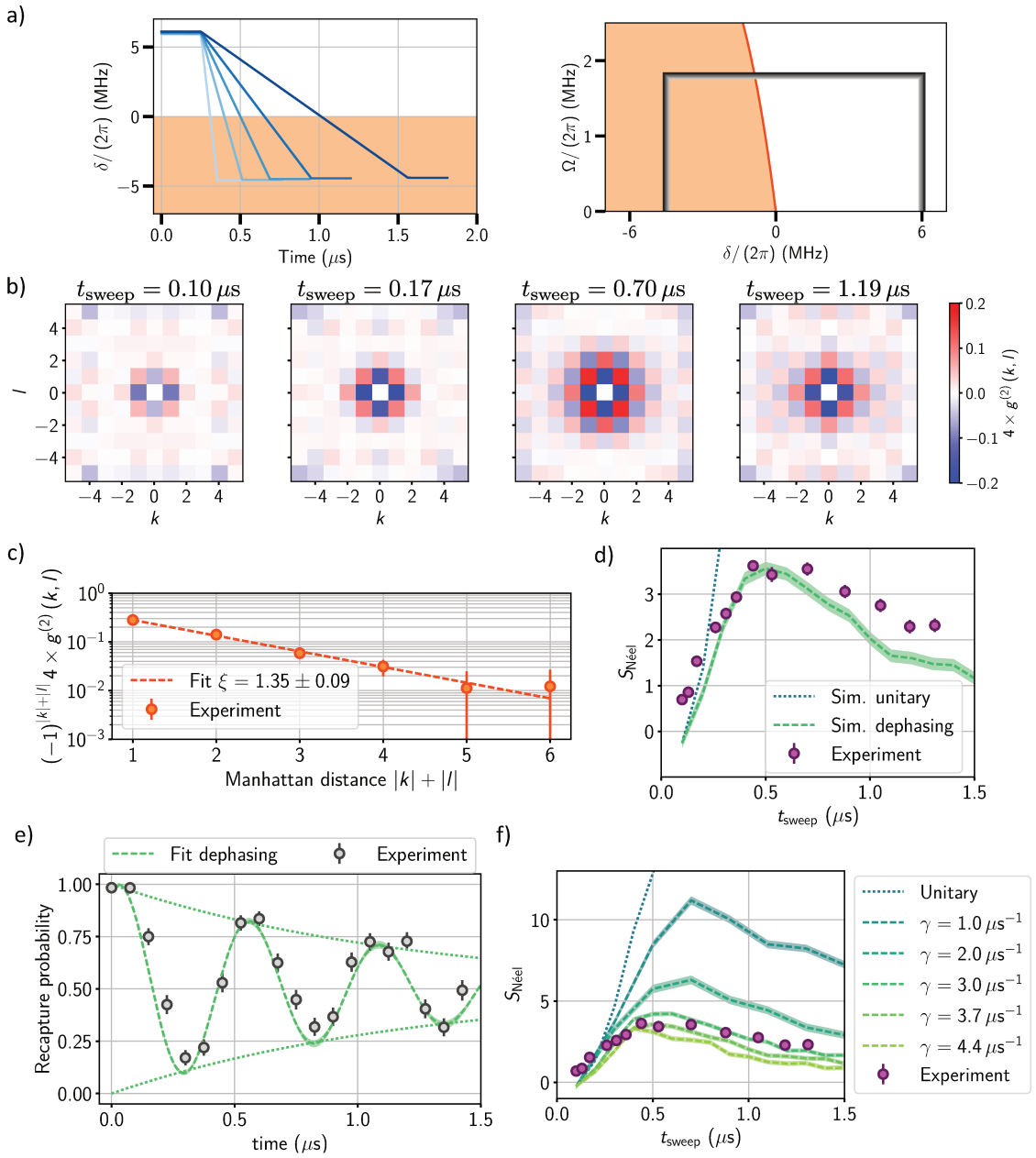

Figure 4.8: Finding an optimal duration. (a) Time profiles $\delta(t)$ and associated trajectories in the phase diagram, for the set of sweeps used here. (b) Measured correlation function for different t_{sweep} values. (c) For $t_{\mathrm{sweep}} = 0.7\,\mu$s, we fit the correlations (disks) with an exponential decay (solid line) to extract a correlation length ξ. (d) Néel factor as a function of t_{sweep}. The solid line is obtained via the resolution of the Schrödinger equation, whereas the dashed line comes from the resolution of the master equation, with an empirical dephasing rate $\gamma = 3.7\,\mu\mathrm{s}^{-1}$. (e) Single-atom Rabi oscillation, fitted with a damped sine to infer the dephasing rate γ. (f) Same as (d) but including additional resolutions of the master equation with various dephasing rates.

result of this simulation (dotted line) matches the experimental data only at low t_{sweep}. The solution given by the Schrödinger equation implies an unitary evolution, with a fully-coherent laser driving. In that case, $t_{\text{sweep}} \approx 0.5\,\mu$s is enough to reach $S_{\text{Néel}} \approx 10$ for a 4×4 array, that is to say antiferromagnetic correlations extended over a large part of the system. Therefore, if the evolution were unitary, the experimentally accessible sweep durations, about $1\,\mu$s, would be large enough to prevent Landau-Zener transitions to occur and we would observe longer-range correlations. The observed correlations are less extended, not because the adiabatic criterion is not fulfilled, but because our system evolution is not unitary.

Local dephasing model We thus need to take into account in the simulation decoherence processes originating from imperfections of our laser-driving [de Léséleuc *et al.*, 2018a]. Including all the different types of imperfection would be too demanding, so we chose for convenience to solve a master equation written in Lindblad form:

$$\frac{\mathrm{d}}{\mathrm{d}t}\hat{\rho} = -\frac{i}{\hbar}\left[\hat{H}, \hat{\rho}\right] + \mathcal{L}\left[\hat{\rho}\right], \tag{4.4}$$

with $\hat{\rho}$ the density matrix of the many-body system, and $\mathcal{L}$ a pure dephasing Liouvillian:

$$\mathcal{L}\left[\hat{\rho}\right] = \sum_i \frac{\gamma}{2}\left(2\hat{n}_i\hat{\rho}\hat{n}_i - \hat{n}_i\hat{\rho} - \hat{\rho}\hat{n}_i\right). \tag{4.5}$$

The Liouvillian is a sum of single-particle jump operators, whose dephasing rate $\gamma \sim 3.2\,\mu\text{s}^{-1}$ is extracted from a fit of the single-atom Rabi oscillation (Figure 4.8(e)). Indeed, by resolving our dephasing model for the single-particle case, we find that the 1/e damping time of the envelope of the measured Rabi oscillations (dotted lines) is equal to $4/\gamma$. In summary, we include the imperfections of our laser-driving by adopting a pure dephasing model, whose dephasing rate is fitted from single-atom Rabi oscillations.

Our empirical dephasing model (dashed line in Figure 4.8(d)) is in a very good agreement with the experimental data. Only a dephasing rate close to the one inferred from the measured Rabi oscillations gives the correct evolution of the Néel factor, as shown by Figure 4.8(f). This justifies the use of our empirical dephasing model. The simulation was in that case also performed for a smaller 4×4 system as the correlations remain relatively short-ranged, and includes the aforementioned detection errors with no adjustable parameters. This agreement suggests that the technical imperfections of our qubit driving, at the single-particle level, are the reason why we cannot generate more extended antiferromagnetic correlations. Implementing the more

coherent qubit driving developed on the Harvard platform [Levine *et al.*, 2018] could extend the time our system follows an unitary evolution, in the end leading to more extended correlations [Bernien *et al.*, 2017; Keesling *et al.*, 2019].

The results presented in this section allow us to determine an optimized sweep in view of generating the largest antiferromagnetic correlations. In the next section, instead of looking at the correlations at the end of different sweeps, we look at their growth during a sweep. Observing the build-up of correlations in time, i.e. measuring how correlations spread in the system, will explain their spatial dependence, namely their relative values inside a Manhattan shell.

4.4 Observing the growth of correlations

In this last section, I will focus on how the correlations build up during an optimized sweep, for a square array and, only in the last subsection, a triangular one. I will show that the experimental results are well captured by a short-time expansion approach, which gives more insight on the many-body dynamics occurring in our system.

4.4.1 Finite speed of spreading

To observe the growth of correlations in time, the experiment consists in abruptly switching off the excitation lasers at different times of the evolution, in order to freeze the many-body dynamics and measure the instantaneous correlations (Figure 4.9(a)). The sweep parameters are the same as in Subsection 4.3.2, with $t_{\text{sweep}} = 0.44\,\mu$s.

I plot in Figure 4.9(b) the Néel factor as a function of the switching off time. Correlations start to appear for $t > 0.5\,\mu$s, which corresponds to the time when δ becomes negative, that is to say when we enter the antiferromagnetic region in the phase diagram. Then, the correlations saturate around $t = 0.8\,\mu$s. As the agreement with the simulation including our empirical dephasing rate is very good (dashed lines) when the value of γ is the one deduced from single-atom Rabi oscillations ($\gamma = 3.0\,\mu\text{s}^{-1}$), we can again conclude that it is because of the imperfections of the laser driving that we cannot follow an unitary evolution (dotted lines) for a longer time.

Time delay for the build up of correlations Figure 4.9(c) shows $g^{(2)}(k,l)$ as a function of time for the three first Manhattan shells. The correlations appear first on

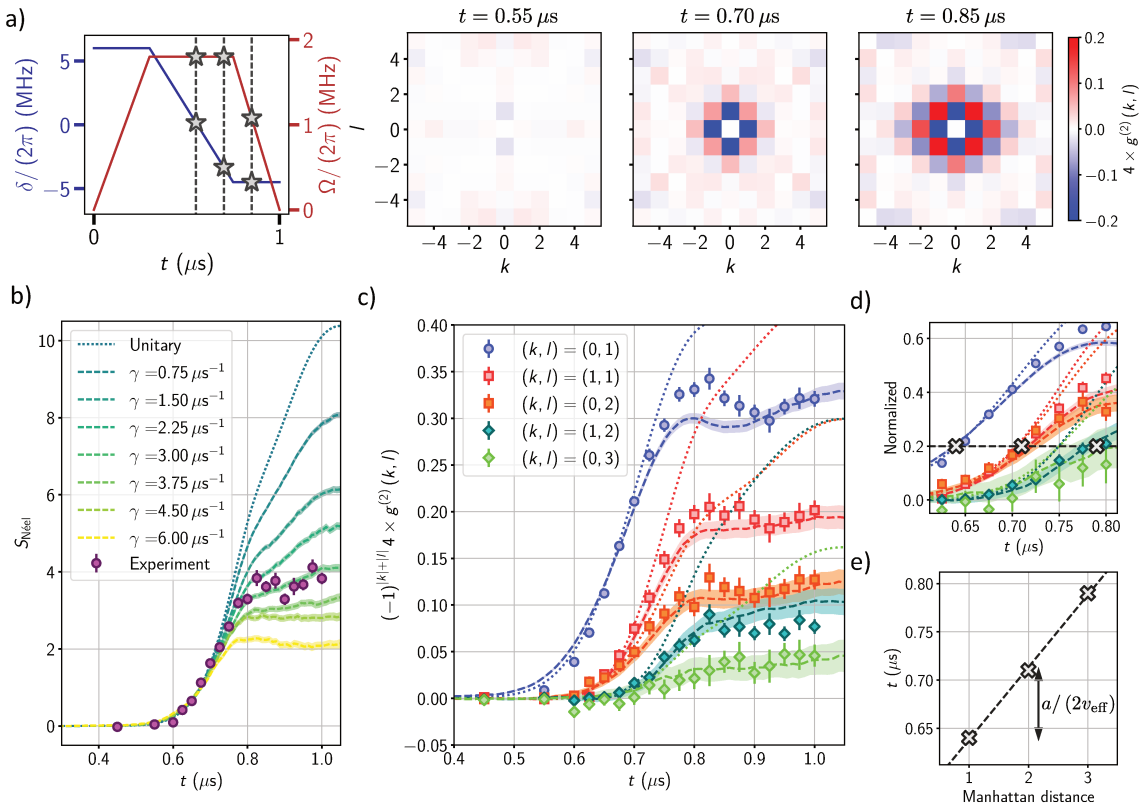

Figure 4.9: Measuring correlations during the dynamical tuning. (a) Time profiles of $\delta(t)$ and $\Omega(t)$ used for this experiment. The stars indicate the various switch off times of the lasers, where the dynamics freeze and we measure the instantaneous correlations. (b) Measured Néel factor as a function of time, to be compared to simulations with (dashed lines) or without (dotted line) dephasing. (c) Correlations for the three first Manhattan shells. The dotted lines are the results of a simulation of the unitary evolution, whereas the dashed lines are the ones including a dephasing rate $\gamma = 3\,\mu s^{-1}$. (d) Same as (c) after normalization of the correlations for each Manhattan shells. The horizontal black dashed line is a threshold to estimate the necessary time (grey crosses) to get significant correlations on each shell. (e) Necessary time to have significant correlations as a function of the Manhattan shell. The time delay between two shells is linked to the effective speed of spreading of the correlations.

the nearest neighbours, and then on the farthest ones. Therefore, we observe a delay in the growth of correlations for increasing Manhattan shells, which is due to their finite speed of spreading. In order to be more quantitative about these delays, we need a more involved analysis of the data. We first normalized the correlations for each Manhattan shells, in such a way that at long times, the unitary evolution would lead to correlations equal to one. Figure 4.9(d) presents the correlations after this normalization. Then, we choose a threshold level at 0.2, and look at the time when the normalized correlations intersect the threshold line. These times are $t \approx 0.64\,\mu$s for the first shell, $t \approx 0.71\,\mu$s for the second, and $t \approx 0.79\,\mu$s for the third, and are plotted in Figure 4.9(e).

Lieb-Robinson bounds This finite speed of spreading of correlations is reminiscent of Lieb-Robinson bounds. Lieb and Robinson proved that in non relativistic quantum mechanics, even if there is no explicit speed of light limiting the propagation of information, one can define a characteristic velocity for sufficiently local interactions [Lieb and Robinson, 1972]. This velocity is an upper bound for the spread of any correlations in our system. The speed of spreading measured from the time delays described above is about 70 times smaller than the bound evaluated by our theory collaborators based on the Lieb-Robinson formalism.

In order to get a better understanding of the values of these time delays, they followed an approach introduced in [Calabrese and Cardy, 2006], where the light-cone-like spreading of the correlations is due to the propagation of excited quasiparticles. They derived a group velocity for these quasiparticles by calculating the dispersion relation applying a linear spin-wave theory. The group velocity can be seen as en effective Lieb-Robinson velocity, and it was found to be equal to $v_{\text{eff}} \approx 2\pi \times 1.11\, a\,\mu\text{s}^{-1}$ for our experimental parameters, with a the lattice constant. The time delay of the spreading of correlation from one shell to the next one is then $a/(2v_{\text{eff}}) \approx 70\,\text{ns}$, which is in a very good agreement with the experimental data. Indeed, we measure that correlations significantly appear on the second shell about 70 ns after they did on the first one, and they appear on the third shell about 80 ns after they did on the second one (see Figure 4.9(e)).

Exponential decay of the correlations In addition to an upper bound for the speed of spreading of the correlations, the theory developed by Lieb and Robinson predicts that correlations are not zero outside the light-cone but decay exponentially. This can also be seen on the experimental data, when the correlation reaches the threshold

line for the first shell, it is not zero for the second. A short time expansion of the evolution operator, which is a perturbative analytic calculation valid at times t such that $|U|\, t/\hbar, \Omega t, \delta t \ll 1$, captures this trend. Indeed, our collaborators derived the expression of the correlations as a function of time in this regime, and found that $g^{(2)}(k,l) \propto (-1)^m\, t^{2+4m}$ with the Manhattan distance $m = |k| + |l|$. These expressions lead to an alternating sign of the correlations when increasing m, and, as in this regime t is small, to an exponential decay of the correlations for increasing m. All the correlation patterns we observe in the antiferromagnetic region exhibit these two features. Even if the regime of times explored in the experiment is not within the range of validity of the short time expansion, the fact that the results are qualitatively similar is instructive. It means that the features of the observed correlations are the same as in their early development, when the evolution is still unitary.

4.4.2 Spatial structure of the correlations

I now describe in more detail the measured correlations at a fixed time for the first three Manhattan shells of the 6×6 square array, plotted in Figure 4.10. They were obtained at the end of the sweep described in the previous subsection. I have already commented on the alternating sign of the correlations as a function of the Manhattan distance m, the feature we expect from an antiferromagnetic state on a square array.

Correlations inside a shell Inside a given Manhattan shell, the correlations do not have the same value. For example, for $m = 2$, we observed $g^{(2)}(1,1) \approx 2 \times g^{(2)}(0,2)$. The short-time expansion described above also reproduces this feature. The expression of the correlations are first derived via this method by considering one chain of m bonds, no matter the lattice geometry. Then, by multiplying the correlations by the number of linking paths of size m between sites $(0,0)$ and (k,l), we obtain the expression of the correlations for a given lattice geometry. For a square lattice, the number of linking paths between sites $(0,0)$ and (k,l) is simply given by the binomial coefficient $\binom{m}{l}$ with $l \geq k \geq 0$, as shown in Figure 4.10(a). Consequently, in the short time regime, we expect $g^{(2)}(1,1) = 2 \times g^{(2)}(0,2)$. In Figure 4.10(c), I show how the experimental data (blue disks) compare with binomial coefficients (green dots). The proportional factor was set for each Manhattan shell in such a way that the maximum estimated value for the correlations (green dots) is equal to the maximum value of the measured correlations (blue disks). This combinatorial argument coming from the short time expansion explains qualitatively the spatial structure of the correlations

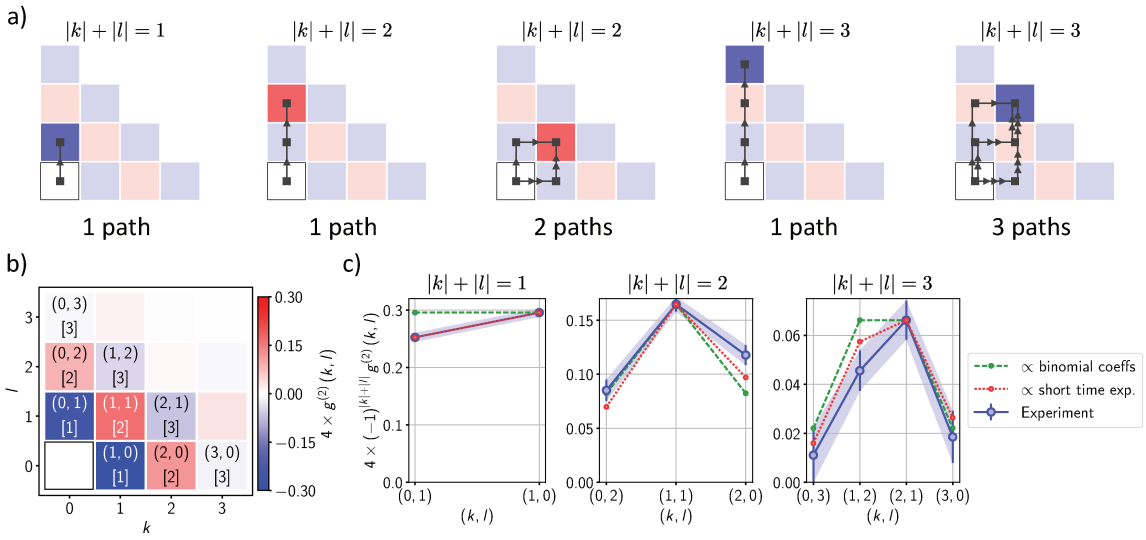

Figure 4.10: Build-up of correlations inside Manhattan shells. (a) Number of paths linking two sites, the central one and the highlighted one, in a square array (b) Measured correlations at the end of an optimized sweep. The coordinates between parenthesis are the lattice indexes (k, l), and the number of paths linking the two lattice sites separated by a (k, l) vector is indicated between brackets. (c) Correlations inside a shell (blue disks), in qualitative agreement with those estimated using binomial coefficients (green dots) or the short-time expansion (red dots).

inside the Manhattan shells.

Residual anisotropy of the van der Waals interaction We can improve our estimation of the correlations by including the residual anisotropy of the interaction in the short time expansion calculation. Indeed, the analytical expression of the correlations in this regime, in addition to the dependence on time already mentioned, depends on the nearest neighbour interaction $|U|$. We then infer from the ratio between $g^{(2)}(0,1)$ and $g^{(2)}(1,0)$ the ratio between interaction along vertical and horizontal bonds. We use this estimated ratio to evaluate the correlations in the further shells (red dots in Figure 4.10(b)). Again, the short time expansion explains qualitatively the measured correlations.

To conclude on the correlations inside a 6×6 square array we have explored on our platform, the observed spatial structure and growth in time are qualitatively reproduced by a short time expansion. It turns out that the correlations at short times, or the correlations at long times (the ones we would obtain with an infinite sweeping time, so the ones of the antiferromagnetic state) show the same alternating

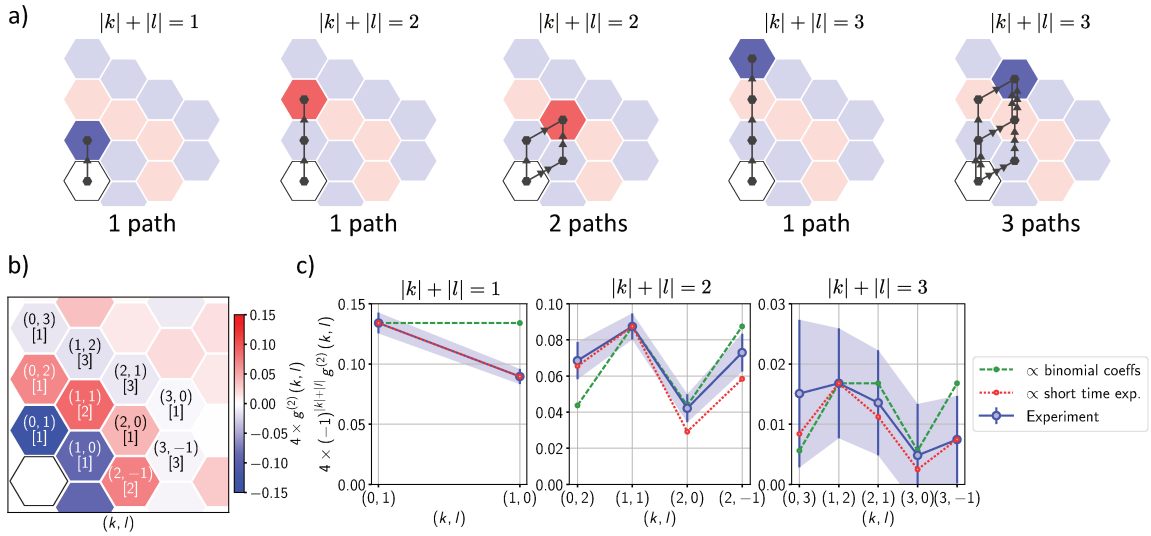

Figure 4.11: Build-up of correlations for an optimized sweep in a triangular array. (a) Number of paths linking two correlated spins for the triangular geometry. (b) and (c) Same quantities as in Figure 4.10, adapted for the triangular case.

sign of the correlations while increasing the Manhattan distance for a square array. It could be a reason why our system, despite the reduced coherence time, exhibits the characteristic feature of antiferromagnetic correlations. Even if the evolution is not fully coherent, the correlations grow with the expected sign as soon as they appear.

4.4.3 The triangular case

Finally, I describe the correlations we have observed on a different lattice geometry, namely a 36-atom triangular array. The parameters of the dynamical tuning of the Hamiltonian used for this specific geometry were: $|U|/h = 0.8\,\mathrm{MHz}$, $\Omega_{\max} = 2\pi\times 0.6\,\mathrm{MHz}$, $\delta_{\mathrm{init}} = 2\pi\times 6.0\,\mathrm{MHz}$, $\delta_{\mathrm{final}} = -2\pi\times 1.6\,\mathrm{MHz}$, $t_{\mathrm{rise}} = 0.25\,\mu\mathrm{s}$, $t_{\mathrm{fall}} = 0.25\,\mu\mathrm{s}$ and $t_{\mathrm{sweep}} = 5.5\,\mu\mathrm{s}$. During this sweep, the phase boundary is crossed while changing the detuning, and we end in a region where the most excited state exhibits a 1/3 Rydberg fraction (see Subsection 4.2.2).

Figure 4.11 shows the measured correlations on the first three Manhattan shells after such a sweep. The experimental data shows again an alternating sign for the correlations when increasing the Manhattan distance. Since the sign of the correlations derived from a short-time expansion only depends on the Manhattan distance $m = |k| + |l|$ whatever the lattice geometry, this alternating sign is still explained with the help of the short-time expansion.

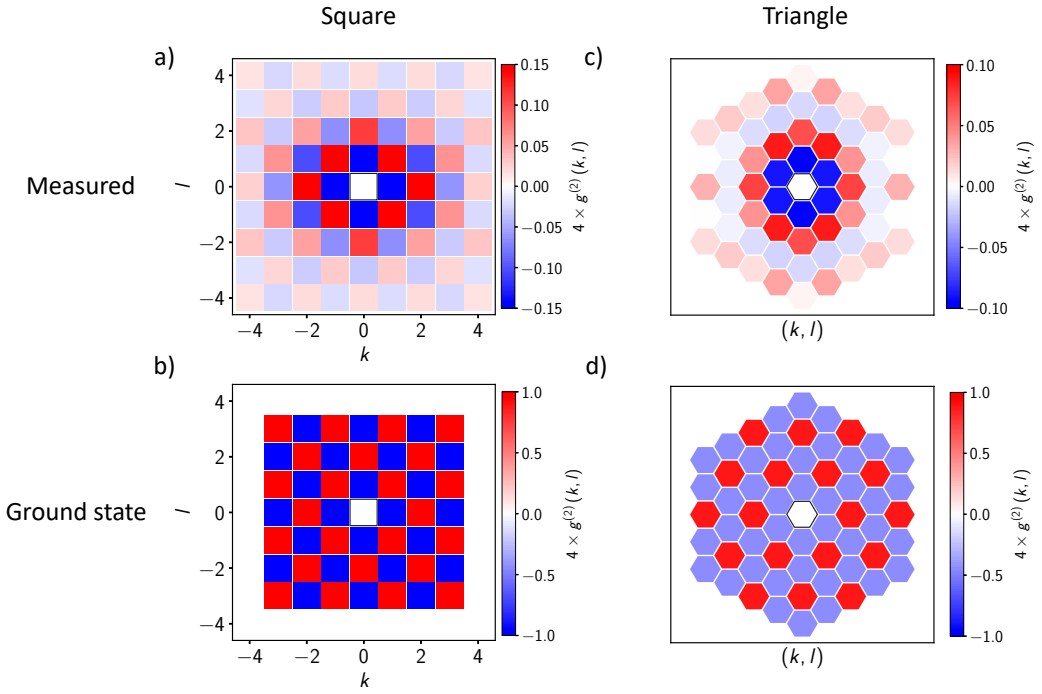

Figure 4.12: Correlations in a square or a triangle. (a) Measured correlations on a 6×6 square array for an optimized sweep. (b) Correlations of the antiferromagnetic state. (c) Measured correlations on a 36-atom triangular array for an optimized sweep. (d) Correlations of the $1/3$-filling Rydberg crystal.

Therefore, we followed the same approach to estimate the values of the correlations with a short-time expansion (Figure 4.11(c)), and we obtained a good qualitative agreement. In the end, this validates our choice to interpret the measured correlations via a short-time expansion, as the qualitative agreement is good for both square and triangular array.

Square versus triangle As a conclusion for our study, Figure 4.12 compares the square and the triangle cases. I plot for both geometries the measured correlations obtained after an optimized sweep, to be compared to the correlations of the targeted ground state of $-\hat{H}$. The measured and targeted correlations are qualitatively similar in the case of a square array, but are not for the triangular case.

I have shown that the spatial structure of both measured correlations could be explained via a short-time expansion. The build-up mechanism of the correlations at play within the short-time expansion approach consists in their spreading from the inner shell to the outer shell. This results in a correlation pattern showing an alternating sign in the different Manhattan shells, which we indeed observed. For

the square array, the antiferromagnetic state exhibits the same type of correlation pattern. This implies that building correlations from the inner shell to the outer shell, as the system does at the very beginning of its evolution according to the short-time expansion, is a possible way to generate a state qualitatively close to the targeted antiferromagnetic state.

On the contrary, for the triangular array, to build the targeted correlation pattern, the correlations must undergo a more complicated phenomenon than the simple propagation from the inner shell to the outer shell. They have to go through closed loops, which is not accounted for in the short-time expansion since in this perturbative treatment, going through closed loops would correspond to higher-order terms. In our platform, the coherence time is not long enough for the system to realize the presence of these closed loops, this is why we do not observe the targeted correlation pattern. These closed loops, whose presence prevents us to generate the targeted state, may be seen as a signature of geometrical frustration.

4.5 Conclusion

In this chapter, I have described our latest work about the quantum simulation of an Ising-like model. We are able to generate antiferromagnetic correlations by a dynamical tuning of the Hamiltonian, following adiabatic protocol widely used in the quantum simulation community. We demonstrate that the limited extension of the observed correlations comes from imperfections of our single-qubit driving rather than from a non-respect of the adiabatic criterion, and that the features of the correlations are qualitatively captured by a short-time expansion, for both square and triangular geometries. In the future, we will use another laser excitation scheme expected to have better coherence properties. We may then go on exploring the problem tackled in this chapter with an extended coherence time, and reach the antiferromagnetic states in a triangular array.

In addition to its use in quantum magnetism, the Ising model is also a toy model to illustrate some features of high-energy physics, such as the confinement of quarks [Kormos *et al.*, 2016], which could also be seen in our platform. In an even wider range of applications, it has been shown that the Ising model can be mapped into different optimization problems [Lucas, 2014]. In that sense, it has been proposed to use Rydberg atoms interacting in the van der Waals regime to solve optimization problems, such as finding the maximum independent set of a graph [Pichler *et al.*, 2018]. We will implement this kind of optimization protocols on our platform in the near future.

Chapter 5

Spin correlations in an XY magnet

Contents

In this chapter, we will study another spin Hamiltonian, the XY model, of canonical form

$$\hat{H}_{\mathrm{XY}} = \sum_{i,j} J_{ij} \left(\hat{\sigma}_i^- \hat{\sigma}_j^+ + \hat{\sigma}_i^+ \hat{\sigma}_j^- \right),$$

where the sum runs over all pairs of spins and J_{ij} is the interaction energy between spins i and j. This Hamiltonian describes the coherent exchange of excitations between pairs of atoms. As stated in the Introduction, for the implementation of this model on our platform, the effective spin-1/2 must be encoded in two dipole-coupled Rydberg levels, whereas it was encoded in the electronic ground state and in one Rydberg level in the Ising case. Here, we will use the states $|\downarrow\rangle = \left|60S_{1/2}, m_J = 1/2\right\rangle$ and $|\uparrow\rangle = \left|60P_{1/2}, m_J = -1/2\right\rangle$. The two Rydberg pair states $|\uparrow\downarrow\rangle$ and $|\downarrow\uparrow\rangle$ are coupled via the resonant dipole-dipole interaction, which gives the value of the coupling J_{ij}. The interaction strength depends on both the interatomic distance R_{ij} and the angle

with respect to the quantization axis θ_{ij}, $J_{ij} \propto C_3\left(\theta_{ij}\right)/R_{ij}^3$, and is typically on the MHz range for atoms separated by a few tens of microns. In Section 5.1, I will describe in more detail the conditions for which a system of Rydberg atoms mimics spins-1/2 interacting via the XY model.

Since the energy separation between two adjacent Rydberg states is on the ten of GHz range (it is about 16.7 GHz for the qubit in use here), the effective spin-1/2 will be manipulated using microwave fields. The microwave field acts as an effective magnetic field for the qubit, in the same way as the two-photon laser field did in the Ising case. Then, we will follow the same kind of adiabatic protocol to study the XY Hamiltonian: we will start from a paramagnetic phase under a strong external field, and slowly decreasing it we will aim at generating correlated phases induced by the interaction. Before presenting the results we obtained, I want to stress out the differences between the Ising and the XY models, which has motivated our implementation of this other spin Hamiltonian on our experimental platform.

An exotic phase diagram The main difference concerns the eigenstates of these two spin Hamiltonians, in the absence of a transverse magnetic field. In the Ising case, the eigenstates can be written as product states of spins up and spins down, i.e. states defined in the N-qubit basis. Since they are product states, they correspond to classical configurations. Such product states are not eigenstates of the XY Hamiltonian [1]. This means that interactions of the XY-form intrinsically produce some entangled eigenstates, fundamentally different from the classical configurations and potentially leading to exotic phases. The characterization of these phases, both theoretically and experimentally in solid-state physics, is still an active research field [Balents, 2010]. Among them, quantum spin liquids [Knolle and Moessner, 2019] have triggered a lot of interest for a few decades as they could be associated with superconductivity [Anderson, 1987]. Such a spin liquid is expected to appear on a honeycomb lattice hosting spins interacting via the XY Hamiltonian [Varney *et al.*, 2011]. Studying these phases is beyond the scope of the present manuscript, but this justifies the interest in the XY model and our implementation on our setup.

Coherent transfer of excitations I have already mentioned in the Introduction the spin-exchange process, a direct consequence of the fact that states defined in the N-qubit basis are not eigenstates of the XY Hamiltonian. For example, a two-atom system prepared in $|\uparrow\downarrow\rangle$ will oscillate between the two states $|\uparrow\downarrow\rangle$ and $|\downarrow\uparrow\rangle$. This

[1] Except the two fully-polarized spin states $|\downarrow\downarrow ... \downarrow\rangle$ and $|\uparrow\uparrow ... \uparrow\rangle$.

oscillation is coherently driven by the dipole-dipole interaction, to be contrasted with regular spin flips driven by external fields. This transfer of excitations driven by the interaction may also occur in biological systems, which makes the XY model relevant to study photochemistry or photosynthesis [Collini, 2013], and more generally to describe transports of excitations in various contexts. For the first implementation of the XY model in our experimental setup, the team explored this coherent excitation transfer in a three-spin chain [Barredo *et al.*, 2015].

Link to hard-core bosons The spin-exchange process can also be seen as the hopping of a particle between two sites instead of the exchange of the two spin states. Hopping particles therefore naturally arise from the atomic interactions, where the particle is a spin excitation or a boson. This leads to a rewriting of the XY Hamiltonian in terms of bosonic annihilation and creation operators (see Hamiltonian (A.5)). Then, we are able to engineer specific hopping Hamiltonians for hard-core bosons, as we demonstrated in our recent work [de Léséleuc *et al.*, 2019]. This work consisted in studying a bosonic version of the Su-Schrieffer-Heeger (SSH) Hamiltonian, one of the simplest models expected to exhibit topological properties. We characterized these topological properties in the single-particle regime and for the many-body ground state.

The spin-exchange process and, more generally, hard-core boson Hamiltonians will be explored in the last part of this manuscript. I will then interpret the result in terms of spin-1/2 physics for convenience in this chapter. For instance, I will show in Section 5.2 how we can generate states with a specific number of spins $|\uparrow\rangle$, so how we can aim at specific values of the magnetization, via microwave sweeps. In the hard-core boson picture, these microwave sweeps would be seen as the way to inject a controlled number of particles in the system, by setting an effective chemical potential. In the case of the SSH chain, we used these sweeps to prepare the many-body ground state corresponding to a half-filled bulk. While describing these sweeps in the particular case of the SSH chain, I will not insist on the topological properties of the system as it is not the central topic of this chapter. I will rather focus on the value of the magnetization and the spin-spin correlations. But I want to make it clear for the reader that the spin-spin correlations described here are not the only interest motivating our study of microwave sweeps on an XY magnet, they were used as a tool to observe topological properties in the many-body regime for an SSH chain.

Long-range effects Finally, another difference between our implementation of the Ising and the XY models is that the interaction decays as $1/R^6$ in the Ising case whereas it decays as $1/R^3$ in the XY case. This is because in the XY case the interaction is the direct dipole-dipole interaction, and not a second order perturbation term like in the Ising case. The dipole-dipole interaction, experienced in our platform by Rydberg atoms, is also the regime of interaction for polar molecules or magnetic atoms, and is therefore a central tool to engineer Hamiltonians on quantum simulation experiments. The extended range of the interaction in this regime enabled the study of the many-body dynamics even in a sparsely filled polar molecule optical lattice [Yan *et al.*, 2013]. For the first implementation of the XY model on our platform, the experimental signatures of this extended range of the interaction were the revivals of the oscillatory dynamics [Barredo *et al.*, 2015]. More fundamentally, the long-distance tail of the dipolar interaction allows for the existence of a true long-range order (correlations are not exponentially vanishing in a two-dimensional system at finite temperature) [Peter *et al.*, 2012]. We will also see in this chapter one manifestation of this long-range feature.

In this chapter, I will report our observation of the many-body features of an XY magnet for increasing system sizes. I will start by a detailed description of the dipole-dipole interaction, exploring it for a two-atom system. Then, I will show how we reach magnetization plateaus for 1D-chains by dynamically tuning the parameters of the external field. Finally, I will present the correlated phases we observed in 1D- and 2D-systems. As explained, part of the experimental results shown in this chapter were used as a tool to study the topological properties of an SSH chain [de Léséleuc *et al.*, 2019]. The other ones are not published yet.

5.1 Resonant dipole-dipole interaction

In this section, I will first develop the dipole-dipole interaction in terms of the different spherical components of the electric dipole operator, to show to what extent we can restrict ourselves to specific terms, depending on the Rydberg levels in use, or the geometry. Then, as the spin-1/2 is now encoded in two Rydberg levels, I will describe what additional experimental steps we must perform to operate in the Rydberg manifold. Finally, I will show the effect of the dipole-dipole interaction on the simplest system composed of two atoms.

5.1.1 Full expression of the dipole-dipole interaction

The dipole-dipole interaction for two atoms labeled as i and j reads in term of electric dipole operators

$$\hat{V}_{\mathrm{ddi}} = \frac{1}{4\pi\epsilon_0} \frac{\hat{\mathbf{d}}_i \cdot \hat{\mathbf{d}}_j - 3\left(\hat{\mathbf{d}}_i \cdot \mathbf{n}_{ij}\right)\left(\hat{\mathbf{d}}_j \cdot \mathbf{n}_{ij}\right)}{R_{ij}^3},$$

with $\mathbf{R}_{ij} = \mathbf{R}_j - \mathbf{R}_i$ the separation of the atomic pair, $R_{ij} = |\mathbf{R}_{ij}|$ and $\mathbf{n}_{ij} = \mathbf{R}_{ij}/R_{ij}$. A convenient way to treat this interaction is to use the decomposition of the dipole operator into the spherical basis, with the components $\hat{d}^0$, $\hat{d}^+$ and $\hat{d}^-$, as these operators correspond to coupling to different states in the single-atom Zeeman manifold. The operator $\hat{d}^0$ couples states such as $\Delta m_J = 0$, whereas operators $\hat{d}^\pm$ couple states such as $\Delta m_J = \pm 1$. With z the direction of the quantization axis, the components in the Cartesian basis of the dipole operator are written $\hat{d}^z = \hat{d}^0$, $\hat{d}^x = \left(\hat{d}^- - \hat{d}^+\right)/\sqrt{2}$ and $\hat{d}^y = \mathrm{i}\left(\hat{d}^- + \hat{d}^+\right)/\sqrt{2}$. Then, with θ and ϕ the usual angles defining the position in spherical coordinates, $\mathbf{n}_{ij} = \left(\sin\left(\theta_{ij}\right)\cos\left(\phi_{ij}\right), \sin\left(\theta_{ij}\right)\sin\left(\phi_{ij}\right), \cos\left(\theta_{ij}\right)\right)$, and the dipole-dipole interaction finally reads

$$\begin{aligned}\hat{V}_{\mathrm{ddi}} = \frac{1}{4\pi\epsilon_0 R_{ij}^3}\Bigg[& \frac{1-3\cos^2\theta_{ij}}{2}\left(\hat{d}_i^+\hat{d}_j^- + \hat{d}_i^-\hat{d}_j^+ + 2\hat{d}_i^0\hat{d}_j^0\right) \\ & + \frac{3}{\sqrt{2}}\sin\theta_{ij}\cos\theta_{ij}\left(\mathrm{e}^{-\mathrm{i}\phi_{ij}}\hat{d}_i^+\hat{d}_j^0 - \mathrm{e}^{\mathrm{i}\phi_{ij}}\hat{d}_i^-\hat{d}_j^0 + \mathrm{e}^{-\mathrm{i}\phi_{ij}}\hat{d}_i^0\hat{d}_j^+ - \mathrm{e}^{\mathrm{i}\phi_{ij}}\hat{d}_i^0\hat{d}_j^-\right) \\ & - \frac{3}{2}\sin^2\theta_{ij}\left(\mathrm{e}^{-2\mathrm{i}\phi_{ij}}\hat{d}_i^+\hat{d}_j^+ + \mathrm{e}^{2\mathrm{i}\phi_{ij}}\hat{d}_i^-\hat{d}_j^-\right)\Bigg].\end{aligned} \tag{5.1}$$

Three terms appear then in the dipole-dipole interaction, with a different action on the total magnetic number of the two atoms $M = m_{J,i} + m_{J,j}$. On the first line, the two-atom operators are such that $\Delta M = 0$, on the second, such that $\Delta M = \pm 1$ and on the third, such that $\Delta M = \pm 2$.

Now, we restrict ourselves to the qubit basis, $|{\downarrow}\rangle = \left|60S_{1/2}, m_J = 1/2\right\rangle$ and $|{\uparrow}\rangle = \left|60P_{1/2}, m_J = -1/2\right\rangle$. Consequently, the dipole-dipole interaction simplifies to

$$\hat{V}_{\mathrm{ddi}} = \frac{1}{4\pi\epsilon_0 R_{ij}^3}\frac{1-3\cos^2\theta_{ij}}{2}\left(\hat{d}_i^+\hat{d}_j^- + \hat{d}_i^-\hat{d}_j^+\right). \tag{5.2}$$

Then, rewriting Equation (5.2) in terms of the raising and lowering spin operators $\hat{\sigma^+}$, $\hat{\sigma^-}$ gives the XY Hamiltonian written at the beginning of this chapter, with $J_{ij} = C_3\left(3\cos^2\theta_{ij} - 1\right) / \left(2R_{ij}^3\right)$. I will present in Subsection 5.1.3 how we can measure the interaction energy J_{ij}, in order to experimentally infer the value of the C_3 coefficient for the involved Rydberg states, $C_3/h = 2.4\,\mathrm{GHz}\cdot\mu\mathrm{m}^3$.

The interacting terms appearing in Equation (5.2) are the most important ones as they couple the degenerate pair states $|\uparrow\downarrow\rangle$ and $|\downarrow\uparrow\rangle$. Some other off-resonant interacting processes may also occur. For example, the term $\hat{d}_i^0\hat{d}_j^0$ couples $|\uparrow\downarrow\rangle$ with $\left|60S_{1/2}, m_j = -1/2\right\rangle \otimes \left|60P_{1/2}, m_j = 1/2\right\rangle$. These off-resonant processes are negligible if the Zeeman splitting is larger than the corresponding interaction energies. For the experiments described in this chapter, the magnetic field defining the quantization axis is set to 47 G, which implies that the energy separation between the two pair states mentioned above is about 90 MHz, one order of magnitude larger than any interaction energy for a typical distance of 10 μm. Consequently, the interaction Hamiltonian derived in Equation (5.2) correctly described the dynamics occurring in our system. This is why I insisted in Chapter 2 on the necessity to generate magnetic fields with large amplitude.

Restricting ourselves to resonant coupling only, Equation (5.2) shows the complete angular dependence of the dipole-dipole interaction. In most of the experiments presented in this chapter, the quantization axis will be set along the vertical axis, that is to say within the atomic array. In that case, θ ranges between 0 and 2π and ϕ is set to an arbitrary value, $\phi = 0$, for example. I will also show experiments with the quantization axis orthogonal to the atomic array, along the aspherical lenses axis. In that case, $\theta = \pi/2$ and the interaction written in Equation (5.2) is isotropic within the atomic array.

In Chapter 6, we will also operate in the geometry $\theta = \pi/2$, but in an extended Zeeman manifold using the state $\left|60P_{3/2}\right\rangle$. Then, the terms corresponding to the third line in Equation (5.1) may play a role, and they will allow us to implement complex hopping amplitude via off-resonant interaction processes like the ones aforementioned.

5.1.2 Quantum simulation with an encoding in the Rydberg manifold

After loading and preparing the atoms in the array, they are all initialized in $|g\rangle$, in a targeted atomic geometrical configuration. This was the starting point of the experiments described in the previous chapter. As the spin-1/2 is now encoded in two Rydberg levels, we need to perform additional operations.

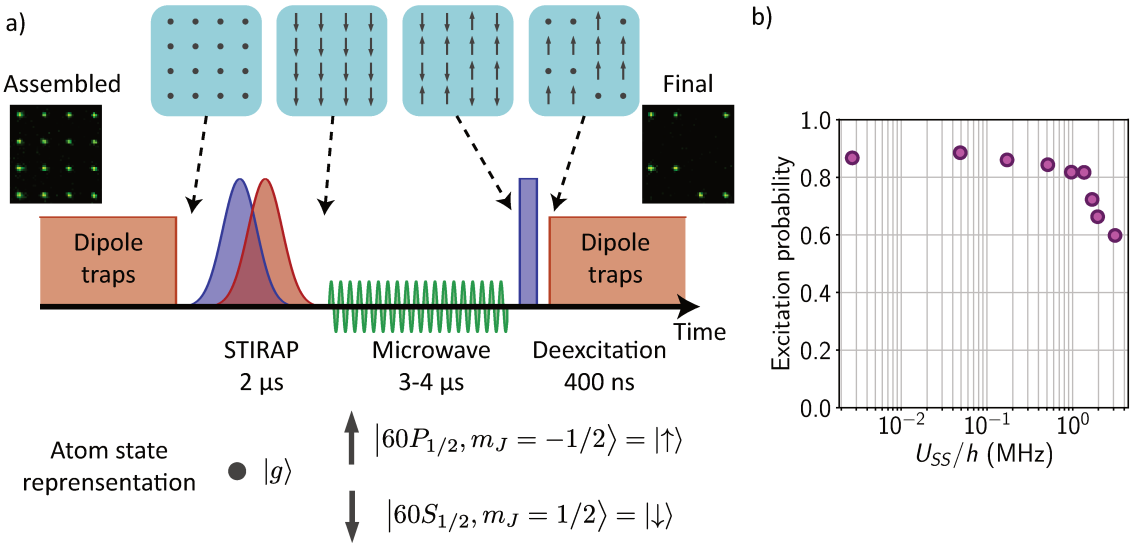

Figure 5.1: Experiment in the Rydberg manifold. (a) Experimental sequence. The usual sequence consists in STIRAP excitation, microwave driving, and deexcitation pulse. The states of the atom in a 4×4 array of optical tweezers are shown for the successive steps of the sequence. I also show the fluorescence images allowing us to infer the final states of the atoms. (b) Average excitation probability for atoms in a 4×4 array, as a function of the van der Waals energy shift between nearest neighbours. There, we increase the energy shift by reducing the size of the array.

Experimental sequence Figure 5.1(a) summarizes the typical experimental sequence we follow to perform quantum simulation when the spin-1/2 is encoded in the Rydberg manifold. We first need to initialize all the atoms in $|\downarrow\rangle$. We do it using the already described STIRAP excitation, introduced in Subsection 2.3.3. Then, we globally drive the assembly of qubits via microwave fields. I will show an example of single-atom microwave driving below. As both spin states $|\uparrow\rangle$ and $|\downarrow\rangle$ are Rydberg states, they would be lost at the end of the sequence, and we would not be able to differentiate between them. Consequently, we have to do an additional read-out operation: we use the deexcitation pulse presented in Subsection 2.3.3 to transfer back the atoms in $|\downarrow\rangle$ to $|g\rangle$. Therefore, if an atom is recaptured in the final image, it will be considered as a $|\downarrow\rangle$; otherwise, it will be considered as a $|\uparrow\rangle$. Measuring the recapture probability for each lattice site allows us to infer the site-dependent population in $|\downarrow\rangle$ and $|\uparrow\rangle$ and the spin-spin correlation function, in the same way as in the previous chapter.

When it was presented, the STIRAP excitation was shown to be more efficient than a Rabi π-pulse procedure in the single-atom case, as it leads to higher excitation probability on a wider atomic array area. It is also more advantageous to use the

STIRAP in the presence of interactions. Indeed, the Rydberg blockade, introduced in the previous chapter, prevents two neighbouring atoms to be excited simultaneously because of the van der Waals energy shift. In the experiments presented below, the typical interatomic distance is $a = 10\,\mu$m, and the van der Waals energy shift between two $60S$ atoms is measured to be $U_{SS}/h = 0.11\,$MHz. To have an efficient Rydberg excitation for the whole atomic array, we should have the blockade radius such that $R_\mathrm{b} \lesssim a/2$, implying an optical Rabi frequency $\Omega/(2\pi) \gtrsim 7\,$MHz. Operating at such a large Rabi frequency would imply important spontaneous emission via the intermediate state, and eventually a quite low Rydberg excitation efficiency. On the contrary, I plot in Figure 5.1(b) the Rydberg excitation efficiency in a 4×4 square array using a STIRAP as a function of the van der Waals energy shift. The efficiency stays higher than 0.9 as long as $U_{SS}/h < 1\,$MHz.

The finite efficiency of the STIRAP means that the initial lattice with $|\downarrow\rangle$ atoms contains "holes", which are atoms remaining in the electronic ground state $|g\rangle$. They will be mistakenly considered as $|\downarrow\rangle$ whereas they do not participate to the dynamics. These holes represent about 10% of the lattice sites. Contrary to the Ising case, there is no way to post select experimental shots with no lattice defects. Indeed, for our study of an Ising-like model, the $|\downarrow\rangle$ is encoded in $|g\rangle$, whose occupation can be checked non destructively by taking an additional fluorescence image after the assembling process. Nevertheless, even in the limited presence of lattice defects we will see that we are able to observe interesting spin-spin correlation features.

Finally, to summarize on the experimental sequence, we use the STIRAP here (and in all this manuscript) to completely Rydberg excite an atomic array despite the van der Waals interaction. The optical Rabi frequencies are larger than this interaction to overcome it. But in a regime where the optical Rabi frequencies are on the same order of magnitude as the van der Waals shift, as the STIRAP is also an adiabatic protocol, it could be used to engineer non-trivial entangled state, as proposed in [Møller, Madsen, and Mølmer, 2008].

Microwave qubit driving Once the lattice of spins is initialized in $|\downarrow\rangle$, we apply a time-dependent effective "magnetic field" to reach correlated phases. This effective field is in practice a microwave radiation, acting on the two qubit levels shown in Figure 5.2(a). The energy separation is $\hbar\omega_0 \approx 16.7\,$GHz, and the detuning from resonance is defined as $\delta_{\mu\mathrm{w}} = \omega_{\mu\mathrm{w}} - \omega_0$. The microwave Rabi frequency can be tuned between $\Omega_{\mu\mathrm{w}}/(2\pi) = 0.1 - 20\,$MHz. The microwave field is generated by an antenna (the output pin of an SMA connector) outside the vacuum chamber (see Figure 5.2(a)).

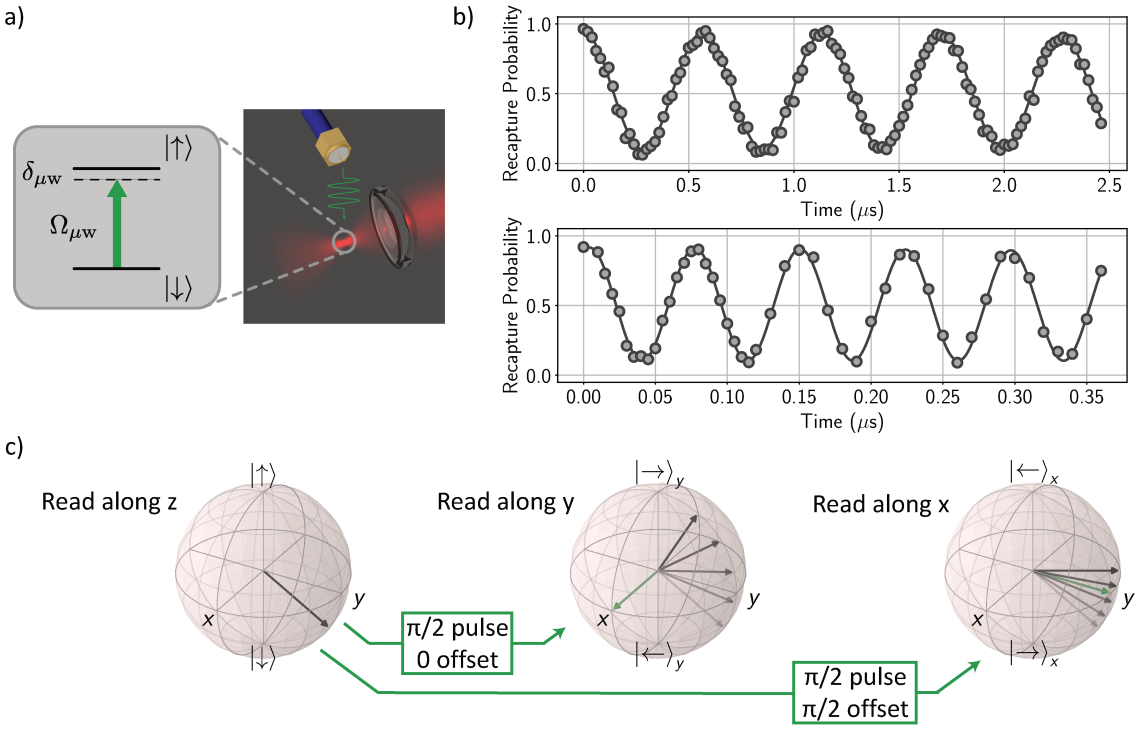

Figure 5.2: Microwave manipulation between two Rydberg states. (a) Scheme of the two-level system. An antenna outside the chamber produce on the atoms a microwave field of Rabi frequency $\Omega_{\mu w}$ and detuning $\delta_{\mu w}$. (b) Typical Rabi oscillations between $|\downarrow\rangle$ and $|\uparrow\rangle$. They were obtained for different microwave powers, and correspond to fitted (solid lines) Rabi frequencies $\Omega_{\mu w}/(2\pi) = 1.76\,\mathrm{MHz}$ (top) and $\Omega_{\mu w}/(2\pi) = 13.6\,\mathrm{MHz}$ (bottom). (c) Rotation of the measurement basis by applying a strong $\pi/2$ microwave pulse with different phase offsets, in order to read the spin components on other axes.

After preparing a single atom in $|\downarrow\rangle$, we apply a microwave pulse at resonance for varying durations, and observe a Rabi oscillation between $|\downarrow\rangle$ and $|\uparrow\rangle$ (Figure 5.2(b)). I show two examples of oscillations corresponding to different measured Rabi frequencies, $\Omega_{\mu w}/(2\pi) = 1.76\,\mathrm{MHz}$ (top) and $\Omega_{\mu w}/(2\pi) = 13.6\,\mathrm{MHz}$ (bottom). The most striking difference with the optically-driven Rabi oscillation shown in Figure 4.8 is that we hardly notice any damping, a promising feature for a more coherent time evolution as compared to our study of the Ising model. For optically-driven Rabi oscillations, the damping is mainly due to the Doppler effect, the phase noise and the spontaneous emission from the intermediate level $|e\rangle$. For the microwave qubit driving, the frequency is way smaller so the Doppler effect has no influence, the microwave sources are more stable so there is no phase noise, and no states with a large spontaneous emission are involved, eventually leading to a more coherent driving.

Our state-detection protocol leads to the measurement of the average population in $|\uparrow\rangle$ and $|\downarrow\rangle$. Therefore, we measure the spin projection on the quantization axis z, the vertical axis of the Bloch spheres shown in Figure 5.2(c). To access the other spin components, we perform additional microwave pulses rotating the measurement basis. By convention, the phase of the Rabi coupling is zero. Therefore, applying a pulse of duration $t_{\mu\mathrm{w}}$ with a zero-phase offset rotates the spin vector (black arrow in the middle Bloch sphere in Figure 5.2(c)) by an angle $\alpha = \Omega_{\mu\mathrm{w}} t_{\mu\mathrm{w}}$ around the effective magnetic field along x (green arrow). For a rotating angle $\alpha = \pi/2$, or $t_{\mu\mathrm{w}} = \pi/(2\Omega_{\mu\mathrm{w}})$, the middle Bloch sphere in Figure 5.2(c) shows that the spin component initially along y is projected along the vertical measurement axis. Applying the same $\pi/2$ pulse, but now with a $\pi/2$ phase offset, projects the spin components initially along $-x$ along the vertical measurement axis (right Bloch sphere in Figure 5.2(c)). Indeed, in that case, due to this phase offset, the rotation axis is now along y. In general, we access all the spin components along axes within the equatorial plane by applying a $\pi/2$ pulse with a phase offset ranging from 0 to 2π. Measuring the spin components in the equatorial plane is crucial for the study of the XY model, because, as we shall see in the following of this chapter, they exhibit characteristic spin-spin correlations.

5.1.3 Dipole-dipole interaction for two atoms

Now that I have introduced all the additional tools we need to perform experiments in the Rydberg manifold, I report here our study of the dipole-dipole interaction for a minimal system of two atoms. This will allow me to introduce the type of correlations we may expect in an XY magnet. The XY Hamiltonian, in presence of an effective external magnetic field, reads (rotating wave approximation):

$$\hat{H} = \sum_i \left(\frac{\hbar\Omega_{\mu\mathrm{w}}}{2} \hat{\sigma}_i^x - \hbar\delta_{\mu\mathrm{w}}\, \hat{n}_i \right) + \sum_{i,j} J_{ij} \left(\hat{\sigma}_i^- \hat{\sigma}_j^+ + \hat{\sigma}_i^+ \hat{\sigma}_j^- \right) \tag{5.3}$$

with $\hat{n}_i = |\uparrow\rangle_i \langle\uparrow|_i$ and, as already introduced in subsection 5.1.1,

$$J_{ij} = C_3 \left(3\cos^2\theta_{ij} - 1 \right) / \left(2R_{ij}^3 \right).$$

We first consider two atoms along the quantization axis, so $\theta_{12} = 0$ and $J_{12} > 0$.

Superradiant and subradiant states Figure 5.3(a) shows the energy diagram of the four two-atom states $|\downarrow\downarrow\rangle$, $|\uparrow\downarrow\rangle$, $|\downarrow\uparrow\rangle$ and $|\uparrow\uparrow\rangle$. The interaction lifts the degeneracy

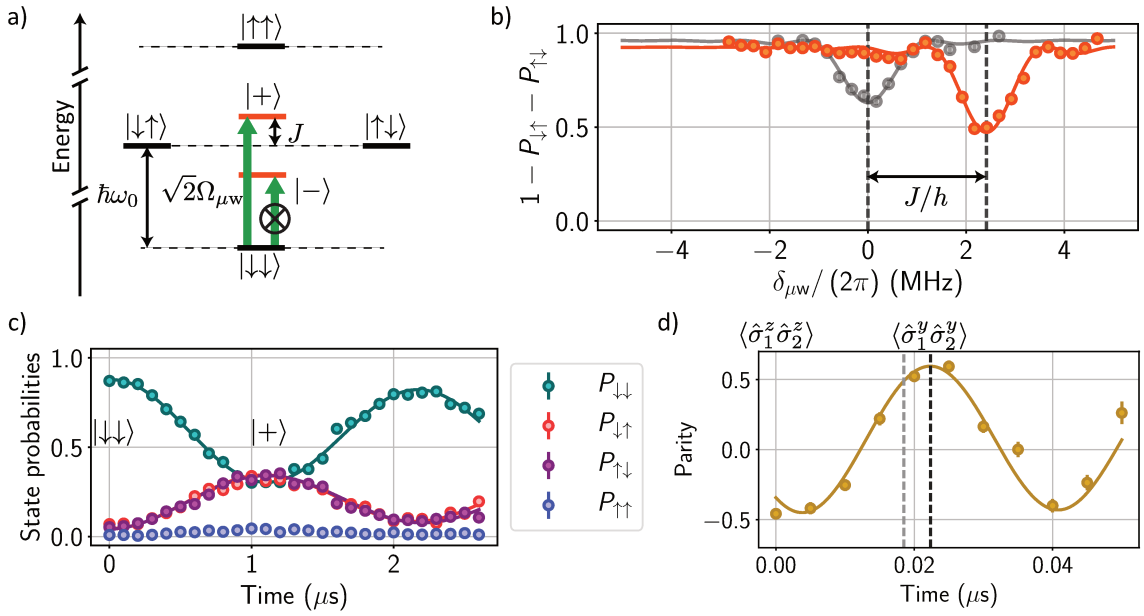

Figure 5.3: Two atoms interacting in the XY Hamiltonian. (a) Energy diagram of the four eigenstates. The state $|+\rangle$ is superradiant whereas $|-\rangle$ is subradiant, hence an enhanced coupling to $|+\rangle$ and a cancelled coupling to $|-\rangle$. (b) Spectroscopy of the single-excitation line (orange), to be compared to the single-atom spectroscopy (grey). The solid lines are spectrum fits (Rabi formula corresponding to a fixed excitation time and a varying detuning), to extract the position of the lines. (c) Rabi oscillation between $|\downarrow\downarrow\rangle$ and $|+\rangle$. Solid lines are fitting damped sine functions to extract the Rabi frequency. (d) Parity oscillation. The solid line is a fitting sine to take into account the time offset due to finite rise and fall times of the microwave rotation pulse.

between $|\uparrow\downarrow\rangle$ and $|\downarrow\uparrow\rangle$, leading to two eigenstates $|+\rangle$ and $|-\rangle$, respectively the symmetric and antisymmetric superposition of $|\uparrow\downarrow\rangle$ and $|\downarrow\uparrow\rangle$. The symmetric state is lifted by J_{12} so corresponds to a higher energy, whereas the antisymmetric state is lifted by $-J_{12}$. These states are written

$$|+\rangle = \frac{|\downarrow\uparrow\rangle + |\uparrow\downarrow\rangle}{\sqrt{2}} \quad \text{and} \quad |-\rangle = \frac{|\downarrow\uparrow\rangle - |\uparrow\downarrow\rangle}{\sqrt{2}}.$$

As $|+\rangle$ is a symmetric superposition, its coupling by a microwave field to $|\downarrow\downarrow\rangle$ or to $|\uparrow\uparrow\rangle$ is enhanced by a factor $\sqrt{2}$. On the contrary, the coupling from $|-\rangle$ to $|\downarrow\downarrow\rangle$ or $|\uparrow\uparrow\rangle$ is cancelled. This enhancement or decrease of the field coupling for collective excited states is called, respectively, superradiance and subradiance. These concepts were originally introduced to describe the spontaneous light emission from these collective excited states [Dicke, 1954], which is not the topic of our study. Rather than their

emission, we are interested here in their coupling to the external field. Nevertheless, I will use the words superradiant and subradiant to refer to these symmetric and antisymmetric superpositions in the following of this manuscript. These two kinds of symmetric and antisymmetric states are also known as bright and dark states in the context of adiabatic passage and state preparation protocol.

Now, I discuss the spin-spin correlations of the states $|+\rangle$ and $|-\rangle$. They both are antiferromagnetic along z as $\langle +|\,\hat{\sigma}_1^z\hat{\sigma}_2^z\,|+\rangle = \langle -|\,\hat{\sigma}_1^z\hat{\sigma}_2^z\,|-\rangle = -1$. On the contrary, along y , $|+\rangle$ is a ferromagnet whereas $|-\rangle$ is an antiferromagnet. Indeed, $\langle +|\,\hat{\sigma}_1^y\hat{\sigma}_2^y\,|+\rangle = 1$ and $\langle -|\,\hat{\sigma}_1^y\hat{\sigma}_2^y\,|-\rangle = -1$. Since this is true for any other spin component within the equatorial plane of the Bloch sphere, $|+\rangle$ is called an XY ferromagnet and $|-\rangle$ an XY antiferromagnet.

Instead of calculating the average of $\hat{\sigma}_1^y\hat{\sigma}_2^y$, we can see the ferro- or antiferromagnetic feature by rewriting $|+\rangle$ and $|-\rangle$ in the eigen-basis of $\hat{\sigma}^y$, defined as $|{\rightarrow}\rangle = (|{\uparrow}\rangle + \mathrm{i}\,|{\downarrow}\rangle)/\sqrt{2}$ and $|{\leftarrow}\rangle = (|{\uparrow}\rangle - \mathrm{i}\,|{\downarrow}\rangle)/\sqrt{2}$. Then, the two eigenstates read

$$|+\rangle = \frac{|{\rightarrow\rightarrow}\rangle - |{\leftarrow\leftarrow}\rangle}{\mathrm{i}\sqrt{2}} \quad \text{and} \quad |-\rangle = \frac{|{\rightarrow\leftarrow}\rangle - |{\leftarrow\rightarrow}\rangle}{\mathrm{i}\sqrt{2}}$$

which is the equal superposition of aligned and anti-aligned spins along y.

In summary, the superradiant state, shifted in energy by $+J_{12}$, is an XY ferromagnetic state, whereas the subradiant state, shifted in energy by $-J_{12}$, is an XY antiferromagnetic state. We are going to study these phases on larger systems later in this chapter. Based on the reduced coupling to subradiant states (in the two-atom case it is even cancelled), we anticipate that it will be hard to generate XY antiferromagnetic correlations.

A two-atom XY ferromagnet I show now our characterization of the two-atom superradiant state $|+\rangle$. First, we perform a spectroscopy experiment, applying a weak microwave pulse with $\Omega_{\mu\mathrm{w}}/(2\pi) = 0.35\,\mathrm{MHz}$ during $0.75\,\mu\mathrm{s}$ for a varying detuning $\delta_{\mu\mathrm{w}}$ (orange curve in Figure 5.3(b)). The plotted quantity is $1 - P_{\downarrow\uparrow} - P_{\uparrow\downarrow}$, with P_{state} the measured probability to obtain such a two-atom state. Therefore, we look at events where only one atom is in $|{\uparrow}\rangle$, and discard double excitation events which could happen if the microwave pulse were too strong. Comparing the position of the line with that of a single atom (grey transparent curve centred at $\delta_{\mu\mathrm{w}} = 0$), we infer the interaction energy $J_{12}/h = 2.4\,\mathrm{MHz}$ for $\theta_{12} = 0$ and $R_{12} = 10\,\mu\mathrm{m}$. We cannot see any signal for negative detuning around $\delta_{\mu\mathrm{w}}/(2\pi) = -J_{12}/h$, because the coupling to the subradiant state $|-\rangle$ vanishes as previously explained.

Then, we prepare $|+\rangle$ by performing a Rabi oscillation at $\delta_{\mu w}/(2\pi) = J_{12}/h$. We do it for the same Rabi frequency $\Omega_{\mu w}/(2\pi) = 0.35\,\mathrm{MHz}$, and measure the populations in the four different two-atom states as a function of the duration of the microwave pulse (Figure 5.3(c)). The populations in $|\downarrow\downarrow\rangle$, $|\uparrow\downarrow\rangle$ and $|\downarrow\uparrow\rangle$ oscillate at around 0.5 MHz, which agrees with the expected enhancement of the Rabi coupling between $|\downarrow\downarrow\rangle$ and $|+\rangle$ by a factor $\sqrt{2}$. As we operate with a weak microwave probe, meaning $\Omega_{\mu w}/(2\pi) \ll J_{12}/h$, the excitation to $|\uparrow\uparrow\rangle$ is inhibited and its population stays close to zero. The finite contrast of the observed oscillations is due to the detection errors, and to the aforementioned imperfect initialization of all the spins of the lattice in $|\downarrow\rangle$.

I finally discuss the spin-spin correlations exhibited by the $|+\rangle$ state, prepared in about 1 μs by applying a weak microwave pulse (see Figure 5.3(c)). To measure the spin-spin correlations for different spin components, we apply on the $|+\rangle$ state a strong microwave pulse $\Omega_{\mu w}/(2\pi) = 13.6\,\mathrm{MHz}$ at the single-atom resonance $\delta_{\mu w} = 0$ for a varying duration $t_{\mu w}$. This strong microwave pulse at resonance rotates all the spins by an angle $\alpha = \Omega_{\mu w} t_{\mu w}$ around the x axis, as introduced in Figure 5.2(c). We write this global rotation operator $\hat{R}(\alpha)$. The spin-spin correlations of the rotated state $\hat{R}(\alpha)|+\rangle$ along the vertical measurement axis are given by $\langle +|\hat{R}^{\dagger}(\alpha)\hat{\sigma}_1^z\hat{\sigma}_2^z\hat{R}(\alpha)|+\rangle = P_{\downarrow\downarrow} + P_{\uparrow\uparrow} - P_{\downarrow\uparrow} - P_{\uparrow\downarrow}$, which is defined as the parity quantity. Figure 5.3(d) shows such a quantity as a function of the rotation angle α. Without applying any rotation pulse, we read the correlations along z and measure negative correlations. After a $\pi/2$ pulse of around 20 ns, we read the correlations along y and measure positive correlations. So we indeed observe on the prepared superradiant $|+\rangle$ state XY ferromagnetic correlations.

The rotation angle α is equal to the microwave pulse area. For a perfect square pulse, $\alpha = \Omega_{\mu w} t_{\mu w}$ as already introduced. But in practice, due to the finite rise and fall times, the pulse area is not proportional to its duration. These times are about 5 ns. This is why the pulse duration corresponding to a $\pi/2$-rotation, indicated by a black dashed line in Figure 5.3(d), does not correspond to the expected duration $\pi/(2\Omega_{\mu w})$, indicated by a grey dashed line. The time offset between these two durations agrees with the one obtained fitting the parity oscillation by an offset sine (solid line in Figure 5.3(d)).

To read the correlations along y, the rotating pulse must be stronger than the interaction energy to act on both atoms as if they would be non-interacting. This is why we choose for the read-out microwave pulse a Rabi frequency larger than 10 MHz. If the driving strength $\hbar\Omega_{\mu w}$ is on the same order of magnitude as the Zeeman splitting, we cannot efficiently rotate the qubit due to the additional coupling to other Zeeman states. This is the second reason why we need a high magnetic field defining

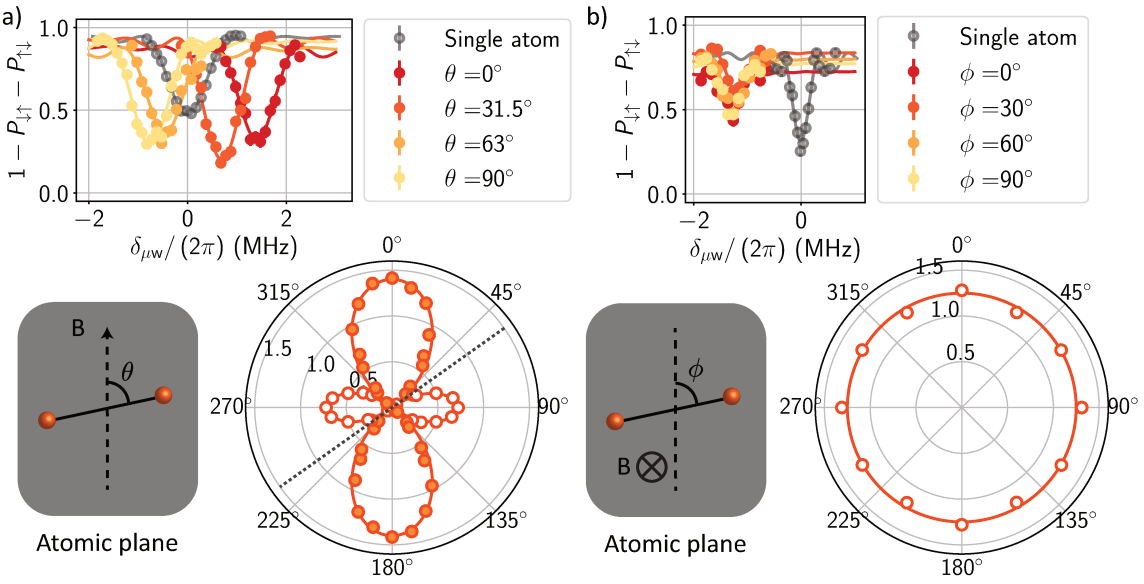

Figure 5.4: Angular dependence of the dipole-dipole interaction. (a) For a magnetic field defining the quantization axis within the atomic plane. (Top) Spectroscopy of the single-excitation line for different interaction angle θ. (Bottom) Polar plot of the interaction energy J/h as a function of θ. Filled solid circles represent positive interaction and empty solid circles negative ones. The dotted line stands for the cancellation angle of the interaction $\theta_{\mathrm{m}} = 54.7°$. The solid line is $\propto 3\cos^2\theta - 1$. (b) Same as (a) for a quantization axis perpendicular to the atomic plane. The interaction is isotropic, so the solid line on the polar plot is a simple circle.

the quantization axis. Its value of 47 G results in a Zeeman splitting for the $60P_{1/2}$ of about 44 MHz, larger than the read-out microwave Rabi frequency.

Angular dependence To finish on the two-atom case, I describe here our measurement of the angular dependence of the resonant dipole-dipole interaction. It consists in repeating the same spectroscopic experiment as the one shown in Figure 5.3(b) for various orientations of the atomic pair.

Figure 5.4(a) shows the result when the quantization axis is along the vertical axis, within the atomic plane. Here, the specific experimental parameters were $\Omega_{\mu\mathrm{w}}/(2\pi) = 0.35\,\mathrm{MHz}$, $R_{12} = 12\,\mu\mathrm{m}$ and the microwave pulse was shone for $1\,\mu\mathrm{s}$. We retrieve the typical shape of the dipole-dipole interaction as a function of the interacting angle $J_{12} \propto 3\cos^2\theta_{12} - 1$. This means that the interaction cancels out at a specific angle, called the magic angle, $\theta_{\mathrm{m}} = 54.7°$, and that it changes sign. This magic angle will allow us to build an Hamiltonian corresponding to the aforementioned Su-Schrieffer-Heeger model, as we will see in the next Section. The alternating sign of

the interaction along vertical and horizontal bonds means that we can expect on a square lattice spins ferromagnetically ordered in one direction and antiferromagnetically ordered in the orthogonal direction. This non-trivial pattern of correlations will be the topic of subsection 5.3.3.

Finally, I present the same kind of measurement for a quantization axis orthogonal to the atomic plane in Figure 5.4(b). Here, we used a microwave pulse of 2.1 μs, $\Omega_{\mu w}/(2\pi) = 0.1$ MHz, and the interatomic distance was $R_{12} = 10\,\mu$m. As expected, we find the same (negative) value for the interaction, whatever the orientation of the atomic pair. I recall that to perform this type of experiments with the quantization axis being orthogonal to the atomic array, we have first used a vertical quantization axis to optically pumped the atoms in $|g\rangle$ and then flipped the magnetic field (see Figure 2.3).

5.2 Observation of magnetization plateaus in 1D-chains

Now that I have described the physics of an XY-magnet for the simplest case of two interacting atoms, I consider the study for larger systems. A fundamental property of the XY Hamiltonian, only considering here the interacting part $\propto \hat{\sigma}_i^- \hat{\sigma}_j^+ + \hat{\sigma}_i^+ \hat{\sigma}_j^-$, is that it conserves the number of spin up $N_\uparrow$ and spin down $N_\downarrow$. In the presence of an external field, $N_\uparrow$ is still conserved for a longitudinal field but not for a transverse one.

This means that the eigenstates of the XY Hamiltonian are also eigenstates of the operator $\hat{N}_\uparrow = \sum_i |\uparrow\rangle_i \langle\uparrow|_i$, with integer eigenvalues. This has two consequences. First, for our numerical study of a N-atom system, we can divide the full Hilbert space of dimension 2^N into several Hilbert subspaces of dimension $\binom{N}{N_\uparrow}$, corresponding to integer values for $N_\uparrow$ ranging from 0 to N. This makes the numerical simulation easier. Second, preparing the different eigenstates of Hamiltonian (5.3) without any transverse field $\Omega_{\mu w} = 0$ means that we reach integer average value of $\hat{N}_\uparrow$. As the magnetization is proportional to $N_\uparrow - N_\downarrow$, we should be then able to generate states exhibiting fractional magnetization values $N_\uparrow/N$. This section aims at demonstrating this ability on different 1D systems.

We are going to reach these eigenstates corresponding to an increasing $N_\uparrow$ via a dynamical tuning of the external field, to be compared to the procedure in the previous section where we used a weak square microwave pulse. The procedure we follow here is very similar to the one presented in the previous chapter, in Figure 4.7(a), where we tried to reveal the antiferromagnetic region by measuring the Rydberg fraction after a sweep with a varying final detuning. In the context of spin-1/2 physics, the detuning

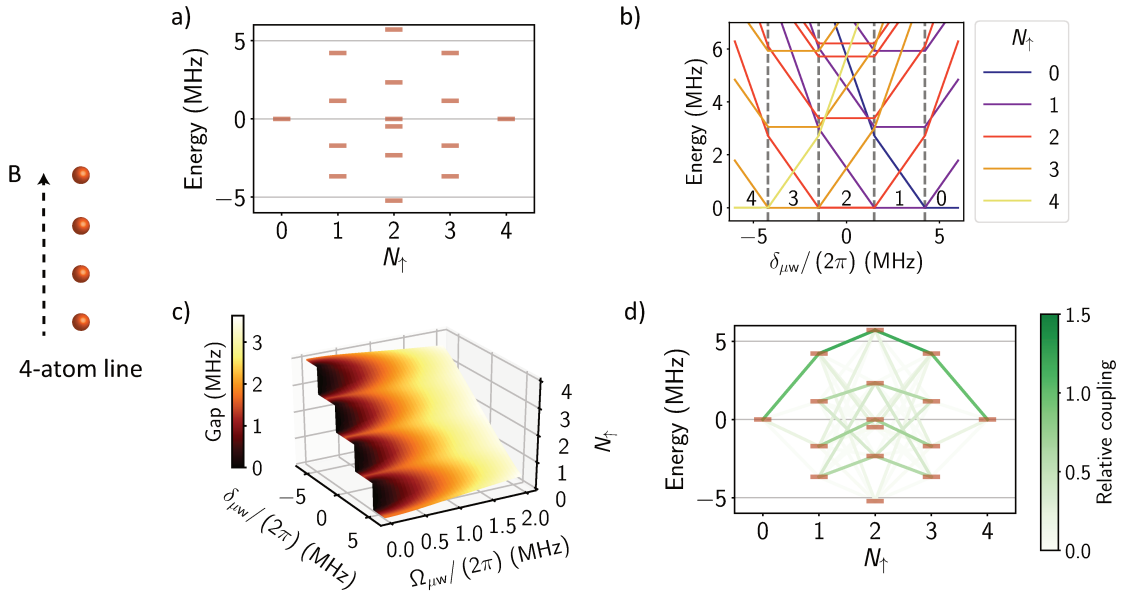

Figure 5.5: 4-atom line. (a) Many-body spectrum of Hamilonian (5.3) without any external field, as a function of the number of spins $|\uparrow\rangle$ hosted by the different eigenstates. (b) Eigen-energies of $\epsilon_0 - \hat{H}$ as a function of the detuning (there is no transverse field), where ϵ_0 is the energy of the local most excited state (see main text for details). The color encodes the value of $N_\uparrow$ and the dashed vertical lines indicate the detuning boundaries between regions corresponding to an increasing eigenvalue of $\hat{N}_\uparrow$ for the local ground state of $-\hat{H}$. (c) Number of spins $|\uparrow\rangle$ in the highest-energy state as a function of the detuning and the Rabi frequency. The color encodes the energy separation with the closest states. Dashed vertical lines indicate the detuning boundaries between regions corresponding to an increasing eigenvalue of $\hat{N}_\uparrow$ for the local ground state of $-\hat{H}$. (d) Microwave relative coupling via a transverse field between the different eigenstates.

is interpreted as an effective longitudinal magnetic field, dictating then the value of the magnetization. For the XY Hamiltonian, results can also be interpreted in the context of hard-core bosons, and the detuning is seen as a chemical potential setting the number of particles.

5.2.1 4- and 8-atom chains

I start by the study of a four-atom chain, aligned along the quantization axis and with a lattice constant $a = 10\,\mu$m. In this situation, the nearest-neighbour interaction is $J/h = 2.4\,$MHz.

Many-body spectrum Figure 5.5(a) shows the eigen-energies of the 2^4 four-atom eigenstates of Hamiltonian (5.3) for $\Omega_{\mu w} = 0$ and $\delta_{\mu w} = 0$. Due to the absence of external transverse field, we can use the aforementioned conservation of $N_\uparrow$ to sort these eigenstates by increasing $N_\uparrow$. The difference between this representation of the eigen-energies and the one in Figure 5.3(a) is that we do not see here the energy of a spin-flip $\hbar\omega_0$. In fact, Hamiltonian (5.3) is written in the rotating wave approximation for an external field $\Omega_{\mu w}$,$\delta_{\mu w}$ which means that the energy difference of a spin-flip is taken into account in the definition of the detuning. In other words, what we exactly represent here are the eigen-energies of the interacting atoms dressed by the driving microwave photons.

A striking feature of the many-body spectrum is that it is symmetric with respect to the middle column at $N_\uparrow = N/2$. This is again a characteristic feature of the XY Hamiltonian, which reflects the particle-hole symmetry in the context of hard-core bosons. Consequently, inverting all $|\uparrow\rangle$ in $|\downarrow\rangle$ and vice-versa does not modify the energy of the system.

The effect of the detuning in Hamiltonian (5.3) is to globally shift each column of Figure 5.5(a) by an amount $-N_\uparrow\hbar\delta_{\mu w}$. Therefore, depending on $\delta_{\mu w}$, the ground state of $\hat{H}$ or $-\hat{H}$ will correspond to different integer eigenvalues of $\hat{N}_\uparrow$, still without any transverse field. This is what is shown in Figure 5.5(b). I plot there the eigen-energies of $\epsilon_0\left(\delta_{\mu w}\right) - \hat{H}\left(\delta_{\mu w}\right)$, with ϵ_0 the highest eigen-energy of $\hat{H}$, as a function of the detuning. This plot is very similar to the one presented in Figure 4.5(b). The color encodes the number of spin $|\uparrow\rangle$ for the associated eigenstate. On the zero-energy line, corresponding to the energy line of the ground state of $-\hat{H}$, we see that $N_\uparrow$ grows from 0 to N when scanning the detuning from positive to negative values.

Magnetization plateaus Consequently, starting from all the atoms initialized in $|\downarrow\rangle$ and a positive detuning, we can increase $N_\uparrow$ while ramping down the detuning, following the same adiabatic protocol as in the previous chapter (more specifically Subsection 4.3.1). If the evolution were perfectly adiabatic, we should see plateaus in the measured $\left\langle \hat{N}_\uparrow \right\rangle$ when scanning the final detuning. The detuning boundaries of these plateaus are indicated by the dashed lines in Figure 5.5(b), and correspond to fractional values of the magnetization $N_\uparrow/N$ with $N_\uparrow$ ranging from 0 to N.

In order to understand better these expected plateaus, I plot in Figure 5.5(c) $\left\langle \hat{N}_\uparrow \right\rangle$ of the ground state of $-\hat{H}$ as a function of $\delta_{\mu w}$ and $\Omega_{\mu w}$. For $\Omega_{\mu w} = 0$, we indeed see the plateaus in $N_\uparrow$, and when increasing $\Omega_{\mu w}$ the steps become less and less abrupt until they are totally smoothed for $\Omega_{\mu w}/\left(2\pi\right) = 2\,\mathrm{MHz}$, i.e. when $\Omega_{\mu w}$ becomes on the

order of the interaction energy J. The colormap on the plotted surface encodes the energy gap between the ground state and the first excited state of $-\hat{H}$. When the gap vanishes, it will be harder to follow an adiabatic evolution.

Positive versus negative initial detuning Since the initial state is the product state of all atoms in $|\downarrow\rangle$, following an adiabatic evolution when starting with a large positive (negative) detuning leads to the preparation of the instantaneous ground state of $-\hat{H}$ ($\hat{H}$), as it has been already discussed in the Ising case when presenting the adiabatic preparation protocol. The highest energy state is an XY ferromagnet and the ground state is an XY antiferromagnet because $J > 0$, as expected from the two-atom study presented before. We have also seen that the coupling to XY ferromagnet is enhanced due to superradiance. We check this is still the case for the 4-atom chain. Considering two eigenstates of $\hat{H}$ with no transverse field whose numbers of spin $|\uparrow\rangle$ differ by one, $|\alpha_m\rangle$ and $|\alpha_{m+1}\rangle$, the enhancement or the inhibition of the coupling between these two states via a transverse magnetic field is $0.5\,|\langle\alpha_m|\sum_i \hat{\sigma}_i^x\,|\alpha_{m+1}\rangle|$. This quantity is the ratio between the Rabi frequency of the transition between $|\alpha_m\rangle$ and $|\alpha_{m+1}\rangle$, and the Rabi frequency in the single-particle case, for the same microwave amplitude. We call it the relative microwave coupling. Figure 5.5(d) shows such a quantity for all the possible coupling between the 2^4 eigenstates. We find again that the coupling is enhanced for higher energy states and reduced for lower energy states, which is reminiscent of the superradiance and subradiance properties discussed in the two-atom case.

As I am focused in this section on reaching a targeted value for $N_\uparrow$ whatever the nature of the correlations, we will choose an initial positive detuning to take advantage of the enhanced coupling to higher energy states.

Observation of magnetization plateaus for a 4-atom line I now report our experimental observation of the generation of states with fractional magnetization. We use the same three-step time profiles for $(\delta_{\mu w}, \Omega_{\mu w})$ as in the previous chapter. In a first set of experiments, the parameters of the sweep are: $t_{\text{rise}} = 1.2\,\mu$s, $t_{\text{sweep}} = 1.2\,\mu$s, $t_{\text{fall}} = 1.2\,\mu$s, $\delta_{\text{init}}/(2\pi) = 6.0\,$MHz, $\Omega_{\text{max}}/(2\pi) = 1.8\,$MHz and we scan the final detuning between 6 and $-6\,$MHz (Figure 5.6(a)). For each value of the final detuning, we measure the fraction of $|\uparrow\rangle$ defined as $f_\uparrow = \left\langle \hat{N}_\uparrow \right\rangle / N$, which is represented as solid disks in Figure 5.6(b). We indeed see an increase of $N_\uparrow$ when scanning the final detuning, but the expected plateaus, dotted line in the Figure corresponding to the number of $|\uparrow\rangle$ for the local ground state of $-\hat{H}$, are quite smoothed. Taking into

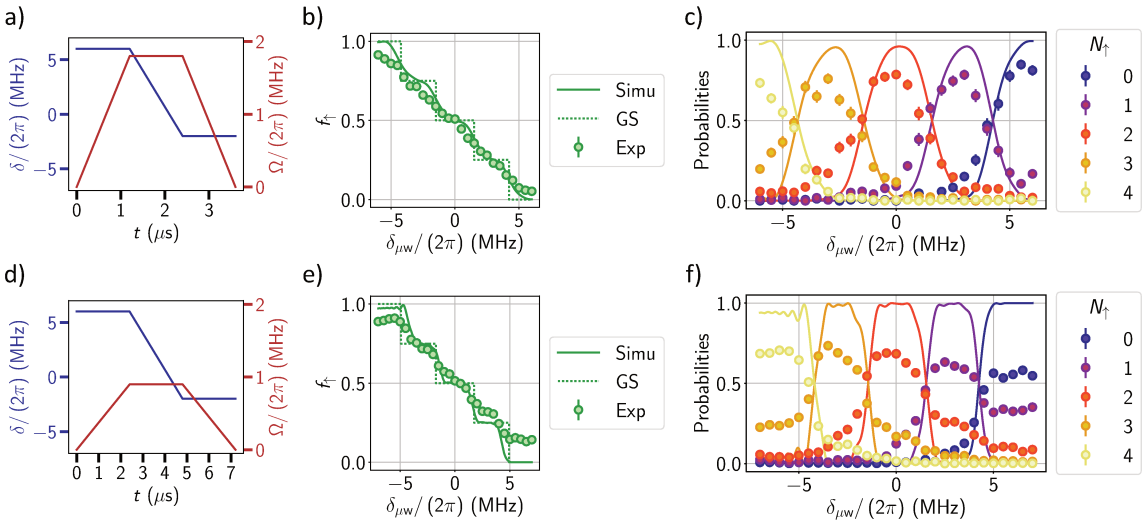

Figure 5.6: Magnetization plateaus in a 4-atom line. (a) Time profiles of the Rabi frequency and the detuning. We repeat the same sweep scanning the value of the final detuning. (b) Average probability to find the atoms in $|\uparrow\rangle$ (solid disks) as a function of the final detuning. The solid line is a simulation of $f_\uparrow$ taking into account the parameters of the sweep, and the dotted line is $f_\uparrow$ for the local ground state of $-\hat{H}$. (c) Probabilities to find a given $N_\uparrow$ as a function of the final detuning. The solid lines are here also simulations taking into account the parameters of the sweep. (d), (e) and (f) are the same as (a), (b) and (c) for a twice as small Rabi frequency and a twice as long dynamical tuning of the Hamiltonian.

account the parameters of the sweep, we compute the expected $f_\uparrow$, solid line in the figure, which is in very good agreement with the experimental data. The agreement is less good for large negative detuning, where we cannot reach the highest values for $f_\uparrow$ due to the finite STIRAP efficiency. This finite efficiency or detection errors were not taken into account in the simulation presented in this chapter.

Rather than the global average quantity $f_\uparrow$, we can also look at the probabilities to get a given number of $|\uparrow\rangle$ as a function of the final detuning (Figure 5.6(c)). The detuning regions where a specific $N_\uparrow$ is the most probable can be clearly identified and match the detuning boundaries of the expected fractional magnetization plateaus. Again, the probabilities are in a fair agreement with simulation which do not take into account preparation and detection errors (solid lines). As the transition from one plateau to the next one as a function of the final detuning is quite slow, the expected plateaus in $f_\uparrow$ are smoothed, as seen in Figure 5.6(b).

The observed smoothing of the magnetization plateaus is due to diabatic transitions when decreasing $\Omega_{\mu w}$, as in these regions the gap vanishes (see Figure 5.5(c)). In order

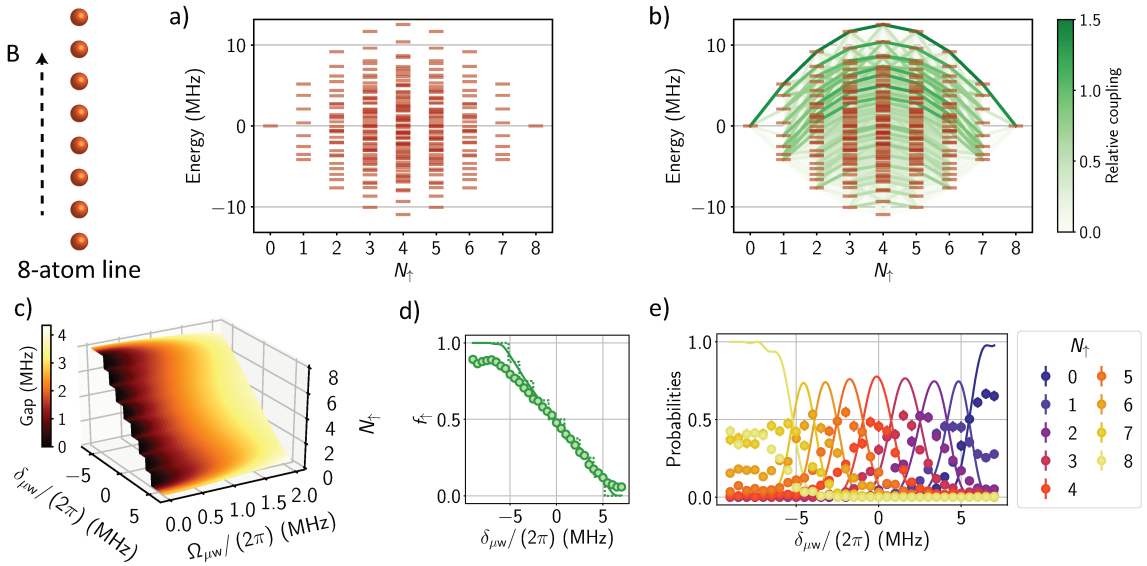

Figure 5.7: 8-atom line. (a) and (b) Many-body spectrum and relative coupling between the 2^8 eigenstates of the system. (c) Number of spins $|\uparrow\rangle$ as a function of $\delta_{\mu w}$ and $\Omega_{\mu w}$ in the many-body ground state of $-\hat{H}$. The value of the gap is encoded in the colormap. (d) and (e) Fraction $f_\uparrow$ or probabilities to find a given $N_\uparrow$ as a function of the final detuning.

to probe the regions closer to the $\Omega_{\mu w} = 0$ line, we run the same type of experiments with an Ω_{max} divided by two (Figure 5.6(d)), $\Omega_{max}/(2\pi) = 0.9\,\text{MHz}$. To keep the same effective driving time, we compensate the reduced Ω_{max} by increasing the time steps by a factor two, $t_{rise} = t_{sweep} = t_{fall} = 2.4\,\mu\text{s}$. The measured $f_\uparrow$ after such a sweep as a function of the final detuning is shown in Figure 5.6(e). Here, the staircase is more visible as compared to Figure 5.6(b), which can be also seen in the simulation taking into account these new parameters of the sweep (solid line). The agreement with the simulation is not as good for large positive detuning because the longer experimental sequence leads to an increase of the probability to lose the atoms in free flight at the end of the sequence (detection error ϵ). Measuring the probabilities to get a given $N_\uparrow$ (Figure 5.6(f)), we observe that in between the aforementioned detuning boundaries these probabilities are almost constant, which explains the plateaus in Figure 5.6(e). We also observe that when one value of $N_\uparrow$ is the most probable, the probabilities for the other values are not reduced to zero, resulting in a discrepancy with the expected value of $f_\uparrow$ for a given plateau. This is again due to an enhanced detection error ϵ.

8-atom line Let's now turn to the 8-atom case. I show as before the 2^8 eigen-energies of $\hat{H}$ for $\Omega_{\mu w} = 0$ and $\delta_{\mu w} = 0$ as a function of $N_\uparrow$ (Figure 5.7(a)). For this larger system, the coupling to higher-energy state is still enhanced (Figure 5.7(b)), this is

why we aim at reaching the ground state of $-\hat{H}$. We expect magnetizaton plateaus for the $\Omega_{\mu w} = 0$ line while scanning the detuning (Figure 5.7(c)), but the detuning boundaries between regions corresponding to different eigenvalues for $\hat{N}_\uparrow$ are closer from each other, and the gap is smaller, as compared to the 4-atom case.

Consequently, we expect that the magnetization staircase will be less visible when performing the same dynamical tuning of the Hamiltonian as we did for Figure 5.6(a). This is indeed what we see in Figure 5.7(d), where the staircase is completely smoothed. Plotting the probabilities to get a given $N_\uparrow$ (Figure 5.7(e)) reveals the successive regions where an increasing $N_\uparrow$ is the most probable state when scanning the final detuning towards negative values, but the transitions are too smooth to see marked steps.

As a conclusion, the larger the system, the more difficult the observation of magnetization plateaus, as the gap decreases with the system size. Nevertheless, for the system described in the next subsection, we will be able to observe plateaus in the evolution of $f_\uparrow$ as a function of the final detuning for an even larger system of 14 atoms.

5.2.2 Dimerized chains

I will here report the same type of experiment aiming at observing magnetization plateaus, but now in the case of an assembly of dimers, weakly coupled between each other. This interaction Hamiltonian, which we could implement using the angular dependence of the dipole-dipole interaction, is a bosonic version of the Su-Schrieffer-Heeger (SSH) model [Su, Schrieffer, and Heeger, 1979]. This model was originally developed to understand the electronic transport in polyacetylene, a macro-chain of carbon atoms with alternating double and single bonds. It has regained interest a few decades later as it is one of the simplest model exhibiting topological properties [Asbóth, Oroszlány, and Pályi, 2016].

Geometry for a dimerized chain In order to implement the SSH model, we have to use a lattice geometry alternating strong and weak coupling links. We could have used the dependence of the dipole-dipole interaction on the interatomic distance and have atomic pairs separated by larger distances. We instead use the angular dependence and work with the configurations shown in Figure 5.8(a). We alternate between pairs oriented along the quantization axis (quasi vertical link with an interaction $J/h \approx 2.4\,\mathrm{MHZ}$) and pairs nearly oriented along the horizontal (weak interaction

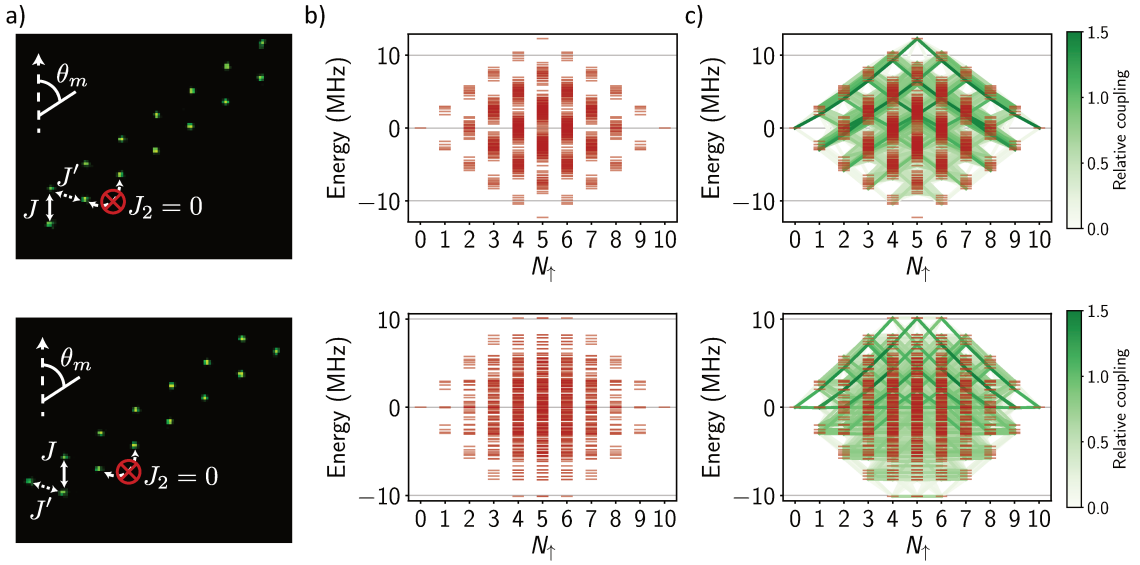

Figure 5.8: Two configurations for a dimerized chain. For the two different configurations of the SSH chain, (top) trivial and (bottom) topological, are displayed (a) single-shot fluorescence images of the atomic configurations. The strong and weak interacting links are indicated. The solid white line stands for the direction of the magic angle θ_{m}. (b) and (c) Many-body spectra and relative coupling between the different eigenstates.

$J'/h \approx -0.9\,\mathrm{MHz}$). The 14-atom chain is then divided into two sub-chains oriented along the magic angle direction θ_{m} for which the interaction cancels out. Therefore, the coupling to next-nearest neighbors is prevented ($J_2 = 0$), and we engineer a dimerized chain neglecting the coupling to third-nearest neighbor.

More precisely about the configuration we use here, as the two sub-chains are aligned along the magic angle, there is no interaction between atoms belonging to the same sub-chain. This means that the lattice can be divided into two sub-lattices, coupled to each other but without intra-coupling. This is known as a chiral, or sub-lattice, symmetry. Fundamentally, this symmetry ensures the existence of topological properties for the SSH model in the free fermion case, because it results in a symmetric many-body spectrum with respect to the zero-energy line. I will not develop this point here, and refer the interested reader to reviews about the SSH model [Asbóth, Oroszlány, and Pályi, 2016; Cooper, Dalibard, and Spielman, 2019], or to our latest publication [de Léséleuc *et al.*, 2019]. I will come back on the symmetry of the many-body spectrum with respect ot the zero-energy line, an up-down symmetry, in the end of this chapter.

Two configurations For the finite-size system we work with, two configurations are possible with an even number of atoms N. We start and end the chain either with a strong link and get seven weakly coupled dimers (top of Figure 5.8(a)), either with a weak link and get six dimers in the bulk of the chain and two half-dimers on the edges (bottom of Figure 5.8(a)). We compute the eigen-energies of Hamiltonian (5.3) without external field for these two configurations (Figure 5.8(b)), for a smaller system of 10 atoms to ease the numerical treatment. I first focus on the column $N_\uparrow = 1$. In both cases, the spectrum shows two bands shifted symmetrically from zero by an amount $\approx J$, corresponding to the binding energy of the dimers. For the configuration at the bottom, the spectrum exhibits two additional levels on the zero-energy line, whose wavefunctions squared have a maximum amplitude on the edges of the chain. These additional eigenstates at zero-energy are known as edge states, a typical signature of the topological properties of our system. Then, the configuration on top of Figure 5.8(a) is called a trivial configuration whereas the configuration at the bottom is a topological one.

We are now able to understand the many-body spectrum shown in Figure 5.8(b). For the trivial case (top), adding spin $|\uparrow\rangle$ creates bands further and further away from zero energy until we reach $N_\uparrow = N/2$ and the many-body ground state of $\hat{H}$ or $-\hat{H}$ can be seen as an assembly of dimers containing one spin $|\uparrow\rangle$ each, at a total energy $\approx \mp J \times N/2$. For the topological case (bottom), the many-body ground state has a four-fold degeneracy, corresponding to the dimers of the bulk hosting one spin $|\uparrow\rangle$ each, and the edges being spin $|\uparrow\rangle$ or $|\downarrow\rangle$ (four possibilities with $N_\uparrow = N/2 - 1$, $N_\uparrow = N/2$ (doubly degenerate) or $N_\uparrow = N/2 + 1$) as flipping spins on the edges costs zero energy. In that case, the energy of the ground state of $\hat{H}$ or $-\hat{H}$ is $\approx \mp J \times (N/2 - 1)$. As in the previous subsection, we compute the coupling between the different eigenstates of the Hamiltonian for both configurations (Figure 5.8(c)), and find that it is still enhanced towards higher energy states. We then keep focusing on the ground state of $-\hat{H}$.

Magnetization plateaus for a dimerized chain I now turn to the experimental observation of a magnetization staircase for the dimerized chain. For the trivial configuration, Figure 5.9(a) shows the expected staircase for the $\Omega_{\mu\mathrm{w}} = 0$ line. As the fractional magnetization steps from $N_\uparrow = 1$ to $N_\uparrow = N/2 - 1$ are too narrow in detuning and the gap vanishes in these regions, we will not observe these steps. On the contrary, the step at zero-magnetization $N_\uparrow = N/2$ is wider and the gap is finite, hence should be observable. This is confirmed by the experimental data (Figure 5.9(b)),

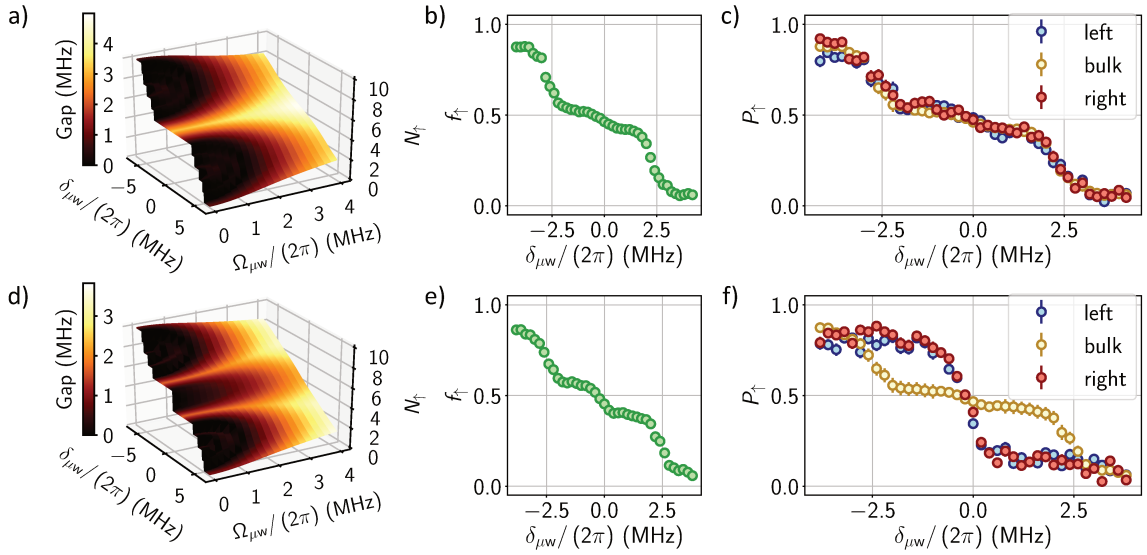

Figure 5.9: Magnetization staircase for a dimerized chain. (a) Number $N_\uparrow$ as a function of $\delta_{\mu w}$ and $\Omega_{\mu w}$ in the many-body ground state of $-\hat{H}$ for the trivial configuration. (b) Fraction of $|\uparrow\rangle$ as a function of the final detuning for the trivial configuration. (c) Probability $P_\uparrow$ to be in $|\uparrow\rangle$, distinguishing between bulk and edge sites, as a function of the final detuning for the trivial configuration. (d), (e) and (f) same as (a), (b) and (c) for the topological configuration.

where we scan the final detuning for the same sweep parameters as in Figure 5.6(a) and measure a plateau at $f_\uparrow \approx 0.5$ in a wide region around zero detuning. I also show in Figure 5.9(c) the probability $P_\uparrow$ to be in the $|\uparrow\rangle$ state distinguishing between edge and bulk sites. In the trivial configuration, these sites have the same behavior.

For the topological configuration, another behavior arises at zero detuning due to the zero-energy edge modes. The expected staircase shows two plateaus with a non vanishing gap at $N_\uparrow = N/2 \pm 1$ (Figure 5.9(d)). These two plateaus are indeed observed in our experiment (Figure 5.9(e)), and by making the distinction between edge and bulk atoms (Figure 5.9(f)), we confirm that the jump by two in the number of spin $|\uparrow\rangle$ around zero detuning is due to the flipping of the spins on the edges. Coming back to Figure 5.9(b), the slight increase around zero detuning for the trivial configuration is due to lattice defects. Indeed, if one atom in the bulk is not initialized in $|\downarrow\rangle$, the total chain can be considered for this experimental realization as two smaller chains. One of the two atoms in the bulk close to the defect will be then on the edge of a smaller chain, and only weakly coupled to it. Consequently, for this peculiar situation in the presence of a near-by defect, this atom will experience a spin-flip around zero detuning. As this is occurring only in the limited presence of defects (about 10%

probability), there is only a slight increase at zero detuning.

To conclude, the specific geometry adopted here (dimerization) leads to many-body ground states with a non-vanishing gap, which enables the preparation of these states even for a relatively high number of spins, namely $N = 14$.

5.3 Generation of correlated-spin states

In the previous chapter, to get more insight on the antiferromagnetic phase we were aiming at generating, we focused on the spin-spin correlations using our site-resolved fluorescence imaging. Following the same approach, I report here our observation of the correlations obtained for the 1D systems already presented, and finally for a 4×4 square array. I recall the definition of the spin-spin connected correlation function between sites i and j ($i \neq j$)

$$C_{i,j} = 4 \times \left(\langle \hat{n}_i \hat{n}_j \rangle - \langle \hat{n}_i \rangle \langle \hat{n}_j \rangle \right)$$

with $\hat{n}_i = |\uparrow\rangle_i \langle\uparrow|_i$. Without any further operations, we measure the correlations of the spin component along the quantization axis z. Applying an additional global microwave pulse to rotate the measurement basis, we have access to correlations for the other spin components.

5.3.1 Assembly of two-spin ferromagnets in a dimerized chain

I first focus on the dimerized chain in the topological configuration. We are interested in the many-body ground state of $-\hat{H}$, corresponding to a bulk with a zero magnetization (one $|\uparrow\rangle$ per dimer). We target the plateau at $N_\uparrow = N/2 - 1$, so we use the same sweep parameters as in Figure 5.6(a) with a final detuning $\delta_{\text{final}}/(2\pi) = 1.0\,\text{MHz}$.

Figure 5.10(a) shows the correlations along the quantization axis. We measure large intra-dimer negative correlations, as the one we were observing for the two-atom case. We apply a strong microwave pulse to rotate the measurement basis, and measure the intra-dimer correlation as a function of the rotating time (Figure 5.10(b)). This result is very similar to the parity quantity we plotted in Figure 5.3(d). After a strong $\pi/2$-pulse, so for about 20 ns, we measure positive intra-dimer correlations along y. This is the case for all the dimers of the chain, as shown by Figure 5.10(c), representing the correlations along y between all the spins of the chain.

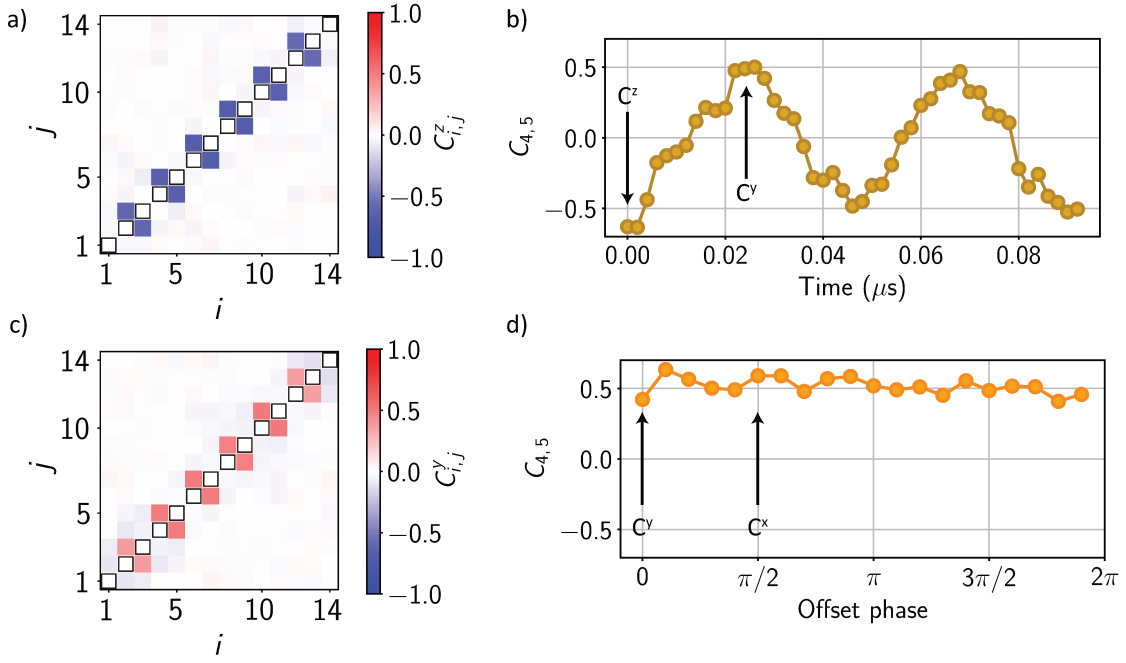

Figure 5.10: Spin-spin correlations on a dimer. (a) Correlations along z for the topological configuration. (b) Correlator between site 4 and site 5 as a function of the duration of the rotating pulse. (c) Correlations along y for the topological configuration. (d) Correlator between site 4 and site 5 for different spin components within the equatorial plane of the Bloch sphere (so as a function of the phase offset of the rotating pulse).

Comparing Figure 5.10(a) and (c), correlations along z have a shorter range than the one along y (or any spin components within the equatorial plane). This is a very general property of correlations appearing in the XY Hamiltonian [Luther and Peschel, 1975]. Another already mentioned property is experimentally demonstrated in Figure 5.10(d). I plot there the measured intra-dimer correlation after a $\pi/2$-rotating-pulse as a function of the phase offset of this read-out pulse. We measure then the intra-dimer correlations scanning the spin components within the equatorial plane, and confirm that in the XY model they are equal no matter the spin projection within the equatorial plane.

The results presented here are very similar to the ones presented in the two-atom case, subsection 5.1.3, here extended to an assembly of dimers: starting with a positive detuning, we generate antiferromagnets along z and XY ferromagnets on each dimer.

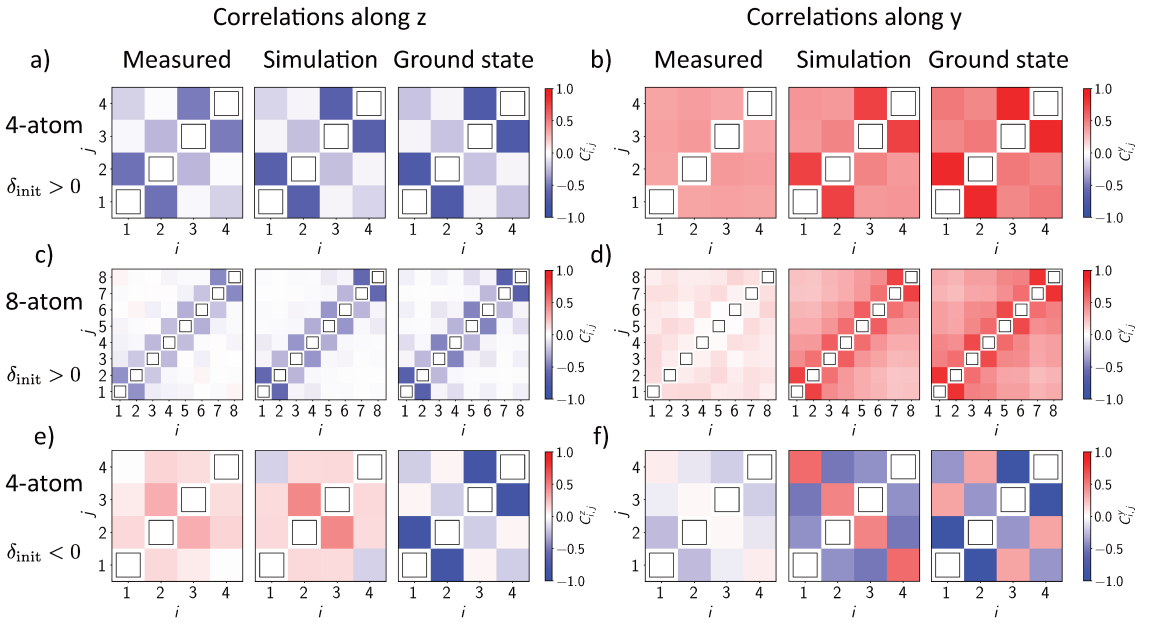

Figure 5.11: Correlations in 1D-systems. For all the correlations plotted here, I show from left to right the measured correlations, the simulated ones taking into account the parameters of the sweep, and the ones we would obtain for the ground state of $\hat{H}$ or $-\hat{H}$. (a) Correlation along z for a 4-atom line starting with a positive detuning. (b) Correlations along y for the same system and sweep. (c) and (d) Correlations along z and y for an 8-atom line starting with a positive detuning. (e) and (f) Correlations along z and y for a 4-atom line starting with a negative detuning.

5.3.2 1D ferromagnets

I now describe the observed correlations for the two remaining 1D systems presented in this chapter, the 4- and 8-atom lines with regular spacing. For these two geometries, the many-body spectra show that the ground states of $\hat{H}$ or $-\hat{H}$ without external field correspond to $N_\uparrow = N/2$, so I will present the measured correlations after the sweep plotted in Figure 5.6(a) with a final detuning $\delta_{\text{final}} = 0$.

XY-ferromagnet I start with the 4-atom case and a positive initial detuning, $\delta_{\text{init}}/(2\pi) = 6.0\,\text{MHz}$. Figure 5.11(a) shows short-range antiferromagnetic correlations along z and Figure 5.11(b) longer-range ferromagnetic correlations along y, as we were expecting with a positive initial detuning. In order to get more quantitative, I compare the measured correlations (left panel) to the calculated ones taking into account the parameters of the sweep (middle panel) and the ones we would obtain if we had prepared the ground state of $-\hat{H}$ (right panel). For both correlations on z

and y, the middle and right panels are quite similar, meaning that the dynamical tuning of the external field is slow enough to follow an adiabatic evolution. Comparing now to the measured correlations, the experimental data is in a good agreement for correlations along z and in a qualitative agreement for correlations along y. Indeed, along y, we should have measured a decay as a function of the distance between correlated spins, and we rather measure quasi homogeneous correlations.

We draw the same kind of conclusion for the 8-atom line with an initial positive detuning. We observe short-ranged antiferromagnetic correlations along z (Figure 5.11(c)) and longer-range ferromagnetic correlations along y (Figure 5.11(d)). As before, the main discrepancy between the measured correlations and the calculated ones is in the case of correlations along y. This could be due to some imperfections in our rotation process of the measurement basis, and is a call for future investigations.

XY antiferromagnet Finally, we tried to generate an XY antiferromagnet on the 4-atom line. For this, we revert the sign of the detuning and start with $\delta_{\text{init}}/(2\pi) = -6.0\,\text{MHz}$ in order to reach the lowest energy state of the many-body spectrum. Figure 5.11(e) shows the correlations along z and Figure 5.11(f) the ones along y. The measured correlations agree with the calculated ones taking into account the parameters of the sweep, they have the same sign with a reduced contrast. The most striking difference is between the calculated correlations and the ones of the ground state of $\hat{H}$, the correlations of an XY antiferromagnet. Indeed, the calculated correlations do not have the expected sign, which means that our sweep is not slow enough to reach adiabatically the ground state of $\hat{H}$.

We were expecting this after computing the coupling between the different eigenstates via a transverse field (Figure 5.5(d)). As the coupling towards lower-energy states is very weak, its adiabatic preparation requires large amounts of time. In order to see correlations with the expected sign, I numerically found that we must follow the same sweep as in Figure 5.6(a) but multiplying the durations by at least a factor 40. I did not scan the other parameters of the sweep, so a shorter sweep may exist to reach the antiferromagnet. Nevertheless, our first trial and failure to reach the antiferromagnet confirms that these states are way more difficult to prepare, due to their intrinsic subradiant nature, resulting in a reduced coupling.

We have not tried experimentally to reach the XY antiferromagnet for the 8-atom line, as we expect to face the same difficulties. Actually, it should be even more difficult for the 8-atom line because the gaps are smaller in that case.

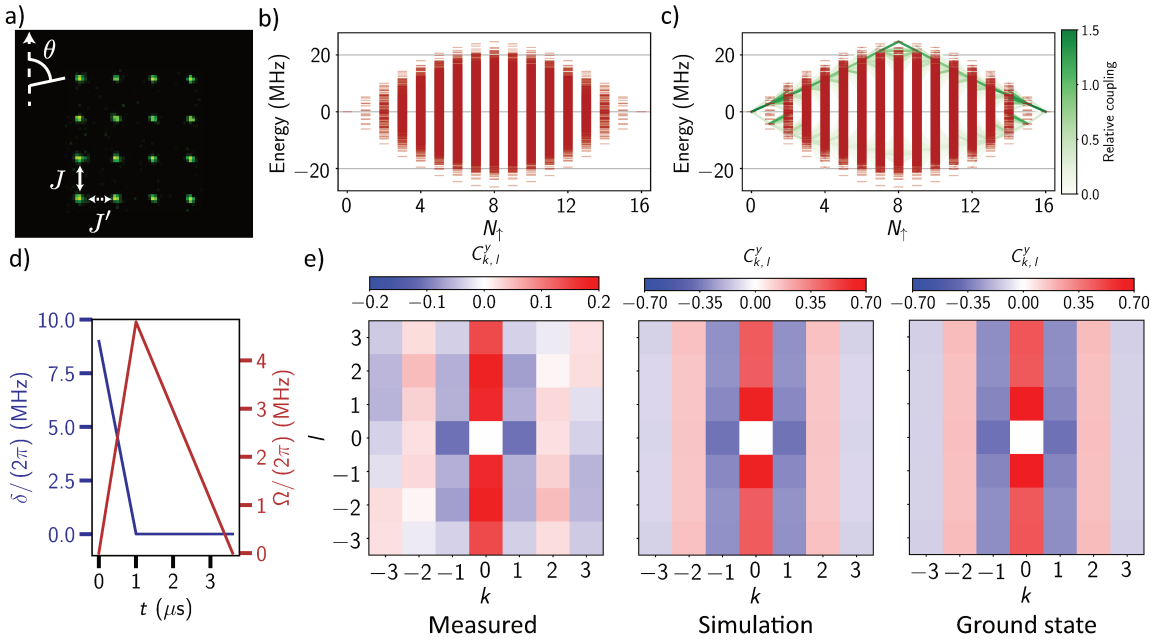

Figure 5.12: Stripy order. (a) Single-shot fluorescence image of a 4×4 atomic array. The quantization axis is within the atomic plane, and we have two different nearest-neighbour interaction energies, J and J'. (b) and (c) many-body spectrum and strongest coupling paths towards higher- and lower-energy states. (d) Time profiles of $\delta_{\mu\mathrm{w}}$ and $\Omega_{\mu\mathrm{w}}$ used to observe the stripy order. (e) Measured correlations along y, compared with the simulated ones and the ones of the ground state of $-\hat{H}$.

5.3.3 Stripy order in a 4×4 array

Finally, I explore in this subsection a 2D geometry, more precisely a 4×4 square array. First, the magnetic field is within the atomic plane, and we have a strong positive interaction along the vertical, $J/h = 2.4\,\mathrm{MHz}$, and a smaller negative interaction along the horizontal, $J'/h = -1.2\,\mathrm{MHz}$ (Figure 5.12(a)). Figure 5.12(b) shows the eigen-energies of the 2^{16} eigenstates, as a function of $N_\uparrow$. For the coupling, I did not compute it between all the eigenstates, as it is too demanding a numerical task, but only computed the strongest coupling path toward states with higher or lower energies (Figure 5.12(c)). As a strong coupling path exists toward the state with the highest energy, the ground state of $-\hat{H}$, we are going to try to reach it, so we will start with a positive detuning.

Observation of a stripy order As the vertical interaction is positive, we expect that the ground state of $-\hat{H}$ is a ferromagnet along the vertical direction. On the contrary, the horizontal interaction being negative, we expect the ground state of $-\hat{H}$ to be an

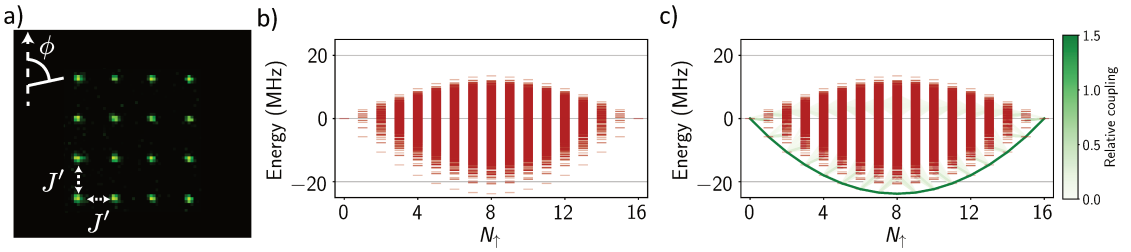

Figure 5.13: Isotropic case. (a) Single-shot fluorescence image of 4×4 array with a quantization axis orthogonal to the atomic plane. In that case, the interaction J' is the same for all the directions in the atomic plane. (b) and (c) Many-body spectrum and strongest coupling paths towards higher- and lower-energy states with isotropic interaction.

antiferromagnet along the horizontal direction. In the end, the ground state of $-\hat{H}$ is composed of vertical stripes of spins aligned in the same direction in the XY plane, and these stripes are anti-aligned with respect to their neighbours, hence the name of stripy order we expect to observe. As the ferromagnetic interaction is stronger than the antiferromagnetic one, the coupling towards this state is enhanced and we can try to reach it.

The time profiles we use for this observation are plotted in Figure 5.12(d). It is a bit different than the ones previously shown, as we combine the rise and sweep steps into a single one. We start with a positive initial detuning of 9.0 MHz and simultaneously ramp down the detuning to 0 and rise the Rabi frequency to 4.8 MHz in 1 μs. We then gradually switch off the Rabi frequency while staying at 0 detuning in 2.6 μs. Figure 5.12(e) shows the measured correlations along y, to be compared with the calculated ones and the ones of the ground state of $-\hat{H}$. For the 2D geometry presented here, we average on all the correlations $C_{i,j}$ corresponding to atomic pairs whose separation is a vector of indexes k, l, as we did in the previous chapter.

We observe a stripy order, in qualitative agreement with the calculated correlations (we almost have the expected sign for all correlations). The calculated correlations and the ones of the ground state are very similar, which means that the chosen durations are large enough to adiabatically reach the XY stripy-ordered structure.

Isotropic case We now work with a magnetic field perpendicular to the atomic plane, so that the interaction is isotropic $J'/h = -1.2$ MHz (Figure 5.13(a)). I show in Figure 5.13(b) and (c) the many-body spectrum and the strongest coupling toward the higher and lower energy states. Here the interaction is negative, so the antiferromagnetic state is the highest energy state. But as in the 1D case, the reduced coupling due

to the subradiant nature of the XY antiferromagnet prevents us to reach it within the accessible time-scale of our experiment, so we have not tried experimentally to generate it. We have not tried either to generate the XY ferromagnet starting with a negative detuning, but in that case we expect to succeed thanks to the enhanced coupling towards this state.

An up-down symmetry So far, I have discussed about the particle-hole symmetry, resulting in a left-right symmetry of the many-body spectrum with respect to the middle column at $N_\uparrow = N/2$. I now discuss about a symmetry with respect to the zero-energy line, an up-down symmetry. In the case of the dimerized chain, I mentioned the sub-lattice symmetry, existing in the peculiar geometry used there because the lattice can be divided into two sub-lattices, the two parallel sub-chains, with no interaction within a sub-chain. A known consequence of the sub-lattice symmetry is this up-down symmetry of the eigen-energies with respect to the zero-energy line.

For the other systems presented in this chapter, as the interaction between next-nearest neighbours is not negligible due to the long range of the dipole-dipole interaction, we cannot operate such a partition into two sub-lattices. As a consequence, the many-body spectra are not symmetric with respect to zero. The difference between the positive eigen-energies and the negative ones is the most important for the square with isotropic interaction, as in that case the number of next-nearest neighbours increases. If we had interaction only between nearest neighbours, the interaction Hamiltonian would respect the sub-lattice symmetry, where a sub-lattice is obtained by taking one site every second lattice site. For the square with the anisotropic interaction, as the link to the next-nearest neighbour is oriented along the 45° line, close to the magic angle, this interaction is very weak. Therefore, we expect a reduced up-down asymmetry in the many-body spectra, which is confirmed by the computation (Figure 5.12(b)).

Finally, I comment on which direction the eigen-energies are shifted due to the long-range interaction, considering the simplest system of three spins on a line. If the two first spins are aligned in the equatorial plane, in an XY ferromagnetic order, aligning the third spin with the two others will fulfil the two-spin ferromagnetic condition at the nearest-neighbour and the next-nearest-neighbour levels. If the two first spins are anti-aligned, in an XY antiferromagnet, anti-aligning the third spin with the second one will fulfil the two-spin antiferromagnetic condition at the nearest-neighbour level, but it cannot simultaneously fulfil it at the next-nearest-neighbour level. This means that ferromagnetic states are shifted further than the zero-energy line and antiferromagnetic states are shifted closer, as compared to the spectrum

giving by nearest-neighbour interaction only. Consequently, the density of states is bigger in the antiferromagnetic band, leading to reduced energy gaps and a more difficult preparation to generate these states. These reduced gaps mean that the states may be almost degenerate, which can be considered as frustration, here due to the longer range of the interaction (see an example with ions [Islam *et al.*, 2013]).

5.4 Conclusion

In this chapter, I have demonstrated our ability to reach targeted many-body ground states of the XY Hamiltonian, for different geometries, if the coupling via a transverse field from the initial trivial product state towards the targeted state was not reduced. The generated states show the expected properties, in terms of number of spin $|\uparrow\rangle$ where we were able to observe magnetization staircases, or spin-spin correlations. I have also explained why we were able to generate these states by a numerical study, computing the gaps and the coupling via a transverse field. As the coupling to ferromagnetic states is enhanced due to the superradiant nature of these states, we mostly observed XY ferromagnets. The only possibility to observe antiferromagnetic correlations was to study an hybrid system of antiferromagnetic and ferromagnetic links, exhibiting a stripy order, where we took advantage of its dominant ferromagnetic nature to have an enhanced coupling to reach it.

In the introduction to this chapter, I made a difference between the eigenstates of the XY Hamiltonian and the ones of the Ising Hamiltonian, in the absence of a transverse field. They are entangled states in the XY case whereas they are classical product states in the Ising case. In fact, in the presence of an external transverse field, the eigenstates of the Ising Hamiltonian are also entangled. This is why some groups have been able to observe entanglement using the Rydberg blockade [Wilk *et al.*, 2010; Isenhower *et al.*, 2010]. We can then write, for the Ising Hamiltonian also, the eigenstates as symmetric or antisymmetric, superradiant or subradiant, superposition of classical product states. For this Hamiltonian, we were only interested in the correlations along the quantization axis z, and both symmetric and antisymmetric superpositions show antiferromagnetic correlations along this axis. So the fact that we can more easily prepare the symmetric superposition did not prevent us to observe antiferromagnetic correlations in the previous chapter. Moreover, in the Ising case, the symmetric and antisymmetric superposition are degenerate, so it does not modify the many-body spectrum, this is why I did not describe this superposition feature at that time. On the contrary, the observation of antiferromagnets is more difficult for the XY

Hamiltonian because these states have subradiant properties only in that case.

Therefore, depending on the many-body states of the XY Hamiltonian we want to study in the future, we shall rely on different approaches. If we study XY ferromagnets, or more generally states with an enhanced coupling via a transverse field, the approach consisting in a dynamical tuning of the parameters, described in this chapter, will still be valid. Otherwise, for XY antiferromagnets, we should either try some more involved dynamical tuning, developed in the optimal control context [Caneva, Calarco, and Montangero, 2011], either engineer a more elaborate product state composed of $|\uparrow\rangle$ and $|\downarrow\rangle$ by locally flipping some of the spins [de Léséleuc *et al.*, 2017] (I will show such a local spin-flip procedure in the next chapter). As this product state is not an eigenstate of the Hamiltonian, it will evolve and studying its dynamics could reveal some interesting out-of-equilibrium physics, such as many-body localization.

Part III.

Towards 2D topological matter

Chapter 6

Emergent gauge fields for Rydberg atoms

Contents

In this last part of the manuscript, we will still study the exchange Hamiltonian between Rydberg atoms (see Equation 5.1), which implements the XY spin model as we have seen in the previous chapter, but considering an additional Zeeman level and other complex-valued exchange terms. The aim of this chapter is to show that, under this consideration, our system can lead to the engineering of topological matter.

One of the signatures of topological matter for finite-sized system is the existence of chiral edge modes, characterized by the circular motion of the particle along the edges of the system, in a preferential direction. The systems hosting chiral edge modes

are called topological insulators, as they are conducting on the edges but insulating in the bulk. They have emerged as a new phase of matter about twenty years ago, and triggered a lot of interest due to their unique transport properties [Moore, 2010; Wang, Dou, and Zhang, 2010].

In order to study these propagation features on our Rydberg-based platform, we need to prepare a localized excitation, meaning we need to change the state of one of the atoms, and this excitation will hop to neighbouring lattice sites with a hopping amplitude between two sites given by the dipole-dipole interaction strength between the two Rydberg atoms. This is a different approach than the one used in the previous chapter. There, we were aiming at preparing the ground state of the Hamiltonian. Here, we prepare a localized excitation, which is not an eigenstate of the system, and see how it propagates. We will use then, for convenience, the framework of hard-core bosons rather than the one of spin-1/2 for this study, the connection between these two pictures having already been made (Chapter 5).

The single-particle transport properties of the system can be expected from the study of its band structure (eigen-energies as a function of the wave vectors of the eigenstates). Indeed, if this diagram exhibits a linear behaviour, associated with a finite group velocity (defined as the derivative of the energy with respect to the wave vector), we expect some propagating modes. We can also extract from the band structure the integrals of the Berry curvature for each band, called the Chern numbers. The Chern numbers are topological invariants. If they are different from zero, the system shows topological properties. Having a non-zero Chern number for an infinite lattice and observing chiral edge modes on a finite-sized system is equivalent. This is known as the bulk-edge correspondence, explaining why observing chiral edge modes is a signature of the topological properties of a system.

One way to engineer such topological band structures is to break the time-reversal symmetry, by implementing some complex hopping amplitude. This is for example the mechanism at play in the Haldane model [Haldane, 1988], experimentally realized with ultracold fermions in an optical lattice [Jotzu *et al.*, 2014]. In this model, the coupling to next-nearest neighbours in a honeycomb lattice are complex-valued.

Implementing complex hopping amplitudes also leads to artificial gauge fields [Jaksch and Zoller, 2003; Goldman, Beugnon, and Gerbier, 2012; Goldman *et al.*, 2014], acting on the motion of the particle. This type of field is a way to mimic the effect of a magnetic field, whereas the particle is not carrying any charge. The link between complex hopping amplitudes and artificial magnetic fields may be understood as an analogue to the Aharonov-Bohm effect [Aharonov and Bohm, 1959]. While the particle

is hopping between lattice sites, a phase, sometimes referred to as the Peierls phase, is imprinted on the particle wavefunction. Then, a particle circulating around a lattice plaquette will acquire a phase proportional to the magnetic flux enclosed by this plaquette. Such complex hopping amplitudes have successfully been implemented on different platforms : among others for ultracold atoms, by using laser-assisted tunnelling in an optical superlattice [Aidelsburger *et al.*, 2011], by periodically driving an optical lattice [Struck *et al.*, 2012], or by using synthetic dimensions and Raman transitions [Mancini *et al.*, 2015; Stuhl *et al.*, 2015]; and for supraconducting qubits, by modulating the coupling strength [Roushan *et al.*, 2017a].

So far, the dipole-dipole coupling strength described in this manuscript was real. To implement complex hopping amplitudes with Rydberg atoms, it has been proposed to use additional terms of the dipole-dipole interaction [Peter *et al.*, 2015; Kiffner, O'Brien, and Jaksch, 2017; Weber *et al.*, 2018], which are non-zero when the quantization axis is perpendicular to the atomic array [1]. Considering a nS level as being a vacant site and a nP level as being a site occupied by one particle, these additional exchange terms change the Zeeman level of the nP excitation while it is hopping between lattice sites, and then involve a second nP level. The two nP levels can be interpreted as the two spin states of the effective particle. This spin-flip hopping is associated to an orbital phase factor, giving rise to the targeted complex hopping amplitude. As this hopping process involves both a spin-flip and an orbital phase factor, it can be seen as an intrinsic spin-orbit coupling.

In this chapter, I will show how this intrinsic spin-orbit coupling can lead to the observation of chiral edge states. I will first describe in more details the different hopping processes at the two-particle level (Section 6.1). Then, I will explain how it results in some topological features for a system of Rydberg atoms in a honeycomb lattice (Section 6.2). Finally, I will report our first experimental observations of the effect of the implemented complex hopping amplitudes on a minimal system of three atoms (Section 6.3). The study described in this chapter corresponds to the ongoing work performed in the lab during the completion of this manuscript, so the experimental results presented here are preliminary. The theoretical work was realized by our collaborators in Stuttgart [Weber *et al.*, 2018].

Most of the discussions in this chapter concern the single-particle regime, and I will comment on the many-body regime only in Subsection 6.3.3.

[1] They are the terms on the third line of Equation (5.1)

6.1 Hopping processes in an extended Zeeman structure

Here, I describe in more details the three Rydberg states and the dipole-dipole exchange terms involved in view of implementing complex hopping amplitudes. Using an additional Rydberg level, we operate in an extended Zeeman manifold, and I will show the microwave control of the Rydberg state in that case (as compared to Subsection 5.1.2 where only two levels were involved). Then, I will explain why an electric field is needed to implement the Hamiltonian of interest. I will present in the following how we prepare a localized excitation among the Rydberg atoms, which is the necessary step to study the propagation of a particle on a lattice. Finally, I will show the calibration of the hopping amplitude, by observing the spin-exchange process in the minimal case of two interacting atoms.

6.1.1 Dipole-dipole interaction and spin-orbit coupling

As stated at the beginning of this chapter, the required additional exchange terms to implement complex hopping amplitudes are non-zero when the quantization axis is perpendicular to the atomic plane. Therefore, we set for this chapter the magnetic field defining the quantization axis along the x axis (aspheric lenses axis), i.e perpendicular to the atomic plane. In that case, $\theta = 0$ (see Equation (5.1)), and the dipole-dipole interaction reads

$$\hat{V}_{\text{ddi}} = \frac{1}{4\pi\epsilon_0 R_{ij}^3}\left[\hat{d}_i^0\hat{d}_j^0 + \frac{1}{2}\left(\hat{d}_i^+\hat{d}_j^- + \hat{d}_i^-\hat{d}_j^+\right) - \frac{3}{2}\left(\mathrm{e}^{-2\mathrm{i}\phi_{ij}}\hat{d}_i^+\hat{d}_j^+ + \mathrm{e}^{2\mathrm{i}\phi_{ij}}\hat{d}_i^-\hat{d}_j^-\right)\right]. \quad (6.1)$$

The expression of the dipole-dipole interaction is displayed on the top of Figure 6.1. The ϕ angle appearing in Equation (6.1) is the one between the interatomic axis and a reference axis in the yz plane. This reference axis is set arbitrarily, so the absolute value of ϕ does not have any physical meaning. In particular, in the two-atom case, the internuclear axis can be chosen as the angle reference, and $\phi = 0$ or $\phi = \pi$. Therefore, we need at least three atoms not on the same line to have some complex amplitude in Equation (6.1). We choose the y axis as the reference axis, and ϕ is positive in the anti-clockwise orientation.

The exchange terms featuring complex amplitudes (framed in green in Figure 6.1) change the total magnetic number of the two-atom system. Therefore, they must involve

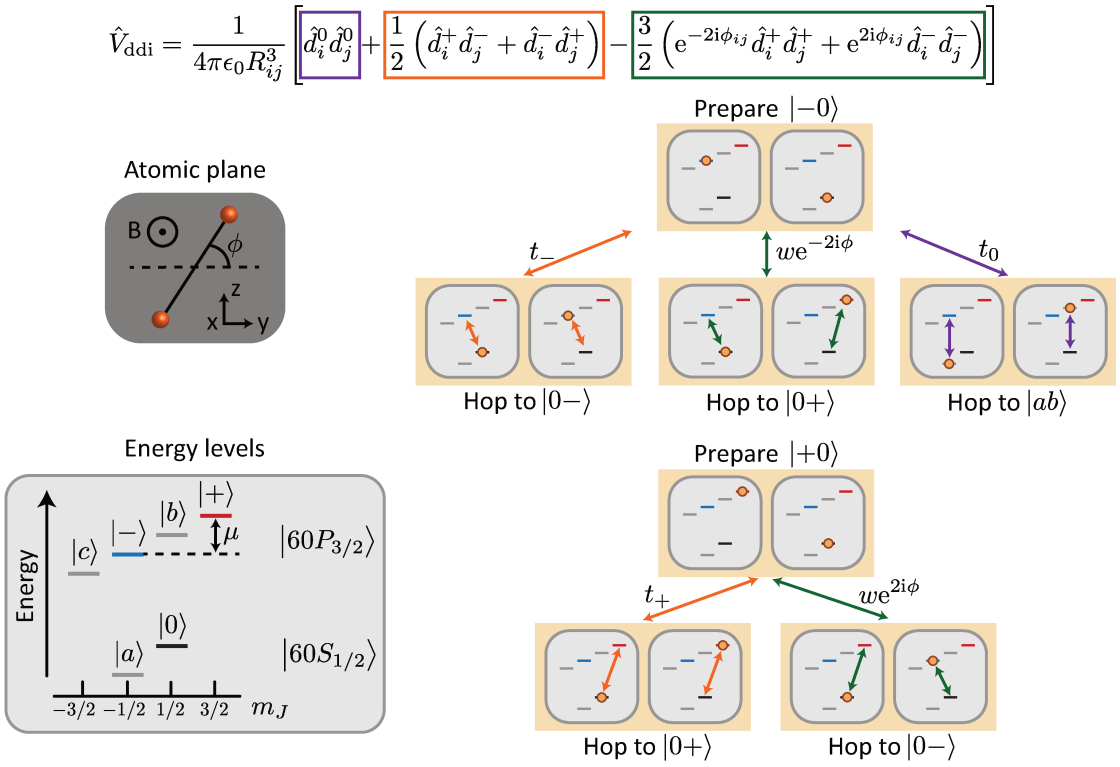

Figure 6.1: Rydberg levels in a V-structure and hopping processes. The expression of the dipole-dipole interaction in the case of a quantization axis perpendicular to the atom array is shown on top of the figure. The angle ϕ is the one between the internuclear axis and a reference axis in the yz plane, which we choose to be the y axis. The energy Zeeman levels of the $60S_{1/2}$ and $60P_{3/2}$ states are displayed, and the three levels $|0\rangle$, $|-\rangle$ and $|+\rangle$ composing the V-structure are highlighted. Right, different hopping processes involving the Rydberg states at play. We distinguish between no-spin-flip hopping (orange arrows) and spin-flip hopping (green arrows).

an additional Zeeman level in the Rydberg manifold. For the implementation of the Hamiltonian of interest in this chapter, we consider three Rydberg levels in a V-structure (bottom left corner of Figure 6.1): an empty-site state $|0\rangle = \left|60S_{1/2}, m_j = 1/2\right\rangle$, and two particle states with different spins, $|+\rangle = \left|60P_{3/2}, m_j = 3/2\right\rangle$ and $|-\rangle = \left|60P_{3/2}, m_j = -1/2\right\rangle$. In order to isolate the V-structure from the three other Zeeman states $|a\rangle$, $|b\rangle$ and $|c\rangle$, we need an electric field, as we will describe in Subsection 6.1.3. The energy difference between $|+\rangle$ and $|-\rangle$ is $\mu = E\left(|+\rangle\right) - E\left(|-\rangle\right)$, we set its value thanks to the quantization magnetic field B_x and an electric field E_x. In Figure 6.1, only a magnetic field is applied to lift the degeneracy between Zeeman levels.

Let us now describe the different hopping processes occurring with the states belonging to the V-structure. Preparing $|-0\rangle$, the $|-\rangle$ excitation has two ways to

hop from site 1 to 2: a resonant process (orange arrow), of amplitude $-t_-$, where the particle keeps the same value of spin and the system goes to the $|0-\rangle$ state; or an off-resonant process by μ (green arrow), of complex amplitude $w\mathrm{e}^{-2\mathrm{i}\phi_{12}}$, where the particle flips spin and the system goes to the $|0+\rangle$ state. The orbital phase factor $\mathrm{e}^{-2\mathrm{i}\phi_{12}}$, resulting from the geometrical dependence of the dipole-dipole interaction, can be understood as follows: while the particle is increasing its internal momentum by two quanta flipping from state $|-\rangle$ to state $|+\rangle$, its orbital momentum must decrease by two quanta, hence the phase factor. This is the intrinsic spin-orbit coupling of the dipole-dipole interaction.

We find the same two types of hopping processes for a $|+\rangle$ particle. The two-atom state prepared in $|+0\rangle$ can jump resonantly to $|0+\rangle$ (orange arrow, amplitude $-t_+$), or off-resonantly to $|0-\rangle$ (green arrow, amplitude $w\mathrm{e}^{2\mathrm{i}\phi_{12}}$). In the case of the spin-flip hopping for $|+\rangle$, the orbital phase factor is the complex conjugate of the one in the $|-\rangle$ case. Indeed, now the particle is decreasing its internal momentum by two quanta, so its orbital momentum must increase by two quanta.

The exchange terms described above involve only Rydberg levels belonging to the V-structure. Then, restricting to these three levels correctly model the dynamics in the system. On the contrary, the static dipole-dipole interaction (purple arrow in Figure 6.1) makes the system prepared in $|-0\rangle$ leave the V-structure. The influence of this last term can be reduced by shifting the $|b\rangle$ state away from the energy window between $|-\rangle$ and $|+\rangle$, hence the necessity to isolate the V-structure (Subsection 6.1.3).

6.1.2 Probing the extended Zeeman manifold with microwave

I now describe the microwave excitation from the $60S_{1/2}$ state to the $60P_{3/2}$ state at the single-atom level (see Figure 6.2). The experimental sequence is the same as the one described in Subsection 5.1.2. The atom is transferred from the electronic ground state to the Rydberg state $|0\rangle$ via a STIRAP, then excited to $|-\rangle$, $|b\rangle$ or $|+\rangle$ shining microwave photons, and finally we send a deexcitation pulse coupling the atom in $|0\rangle$ back in the electronic ground state. In the end, an atom in $|0\rangle$ before the deexcitation pulse will be recaptured at the end of the sequence, whereas if it is in any other Rydberg state, it will be lost. Consequently, our detection method does not allow to distinguish between the two particle spin states $|-\rangle$ and $|+\rangle$, and we will write the particle state in a simplified notation $|1\rangle$. The probability to be in $|1\rangle$ is thus the probability to be in the states of interest $|+\rangle$ or $|-\rangle$, or in $|b\rangle$.

Figure 6.2 (bottom) shows the spectroscopic signal we obtain varying the microwave

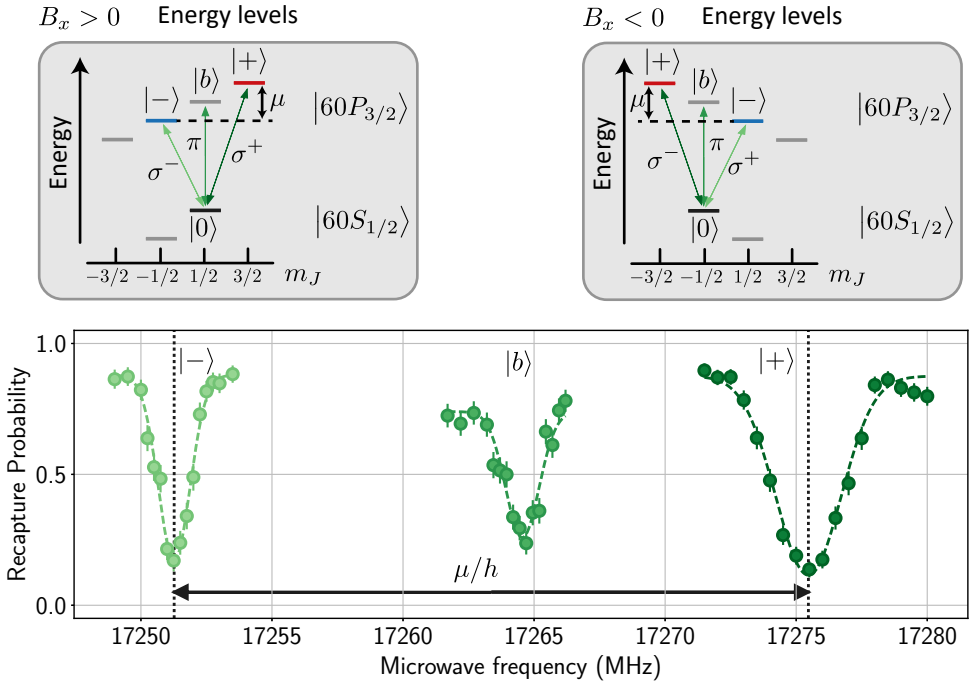

Figure 6.2: Microwave transitions in an extended Zeeman structure. Energy diagram of the Rydberg levels involed, as a function of the direction of the quantization field B_x, for $|B_x| = 6.8\,\mathrm{G}$. The three possible transitions from the $|0\rangle$ state are indicated by arrows. Bottom, spectroscopic signal (recapture probability as a function of the microwave frequency) showing the three different transitions.

frequency. The three dips in the recapture probability indicate the three transitions from $|0\rangle$ to $|-\rangle$, $|b\rangle$ or $|+\rangle$. We measure an energy separation between $|-\rangle$ and $|+\rangle$ $\mu/h \approx 25\,\mathrm{MHz}$, for a quantization magnetic field $B_x = 6.8\,\mathrm{G}$ and a cancelled electric field. The spectra do not have the same width. Actually, the three different spectra were recorded with different microwave powers (the power was three times as large to observe the transition to the $|b\rangle$ state). This is because the Rabi coupling between $|0\rangle$ and the levels of the $60P_{3/2}$ manifold depends on the targeted level, due to the polarization of the microwave field and the different angular parts of the electric dipole matrix elements. For example, for an equally polarized circular microwave (as many σ^+ photons as σ^- ones), the Rabi frequency for the transition to $|+\rangle$ is enhanced by a factor $\sqrt{3}$ with respect to the one for the transition to $|-\rangle$.

Controlling the polarization of the microwave field inside the vacuum chamber is quite hard, due to the multiple reflections of the field on the elements under vacuum, namely the metallic lens holders, whose separation is on the order of the microwave wavelength. Indeed, the microwave frequency being in the $\approx 10\,\mathrm{GHz}$ range,

its wavelength is about a few centimetres. Nevertheless, tweaking the alignment of the microwave antenna, placed above the chamber, along the Zeeman axis y, we achieve reducing the generation of π-polarized microwave photons (photons linearly polarized along the quantization magnetic field direction x). Therefore, to observe the transition to $|b\rangle$, we need much more microwave power. For this power and magnetic field, the energy separation is on the order of the Rabi frequencies for the transition to $|-\rangle$ or $|+\rangle$, and when the microwave field is at resonance for the transition to $|b\rangle$, the coupling to $|-\rangle$ or $|+\rangle$ prevents an efficient driving to $|b\rangle$. This is why the $|b\rangle$ line is less contrasted than the other ones.

In the previous chapter, to inhibit the coupling to other Zeeman levels, we were operating with a large magnetic field, increasing the Zeeman splitting. Here this is not a valid solution, since the value of μ controls the phase of the implemented complex hopping amplitude, as we shall see in the following of this chapter. It cannot be set to a arbitrarily high value. Then, the Rabi frequency to transfer the atom from $|0\rangle$ to a particle state must be smaller than the energy separation (in practice it will be on the megahertz range), which means a duration for the preparation on the order of the microsecond.

The solution to operate with larger Rabi frequencies keeping the same Zeeman splitting would be to generate some circular polarized microwave field. In order to do so, we have installed a second antenna, in that case aligned along the z direction. Again, tweaking the alignment of this antenna, we avoid the generation of π-polarized photon. In the near future, we will control the relative amplitudes and phases of the signals sent to the antennas to produce circular polarized microwaves, leading to faster and more efficient preparation.

Finally, I show in Figure 6.2 how the V-structure is changed when we invert the direction of the quantization axis B_x. It turns out that the m_J of the Rydberg levels involved in the V-structure are inverted, but μ keeps the same sign. This is because when we work with a quantization axis along x, the atoms are first optically pumped into the highest energy level of the $\left|5S_{1/2}, F = 2\right\rangle$ manifold with a quantization axis along z (see Subsection 2.1.2). Then, when we flip the field along the x direction, they adiabatically follow the direction of the field and stay in the highest energy level. If $B_x > 0$, they are in the $\left|5S_{1/2}, F = 2, m_F = 2\right\rangle$ electronic ground state, whereas if $B_x < 0$, they are in $\left|5S_{1/2}, F = 2, m_F = -2\right\rangle$. In the end, the m_J of the Rydberg states belonging to the V-structure are inverted. If we want to operate in the regime $\mu < 0$, we must invert the direction of the quantization field B_z during the optical pumping.

This inversion of the m_J while inverting the magnetic field B_x has two consequences. First, performing the spectroscopy of the $|-\rangle$ line for both directions of B_x and the same microwave power, we deduce the imbalance between σ^+ and σ^- polarized photons, to characterize more quantitatively the polarization of our microwave source. The Rabi frequencies, measured in both cases, differ by approximately 10%. Second, in the inverted case, the spin-flip hopping of a $|+\rangle$ particle now corresponds to a increase of the internal momentum by two quanta, so the orbital momentum must decrease by two quanta. In the end, in the $B_x < 0$ case, the implemented complex hopping amplitudes show the opposite phases, leading to the inversion of the circular motion as we shall see in Subsection 6.3.1.

6.1.3 Isolating the V-structure with electric fields

As mentioned in Subsection 6.1.1, one exchange term of the dipole-dipole interaction (Equation (6.1)) involve other levels than the ones belonging to the V-structure $\{|0\rangle, |-\rangle, |+\rangle\}$. It turns out that an interacting model involving only the V-structure levels accurately describes the hopping dynamics for a wise choice of magnetic and electric fields. Our collaborators find out the values of these fields by conducting the same type of investigation as they did to accurately map the problem of interacting Rydberg atoms into an Ising problem (see Subsection 4.2.1).

Only applying a magnetic field, the dynamics occurring in the system is not accurately described only considering the levels belonging to the V-structure because the $|b\rangle$ state is in between the $|-\rangle$ and $|+\rangle$ states (Subsection 6.1.1). To shift it away from the V-structure, the solution is to apply an electric field, as the Stark effect experienced by a level depends on the absolute value of m_J. This is what is shown in Figure 6.3(a). For a high enough electric field ($E_x > 0.5\,\mathrm{V/cm}$), the transitions from $|0\rangle$ to $|-\rangle$ and $|b\rangle$ ($|m_J| = 1/2$) are separated from the ones to $|c\rangle$ and $|+\rangle$ ($|m_J| = 3/2$). Then, choosing accordingly the magnetic field (plot on the bottom-right corner of Figure 6.3(a)), we reach the same value for μ as before (situation (ii)), or the regime $\mu < 0$ (situation (iii)), while $|b\rangle$ is shifted away from the V-structure. The last set of parameters (situation (iii)) was found to lead to an accurate mapping of the hopping dynamics only considering the levels of the V-structure, and will be the one considered for the theoretical discussion in Section 6.2.

Such a high electric field, $E_x = 0.7\,\mathrm{V/cm}$, implies an energy shift of the microwave transitions by about 250 MHz. Therefore, even small spatial inhomogeneities of the generated electric field over the size of the array, at the percent level, would lead to

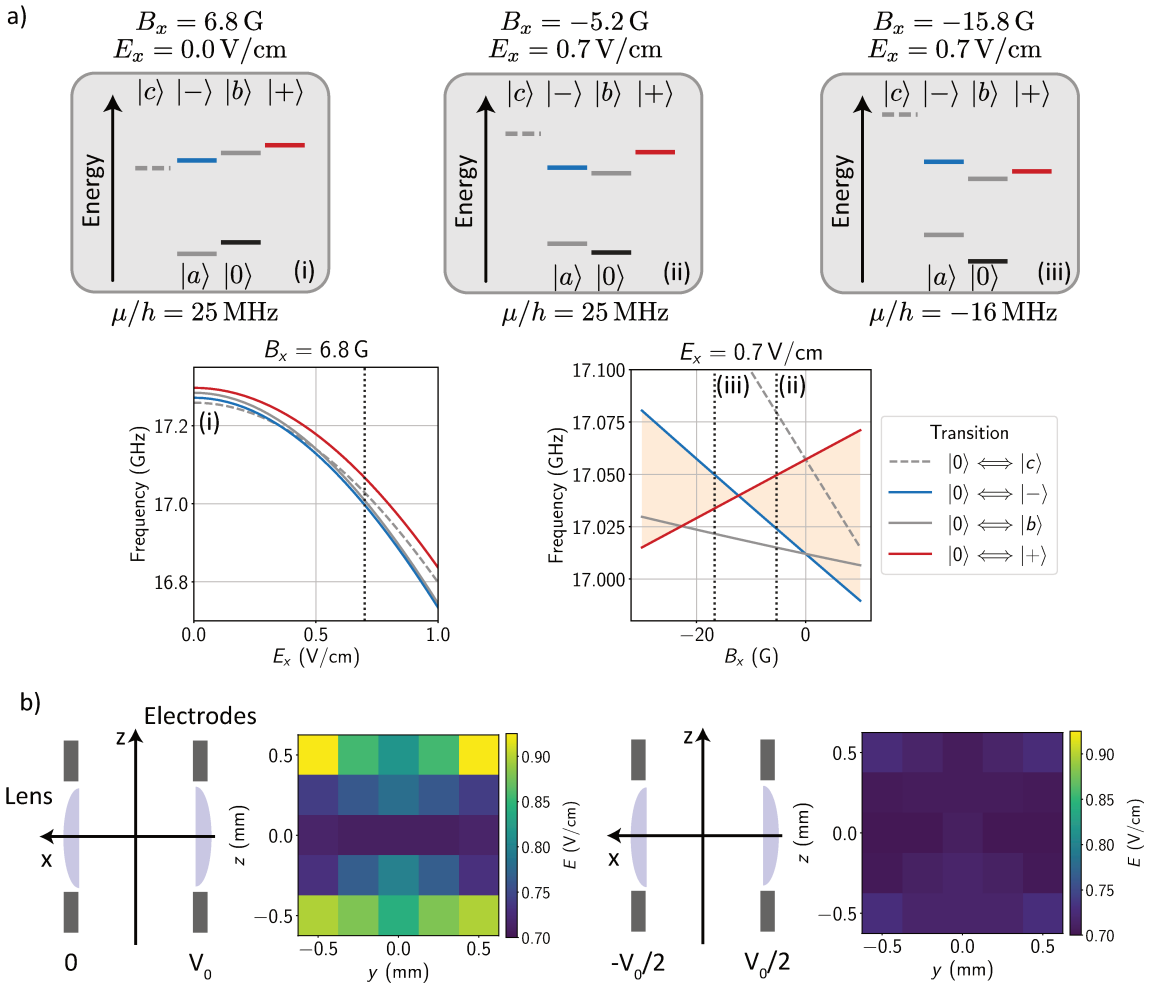

Figure 6.3: Need for a non-zero electric field. (a) Frequencies of the transitions between $|0\rangle$ and the Zeeman levels of the $|60P_{3/2}\rangle$ manifold as a function of the electric and magnetic fields. The energy diagrams for different values of (B_x, E_x) are shown. (b) Computed electric field in the yz plane for two different voltage repartition, with $V_0 = 25\,V$.

inhomogeneities between lattice sites of the microwave transition frequencies on the MHz range, which would prevent the resonant hopping process to happen.

Until the end of this thesis, to generate a field E_x on the atoms, we were setting the voltages of the four electrodes aside an aspheric lens to $V_0 = E_x \times l_x$, with $l_x = 36\,\mathrm{cm}$, and the voltages of the four other ones are set to zero. The effective length l_x was calibrated experimentally by Stark spectroscopy and also deduced from the numerical computation of the field (see the thesis of Sylvain Ravets [2014] for more details). The result of this numerical computation of the electric field is shown in Figure 6.3(b). For this voltage repartition, the electric field is quite inhomogeneous, leading to

inhomogeneities of the microwave transition frequencies. These inhomogeneities were confirmed experimentally by measuring the transition frequencies at different lattice sites, and we found discrepancies on the MHz range over a 10 μm distance.

Adopting a more symmetric repartition of the voltages (right of Figure 6.3(b)), we obtain a more homogeneous field. The electronic setup to operate with this more symmetric repartition of the voltages was developed at the very end of this thesis, and it indeed results in a more homogeneous distribution of the transition frequencies among lattice sites (fluctuations below 100 kHz over 10 μm). In addition to a more flexible voltage repartition, this new setup allows us to quickly ramp the value of the electric field.

6.1.4 Preparation of a localized excitation

To observe the different hopping processes previously described, we must prepare on a targeted lattice site a $|-\rangle$ or $|+\rangle$ excitation. We use, as described in the single-atom case, a microwave field to excite the atom from $|0\rangle$ to $|-\rangle$ or $|+\rangle$. Without any further operation, we cannot locally excite one of the atoms to the particle state. Indeed, the microwave has a global effect on the atomic array, since its wavelength is a few centimetres, way larger than the size of the array. We have seen in Subsection 5.1.3 that exciting a two-atom system, in the presence of the resonant dipole-dipole interaction, generates the symmetric superposition state $(|0+\rangle + |+0\rangle)/\sqrt{2}$ or $(|0-\rangle + |-0\rangle)/\sqrt{2}$, corresponding to an excitation shared among two sites. This is not the type of state we want to prepare in this chapter. Hence the necessity to use an additional laser addressing beam, focused on one of the atoms to shift its energy levels, and we can change its state with microwaves while leaving the states of the other atoms unchanged. We reported the demonstration of this technique in [de Léséleuc *et al.*, 2017], and I refer the interested reader to the thesis of Sylvain de Léséleuc [2018] for more details.

The addressing beam, at 1013 nm, couples the Rydberg state $|0\rangle$ with the low-lying state $\left|6P_{3/2}\right\rangle$ (see Figure 6.4(a)). It is focused on one lattice site, its waist is about 4 μm, which is larger than that of the optical tweezers (1 μm) but smaller than the typical interatomic distance (10 μm). For an addressing power of about 100 mW, we measured a Rabi frequency $\Omega_{\text{addr}}/(2\pi) = 218$ MHz. Depending on the detuning Δ_{addr} we set, we control the energy shift experienced by the $|0\rangle$ state. If we work at resonance, $|0\rangle$ is split into two levels separated by Ω_{addr}, via the Autler-Townes effect. If the atom is in $|0\rangle$ when the addressing beam is shone, it will decay back to $\left|6P_{3/2}\right\rangle$ and then to the electronic ground state. Consequently, we must shine this resonant

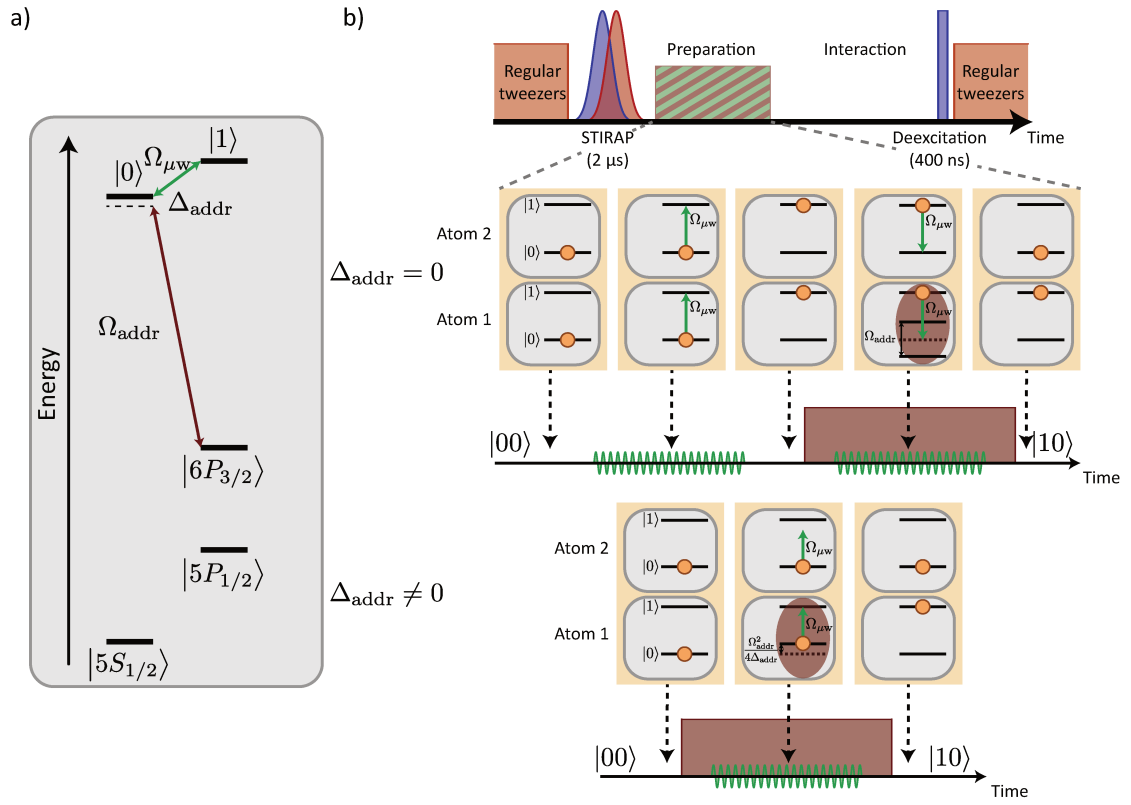

Figure 6.4: Preparation of a particle on a single lattice site. (a) Energy scheme of the atomic levels involved for the preparation of the state $|10\rangle$. The addressing beam couples the states $|6P_{3/2}\rangle$ and $|0\rangle$ with a Rabi frequency Ω_{addr} and a detuning Δ_{addr}. (b) Experimental sequence to prepare the state $|10\rangle$ starting from $|00\rangle$. Two ways are possible, corresponding to a resonant or off-resonant addressing beam.

addressing beam only when the atom is in the $|1\rangle$ state. When the addressing beam is off-resonant, the energy of $|0\rangle$ is shifted by $\Omega_{\text{addr}}^2/(4\Delta_{\text{addr}})$ via the AC-Stark effect. For $\Delta_{\text{addr}}/(2\pi) = 2\,\text{GHz}$, we then obtain a light-shift of 6 MHz. In the off-resonant case, only a small fraction $(\Omega_{\text{addr}}^2/\Delta_{\text{addr}}^2)$ of the atomic wavefunction is coupled back to the electronic ground state, so we can induce such a light-shift while the atom is in $|0\rangle$.

Figure 6.4(b) shows the experimental sequence used to prepare the state $|10\rangle$ in both cases $\Delta_{\text{addr}} = 0$ and $\Delta_{\text{addr}} \neq 0$. We perform this preparation via a combination of the global microwave field and the local addressing beam after having prepared $|00\rangle$ via the STIRAP process. In the $\Delta_{\text{addr}} = 0$ case, both atoms are first excited to $|1\rangle$ via a microwave π-pulse, and when sending a second π-pulse we shine the addressing beam on the first atom. Consequently, the first atom stays in $|1\rangle$ whereas the other one is coupled back to $|0\rangle$. In the $\Delta_{\text{addr}} \neq 0$ case, we send a microwave π-pulse set at resonance with the addressed atom, while the other atom stays in $|0\rangle$.

For the first method to succeed, the π-pulse must be strong enough to excite both atoms to $|1\rangle$ despite the interaction energy. The interaction is typically on the MHz range, so the microwave Rabi frequency must be on the 10 MHz range, which is still below the Autler-Townes splitting, on the 100 MHz range. We followed this method to prepare the $|10\rangle$ state when observing the spin-exchange process between two Rydberg atoms (Subsection 3.3.2). Here, as already explained, we cannot operate at such a high microwave Rabi frequency because of the restriction on the value of the Zeeman splitting. Consequently, we choose to follow the second method.

In addition to enable for the preparation of a localized excitation, the second method was also used in [de Léséleuc *et al.*, 2017] to freeze the dipole-dipole interaction at will, by shifting one of the two-atom states out of resonance. We will not focus on this feature for this chapter, but it is of interest for our study reported in Chapter 5. Indeed, the addressing beam imprints a phase on the shifted two-atom state, in such a way that for a specific freezing duration, we have generated the antisymmetric superposition of the single-excited states, i.e. the two-atom XY antiferromagnetic state. Using several addressing beams, this method may be a way to engineer larger XY antiferromagnets.

6.1.5 Spin-exchange experiment

After having prepared the $|10\rangle$ state, the system freely oscillates between $|10\rangle$ and $|01\rangle$. The frequency of the oscillation is $2t_-/h$ if we prepare $|-0\rangle$, and is $2t_+/h$ if we prepare $|+0\rangle$.

Figure 6.5 shows the observed spin-exchange oscillation preparing $|-0\rangle$ (a) or $|+0\rangle$ (b). For the preparation, we have used a 1 μs square microwave pulse with a Rabi frequency $\Omega_{\mu w}/(2\pi) = 0.5$ MHz, resonant with the $|-\rangle$ or $|+\rangle$ line (Figure 6.2) shifted by 6 MHz due to the addressing beam. We extract the interaction energies $t_-/h = 0.45$ MHz and $t_+/h = 1.45$ MHz from the fitting damped sine functions, for an interatomic distance $a = 11\,\mu$m. The observed ratio $t_+ \approx 3t_-$ agrees with the $\sqrt{3}$ ratio of the angular parts of the dipole matrix elements.

The finite contrast is explained, as in the previous chapters, by the detection errors and the finite STIRAP efficiency, and also by the finite efficiency of the preparation of a localized excitation described above. Indeed, such a preparation is difficult in the presence of the other Rydberg states of the Zeeman manifold, even if we work with a rather small microwave Rabi frequency. The damping originates from the shot-to-shot fluctuations of the interatomic distance, and the additional off-resonant hopping terms

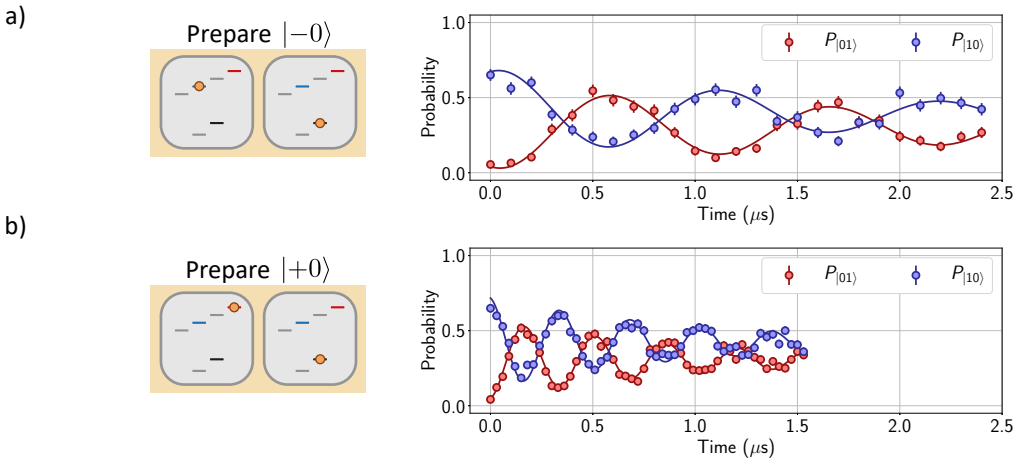

Figure 6.5: Spin-exchange processes. After having prepared $|-0\rangle$ (a) and $|+0\rangle$ (b), we measure the probabilities to be in $|10\rangle$ and $|01\rangle$ as a function of time. The solid lines are fitting damped sine to extract the interaction energy.

which perturbs the dynamics involving only two levels.

To conclude, I have presented here the different hopping processes occurring when the particle state is encoded into two levels of the Zeeman structure, and is therefore considered as a particle with an internal degree of freedom (a "spin"). The additional spin-flip hopping comes along with a phase factor, and will be the basic ingredient in the following of this chapter to implement complex hopping amplitude. Since we operate in a Zeeman manifold which cannot be arbitrarily split, the microwave manipulation is less efficient than in the previous chapter, and the high-fidelity preparation of a localized excitation is more difficult. Even with a finite preparation efficiency, we will be able to observe the effect of the implemented complex hopping amplitude on a minimal system of three atoms (see Section 6.3). The experiments reported there follow the same procedure as the ones described here to observe the spin-exchange (preparation of a particle and observation of its propagation) except that they involve a third lattice site.

6.2 Towards the observation of chiral edge states on honeycomb lattices

Before describing the observed experimental signatures of the spin-flip hopping, I will explain how the latest leads to the engineering of topological matter hosting chiral edge states. This theoretical work was realized by our collaborators in Stuttgart [Weber

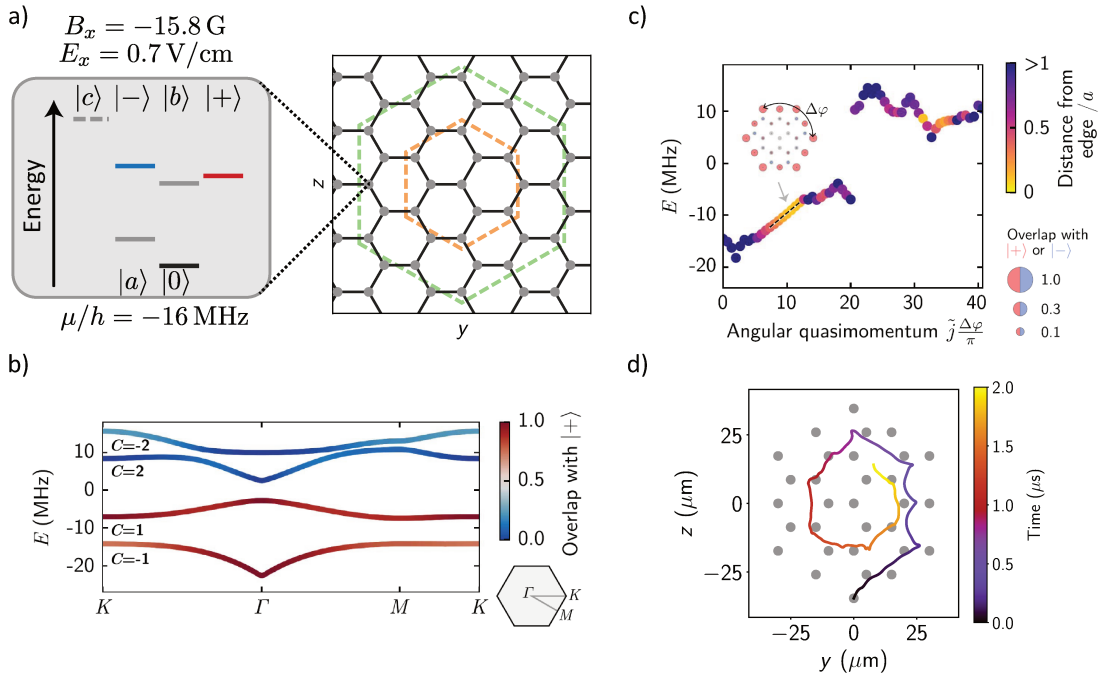

Figure 6.6: Chiral edge states in arrays of Rydberg atoms. (a) The system under study is composed of Rydberg atoms on a honeycomb lattice. The infinite lattice is represented, and the dashed brown and green lines indicate how the infinite lattice is cut into finite-size 10- or 31-site patches. The V-structure is also shown. (b) Band structure of the infinite honeycomb lattice, for $\mu/h = -16\,\mathrm{MHz}$. The Chern numbers associated to each band are indicated, as well as the overlap of the eigenstates with the particle state $|+\rangle$. (c) For the 31-site honeycomb lattice, eigen-energies as a function of the angular quasimomentum. The color encodes the distance of the eigenstate from the edge. A spatial representation of the wavefunction of one eigenstate is shown, with the overlap to the particle state $|+\rangle$ or $|-\rangle$. (d) Trajectory of the center of mass of the $|+\rangle$ excitation, initially injected on the bottom site of the 31-atom honeycomb lattice, as a function of time.

et al., 2018], and I will report here their analysis. It is based on a description of the hopping dynamics involving the three Rydberg levels of the V-structure mentioned above. Then, I will show that one of the particle spin state is only virtually populated, leading to a perturbative description of the dynamics only involving two Rydberg levels.

6.2.1 Hopping dynamics for a V-structure interacting model

Here, I show how the dynamics induced by the hopping terms involving the levels of the V-structure leads to the generation of chiral edge states, signature of topological

properties. Such a topological state is engineered with Rydberg atoms in a honeycomb lattice configuration (Figure 6.6(a)). Restricting ourselves to the levels of the V-structure, as it is well isolated using an electric field (Subsection 6.1.3), we write the hopping interaction between sites i and j

$$\hat{H}_{ij}^{\text{hop}} = \frac{a^3}{|\mathbf{R}_{ij}|^3} \hat{\psi}_i^\dagger \begin{pmatrix} -t_+ & w\mathrm{e}^{-2\mathrm{i}\phi_{ij}} \\ w\mathrm{e}^{2\mathrm{i}\phi_{ij}} & -t_- \end{pmatrix} \hat{\psi}_j + \text{h.c.}, \tag{6.2}$$

with a the lattice spacing, $\mathbf{R}_{ij}$ the separation between both lattice sites and $\hat{\psi}_i^\dagger = \left(\hat{b}_{i,+}^\dagger, \hat{b}_{i,-}^\dagger\right)$, where $\hat{b}_{i,\pm}^\dagger = |\pm\rangle_i \langle 0|_i$ are the creation operators of a $|\pm\rangle$ particle on site i. The prefactor $\kappa_{ij} = a^3/|\mathbf{R}_{ij}|^3$ takes into account the $1/R^3$ dependence of the dipole-dipole interaction as a function of the distance. Considering the energy difference between $|+\rangle$ and $|-\rangle$, the total Hamiltonian of the system reads

$$\hat{H} = \frac{1}{2} \sum_{i \neq j} \hat{H}_{ij}^{\text{hop}} + \sum_i \hat{\psi}_i^\dagger \begin{pmatrix} \mu/2 & 0 \\ 0 & -\mu/2 \end{pmatrix} \hat{\psi}_i. \tag{6.3}$$

For the Rydberg states considered in [Weber *et al.*, 2018] and a lattice spacing $a = 10\,\mu$m, the hopping amplitudes are $w/h = 4.17\,$MHz, $t_+/h = 2.41\,$MHz and $t_-/h = 0.80\,$MHz. The value of the electric and magnetic fields are such that $\mu/h = -16\,$MHz. The following results presented in this section were obtained with these values.

For an infinite honeycomb lattice, one can compute the band structure originating from the hopping Hamiltonian (6.3), shown in Figure 6.6(b) and extracted from the publication [Weber *et al.*, 2018]. This diagram shows four bands, as the elementary cell of the honeycomb lattice contains two sites and there are two spin components. All the bands are associated with non-zero Chern numbers, the signature of a topological system. Another interesting feature of these bands is that the associated eigenstates mostly overlap with one of the two spin components. This means that occupying one particle state, the other one is hardly populated, justifying its adiabatic elimination via a perturbative approach, as we shall see in the next subsection.

Now, for a finite-size system, the bulk topological properties (non-zero Chern numbers) should be revealed by a specific behaviour on the edges, according to the bulk-edge correspondence. We focus on the 31-site honeycomb lattice (indicated by a green dashed line in Figure 6.6(a)). We compute for this finite-sized system the eigen-energies, and represent them as a function of the angular quasimomentum of the associated eigenstate 6.6(c). An angular quasimomentum can be defined as the

system exhibits a discrete $2\pi/3$-rotational symmetry. The dispersion relation shows a linear behaviour, hallmark of the directed propagation of the excitation. This mode propagates on the edge of the system, as expected from a chiral edge mode, and mostly overlaps with the $|+\rangle$ spin component.

To confirm the presence of chiral edge modes in this honeycomb lattice, we compute the hopping dynamics after having prepared a localized $|+\rangle$ excitation on a site on the edge of the lattice. The trajectory of the center of mass of the excitation (Figure 6.6(d)) indeed reveals a directed motion on the edge of the system. Here also, preparing a $|+\rangle$ particle, the lattice sites show a very small probability to be in the $|-\rangle$ state, the other spin component.

In summary, the system under study exhibits chiral edge states. To get more insight on the reason why the system exhibits such topological properties, we follow in the next subsection a perturbative approach, to adiabatically eliminate one of the two spin components and obtain a simpler two-level model. Such an elimination is justified because we have seen here that one of the two spin components is hardly populated during the computed dynamics.

6.2.2 Adiabatic elimination of one spin component

When μ is larger than the other energies of the system t_-, t_+ and w, a particle initialized in a given spin component will hop between lattice sites while keeping the same value of spin, since the spin-flip hopping is an off-resonant process and there are only virtual transitions to the other spin state. Then, the spin-flip hopping can be treated as a perturbation. This perturbative treatment will result in some complex hopping amplitude for the particle, while still keeping the same value of spin. Consequently, only one particle state is involved in this perturbative approach, but the hopping amplitudes are nevertheless complex. This implementation of complex hopping amplitude can be interpreted as the imprinting of a Peierls phase on the particle wavefunction, and we will observe the signature of this phase in the following section. Here, to validate our perturbative approach, we will compare the hopping dynamics induced by Hamiltonian (6.3) with the one resulting from the derived effective hopping amplitudes.

Implementation of a complex hopping amplitude For the discussion of the perturbative approach, I start considering a three-atom system (Figure 6.7(a)). When we prepare a single excitation on one lattice site, as the dipole-dipole interaction

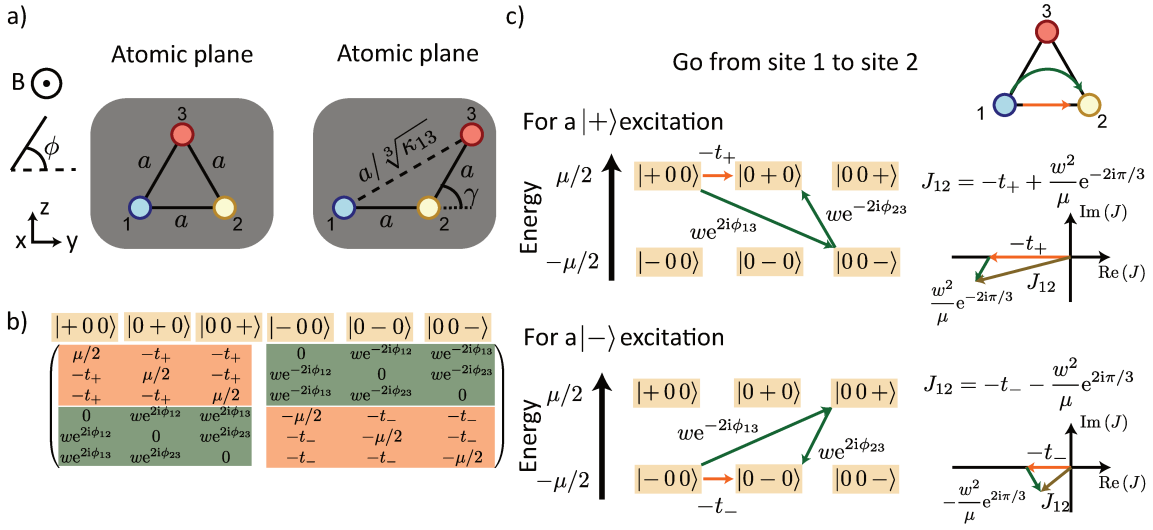

Figure 6.7: Perturbative approach. (a) Three-atom configurations used in this work. (b) Hopping Hamiltonian in the single-particle manifold for an equilateral triangle. (c) Illustration of the two possible processes for a $|+\rangle$ or $|-\rangle$ particle to hop from site 1 to site 2. The effective coupling J_{12} is shown in the complex plane (here $\mu > 0$).

conserves the number of excitations, the system will stay in the single-particle Hilbert subspace. Figure 6.7(b) explicitly shows Hamiltonian (6.3) written in this Hilbert subspace for the equilateral triangle. The orange blocks contain the resonant hopping terms coupling states having the same spin component, whereas the green blocks contain the off-resonant terms coupling the two spin components, which are treated as perturbations.

We compute according to perturbation theory the modification of the energies of the eigenstates of the orange blocs. Rewriting the states of the Hilbert subspace on the eigen-basis, this leads to an additional term in the effective coupling strength $J_{12}^{\pm}$ describing the hopping of a $|\pm\rangle$ particle from site 1 to site 2

$$J_{12}^{+} = -t_{+} + \frac{w^2}{\mu} e^{-2i\pi/3} \quad \text{and} \quad J_{12}^{-} = -t_{-} - \frac{w^2}{\mu} e^{2i\pi/3}. \tag{6.4}$$

The opposite sign in front of the added term $\propto w^2/\mu$ is due to the fact that the sign of the perturbation corrections depends on the sign of the energy difference between the perturbed and the perturbing states. The perturbative approach described here leads to the derivation of an effective Hamiltonian [Cohen-Tannoudji, Dupont-Roc, and Grynberg, 1996], defined in the Hilbert subspace involving only one spin component.

These expressions may be interpreted as the sum of the amplitudes of the two hopping processes corresponding to the two ways a $|\pm\rangle$ particle hops from site 1 to

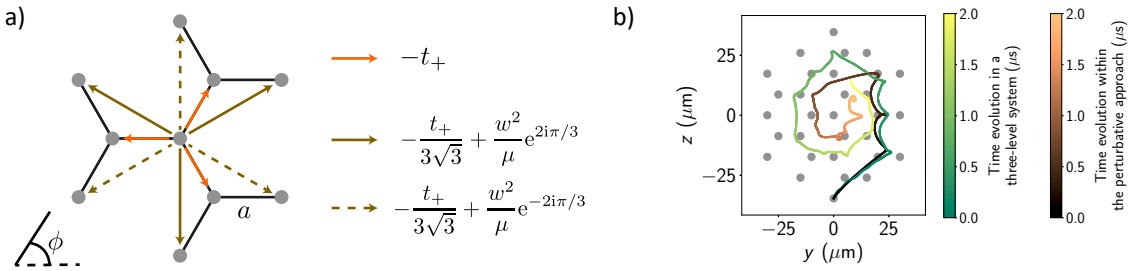

Figure 6.8: Link to the Haldane model. (a) Effective hopping amplitudes for a $|+\rangle$ particle propagating in a honeycomb lattice according to our perturbative approach. (b) Time evolution of the center of mass of the excitation, computed resolving Hamiltonian (6.3) (colorscale from green to yellow) or the effective Hamiltonian (colorscale from black to orange).

site 2 (Figure 6.7(c)). Either it hops directly from site 1 to 2 with an amplitude $-t_\pm$, either it virtually goes through the third lattice site while changing spin twice (so in the end keeping the same value of spin). During this off-resonant process, the particle picks up a phase and the amplitude of this process is the product of the amplitudes of the two successive hops $w^2\,\mathrm{e}^{\pm 2\mathrm{i}(\phi_{13}-\phi_{23})}/\mu$. Since a difference of angles ϕ appears in the complex exponential, whatever the orientation of the angle reference axis, the value of this difference will still be the same, so what only matters is the relative orientation of the three atoms with respect to each other.

This picture of two successive spin-flip hops allows to understand why the particle hops with complex amplitudes whereas it never populates the other spin component. The advantage of this picture is that it agrees with the expression of the effective hopping amplitude derived from the perturbation theory (Equation (6.4)), without having to diagonalize the part of the Hamiltonian corresponding to one spin component (see orange blocs in Figure 6.7(b)). Consequently, we are going to test the validity of this picture for a larger system, the 31-site honeycomb lattice studied in the previous subsection.

Link to the Haldane model Figure 6.8(a) shows the effective hopping amplitudes for a $|+\rangle$ particle travelling around a honeycomb lattice, derived according to the previously described perturbative approach. The hopping amplitude to nearest neighbours is real, as the two successive spin-flip hopping process would imply in that case one hop between next-nearest neighbours, and therefore is negligible comparing to $-t_+$. For the hopping to next-nearest neighbours, we have to consider the resonant hopping of amplitude $-t_+/\left(3\sqrt{3}\right)$ and the off-resonant process of two successive spin-flip hopping

between nearest neighbour $\propto w^2/\mu$. Such an effective hopping Hamiltonian, with real hopping amplitudes to nearest neighbours and complex hopping amplitudes to next-nearest neighbours, is reminiscent of the Haldane model [Haldane, 1988].

We compare the hopping dynamics of an injected $|+\rangle$ particle obtained by solving the Schrödinger equation for Hamiltonian (6.3) (this result was already presented in Figure 6.6(d)), or by solving it for an effective Hamiltonian written in the one-$|+\rangle$-excitation Hilbert subspace with the effective hopping terms described above. The agreement between the computed trajectories of the center of mass of the excitation is quite good, especially at short times, as it is usually the case for perturbative approach. This validates the use of our perturbative approach to describe, at least qualitatively, the hopping dynamics induced by Hamiltonian (6.3), in the regime where $\mu \gg w, t_+, t_-$. Moreover, the perturbative approach allows us to connect Hamiltonian (6.3) to the Haldane model, explaining in a different way why our system exhibits topological properties.

6.3 Implementation of a complex hopping amplitude on a three-atom system

Now that we have understood, via a perturbative approach, how Hamiltonian (6.3) leads to the implementation of complex hopping amplitude, imprinting on the particle circulating among lattice sites a phase similar to the Peierls phase, we will observe the effect of such a phase on a minimal three-atom system. Considering the representation in the complex plane of the effective hopping amplitudes $J_{12}^{\pm}$ (see Figure 6.7(c)) derived in the case of an equilateral triangle, for a given μ, the ratio $|\mathrm{Im}\left(J_{12}^{\pm}\right)/\mathrm{Re}\left(J_{12}^{\pm}\right)|$ is larger for the $|-\rangle$ state as $t_+ > t_-$. This means that we expect stronger effects of the implemented Peierls phase on the $|-\rangle$ particle. We could increase this ratio by decreasing μ, but at the risk of leaving the range of validity of the perturbative regime. This is why we will study the implementation of the Peierls phase on a $|-\rangle$ particle. In that case, the aforementioned ratio is the largest when $\mu > 0$, as shown by the representation in the complex plane.

The implemented Peierls phase depends on two experimental knobs: the energy splitting μ and the geometrical arrangement of the three-atom system. We will first vary μ to observe the cyclotron-like orbit of a $|-\rangle$ particle on an equilateral triangle. We will then vary the three-atom configuration to observe the geometry-dependent recombination of a $|-\rangle$ excitation. Finally, I will say a few words about the

two-excitation case.

6.3.1 Cyclotron-like orbit on an equilateral triangle

In a first experiment, we observe the motion of a $|-\rangle$ particle in an equilateral triangle. In that case, the effective coupling reads $J_{12} = -t_- - w^2\,\mathrm{e}^{-2\mathrm{i}\pi/3}/\mu$ (see Equation (6.4)), which can be written $J_{12} = J\mathrm{e}^{\mathrm{i}\theta}$ with $J > 0$. At lowest order in w/μ, the modulus and phase of the effective coupling read $J \approx t_-\,(1 - w^2/\,(2\mu t_-))$ and $\theta \approx \pi + \sqrt{3}w^2/\,(2\mu t_-)$. Due to the rotational symmetry of the system, the hopping amplitudes towards the following site in the clockwise direction are equal, $J_{12} = J_{23} = J_{31} = J\mathrm{e}^{\mathrm{i}\theta}$, and the hopping corresponding to a circulation in the anti-clockwise direction have the conjugate amplitude $J_{21} = J_{13} = J_{32} = J\mathrm{e}^{-\mathrm{i}\theta}$.

The effective implemented Hamiltonian in this regime[2] is the same as the one studied in [Roushan *et al.*, 2017a] on a superconducting circuit platform. When the particle travels around the triangle, i.e. an elementary lattice plaquette, in the clockwise direction, it acquires a total phase 3θ. This phase is proportional to the flux of the artificial magnetic field enclosed by the lattice plaquette. For a total phase $3\theta = \pi/2$, the particle follows a circular trajectory in the anti-clockwise direction, akin to the cyclotron orbit an electron would follow in the presence of a magnetic field.

Periodic motion for specific values of θ To understand why the specific value $\theta = \pi/6$ leads to a circular motion, we study in more details the $J\mathrm{e}^{\mathrm{i}\theta}$ model. The eigen-energies of the three-site system are written $\epsilon_k = 2J\cos\,(\theta + 2k\pi/3)$, and are plotted as a function of θ in Figure 6.9(a). The probability to find the particle at a given site oscillates at frequencies which are proportional to the eigen-energy differences, corresponding to beating between eigenstates. As only the eigen-energy differences matter, and that the values of these differences are $2\pi/3$-periodic as a function of θ, we can restrict ourselves to the θ range $[0, 2\pi/3]$.

There, for θ equal 0, $\pi/3$ or $2\pi/3$, one beating frequency vanishes, and we predict a symmetric propagation on the triangle. For θ ranging from 0 to $\pi/3$, the particle propagates with a preferential circulation in the clockwise orientation, and for the specific value $\theta = \pi/6$, the beating frequencies are commensurate (one is twice as large as the others). This results in the fact that the particle fully comes back on the site it was at time origin after having circulated around the triangle. In other words, it leads to the periodic cyclotron orbit we were referring to. In the end, having commensurate

[2] We will refer to this Hamiltonian as the $J\mathrm{e}^{\mathrm{i}\theta}$ model in the following.

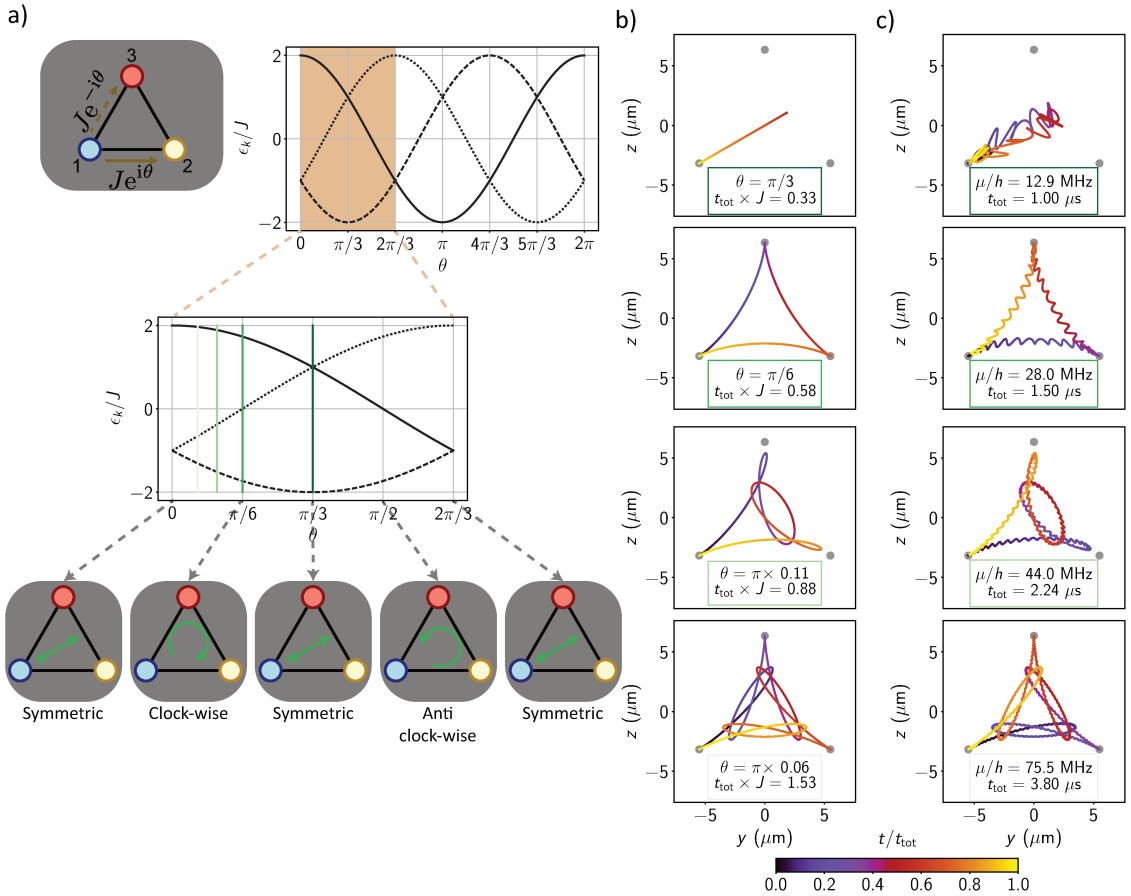

Figure 6.9: Effect of the phase of the hopping amplitude in an equilateral triangle. (a) Eigen-energies of the system as a function of the phase θ of the hopping amplitude, on the $[0, 2\pi]$ and $[0, 2\pi/3]$ ranges. (b) Computed trajectory of the center of mass of the excitation solving the $Je^{i\theta}$ model, for different phases θ indicated by green lines in (a). The total duration of the dynamics was set to observe one cycle of the periodic motion. (c) Computed trajectory of the center of mass of the excitation solving Hamiltonian (6.3). The value of μ was set in order to have the same phase of the hopping amplitude as in (b), and the total duration of the dynamics is here also the one required to observe one cycle of the periodic motion.

beating frequencies is similar to have a linear dispersion relation (see Figure 6.6(c)), so this is why we expect in that case also to observe a chiral propagation. It turns out that the beating frequencies are commensurate for other values of θ, indicated by green lines in Figure 6.9(a). The results are the same for θ ranging from $\pi/3$ to $2\pi/3$, but in that case the motion will be preferentially in the anti-clockwise direction.

The trajectory of the center of mass of the excitation, initially prepared on site 1, obtained by solving the Schrödinger equation for the $Je^{i\theta}$ model involving only the one-$|-\rangle$-excitation states, confirms our prediction (Figure 6.9(b)). For the different values of θ highlighted before, the computed trajectories reveal a periodic motion, symmetric for $\theta = \pi/3$ and in the clockwise direction for the other phases.

Now, we want to see if the dynamics induced by the full Hamiltonian (6.3) shows the same type of periodic motion (Figure 6.9(c)). The parameters of the Hamiltonian are $w/h = 2.65\,\mathrm{MHz}$, $t_+/h = 1.45\,\mathrm{MHz}$, $t_-/h = 0.45\,\mathrm{MHz}$ (corresponding for the considered Rydberg states to a lattice spacing $a = 11\,\mu\mathrm{m}$) and $\mu > 0$. The phase of the implemented hopping amplitude ranges between π and $4\pi/3$, so the motion will be preferentially oriented towards the anti-clockwise direction. We numerically tune the value of μ to implement the same phase for the effective hopping amplitude as in Figure 6.9(b). Based on our perturbative approach, neglecting the π offset, the phase of the hopping amplitude is $\sqrt{3}w^2/(2\mu t_-)$. So to obtain the symmetric propagation mode, $\theta = \pi/3$, taking into account our parameters, we must have $\mu/h = 12.9\,\mathrm{MHz}$. Such a value of μ indeed leads to a symmetric propagation. To obtain the circular motion, $\theta = \pi/6$, we must have $\mu/h = 25.8\,\mathrm{MHz}$ according to our perturbative derivation, and the most suitable value for μ to do so was numerically found to be $\mu/h = 28\,\mathrm{MHz}$. We were able to find the most suitable value for μ guided by our perturbative approach for all the phases of hopping amplitudes we studied in Figure 6.9(b). Trajectories in Figure 6.9(c) feature additional fast oscillations around the position of the center of mass displayed in Figure 6.9(b). They are due to the spin-flip hopping, and are the smallest for the largest μ, for which the perturbative approach is the most accurate.

As the results computed from Hamiltonian (6.3) were predicted with our perturbative approach, its use is validated to efficiently describe the hopping dynamics, also in the three-atom case.

Observation of circular propagation We now aim at observing the chiral motion described above on our experimental platform. We prepare one $|-\rangle$ excitation on site 1 and let the system interact for a varying duration τ (see Figure 6.10(a)). For the preparation, we have used the same parameters as in the two-atom spin-exchange

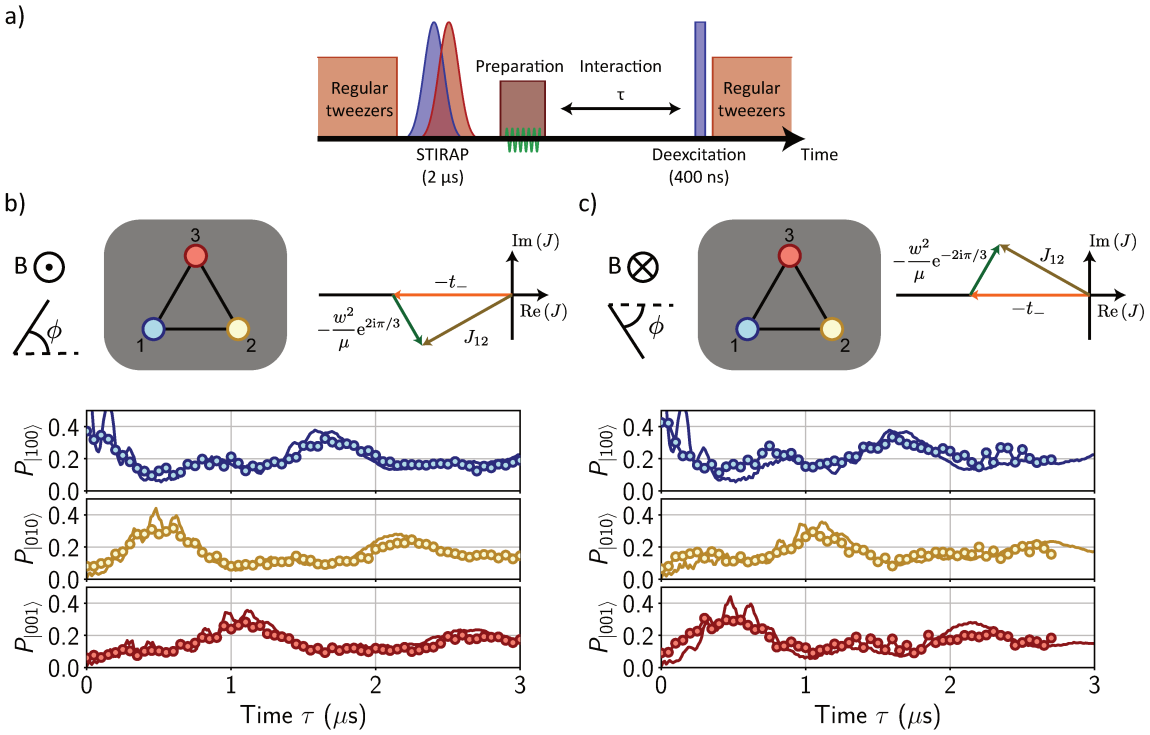

Figure 6.10: Experimental observation of a chiral motion. (a) Experimental sequence to observe the hopping dynamics. (b) For $B_x > 0$, probabilities $P_{|100\rangle}$, $P_{|010\rangle}$ and $P_{|001\rangle}$ as a function of the interacting time τ. The effective coupling J_{12} is shown in the complex plane in that case. The solid lines are simulations taking into account the finite efficiency preparation and detection errors. (c) Same as (b), but for $B_x < 0$.

experiment (Subsection 6.1.5). The interatomic distance is $a = 11\,\mu$m, resulting in hopping amplitudes $w/h = 2.65\,$MHz, $t_+/h = 1.45\,$MHz and $t_-/h = 0.45\,$MHz.

The energy separation μ was set to $\mu/h = 25\,$MHz. In that case, the phase of the effective coupling J_{12} is about $7\pi/6$, and we indeed observe a circular motion of the excitation in the anti-clockwise orientation $1 \to 2 \to 3 \to 1$ (Figure 6.10(b)). Now, inverting the direction of B_x, we observe the circular motion of the excitation in the reversed orientation $1 \to 3 \to 2 \to 1$ (Figure 6.10(c)). This is because inverting the direction of B_x, the signs of the m_J Rydberg states involved in the V-structure are inverted, and the phase factor of the spin-flip hopping amplitude are complex conjugated, as already explained in Figure 6.2. Then, the phase of the effective coupling J_{12} is about $5\pi/6$, resulting in a circulation in the clockwise orientation.

Simulations taking into account the finite preparation efficiency and detection errors, shown as solid lines in Figure 6.10(b) and (c), are in good agreement with the measured dynamics, and explain the observed finite contrast. This result was obtained without applying an electric field, since the new setup for the generation of

more homogeneous electric fields was not developed at that time. The new set of data, obtained during the writing of this thesis, shows an improved contrast and a reduced damping in the presence of an electric field.

The use of an electric field improves the results for several reasons. First, the mapping into a three-level system is more accurate in that case (Subsection 6.1.3), so that the exchange term which makes the system leave the V-structure has less effect. This leads to a reduced damping. Moreover, the isolation of the V-structure required for an accurate mapping allows also for a more efficient preparation as the levels are more separated. Finally, another advantage of using an electric field to control the relative position of the energy levels, with respect to a magnetic field, is that we can change the value of the electric field more quickly. This implies that we could do the preparation for a given value of the electric field for which the levels are well separated, and then switch to another value to have the system interacting in the expected way. We have not yet explored this possibility of quickly ramping the electric fields, but the new setup for the generation of electric fields was designed in order to do it in the future.

6.3.2 Geometry-dependent recombination of an excitation

So far, I have shown how tuning μ, we can implement a hopping amplitude with a phase such that we observe a chiral motion on an equilateral triangle. Now, we keep the same value for μ and study the influence of the three-atom configuration on the engineered Peierls phase, i.e. the influence of the κ_{ij} and ϕ_{ij}.

An interferometry-like experiment For this experiment, we prepare a $|-\rangle$ excitation on site 2 and see how it recombines back on the same site after having circulated around the triangle, for different configurations of an isosceles triangle (see Figure 6.11(a)). As an intuitive picture, we can see this experiment as a Sagnac interferometer: initially on site 2, the particle splits and propagates circularly in both orientations around the triangle, picks up different phases during the circular motions which interfere when the particle is back on site 2.

Our perturbative approach is again useful to predict the hopping dynamics. In the isosceles triangle configuration, we have $\phi_{12} = 0$, $\phi_{23} = \gamma$, $\phi_{13} = \gamma/2$, and $\kappa_{12} = \kappa_{23} = 1$, $\kappa_{13} = (2\,(1+\cos\gamma))^{-3/2}$. Then, $J_{12} = t_- - \kappa_{13} w^2\, \mathrm{e}^{-\mathrm{i}\gamma}/\mu$, $J_{23} = t_- - \kappa_{13} w^2\, \mathrm{e}^{\mathrm{i}\gamma}/\mu$ and $J_{13} = \kappa_{13} t_- - w^2\, \mathrm{e}^{-2\mathrm{i}\gamma}/\mu$. Neglecting the long-range hopping ($\kappa_{13} = 0$), only the hopping from site 1 to site 3 would have a complex amplitude. When the particle

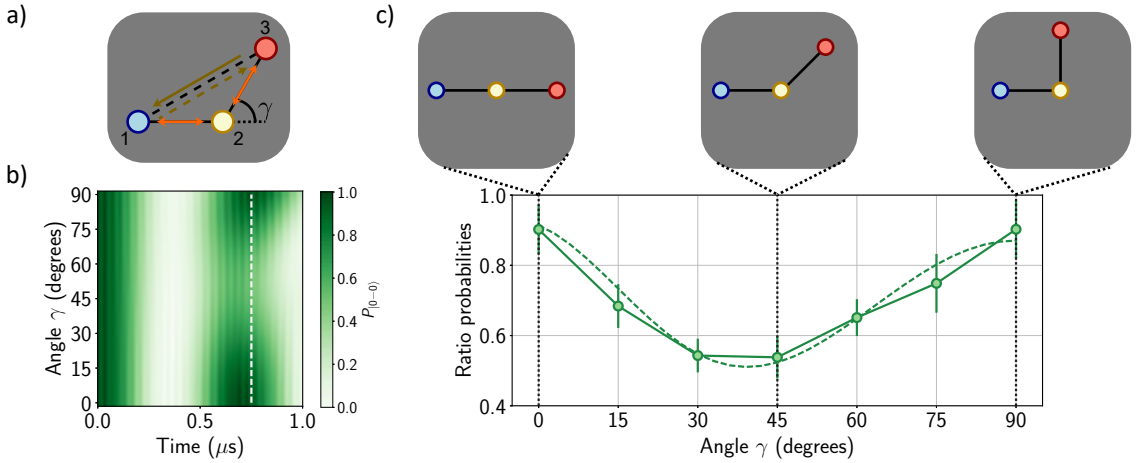

Figure 6.11: Hopping dynamics for various isosceles configurations. (a) Triangular configuration used for this experiment. (b) Computed probability to find a $|-\rangle$ particle on site 2, as a function of the interacting time τ and the angle γ, obtained by solving the Schrödinger equation for Hamiltonian (6.3). The dashed line indicates the time when the particle fully recombines on site 2 in the linear ($\gamma = 0$) configuration. (c) Probability to be in state $|010\rangle$ after $\tau = 1.0\,\mu$s, normalized by the same probability at time origin, as a function of the angle γ.

is circulating in the clockwise direction, it picks up a phase factor $e^{-2i\gamma}$ during the hopping from site 1 to site 3, whereas it picks up an opposite phase $e^{2i\gamma}$ while circulating in the anti-clockwise direction during the hopping from site 3 to site 1.

Figure 6.11(b) shows the computed probability to find the particle on site 2, as a function of the interaction time τ and the angle γ. As before, we obtained this probability via the resolution of the Schrödinger equation with Hamiltonian (6.3), for the same values for the hopping amplitudes and $\mu/h = 25\,\text{MHz}$. In the linear ($\gamma = 0$) configuration, the particle recombines back on site 2 in about $0.75\,\mu$s (this time is indicated as a white dashed line in the figure). At this specific time, the probability drops for $\gamma = \pi/4$ and is high again for $\gamma = \pi/2$. This can be interpreted with our interferometric argument. Back on site 2, the circulating wavefunctions exhibit a phase factor $e^{\pm 2i\gamma}$, and the probability to find the particle on this site at that specific recombination time is such that $P_{|0-0\rangle} \propto \left|e^{-2i\gamma} + e^{2i\gamma}\right|^2 \propto \cos^2(2\gamma)$. Consequently, for $\gamma = 0$ or $\gamma = \pi/2$, we expect a high population on site 2, whereas for $\gamma = \pi/4$ we expect a low population.

Observation of a geometry-dependent recombination These predictions are confirmed by the experiment (Figure 6.11(c)). We first observed the propagation of

the prepared $|-\rangle$ excitation in the $\gamma = 0$ case, and measure a recombination time $\tau = 1\,\mu$s, different from the one extracted from the simulations. Figure 6.11(c) shows the measured probability of the state $|010\rangle$ at time $\tau = 1\,\mu$s, divided by the same probability at origin $\tau = 0$, as a function of the angle γ. We observe the expected signal, bright fringes for $\gamma = 0$ or $\gamma = \pi/2$, and a dark fringe for $\gamma = \pi/4$. We normalize the probability of interest by the probability at origin to get rid off preparation and detection errors. The dashed line in Figure 6.11(c) is the probability computed for the recombination time in Figure 6.11(b). It is in a very good agreement with the experimental data.

In this isosceles configuration, the implemented Peierls phase depends on the localization of the particle (in our approximation $\kappa_{13} = 0$, the hopping amplitude is complex-valued only between site 1 and 3), whereas this was not the case for the equilateral triangle. Extending to the case of larger lattices composed of several plaquettes, we then expect than the fluxes enclosed by the different plaquettes are not equal, leading to inhomogeneous gauge fields, which is different from the artificial gauge fields generated by laser-assisted tunneling [Miyake *et al.*, 2013].

6.3.3 Two-excitation case

So far, we have explored the consequences of Hamiltonian (6.3) on a three-atom system, still in the single-particle regime. This Hamiltonian leads to a complex hopping amplitude, whose phase depends on the energy separation μ and the geometry. This phase was revealed by two types of experiment, the observation of a cyclotron orbit or an interferometric signal. Now, let us see what happens in the two-excitation case. More precisely, we want to briefly study the effect of the interactions (hard-core bosons) on the hopping dynamics.

Reversed motion for a hole in the $Je^{i\theta}$ model I first compare the hopping dynamics we expect while preparing the state $|011\rangle$, with the one preparing the state $|100\rangle$, considering the $Je^{i\theta}$ model (top of Figure 6.12(a)). For $\theta = 7\pi/6$, we find a circular motion in the anti-clockwise direction in the one-excitation case, as shown by the site-dependent probability to find a particle (highlighted with the filled area). For the same θ, starting with $|011\rangle$, i.e. a hole on site 1, the hole circulates in the other direction. This is explained by the hard-core constraint. The particles tend to circulate in the anti-clockwise direction. Starting from $|011\rangle$, the particle on site 2 cannot hop to site 3 as it is occupied, whereas the particle on site 3 can hop to site 1, and we

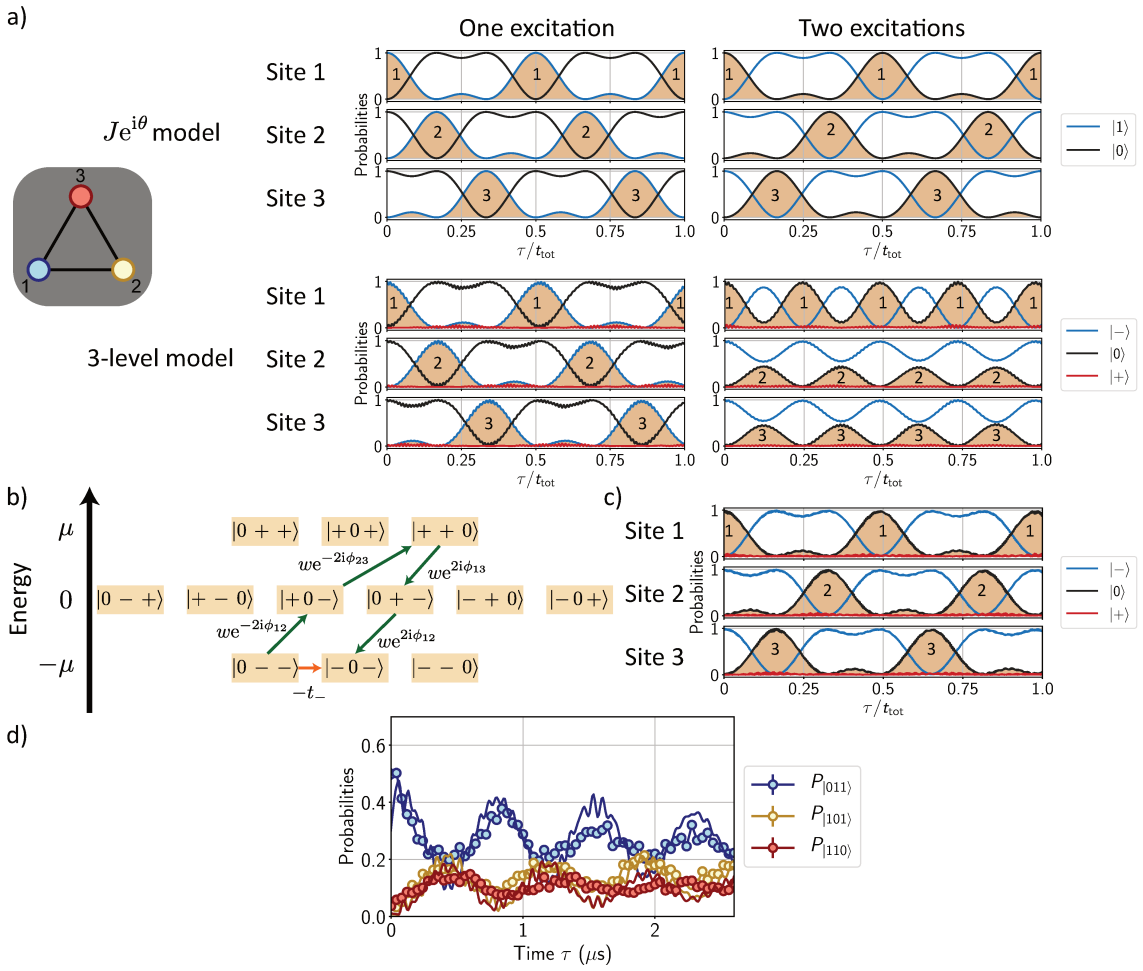

Figure 6.12: Two-excitation case. (a) Comparison of the one- and two-excitation cases, for the $Je^{i\theta}$ model or Hamiltonian (6.3). We plot as a function of time the site-dependent probabilities to be in the particle state ($|1\rangle$ or distinguishing between the spin states $|-\rangle$ and $|+\rangle$ for the three-level model) or the vacuum state $|0\rangle$. The total duration $t_{\rm tot}$ was set in order to have in the one-excitation case two cycles of the periodic motion. (b) Perturbative approach in the two-excitation case, revealing a fourth-order off-resonant process. (c) Same as (a) for Hamiltonian (6.3), but increasing both w and μ by a factor 210 to obtain again two cycles of the periodic motion of a hole. (d) Measured probabilities to be in the different two-excitation states as a function of time, after having prepared $|0--\rangle$, for the parameters corresponding to the circular motion in the single-excitation case.

obtain $|110\rangle$. This corresponds to the hopping of a hole from site 1 to site 3, so in the end the hole circulates in the reversed direction. This inversion of motion for a hole was observed experimentally in [Roushan *et al.*, 2017a] with superconducting qubits.

Hole propagation induced by Hamiltonian (6.3) I now compare the dynamics preparing $|-00\rangle$ or $|0--\rangle$ for Hamiltonian (6.3), with the same parameters as in Figure 6.9(c) and $\mu/h = 28\,\mathrm{MHz}$. In the one-excitation case, the excitation circulates in the anti-clockwise direction, but in the two-excitation case, the hole spreads symmetrically towards the two other sites (see Figure 6.12(a) bottom). This could seem unexpected because, as in the $Je^{i\theta}$ model, we have the hard-core constraint.

Dynamical gauge fields Actually, we found the correspondence between Hamiltonian (6.3) and the $Je^{i\theta}$ model using the perturbative approach, and considering the one-excitation manifold (see Subsection 6.2.2). We follow the same approach to predict the phase of the hopping amplitude in the two-excitation case (Figure 6.12(b)). For a hole to hop from site 1 to 2 while picking up a phase, we need four successive spin-flip hoppings, virtually going to the intermediate state $|++0\rangle$. As it is a fourth-order process, the phase of the total hopping amplitude is in the end $\propto w^4/(\mu^3 t_-)$, i.e. $\mu^2/w^2 \approx 100$ times smaller than the one in the one-excitation case. Consequently, the motion of a hole in the two-excitation case is still reproduced by the $Je^{i\theta}$ model, but for the same parameters t_-, t_+, w, μ the phase of the hopping amplitude is way smaller. Actually, the computed motion of the hole in that case show a slightly preferential motion towards site 3 rather than site 2 (see bottom right corner of Figure 6.12(a)).

We artificially increase the phase of the hopping amplitude in the two-excitation case by multiplying w by a factor 210, and we multiply by the same factor μ to still be in the perturbative regime. Under this non-realistic condition (there is no way to increase w while the other hopping amplitudes t_- and t_+ stay the same), and only for such a high multiplication factor, we retrieve a chiral motion of the hole, i.e. the same situation as in the one-excitation case, in the inverse direction (see Figure 6.12(c)). This high factor, found numerically, corresponds to the inhibition of the Peierls phase due to the second excitation.

In summary, we have seen that the phase of the hopping amplitude is not the same in the one- and two-excitation cases, because the off-resonant spin-flip hopping process which gives rise to this phase is a second-order process in the one-excitation case, whereas it is a fourth-order process in the two-excitation case. This result may be interpreted as a dynamical gauge field, as the artificial gauge field experienced by a

particle depends on the presence or not of other particles in the system. At the very end of the completion of this work, the effect of such a density-dependent Peierls phase was observed in preliminary experiments (Figure 6.12(d)), and we indeed measured a symmetric propagation of a hole after having prepared the $|0--\rangle$ state, whereas the motion of a single excitation was circular for the same energy separation. A similar density-dependent Peierls phase was recently engineered with ultracold fermions in the group of Prof. Tilman Esslinger [Görg *et al.*, 2019].

6.4 Conclusion

In this chapter, I have shown how the spin-flip hopping process, seen as a spin-orbit coupling encoded in the dipole-dipole interaction, leads to a topological band structure for Rydberg atoms in a honeycomb lattice. Treated in a perturbative way, the spin-flip hopping results in a complex hopping amplitude for the particle, experiencing an artificial gauge field. I presented the preliminary results of the observation of such a gauge field, in two types of experiments involving three Rydberg atoms: the cyclotron motion in an equilateral triangle and the geometry-dependent recombination of an excitation.

The next step is to study the hopping of a particle in larger systems, and to confirm the theoretical prediction of the presence of chiral edge modes in 10- and 31-site honeycomb lattices. The existence of chiral edge modes is a single-particle property, since it is deduced from the band structure of the system. The longer-term direction for future investigation is to inject several particles, and I already mention the two-particle case in a triangle. Reaching the many-body regime, the rich phase diagram of interacting topological insulators [Varney *et al.*, 2010; He *et al.*, 2015] holds the promise for the generation of exotic phases such as a bosonic fractional Chern insulator. In our previous study of a topological system, the SSH model, we followed the same approach [de Léséleuc *et al.*, 2019]. We started by studying the single-particle properties of the system and observed its edge states, and then reaching the many-body regime we generated a symmetry protected topological phase.

Chapter 7

Outlook

In this manuscript, I have presented several projects realized on our quantum simulation Rydberg-based platform. Some of them were technical improvements of the experimental apparatus, and I have reported the generation of fully-loaded atomic arrays held in optical tweezers, extended to 3D, and the demonstration of Rydberg atom trapping. The others concerned the quantum simulation of spin models or hopping Hamiltonians, where we studied the spin-spin correlations in Ising or XY magnets, and the implementation of complex hopping amplitude using the intrinsic spin-orbit coupling of the dipole-dipole interaction. I now describe the further projects the team will work on.

Chiral edge states and bosonic fractional Chern insulators One of them is the natural extension of the work presented in Chapter 6. After having demonstrated the implementation of complex hopping amplitude on a minimal system of three Rydberg atoms, the next step is to observe the chiral motion of the particle on the edge of larger systems, a 10- or 31-site honeycomb lattice. The presence of chiral edge states is a well-known property of topological insulators, in the single-particle regime, and has already been observed on several platforms, for example with photonic devices [Rechtsman *et al.*, 2013; Hafezi *et al.*, 2013] or with classical coupled mechanical oscillators [Süsstrunk and Huber, 2015].

On the other hand, studying the many-body regime is challenging, both theoretically and experimentally, and is a longer-term goal which could lead the team to observe exotic phenomena such as a bosonic fractional Chern insulator or anyonic excitations. The theoretical predictions are harder to derive in the many-body regime for our implementation with Rydberg atoms, as can already be expected from the discussion of the two-excitation case for a three-atom system at the end of Chapter 6. On the experimental side, studying the many-body regime would rely on the same kind of sweeps used in Chapter 5. We have seen there that the many-body ground state can be prepared if the coupling towards this state via a microwave field does not vanish due to antisymmetric superpositions of states. This needs to be checked in the

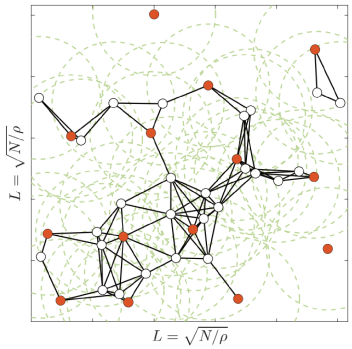

Figure 7.1: Finding the maximum independent set of a graph with Rydberg atoms. For a given graph composed of vertices (disks) and edges (solid lines), the maximum independent set is indicated (set of red filled disks). The green dashed lines are blockade radius circles, centred on each of the vertices. This figure is extracted from [Pichler *et al.*, 2018].

case of this Hamiltonian. Moreover, since we have to operate with a finite Zeeman splitting, realizing sweeps without populating the other spin component is difficult, in the same way as it is difficult to prepare one particle on a given site, as pointed out in Chapter 6. Solutions have been proposed in that case for a higher-fidelity preparation (controlling the polarization of the microwave field or quickly ramping the electric fields), which could also work for microwave sweeps, and still need to be implemented on our experimental platform.

Rydberg atoms and optimization problems In the work presented in Chapter 4, we were also aiming at generating the ground state of a Hamiltonian via a dynamical tuning of the parameters. In that case, we were implementing an Ising-like problem, originating from the Rydberg blockade occurring in the van der Waals interaction regime. The Rydberg blockade picture allows also to connect the interacting Rydberg atom problem to a paradigmatic optimization problem in computer science, finding the maximum independent set of a graph [Pichler *et al.*, 2018]. In a few words, this optimization problem consists in finding, for a given graph with known vertices and edges (connection between vertices), the largest set of vertices with no pair directly connected by an edge. Choosing an atomic configuration where the connected vertices have a large van der Waals interaction energy, corresponding to nearby atoms, the Rydberg blockade mechanism would prevent the excitation of connected vertices, and the ground state would correspond to the maximum independent set (see Figure 7.1).

We need to perform two improvements of the experimental setup to implement this

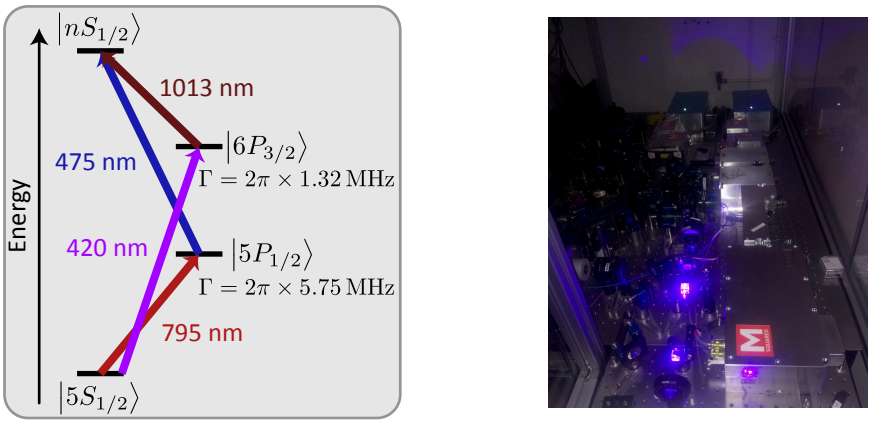

Figure 7.2: New laser setup for a different excitation scheme. (Left) States involved in the two-photon transitions towards Rydberg states. So far, we use the scheme using $|5P_{1/2}\rangle$ as the intermediate state, the inverted scheme consists in using $|6P_{3/2}\rangle$ instead. (Right) Picture of the two Ti-sapphire lasers used to generate the 420- and 1013-nm light.

type of optimization problem. First, as already explained in Chapter 4, the efficiency of the preparation of the many-body ground state in the van der Waals regime is limited by the imperfections of the two-photon laser-driving. The laser-driving should be more coherent by adopting the "inverted scheme" [Bernien *et al.*, 2017], with Ti-sapphire lasers instead of diode lasers. This new laser setup is currently being installed in the lab (see Figure 7.2). This new laser-driving should be more coherent for several reasons. First, since $|6P_{3/2}\rangle$ has a longer radiative lifetime than $|5P_{1/2}\rangle$ (almost five times as large), there will be approximately five times as less losses due to spontaneous emission. Second, we will reach higher Rabi frequencies for the transition from the intermediate state to the Rydberg state[1], since high powers are more easily generated at 1013 nm than at 475 nm. Finally, Ti-sapphire lasers are expected to exhibit a reduced phase noise with respect to diode lasers.

The second improvement of the experimental setup we need is more related to the specific optimization problem we want to study. In order to realize a given graph of vertices and edges, a fully loaded array of atoms in an arbitrary configuration is required, whereas our sorting algorithm is limited so far to the case of regular (Bravais) lattices. We then need to extend our sorting protocol to arbitrary geometries.

Optimal control protocol The new laser setup presented above is expected to lead to a higher fidelity for the preparation of the many-body ground state. To reach this

[1]The Rabi frequency for this transition was proven to be the limiting factor, see [de Léséleuc *et al.*, 2018a]

goal, the team also plans to implement optimal control protocols [Doria, Calarco, and Montangero, 2011; Heck *et al.*, 2018], as this was done in [Omran *et al.*, 2019] to generate large Schrödinger cat states with Rydberg atoms. These protocols rely on a feedback loop between our experimental apparatus measuring the fidelity of the prepared state and an algorithm optimizing the parameters. The group of Prof. Tommaso Calarco have developed a server where this type of algorithm is running, and we have already started, in collaboration with them, to work on linking our experimental apparatus to their server.

The same kind of feedback loop between the experiment and an optimization algorithm is required to perform the variational quantum simulation of many-body physics [Kokail *et al.*, 2019], and we also start a collaboration with the group of Prof. Peter Zoller in view of exploring this type of quantum simulation on our platform.

Implementing new types of interactions In Chapter 6, we have used for the first time the exchange terms of the dipole-dipole interaction involving a third Rydberg state to engineer complex hopping amplitudes. Similarly, we can engineer new types of interactions considering additional processes. For example, I mentioned in Chapter 3 that the interplay between the resonant dipole-dipole interaction and the vibrational modes of trapped Rydberg atoms may lead to an exotic three-body interaction [Gambetta *et al.*, 2019].

The van der Waals energy shift comes from a second-order perturbation treatment of the dipole-dipole interaction, modifying the energy of the considered Rydberg pair state. As the system experiences an energy shift without modifying its state, this perturbation is sometimes described by a diagonal C_6 coefficient. Other second-order processes exist, which were not yet mentioned in this manuscript. They imply that the system changes state, and are therefore described by an off-diagonal C_6 coefficient. These two types of second-order perturbations result in the implementation of the XXZ spin model [van Bijnen, 2013; Whitlock, Glaetzle, and Hannaford, 2017; Nguyen *et al.*, 2018], experimentally studied with a disorder ensemble of atoms [Signoles *et al.*, 2019]. The canonical form of the Hamiltonian is

$$\hat{H}_{\mathrm{XXZ}} = -J \sum_{i<j} \left(\hat{\sigma}_i^x \hat{\sigma}_j^x + \hat{\sigma}_i^y \hat{\sigma}_j^y + \delta\, \hat{\sigma}_i^z \hat{\sigma}_j^z \right), \tag{7.1}$$

where δ is known as the anisotropy coefficient (for $\delta = 0$, we retrieve the XY model), and depends on the ratio between diagonal and off-diagonal C_6 coefficients. A mid-term goal is to implement this Hamiltonian on our platform, extending the range of spin

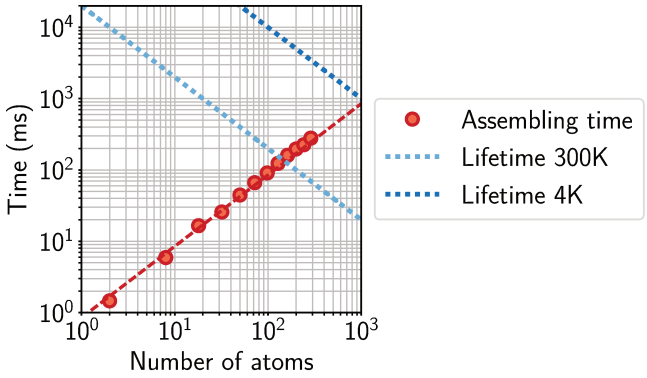

Figure 7.3: Towards larger systems. Comparison between the assembling time and the vacuum-limited lifetime of a configuration, as a function of the number of atoms.

Hamiltonians we can study.

Routes towards extending the number of spins The experiments reported in this manuscript, as well as recent experiments carried out by groups also working with Rydberg atoms, show that Rydberg-based platforms are attractive quantum simulators for various many-body problems. However so far, these experiments involve at most a few tens of spins, or qubits, in the more general context of quantum computing. One of the challenges for the community is to increase the number of interacting qubits.

To estimate the maximum size of the system experimentally achievable, one needs to compare the lifetime of the assembly of N atoms versus the duration of an experimental cycle (see Figure 7.3). The lifetime is proportional to the one of a single ground-state atom in the optical tweezers $\tau \approx 20\,\mathrm{s}$ (see Chapter 2), divided by the number of atoms, eventually leading to τ/N (blue dotted line). The finite value of τ is due to collisions with the remaining background gas. The experimental cycle time is given by the necessary time to fully load an array of N traps (red dashed line), and grows as N (see [Barredo *et al.*, 2016]). The intersection between the two lines means that the current limit in terms of number of qubits is ≈ 100.

Our team is developing a next generation experimental apparatus, whose major upgrade is the use of a cryogenic environment [Magnan, 2018]. We expect that this will lead to a considerably lower background gas pressure and an extended lifetime (darker blue dotted line), and in the end atom numbers in the range of one thousand qubits should be achievable. To reach this goal, the team also plan to implement new sorting algorithms to have a faster assembling procedure for fully-loaded arrays of atoms.

In the end, Rydberg-based platforms hold the promise for exciting prospects. We first expect to explore exotic phenomena reaching the many-body ground state of interacting systems. We should also reach higher fidelity by using another laser setup, or by implementing optimal control protocol. Finally, we expect the scalability to a larger number of qubits by designing new cryogenic experimental apparatuses. One hint of the attractiveness of Rydberg-based platforms as quantum simulators is that several versions of this platform are being developed in many labs around the world, and that companies are now investing on this type of platform.

Appendix A

From Rydberg atoms to spins or hard-core bosons

In this Appendix, I will explain how a system of interacting Rydberg atoms can be seen as a system of spins or hopping hard-core bosons. The targeted Hamiltonian involve genuine two-level systems, spins-1/2 or lattice sites hosting hard-core bosons. Consequently, such a connection is possible if the Rydberg interacting dynamics can fully be described using only two atomic states, which will be shown in this part. Then, rewriting the interaction in terms of spin or bosonic operators ensures the mapping to the targeted model situation.

Origin of the Rydberg-Rydberg interaction In the experiments described in this manuscript, the minimal distance between Rydberg atoms is about $5\,\mu$m. As this distance is still larger than the electronic wavefunction size even for large n, the interaction originates from the dipole-dipole interaction. For two atoms, labeled as i and j, this interaction reads

$$\hat{V}_{\text{ddi}} = \frac{1}{4\pi\epsilon_0}\frac{\hat{\mathbf{d}}_i \cdot \hat{\mathbf{d}}_j - 3\left(\hat{\mathbf{d}}_i \cdot \mathbf{n}\right)\left(\hat{\mathbf{d}}_j \cdot \mathbf{n}\right)}{R^3},$$

with $\hat{\mathbf{d}}_i$ being the electric dipole operator of atom i, R the distance between the atoms and $\mathbf{n} = \mathbf{R}/R$. As $\left|\hat{\mathbf{d}}\right|$ scales as n^2, we can reach large interaction values using Rydberg atoms.

Depending on the Rydberg states involved, that is to say depending on the two atomic levels we use to encode a qubit, different regimes of interaction will have to be considered. Here I will focus on the van der Waals and the resonant dipole-dipole regimes.

The van der Waals regime We first consider two atoms in the same Rydberg state, characterized by a set of quantum numbers $|n, l, j, m_j\rangle$ gathered in the simplified notation $|\alpha\rangle$. Without any interaction, the pair state $|\alpha\alpha\rangle$ would be an eigenstate of the

two-atom system. In most cases, $|\alpha\alpha\rangle$ is not degenerate with another pair of Rydberg states $|\beta\gamma\rangle$ and the effect of interaction can be treated using a perturbative approach. To first order, there is no energy shift. Indeed, as $\hat{V}_{\text{ddi}}$ is an odd-parity operator and $|\alpha\alpha\rangle$ has a defined parity, $\langle\alpha\alpha|\,\hat{V}_{\text{ddi}}\,|\alpha\alpha\rangle = 0$. The second-order perturbation theory enables the computation of an energy shift for the $|\alpha\alpha\rangle$ state

$$\Delta E_{\alpha\alpha} = \sum_{\langle\beta,\gamma\rangle} \frac{\left|\langle\alpha\alpha|\,\hat{V}_{\text{ddi}}\,|\beta\gamma\rangle\right|^2}{E_{\alpha\alpha} - E_{\beta\gamma}},$$

where the sum runs over all the pair states coupled to $|\alpha\alpha\rangle$ via the dipole-dipole interaction.

This shift depends on the distance between the atoms; being second order in $\hat{V}_{\text{ddi}}$, it scales as $1/R^6$, this is why it is called the van der Waals interaction. It also depends on the Rydberg state $|\alpha\rangle$, and possibly on the orientation of the internuclear axis with respect to the quantization axis (in the specific case of nS states, it is isotropic). We usually write the shift $\Delta E_{\alpha\alpha} = C_6/R^6$. It can vary by orders of magnitude as the C_6 coefficient scales as n^{11}, resulting in a high tunability of the interaction energy between Rydberg atoms. In the work presented here, we have been working with interactions ranging from 1 to 10 MHz for a typical interatomic distance of 10 μm.

We now consider N atoms, restricting ourselves to two levels : the electronic ground state $|g\rangle$ and a Rydberg state $|r\rangle$. We can operate such a restriction because the interaction simply results in an energy shift of the Rydberg pair states while the two-atom eigenstate stay close to the unperturbed state $|rr\rangle$. This enables the encoding of a qubit, in the two-level basis $\{|g\rangle, |r\rangle\}$. As the interactions between two ground-state atoms or between one ground-state and one Rydberg atoms are negligible compared to the one between two Rydberg atoms, the interaction Hamiltonian in the van der Waals regime simply reads

$$\hat{H}_{\text{int}} = \sum_{i<j} \frac{C_6}{R_{ij}^6}\,\hat{n}_i\hat{n}_j,$$

where the sum runs over every pair of atoms labeled i,j. Here, $\hat{n}_i = |r\rangle_i\,\langle r|_i$ is the Rydberg projector operator acting on atom i.

As stated in Chapter 2, we use a laser driving, with a Rabi frequency Ω and a detuning δ, to couple the states $|g\rangle$ and $|r\rangle$. It acts as a global rotation operator for all the qubits. In the end, the total Hamiltonian on this assembly of two-level systems reads in the rotating wave approximation

$$\hat{H} = \sum_i^N \left(\frac{\hbar\Omega}{2} \left(|r\rangle_i \langle g|_i + |g\rangle_i \langle r|_i \right) - \hbar\delta\, \hat{n}_i \right) + \sum_{i<j} \frac{C_6}{R_{ij}^6}\, \hat{n}_i \hat{n}_j. \tag{A.1}$$

It turns out, as we shall see soon, that this Hamiltonian corresponds to an Ising-like model.

The resonant dipole-dipole interaction We now consider two atoms in different Rydberg states, $|\alpha\rangle$ and $|\beta\rangle$. Without any interaction, an eigenstate of the two-atom system is again the product state $|\alpha\beta\rangle$, but in that case, it is degenerate with the other eigenstate $|\beta\alpha\rangle$. Consequently, if the dipole-dipole interaction couples the two two-atom states, a perturbative approach is no longer possible. We can write the interaction restricting ourselves to the basis $\{|\alpha\beta\rangle, |\beta\alpha\rangle\}$

$$\hat{V}_{\text{ddi}} = \frac{C_3}{R^3} \left(|\alpha\beta\rangle \langle\beta\alpha| + |\beta\alpha\rangle \langle\alpha\beta| \right),$$

where we use again a coefficient, C_3, to take into account the specific values of the dipole moments of the Rydberg states involved. Here, the interaction is longer-range and decays as $1/R^3$. It depends also on the orientation of the internuclear axis with respect to the quantization axis, I give more details about this dependence in Chapter 5. The coefficient C_3 scales as n^4, ensuring again the tunability of the interaction energy between Rydberg atoms. We reach interaction on the MHz range for typical distance of $20\,\mu$m.

We have mostly used in this work for $|\alpha\rangle$ and $|\beta\rangle$ the two dipole-coupled states nS and $n'P$, which we will write $|nS\rangle = |a\rangle$ and $|n'P\rangle = |b\rangle$ for simpler notations. The energy separation being in the ten of GHz range, we use a microwave field to couple these two states, acting again as a rotation operator for the qubits encoded in the two-level basis $\{|a\rangle, |b\rangle\}$.

In the end, considering N atoms, restricting ourselves for one atom to the qubit basis, we obtain the following total Hamiltonian in the rotating wave approximation

$$\begin{aligned} \hat{H} = &\sum_i^N \left(\frac{\hbar\Omega_{\mu\text{w}}}{2} \left(|b\rangle_i \langle a|_i + |a\rangle_i \langle b|_i \right) - \hbar\delta_{\mu\text{w}}\, |b\rangle_i \langle b|_i \right) \\ &+ \sum_{i<j} \frac{C_3}{R_{ij}^3} \left(|a\rangle_i \langle b|_i \otimes |b\rangle_j \langle a|_j + |b\rangle_i \langle a|_i \otimes |a\rangle_j \langle b|_j \right). \end{aligned} \tag{A.2}$$

This Hamiltonian can be seen either as the spin XY-model, either as the Bose-Hubbard

model for hard-core bosons.

To conclude on this description of the interaction between Rydberg atoms, I have shown that in two different regimes we can write the Hamiltonian considering only two atomic levels, encoding that way qubits. In addition to the interacting term, both Hamiltonians (A.1) and (A.2) feature a single-qubit rotation operator coming from the coupling to an external field. Now, to map the interacting Rydberg atom problem into spin-1/2 or hard-core boson Hamiltonians, we can rewrite these Hamiltonians using spin or bosonic operators.

An Ising-like model In the van der Waals regime, the encoded qubit basis can be mapped into the spin-1/2 basis $\{|g\rangle, |r\rangle\} = \{|\downarrow\rangle, |\uparrow\rangle\}$. Then, $|r\rangle_i \langle g|_i + |g\rangle_i \langle r|_i = |\uparrow\rangle_i \langle\downarrow|_i + |\downarrow\rangle_i \langle\uparrow|_i = \hat{\sigma}_i^x$ and $\hat{n}_i = (1 + \hat{\sigma}_i^z)/2$. To some constants, Hamiltonian (A.1) finally reads

$$\hat{H} = \sum_i^N \left(\frac{\hbar\Omega}{2} \hat{\sigma}_i^x - \frac{\hbar}{2} \left(\delta - \frac{C_6}{2\hbar} \sum_{j \neq i} \frac{1}{R_{ij}^6} \right) \hat{\sigma}_i^z \right) + \sum_{i<j} \frac{C_6}{4R_{ij}^6} \hat{\sigma}_i^z \hat{\sigma}_j^z, \tag{A.3}$$

which is an implementation of an Ising-like model. We have indeed an interaction term $\propto \hat{\sigma}_i^z \hat{\sigma}_j^z$, and a global rotation due to an external effective magnetic field. The transverse field along x is proportional to the Rabi frequency, whereas the longitudinal field along z does not depend only on the detuning δ, there is an added inhomogeneous component. As the longitudinal field is not homogeneous, we do not implement strictly speaking the Ising model but an Ising-like model.

XY model We follow the same procedure to link Hamiltonian (A.2) to the XY model. Here, the mapping consists in considering the $|b\rangle$ state as the $|\uparrow\rangle$ state, and the $|a\rangle$ state as the $|\downarrow\rangle$ state. Hamiltonian (A.2) involves the raising and lowering spin operators $|b\rangle_i \langle a|_i = |\uparrow\rangle_i \langle\downarrow|_i = \hat{\sigma}_i^+$ and $|a\rangle_i \langle b|_i = |\downarrow\rangle_i \langle\uparrow|_i = \hat{\sigma}_i^-$. It finally gives

$$\hat{H} = \sum_i^N \left(\frac{\hbar\Omega_{\mu\mathrm{w}}}{2} \hat{\sigma}_i^x - \frac{\hbar\delta_{\mu\mathrm{w}}}{2} \hat{\sigma}_i^z \right) + \sum_{i<j} \frac{C_3}{R_{ij}^3} \left(\hat{\sigma}_i^- \hat{\sigma}_j^+ + \hat{\sigma}_i^+ \hat{\sigma}_j^- \right). \tag{A.4}$$

As $\hat{\sigma}_i^- \hat{\sigma}_j^+ + \hat{\sigma}_i^+ \hat{\sigma}_j^- = \hat{\sigma}_i^x \hat{\sigma}_j^x + \hat{\sigma}_i^y \hat{\sigma}_j^y$, we have indeed implemented the XY model with an effective external field such that $B_\perp \propto \Omega_{\mu\mathrm{w}}$ and $B_\parallel \propto \delta_{\mu\mathrm{w}}$.

Hard-core boson Hamiltonian I have already explained in Section 1.1 how the XY model and hard-core boson hopping Hamiltonian describe the same situation.

Linking the encoded qubit basis $\{|a\rangle, |b\rangle\}$ to the one of a lattice site occupied by hard-core bosons $\{|0\rangle, |1\rangle\}$ leads to rewrite Hamiltonian (A.2) in terms of creation and annihilation bosonic operators. Then, $|nS\rangle = |a\rangle$ and $|b\rangle = |1\rangle = \hat{b}^\dagger |0\rangle$, with $\left(\hat{b}^\dagger\right)^2 = 0$. The Hamiltonian will read

$$\hat{H} = \sum_i^N \left(\frac{\hbar\Omega_{\mu\mathrm{w}}}{2} \left(\hat{b}_i^\dagger + \hat{b}_i \right) - \hbar\delta_{\mu\mathrm{w}}\, \hat{b}_i^\dagger \hat{b}_i \right) + \sum_{i<j} \frac{C_3}{R_{ij}^3} \left(\hat{b}_i \hat{b}_j^\dagger + \hat{b}_i^\dagger \hat{b}_j \right). \tag{A.5}$$

The first term proportional to $\Omega_{\mu\mathrm{w}}$ reflects the possibility to coherently add or remove particles in the lattice, the second term proportional to $\delta_{\mu\mathrm{w}}$ acts as a chemical potential setting the number of particles, and the last term holds for the ability for one particle to hop between sites i and j via the resonant dipole-dipole interaction.

Appendix B

Résumé en français

Depuis plusieurs décennies, les physiciens ont appris à isoler et contrôler des objets quantiques individuels, et ont observé sur ces objets les propriétés quantiques fondamentales, comme la superposition d'états ou l'intrication. Ces premières démonstrations expérimentales ont déclenché l'apparition des technologies quantiques. Elles consistent, à l'aide d'un ensemble contrôlé d'objets quantiques individuels en interaction, à mettre en œuvre des algorithmes plus puissants que ceux utilisés sur des dispositifs classiques, pour diverses applications. Une de ces applications est la simulation quantique, ayant pour but d'étudier des problèmes à N corps, grâce à de tels ensembles de particules en interaction.

Des atomes individuels piégés dans des matrices de pinces optiques et excités vers des états de Rydberg forment une plateforme expérimentale performante pour la simulation quantique de problèmes à N corps, comme le confirment les récents progrès dans le domaine. Le but de cette thèse est de décrire plusieurs expériences de simulation quantique réalisées sur ce type de plateformes, montrant qu'il est possible d'étudier des phénomènes à N corps tels que les phases ordonnées de spins, ou la matière topologique, grâce à ces systèmes artificiels. Le travail présenté peut se diviser en trois parties : la première traite du dispositif expérimental permettant de produire des matrices d'atomes uniques, la seconde de la génération d'états multi-atomes corrélés, pouvant se voir comme des phases ordonnées de spins, et la troisième de l'émergence d'un champ de jauge artificiel pour des atomes de Rydberg.

Partie I: Matrices d'atomes uniques

Chapitre 2 Ce chapitre décrit l'ensemble du système expérimental, composé d'atomes individuels de Rubidium 87, piégés dans leur état fondamental dans des matrices de pinces optiques, et excités vers des états de Rydberg. Tout d'abord, je présente la brique élémentaire de notre dispositif, à savoir le piégeage et l'imagerie d'un atome unique dans une pince optique, technique qui a été pour la première fois démontrée

dans notre laboratoire il y a une vingtaine d'années. Ensuite, la génération de matrices de pinces optiques, à l'aide de techniques holographiques, dans des configurations à une, deux ou trois dimensions, toutes occupées par des atomes individuels, est expliquée. Ce procédé, nécessaire pour l'étude de problèmes à N corps, a été développé lors de la première moitié de mon doctorat. Enfin, je décris le dispositif d'excitation des atomes vers des états de Rydberg, autre ingrédient essentiel pour la réalisation d'expériences de simulation quantique sur notre plateforme, puisque cette excitation donne naissance á des interactions entre atomes mesurables. Les deux procédés d'excitation, par pulse π ou par STIRAP, utilisés dans les différentes parties du manuscrit, sont présentés.

Chapitre 3 Ce chapitre décrit la dernière évolution de notre dispositif expérimental en date : le piégeage d'atomes uniques alors qu'ils sont excités dans un état de Rydberg. Les atomes dans un état de Rydberg sont soumis à la force pondéromotrice, ce qui implique qu'ils sont chassés des zones de haute intensité lumineuse. Pour les piéger, il faut donc produire une zone sombre entourée de lumière ("bottle beam" en anglais, ou faisceau creux). Après avoir expliqué la génération de tels faisceaux creux par holographie, et montré les signes expérimentaux du piégeage des atomes dans l'état de Rydberg, je présente une étude mêlant résulats expérimantaux et simulations numériques pour caractériser le piège ainsi créé en terme de profondeur de potentiel, de durée de vie et de fréquences de piégeage, en fonction du nombre quantique principal de l'état de Rydberg. Le chapitre se termine par la description de deux expériences, une oscillation de Rabi dans le domaine des micro-ondes et une interaction d'échange de spins, réalisées avec des atomes de Rydberg piégés. La première est une opération récurrente lorsqu'il s'agit de simuler des Hamiltoniens de type XY (voir le Chapitre 5), et la deuxième est un effet de l'interaction dipolaire résonnante. L'observation de ces deux résultats valide l'utilisation de notre technique de piégeage pour de futures expériences de simulation quantique de l'Hamiltonien XY.

Partie II: Phases ordonnées de spins

Chapitre 4 Ce chapitre inaugure la partie consacrée à la création de phases ordonnées de spins. Il débute par la présentation de deux concepts essentiels pour la compréhension du chapitre : la similitude entre l'interaction de van der Waals entre atomes de Rydberg et le modèle de Ising, et la notion de variation temporelle de l'Hamiltonien pour créer un état multi-particules corrélé, induit par les interactions. Cette dernière notion de variation temporelle, proche du concept de passage adiabatique, est aussi au cœur du

Chapitre 5.

Suite à ces concepts génŕaux, j'explique de manière plus détaillée comment une phase antiferromagnétique peut être observée sur notre plateforme. Il faut d'abord s'assurer que l'interaction entre atomes de Rydberg se résume bien à une contrainte de blocage et ne fait intervenir qu'un seul niveau de Rydberg. Dès lors, cette interaction donne lieu à un diagramme de phase de type Ising, lorsqu'elle est mise en compétition avec un champ magnétique effectif, qui est dans notre implémentation le champ d'excitation laser vers le niveau de Rydberg. Je montre alors numŕiquement qu'une variation de désaccord laser, suffisamment lente pour respecter la contrainte adiabatique, permet le passage d'une configuration triviale (tous les atomes sont dans leur état fondamental) à une configuration antiferromagnétique (alternance entre atomes dans leur état fondamental et dans l'état de Rydberg), si le désaccord laser final se trouve bien dans le domaine de stabilité de la phase antiferromagnétique.

La suite du chapitre présente l'observation expérimentale d'une telle phase antiferromagnétique suite à une variation du désaccord laser dans une matrice carrée de 36 atomes. Le changement du désaccord laser final permet de mesurer le domaine d'existence de cette phase antiferromagnétique. La modification de la durée de la variation du désaccord laser met quant à elle au jour une durée optimale. Si cette durée est trop courte, l'évolution n'est pas adiabatique et le système n'atteint pas l'état d'équilibre. Si elle est trop longue, l'évolution n'est pas cohérente à cause des phénomènes de déphasage inhérents à notre dispositif d'excitation laser, et le système n'atteint pas non plus la phase antiferromagnétique. Le taux de décohérence de notre dispositif d'excitation laser a été mesuré grâce à l'étude d'oscillations de Rabi d'atomes uniques. La valeur expérimentale de ce taux a été incluse dans une simulation numérique non-unitaire de l'évolution du système multi-particule qui reproduit bien les données. Pour une durée optimale de 1 μs, nous produisons un état antiferromagnétique caractérisé par une longueur de corrélation de 1,5 sites.

La fin du chapitre se consacre à l'étude de l'établissement des corrélations antiferromagnétiques au cours de l'évolution de durée optimale. Cette étude expérimentale met au jour une vitesse finie pour la propagation des corrélations au sein du système, bien reproduite par une approximation linéaire d'ondes de spins. Cette vitesse finie est liée au concept plus général de bornes de Lieb-Robinson. Le processus d'établissement des corrélations, qui se propagent de proches en proches, permet d'expliquer la structure spatiale des corrélations observées dans le cas de configuration carrée ou triangulaire. Ce processus de croissance site-à-site des corrélations est celui en œuvre au début de l'évolution unitaire du système. L'établissement des corrélations qui conduirait à celles

caractéristiques de l'état fondamental dans une configuration triangulaire est quant à lui un processus plus long, qui n'a pas pu être observé sur notre plateforme à cause du trop court temps de cohérence.

Chapitre 5 Si le modèle de Ising est aujourd'hui étudié par de nombreux groupes à l'aide d'atomes de Rydberg, ce n'est pas le cas du modèle XY, qui peut être simulé en utilisant un autre régime d'interaction que celui de van der Waals, le régime dipolaire résonnant. Ce chapitre présente une étude préliminaire de ce modèle avec des atomes de Rydberg.

Tout d'abord, pour travailler avec cet autre Hamiltonien, la base à deux niveaux à utiliser, qui imite celle du spin-1/2 simulé, comporte deux états de Rydberg de parités différentes, ce qui implique des opérations expérimentales supplémentaires (excitation de l'ensemble des atomes vers un état de Rydberg puis manipulation via un champ micro-onde couplant ces deux états de Rydberg) par rapport aux études sur le modèle d'Ising. Ces opérations sont présentées en début de chapitre. Je décris alors l'interaction dipôle-dipôle dans le système le plus simple, c'est-à-dire entre deux atomes. Ce cas simple permet d'aborder les notions essentielles pour la compréhension du chapitre. Dans le modèle XY, comme son nom l'indique, les corrélations significatives entre spins sont celles entre leurs composantes équatoriales, ce qui nécessite une rotation de la base de lecture. Les états propres de l'Hamiltonien sont des états où les excitations de spins sont délocalisées, correspondant soit à des superpositions d'états symmétriques (les corrélations XY sont alors positives, on parle d'un ferromagnétique XY) ou antisymmétriques (les corrélations XY sont négatives et nous sommes en présence d'un antiferromagnétique XY). Le but du chapitre est donc d'observer ces corrélations ferro- ou antiferromagnétiques sur notre plateforme à l'aide d'une variation temporelle de l'Hamiltonien (contrairement au chapitre précédent, c'est ici le champ micro-onde que l'on fait varier, il joue le rôle de champ magnétique effectif).

Avant de mesurer ces corrélations, je montre qu'il est possible de contrôler le nombre d'excitations de spins dans des chaînes d'atomes (4 ou 8 atomes dans une chaîne linéaire, et 14 atomes dans une chaîne dimérisée), en faisant varier la valeur finale du désaccord micro-onde du balayage en fréquences. Les résultats observés sont en accord avec des simulations numériques unitaires de l'évolution du système, ce qui n'était pas le cas dans le chapitre précédent, comme une source laser est moins cohérente qu'une source micro-onde. La préparation d'états à nombre contrôlé d'excitations permet donc d'observer des plateaux de magnétisation, et valide l'utilisation de notre protocole pour créer des états multi-particules à l'aide d'une variation de champ micro-onde.

Enfin, la dernière partie du chapitre est consacrée à l'étude des corrélations de type XY. D'abord, sur les chaînes d'atomes étudiées précédemment, nous avons pu oberver les corrélations caractéristiques d'un ferromagnétique XY, mais pas celles d'un antiferromagnétique. En effet, les états antiferromagnétiques étant des superpositions antisymmétriques d'états, le couplage par micro-ondes (qui lui est un opérateur symmtrique) vers ces états est inhibé, alors que le couplage vers des états ferromagnétiques est augmenté. Ceci explique pourquoi les ferromagnétiques ont pu être observés sur notre plateforme et pas les antiferromagnétiques. Cette observation expérimentale a été confirmée par une simulation numérique, montrant qu'il faudrait des variations temporelles d'Hamiltonien environ dix fois plus longues pour atteindre l'état antiferromagnétique du fait de ce couplage inhibé. Ces échelles de temps ne sont pour l'instant pas accessibles sur notre plateforme. Néanmoins, il nous a été possible d'observer des corrélations de type antiferromagnétique dans une matrice carrée à 16 atomes, comportant deux genres de liens du fait de l'anisotropie de l'interaction dipôle-dipôle : des liens verticaux ferromagnétiques et horizontaux antiferromagnétiques. Nous avons ainsi observé une phase comportant des chaînes verticales ferromagnétiques anti-alignées deux-à-deux, qui a été produite grâce au couplage non-négligeable via la partie ferromagnétique de cette phase hybride.

Partie III: Vers de la matière topologique à deux dimensions

Chapitre 6 Ce dernier chapitre traite de l'émergence d'un champ de jauge pour les excitations portées par les atomes de Rydberg. En utilisant à nouveau la base comportant deux niveaux de Rydberg de parité différente, si l'on prépare un des atomes dans l'état excité, cette excitation va passer d'un atome à l'autre sous l'effet de l'interaction dipolaire résonnante. Cet effet, qu'on appelle échange de spins, permet d'étudier à l'aide d'atomes de Rydberg les phénomènes de transport, l'excitation étant vue comme une particule se déplaçant entre les sites des atomes piégés.

Le chapitre débute par la description de ces effets d'échange de spins en considérant l'ensemble des six niveaux internes de la structure atomique des atomes de Rydberg. Notamment, certains termes de l'interaction dipôle-dipôle modifient le moment interne de la particule échangée, et s'accompagnent d'une amplitude de saut complexe par conservation du moment cinétique total, ce qui rappelle un couplage spin-orbite. Ces termes sont à l'origine du champ de jauge vu par les particules effectives. Je présente ensuite l'effet des ces termes d'échange dans le cas le plus simple, celui à deux particules, ainsi que la préparation d'une excitation localisée à l'aide d'un faisceau

d'addressage.

La suite du chapitre montre comment, en considérant un modèle d'interaction faisant intervenir trois niveaux de Rydberg, les termes d'échange à amplitude complexe mènent à l'observation possible d'états de bords chiraux dans des résaux de type graphène. Cette idée a d'abord été développée par nos collègues théoriciens, nous la revisitons ici en ajoutant un traitement pertubatif du problème. Ce traitement permet de retrouver un modèle d'interaction à deux niveaux, avec une particule se propageant de site en site avec une amplitude de saut complexe, correspondant à l'émergence d'un champ de jauge. Le modèle perturbatif reproduit bien numériquement la propagation d'une particule sur un réseau de type graphène qui avait été calculée par nos collègues à l'aide du modèle à trois niveaux, ce qui justifie son utilisation. De plus, il permet de comprendre pourquoi notre système montre de telles propriétés topologiques (la propagation d'états de bords chiraux). En effet, le modèle perturbatif fait le lien entre l'Hamiltonien décrivant notre système et le modèle de Haldane, qui a été conçu pour accueillir de tels états topologiques.

Le chapitre se termine par la démonstration expérimentale de l'émergence de ce champ de jauge, dans un système de trois atomes, grâce à l'observation du déplacement de la particule, en début d'expérience localisée sur un site. Sous l'effet de l'amplitude de saut complexe, pouvant être considérée ici comme un champ magnétique artificiel par effet Aharonov-Bohm, la particule se déplace préférentiellement dans une direction, direction que l'on peut inverser si on change le sens du champ magnétique artificiel. La démonstration se poursuit en étudiant un autre facteur contrôlant la valeur du champ de jauge créé, la disposition relative des trois atomes. C'est ainsi que nous observons la recombinaison d'une excitation initialement prépar'ee sur le site intermédiaire, pour différents angles de la configuration. Enfin, l'effet de la présence d'une deuxième particule est étudié. Cette deuxième particule change le champ de jauge créé, et l'état absence de particule, ou trou, se propage symétriquement au sein du triangle. Cela s'explique par le fait qu'en présence de deux particules, le système doit suivre de multiples processus de sauts pour avoir au final une amplitude de saut effectif complexe, ce qui rend le champ de jauge émergent négligeable.

Bibliography

Aharonov, Y. and Bohm, D., *"Significance of electromagnetic potentials in the quantum theory,"* Phys. Rev. **115**, 485 (1959) [cited in page 156].

Aidelsburger, M., Atala, M., Nascimbène, S., Trotzky, S., Chen, Y.-A., and Bloch, I., *"Experimental realization of strong effective magnetic fields in an optical lattice,"* Phys. Rev. Lett. **107**, 255301 (2011) [cited in page 157].

Aidelsburger, M., Nascimbène, S., and Goldman, N., *"Artificial gauge fields in materials and engineered systems,"* Comptes Rendus Physique **19**, 394 (2018) [cited in page 15].

Anderson, P. W., *"The resonating valence bond state in La_2CuO_4 and superconductivity,"* Science **235**, 1196 (1987) [cited in page 120].

Anderson, S. E., Younge, K. C., and Raithel, G., *"Trapping Rydberg atoms in an optical lattice,"* Phys. Rev. Lett. **107**, 263001 (2011) [cited in page 60].

Andor, *"iXon Ultra 897 Hardware User Guide,"* [cited in page 32].

Archimi, M., Simonelli, C., Di Virgilio, L., Greco, A., Ceccanti, M., Arimondo, E., Ciampini, D., Ryabtsev, I. I., Beterov, I. I., and Morsch, O., *"Measurements of single-state and state-ensemble lifetimes of high-lying Rb Rydberg levels,"* Phys. Rev. A **100**, 030501 (2019) [cited in page 70].

Arute *et al.*,, *"Quantum supremacy using a programmable superconducting processor,"* Nature **574**, 505 (2019) [cited in page 12].

Asbóth, J. K., Oroszlány, L., and Pályi, A., A Short Course on Topological Insulators (Springer, Cham, 2016) [cited in pages 139 and 140].

Ashkin, A., Dziedzic, J. M., Bjorkholm, J. E., and Chu, S., *"Observation of a single-beam gradient force optical trap for dielectric particles,"* Opt. Lett. **11**, 288 (1986) [cited in page 28].

Aspect, A., Grangier, P., and Roger, G., *"Experimental realization of Einstein-Podolsky-Rosen-Bohm gedankenexperiment: A new violation of Bell's inequalities,"* Phys. Rev. Lett. **49**, 91 (1982) [cited in page 11].

Atala, M., Aidelsburger, M., Barreiro, J. T., Abanin, D., Kitagawa, T., Demler, E., and Bloch, I., *"Direct measurement of the Zak phase in topological Bloch bands,"* Nature Physics **9**, 795 (2013) [cited in page 17].

Autler, S. H. and Townes, C. H., *"Stark effect in rapidly varying fields,"* Phys. Rev. **100**, 703 (1955) [cited in page 55].

Bakr, W. S., Gillen, J. I., Peng, A., Fölling, S., and Greiner, M., *"A quantum gas microscope for detecting single atoms in a Hubbard-regime optical lattice,"* Nature **462**, 74 (2009) [cited in page 17].

Balents, L., *"Spin liquids in frustrated magnets,"* Nature **464**, 199 (2010) [cited in page 120].

Barends, R., Kelly, J., Megrant, A., Sank, D., Jeffrey, E., Chen, Y., Yin, Y., Chiaro, B., Mutus, J., Neill, C., O'Malley, P., Roushan, P., Wenner, J., White, T. C., Cleland, A. N., and Martinis, J. M., *"Coherent Josephson qubit suitable for scalable quantum integrated circuits,"* Phys. Rev. Lett. **111**, 080502 (2013) [cited in page 19].

Barends, R., Kelly, J., Megrant, A., Veitia, A., Sank, D., Jeffrey, E., White, T. C., Mutus, J., Fowler, A. G., Campbell, B., Chen, Y., Chen, Z., ,, Chiaro, B., Dunsworth, A., Neill, C., O'Malley, P., Roushan, P., Vainsencher, A., Wenner, J., Korotkov, A. N., Cleland, A. N., and Martinis, J. M., *"Superconducting quantum circuits at the surface code threshold for fault tolerance,"* Nature **508**, 500 (2014) [cited in page 12].

Barredo, D., Labuhn, H., Ravets, S., Lahaye, T., Browaeys, A., and Adams, C. S., *"Coherent excitation transfer in a spin chain of three Rydberg atoms,"* Phys. Rev. Lett. **114**, 113002 (2015) [cited in pages 22, 60, 81, 121, and 122].

Barredo, D., de Léséleuc, S., Lienhard, V., Lahaye, T., and Browaeys, A., *"An atom-by-atom assembler of defect-free arbitrary two-dimensional atomic arrays,"* Science **354**, 1021 (2016) [cited in pages 23, 24, 42, 45, and 189].

Barredo, D., Lienhard, V., de Léséleuc, S., Lahaye, T., and Browaeys, A., *"Synthetic three-dimensional atomic structures assembled atom by atom,"* Nature **561**, 79 (2018) [cited in pages 23, 42, and 47].

Barredo, D., Lienhard, V., Scholl, P., de Léséleuc, S., Boulier, T., Browaeys, A., and Lahaye, T., *"Three-dimensional trapping of individual Rydberg atoms in ponderomotive bottle beam traps,"* arXiv:1908.00853 (2019) [cited in page 61].

Battaglia, D. A. and Stella, L., *"Optimization through quantum annealing: theory and some applications,"* Contemporary Physics **47**, 195 (2006) [cited in page 91].

Béguin, L., Measurement of the van der Waals interaction between two Rydberg atoms, Ph.D. thesis, Université Paris-Saclay (2013) [cited in pages 29, 32, and 74].

Bernien, H., Schwartz, S., Keesling, A., Levine, H., Omran, A., Pichler, H., Choi, S., Zibrov, A. S., Endres, M., Greiner, M., Vuletić, V., and Lukin, M. D., *"Probing many-body dynamics on a 51-atom quantum simulator,"* Nature **551**, 579 (2017) [cited in pages 56, 92, 111, and 187].

Beterov, I. I., Ryabtsev, I. I., Tretyakov, D. B., and Entin, V. M., *"Quasiclassical calculations of blackbody-radiation-induced depopulation rates and effective lifetimes of Rydberg nS, nP, and nD alkali-metal atoms with $n \leq 80$,"* Phys. Rev. A **79**, 052504 (2009) [cited in page 70].

Beugnon, J., Tuchendler, C., Marion, H., Gaetan, A., Miroshnychenko, Y., Sortais, Y., Lance, A., Jones, M., Messin, G., Browaeys, A., and Grangier, P., *"Two-dimensional transport and transfer of a single atomic qubit in optical tweezers,"* Nature Physics **3**, 4 (2007) [cited in page 45].

van Bijnen, R., Quantum engineering with ultracold atoms, Ph.D. thesis, Department of Applied Physics (2013) [cited in page 188].

van Bijnen, R. M. W., Smit, S., van Leeuwen, K. A. H., Vredenbregt, E. J. D., and Kokkelmans, S. J. J. M. F., *"Adiabatic formation of Rydberg crystals with chirped laser pulses,"* Journal of Physics B **44**, 184008 (2011) [cited in page 92].

Billy, J., Josse, V., Zuo, Z., Bernard, A., Hambrecht, B., Lugan, P., Clément, D., Sanchez-Palencia, L., Bouyer, P., and Aspect, A., *"Direct observation of Anderson localization of matter waves in a controlled disorder,"* Nature **453**, 891 (2008) [cited in page 18].

Blatt, R. and Roos, C. F., *"Quantum simulations with trapped ions,"* Nature Physics **8**, 277 (2012) [cited in page 17].

Blatt, R. and Wineland, D., *"Entangled states of trapped atomic ions,"* Nature **453**, 1008 (2008) [cited in page 18].

Bloch, I., *"Ultracold quantum gases in optical lattices,"* Nature Physics **1**, 23 (2005) [cited in page 17].

Bloch, I., Dalibard, J., and Nascimbène, S., *"Quantum simulations with ultracold quantum gases,"* Nature Physics **8**, 267 (2012) [cited in page 17].

Blöte, H. W. J. and Deng, Y., *"Cluster Monte Carlo simulation of the transverse Ising model,"* Phys. Rev. E **66**, 066110 (2002) [cited in page 99].

Blundell, S., Magnetism in Condensed Matter, Oxford Master Series in Condensed Matter Physics (OUP Oxford, 2001) [cited in page 13].

Böttcher, F., Schmidt, J.-N., Wenzel, M., Hertkorn, J., Guo, M., Langen, T., and Pfau, T., *"Transient supersolid properties in an array of dipolar quantum droplets,"* Phys. Rev. X **9**, 011051 (2019) [cited in page 18].

Browaeys, A., Barredo, D., and Lahaye, T., *"Experimental investigations of dipole-dipole interactions between a few Rydberg atoms,"* Journal of Physics B **49**, 152001 (2016) [cited in pages 23 and 24].

Brown, M. O., Thiele, T., Kiehl, C., Hsu, T.-W., and Regal, C. A., *"Gray-molasses optical-tweezer loading: Controlling collisions for scaling atom-array assembly,"* Phys. Rev. X **9**, 011057 (2019) [cited in page 45].

Cabrera, C. R., Tanzi, L., Sanz, J., Naylor, B., Thomas, P., Cheiney, P., and Tarruell, L., *"Quantum liquid droplets in a mixture of Bose-Einstein condensates,"* Science **359**, 301 (2018) [cited in page 18].

Calabrese, P. and Cardy, J., *"Time dependence of correlation functions following a quantum quench,"* Phys. Rev. Lett. **96**, 136801 (2006) [cited in page 113].

Caneva, T., Calarco, T., and Montangero, S., *"Chopped random-basis quantum optimization,"* Phys. Rev. A **84**, 022326 (2011) [cited in pages 38 and 151].

Cassidy, D. B., *"Experimental progress in positronium laser physics,"* The European Physical Journal D **72**, 53 (2018) [cited in page 60].

Chaloupka, J. L., Fisher, Y., Kessler, T. J., and Meyerhofer, D. D., *"Single-beam, ponderomotive-optical trap for free electrons and neutral atoms,"* Opt. Lett. **22**, 1021 (1997) [cited in page 61].

Chen, Y., Neill, C., Roushan, P., Leung, N., Fang, M., Barends, R., Kelly, J., Campbell, B., Chen, Z., Chiaro, B., Dunsworth, A., Jeffrey, E., Megrant, A., Mutus, J. Y., O'Malley, P. J. J., Quintana, C. M., Sank, D., Vainsencher, A., Wenner, J., White,

T. C., Geller, M. R., Cleland, A. N., and Martinis, J. M., *"Qubit architecture with high coherence and fast tunable coupling,"* Phys. Rev. Lett. **113**, 220502 (2014) [cited in page 19].

Cheneau, M., Barmettler, P., Poletti, D., Endres, M., Schauß, P., Fukuhara, T., Gross, C., Bloch, I., Kollath, C., and Kuhr, S., *"Light-cone-like spreading of correlations in a quantum many-body system,"* Nature **481**, 484 (2012) [cited in page 93].

Chin, C., Grimm, R., Julienne, P., and Tiesinga, E., *"Feshbach resonances in ultracold gases,"* Rev. Mod. Phys. **82**, 1225 (2010) [cited in page 17].

Choi, J.-H., Guest, J. R., Povilus, A. P., Hansis, E., and Raithel, G., *"Magnetic trapping of long-lived cold Rydberg atoms,"* Phys. Rev. Lett. **95**, 243001 (2005) [cited in page 60].

Chomaz, L., Petter, D., Ilzhöfer, P., Natale, G., Trautmann, A., Politi, C., Durastante, G., van Bijnen, R. M. W., Patscheider, A., Sohmen, M., Mark, M. J., and Ferlaino, F., *"Long-lived and transient supersolid behaviors in dipolar quantum gases,"* Phys. Rev. X **9**, 021012 (2019) [cited in page 18].

Cirac, J. I. and Zoller, P., *"Quantum computations with cold trapped ions,"* Phys. Rev. Lett. **74**, 4091 (1995) [cited in page 19].

Cladé, *"PyDAQmx : a Python interface to the National Instruments DAQmx driver,"* [cited in page 38].

Cohen-Tannoudji, C., Dupont-Roc, J., and Grynberg, G., Processus d'interaction entre photons et atomes (EDP Sciences, 1996) [cited in page 172].

Collini, E., *"Spectroscopic signatures of quantum-coherent energy transfer,"* Chem. Soc. Rev. **42**, 4932 (2013) [cited in page 121].

Cooper, N. R., Dalibard, J., and Spielman, I. B., *"Topological bands for ultracold atoms,"* Rev. Mod. Phys. **91**, 015005 (2019) [cited in page 140].

Dalmonte, M., Mirzaei, S. I., Muppalla, P. R., Marcos, D., Zoller, P., and Kirchmair, G., *"Realizing dipolar spin models with arrays of superconducting qubits,"* Phys. Rev. B **92**, 174507 (2015) [cited in page 19].

Das, A. and Chakrabarti, B. K., *"Colloquium: Quantum annealing and analog quantum computation,"* Rev. Mod. Phys. **80**, 1061 (2008) [cited in page 102].

Devoret, M. H. and Schoelkopf, R. J., *"Superconducting circuits for quantum information: An outlook,"* Science **339**, 1169 (2013) [cited in page 19].

Dicke, R. H., *"Coherence in spontaneous radiation processes,"* Phys. Rev. **93**, 99 (1954) [cited in page 129].

Doria, P., Calarco, T., and Montangero, S., *"Optimal control technique for many-body quantum dynamics,"* Phys. Rev. Lett. **106**, 190501 (2011) [cited in page 188].

Duan, L.-M., Demler, E., and Lukin, M. D., *"Controlling spin exchange interactions of ultracold atoms in optical lattices,"* Phys. Rev. Lett. **91**, 090402 (2003) [cited in page 18].

Dudin, Y. O. and Kuzmich, A., *"Strongly interacting Rydberg excitations of a cold atomic gas,"* Science **336**, 887 (2012) [cited in page 59].

Dutta, S. K., Guest, J. R., Feldbaum, D., Walz-Flannigan, A., and Raithel, G., *"Ponderomotive optical lattice for Rydberg atoms,"* Phys. Rev. Lett. **85**, 5551 (2000) [cited in page 67].

Edwards, E. E., Korenblit, S., Kim, K., Islam, R., Chang, M.-S., Freericks, J. K., Lin, G.-D., Duan, L.-M., and Monroe, C., *"Quantum simulation and phase diagram of the transverse-field Ising model with three atomic spins,"* Phys. Rev. B **82**, 060412 (2010) [cited in page 92].

Endres, M., Bernien, H., Keesling, A., Levine, H., Anschuetz, E. R., Krajenbrink, A., Senko, C., Vuletic, V., Greiner, M., and Lukin, M. D., *"Atom-by-atom assembly of defect-free one-dimensional cold atom arrays,"* Science **354**, 1024 (2016) [cited in page 23].

Ferrier-Barbut, I., Kadau, H., Schmitt, M., Wenzel, M., and Pfau, T., *"Observation of quantum droplets in a strongly dipolar bose gas,"* Phys. Rev. Lett. **116**, 215301 (2016) [cited in page 18].

Feynman, R. P., *"Simulating physics with computers,"* Int. J. Theor. Phys. **21**, 467 (1982) [cited in page 12].

Firstenberg, O., Peyronel, T., Liang, Q.-Y., Gorshkov, A. V., Lukin, M. D., and Vuletić, V., *"Attractive photons in a quantum nonlinear medium,"* Nature **502**, 71 (2013) [cited in page 59].

Fuhrmanek, A., From single to many atoms in a microscopic optical dipole trap, Ph.D. thesis, Université Paris Sud - Parisfleach XI (2011) [cited in page 29].

Fuhrmanek, A., Bourgain, R., Sortais, Y. R. P., and Browaeys, A., *"Light-assisted collisions between a few cold atoms in a microscopic dipole trap,"* Phys. Rev. A **85**, 062708 (2012) [cited in page 31].

Gaëtan, A., Miroshnychenko, Y., Wilk, T., Chotia, A., Viteau, M., Comparat, D., Pillet, P., Browaeys, A., and Grangier, P., *"Observation of collective excitation of two individual atoms in the Rydberg blockade regime,"* Nature Physics **5**, 115 (2009) [cited in page 21].

Gallagher, T. F., Rydberg Atoms (Cambridge University Press, 1994) [cited in page 21].

Gambetta, F. M., Li, W., Schmidt-Kaler, F., and Lesanovsky, I., *"Engineering non-binary Rydberg interactions via electron-phonon coupling,"* arXiv:1907.11664 (2019) [cited in pages 82 and 188].

Georgescu, I. M., Ashhab, S., and Nori, F., *"Quantum simulation,"* Rev. Mod. Phys. **86**, 153 (2014) [cited in page 12].

Goban, A., Hutson, R. B., Marti, G. E., Campbell, S. L., Perlin, M. A., Julienne, P. S., DIncao, J. P., Rey, A. M., and Ye, J., *"Emergence of multi-body interactions in a fermionic lattice clock,"* Nature **563**, 369 (2018) [cited in page 18].

Goldman, N., Beugnon, J., and Gerbier, F., *"Detecting chiral edge states in the Hofstadter optical lattice,"* Phys. Rev. Lett. **108**, 255303 (2012) [cited in page 156].

Goldman, N., Juzeliūnas, G., hberg, P., and Spielman, I. B., *"Light-induced gauge fields for ultracold atoms,"* Rep. Prog. Phys. **77**, 126401 (2014) [cited in page 156].

Görg, F., Sandholzer, K., Minguzzi, J., Desbuquois, R., Messer, M., and Esslinger, T., *"Realization of density-dependent Peierls phases to engineer quantized gauge fields coupled to ultracold matter,"* Nature Phys. (2019), 10.1038/s41567-019-0615-4 [cited in page 184].

Gorniaczyk, H., Tresp, C., Schmidt, J., Fedder, H., and Hofferberth, S., *"Single-photon transistor mediated by interstate Rydberg interactions,"* Phys. Rev. Lett. **113**, 053601 (2014) [cited in page 59].

Gorshkov, A. V., Manmana, S. R., Chen, G., Ye, J., Demler, E., Lukin, M. D., and Rey, A. M., *"Tunable superfluidity and quantum magnetism with ultracold polar molecules,"* Phys. Rev. Lett. **107**, 115301 (2011) [cited in page 18].

Greiner, M., Mandel, O., Esslinger, T., Hänsch, T. W., and Bloch, I., *"Quantum phase transition from a superfluid to a Mott insulator in a gas of ultracold atoms,"* Nature **415**, 39 (2002) [cited in page 17].

Grünzweig, T., Hilliard, A., McGovern, M., and Anderson, M., *"Near-deterministic preparation of a single atom in an optical microtrap,"* Nature Physics **6**, 951 (2010) [cited in page 45].

Guardado-Sanchez, E., Brown, P. T., Mitra, D., Devakul, T., Huse, D. A., Schauß, P., and Bakr, W. S., *"Probing the quench dynamics of antiferromagnetic correlations in a 2D quantum Ising spin system,"* Phys. Rev. X **8**, 021069 (2018) [cited in page 92].

Hafezi, M., Mittal, S., Fan, J., Migdall, A., and Taylor, J. M., *"Imaging topological edge states in silicon photonics,"* Nature Photonics **7**, 1001 (2013) [cited in page 185].

Haldane, F. D. M., *"Model for a quantum Hall effect without Landau levels: condensed-matter realization of the "parity anomaly","* Phys. Rev. Lett. **61**, 2015 (1988) [cited in pages 156 and 174].

He, Y.-C., Bhattacharjee, S., Moessner, R., and Pollmann, F., *"Bosonic integer quantum Hall effect in an interacting lattice model,"* Phys. Rev. Lett. **115**, 116803 (2015) [cited in page 184].

Heck, R., Vuculescu, O., Sørensen, J. J., Zoller, J., Andreasen, M. G., Bason, M. G., Ejlertsen, P., Elíasson, O., Haikka, P., Laustsen, J. S., Nielsen, L. L., Mao, A., Müller, R., Napolitano, M., Pedersen, M. K., Thorsen, A. R., Bergenholtz, C., Calarco, T., Montangero, S., and Sherson, J. F., *"Remote optimization of an ultracold atoms experiment by experts and citizen scientists,"* Proceedings of the National Academy of Sciences **115**, E11231 (2018) [cited in page 188].

Heidemann, R., Raitzsch, U., Bendkowsky, V., Butscher, B., Löw, R., Santos, L., and Pfau, T., *"Evidence for coherent collective Rydberg excitation in the strong blockade regime,"* Phys. Rev. Lett. **99**, 163601 (2007) [cited in page 21].

Heyl, M., *"Dynamical quantum phase transitions: A brief survey,"* EPL (Europhysics Letters) **125**, 26001 (2019) [cited in page 14].

Hogan, S. D. and Merkt, F., *"Demonstration of three-dimensional electrostatic trapping of state-selected Rydberg atoms,"* Phys. Rev. Lett. **100**, 043001 (2008) [cited in page 60].

Houck, A. A., Türeci, H. E., and Koch, J., *"On-chip quantum simulations with superconducting circuits,"* Nature Physics **8**, 292 (2012) [cited in page 17].

Isenhower, L., Urban, E., Zhang, X. L., Gill, A. T., Henage, T., Johnson, T. A., Walker, T. G., and Saffman, M., *"Demonstration of a neutral atom controlled-not quantum gate,"* Phys. Rev. Lett. **104**, 010503 (2010) [cited in pages 21, 59, and 150].

Islam, R., Senko, C., Campbell, W. C., Korenblit, S., Smith, J., Lee, A., Edwards, E. E., Wang, C.-C. J., Freericks, J. K., and Monroe, C., *"Emergence and frustration of magnetism with variable-range interactions in a quantum simulator,"* Science **340**, 583 (2013) [cited in pages 92 and 150].

Jaksch, D., Cirac, J. I., Zoller, P., Rolston, S. L., Côté, R., and Lukin, M. D., *"Fast quantum gates for neutral atoms,"* Phys. Rev. Lett. **85**, 2208 (2000) [cited in page 21].

Jaksch, D. and Zoller, P., *"Creation of effective magnetic fields in optical lattices: the Hofstadter butterfly for cold neutral atoms,"* New Journal of Physics **5**, 56 (2003) [cited in page 156].

Jau, Y.-Y., Hankin, A. M., Keating, T., Deutsch, I. H., and Biedermann, G. W., *"Entangling atomic spins with a Rydberg-dressed spin-flip blockade,"* Nature Physics **12**, 71 (2016) [cited in page 59].

Jentschura, U. D., Mohr, P. J., Tan, J. N., and Wundt, B. J., *"Fundamental constants and tests of theory in Rydberg states of hydrogenlike ions,"* Phys. Rev. Lett. **100**, 160404 (2008) [cited in page 60].

Jones, P. H., Marag, O. M., and Volpe, G., Optical Tweezers: Principles and Applications (Cambridge University Press, 2015) [cited in page 28].

Jotzu, G., Messer, M., Desbuquois, R., Lebrat, M., Uehlinger, T., Greif, D., and Esslinger, T., *"Experimental realization of the topological Haldane model with ultracold fermions,"* Nature **515**, 237 (2014) [cited in page 156].

Jurcevic, P., Lanyon, B. P., Hauke, P., Hempel, C., Zoller, P., Blatt, R., and Roos, C. F., *"Quasiparticle engineering and entanglement propagation in a quantum many-body system,"* Nature **511**, 202 (2014) [cited in page 93].

Keesling, A., Omran, A., Levine, H., Bernien, H., Pichler, H., Choi, S., Samajdar, R., Schwartz, S., Silvi, P., Sachdev, S., Zoller, P., Endres, M., Greiner, M., Vuletić, V., and Lukin, M., *"Quantum Kibble–Zurek mechanism and critical dynamics on a programmable Rydberg simulator,"* Nature **568**, 207 (2019) [cited in pages 92 and 111].

Kiffner, M., O'Brien, E., and Jaksch, D., *"Topological spin models in Rydberg lattices,"* Applied Physics B **123**, 46 (2017) [cited in page 157].

Kim, H., Lee, W., Lee, H., Jo, H., Song, Y., and Ahn, J., *"In situ single-atom array synthesis using dynamic holographic optical tweezers,"* Nature Communications **7**, 13317 (2016) [cited in page 23].

Kim, H., Park, Y., Kim, K., Sim, H.-S., and Ahn, J., *"Detailed balance of thermalization dynamics in Rydberg-atom quantum simulators,"* Phys. Rev. Lett. **120**, 180502 (2018) [cited in page 90].

Kim, K., Korenblit, S., Islam, R., Edwards, E. E., Chang, M.-S., Noh, C., Carmichael, H., Lin, G.-D., Duan, L.-M., Wang, C. C. J., Freericks, J. K., and Monroe, C., *"Quantum simulation of the transverse Ising model with trapped ions,"* New Journal of Physics **13**, 105003 (2011) [cited in page 19].

King, A. D., Carrasquilla, J., Raymond, J., Ozfidan, I., Andriyash, E., Berkley, A., Reis, M., Lanting, T., Harris, R., Altomare, F., Boothby, K., Bunyk, P., Enderud, C., Fréchette, A., Hoskinson, E., Ladizinsky, N., Oh, T., Poulin-Lamarre, G., Rich, C., Sato, Y., Smirnov, A., Swenson, L., Volkmann, M., Whittaker, J., Yao, J., Ladizinsky, E., Johnson, M., Hilton, J., and Amin, M., *"Observation of topological phenomena in a programmable lattice of 1,800 qubits,"* Nature **560**, 460 (2018) [cited in page 91].

Kitching, J., Knappe, S., and Donley, E. A., *"Atomic sensors A review,"* IEEE Sensors Journal **11**, 1749 (2011) [cited in page 11].

Klitzing, K. v., Dorda, G., and Pepper, M., *"New method for high-accuracy determination of the fine-structure constant based on quantized Hall resistance,"* Phys. Rev. Lett. **45**, 494 (1980) [cited in page 15].

Knolle, J. and Moessner, R., *"A field guide to spin liquids,"* Annual Review of Condensed Matter Physics **10**, 451 (2019) [cited in page 120].

Kokail, C., Maier, C., van Bijnen, R., Brydges, T., Joshi, M. K., Jurcevic, P., Muschik, C. A., Silvi, P., Blatt, R., Roos, C. F., and Zoller, P., *"Self-verifying variational quantum simulation of lattice models,"* Nature **569**, 355 (2019) [cited in pages 19, 39, and 188].

Kormos, M., Collura, M., Takács, G., and Calabrese, P., *"Real-time confinement following a quantum quench to a non-integrable model,"* Nature Physics **13**, 246 (2016) [cited in page 118].

Ku, M. J. H., Sommer, A. T., Cheuk, L. W., and Zwierlein, M. W., *"Revealing the superfluid lambda transition in the universal thermodynamics of a unitary Fermi gas,"* Science **335**, 563 (2012) [cited in page 18].

Labuhn, H., Rydberg excitation dynamics and correlations in arbitrary 2D arrays of single atoms, Ph.D. thesis, Université Paris-Saclay (2016) [cited in page 42].

Labuhn, H., Barredo, D., Ravets, S., de Léséleuc, S., Macrì,, Lahaye, T., and Browaeys, A., *"Tunable two-dimensional arrays of single Rydberg atoms for realizing quantum Ising models,"* Nature **534**, 667 (2016) [cited in pages 23, 90, 94, and 95].

Lanyon, B. P., Hempel, C., Nigg, D., Müller, M., Gerritsma, R., Zähringer, F., Schindler, P., Barreiro, J. T., Rambach, M., Kirchmair, G., Hennrich, M., Zoller, P., Blatt, R., and Roos, C. F., *"Universal digital quantum simulation with trapped ions,"* Science **334**, 57 (2011) [cited in page 19].

Leibfried, D., Barrett, M. D., Schaetz, T., Britton, J., Chiaverini, J., Itano, W. M., Jost, J. D., Langer, C., and Wineland, D. J., *"Toward Heisenberg-limited spectroscopy with multiparticle entangled states,"* Science **304**, 1476 (2004) [cited in page 12].

Léonard, J., Morales, A., Zupancic, P., Esslinger, T., and Donner, T., *"Supersolid formation in a quantum gas breaking a continuous translational symmetry,"* Nature **543**, 87 (2017) [cited in page 18].

Leonardo, R. D., Ianni, F., and Ruocco, G., *"Computer generation of optimal holograms for optical trap arrays,"* Opt. Express **15**, 1913 (2007) [cited in pages 42 and 47].

Lepoutre, S., Schachenmayer, J., Gabardos, L., Zhu, B., Naylor, B., Maréchal, E., Gorceix, O., Rey, A. M., Vernac, L., and Laburthe-Tolra, B., *"Out-of-equilibrium quantum magnetism and thermalization in a spin-3 many-body dipolar lattice system,"* Nature Communications **10**, 1714 (2019) [cited in page 18].

de Léséleuc, S., Quantum simulation of spin models with assembled arrays of Rydberg atoms, Ph.D. thesis, Université Paris-Saclay (2018) [cited in pages 27, 35, 36, 42, 45, 47, 51, 54, 94, and 165].

de Léséleuc, S., Barredo, D., Lienhard, V., Browaeys, A., and Lahaye, T., *"Optical control of the resonant dipole-dipole interaction between Rydberg atoms,"* Phys. Rev. Lett. **119**, 053202 (2017) [cited in pages 151, 165, and 167].

de Léséleuc, S., Barredo, D., Lienhard, V., Browaeys, A., and Lahaye, T., *"Analysis of imperfections in the coherent optical excitation of single atoms to Rydberg states,"* Phys. Rev. A **97**, 053803 (2018a) [cited in pages 54, 56, 60, 105, 110, and 187].

de Léséleuc, S., Lienhard, V., Scholl, P., Barredo, D., Weber, S., Lang, N., Büchler, H. P., Lahaye, T., and Browaeys, A., *"Observation of a symmetry-protected topological phase of interacting bosons with Rydberg atoms,"* Science **365**, 775 (2019) [cited in pages 23, 121, 122, 140, and 184].

de Léséleuc, S., Weber, S., Lienhard, V., Barredo, D., Büchler, H. P., Lahaye, T., and Browaeys, A., *"Accurate mapping of multilevel Rydberg atoms on interacting spin-1/2 particles for the quantum simulation of Ising models,"* Phys. Rev. Lett. **120**, 113602 (2018b) [cited in page 94].

Lester, B. J., Luick, N., Kaufman, A. M., Reynolds, C. M., and Regal, C. A., *"Rapid production of uniformly filled arrays of neutral atoms,"* Phys. Rev. Lett. **115**, 073003 (2015) [cited in page 45].

Levine, H., Keesling, A., Omran, A., Bernien, H., Schwartz, S., Zibrov, A. S., Endres, M., Greiner, M., Vuletić, V., and Lukin, M. D., *"High-fidelity control and entanglement of Rydberg-atom qubits,"* Phys. Rev. Lett. **121**, 123603 (2018) [cited in pages 23, 24, 56, 59, and 111].

Levine, H., Keesling, A., Semeghini, G., Omran, A., Wang, T. T., Ebadi, S., Berniern, H., Greiner, M., Vuletić, V., Pichler, H., and Lukin, M. D., *"Parallel implementation of high-fidelity multi-qubit gates with neutral atoms,"* arXiv:1908.06101 (2019) [cited in pages 23 and 24].

Li, L., Dudin, Y. O., and Kuzmich, A., *"Entanglement between light and an optical atomic excitation,"* Nature **498**, 466 (2013) [cited in page 60].

Lieb, E. H. and Robinson, D. W., *"The finite group velocity of quantum spin systems,"* Comm. Math. Phys. **28**, 251 (1972) [cited in pages 93 and 113].

Lienhard, V., de Léséleuc, S., Barredo, D., Lahaye, T., Browaeys, A., Schuler, M., Henry, L.-P., and Läuchli, A. M., *"Observing the space- and time-dependent growth of correlations in dynamically tuned synthetic Ising models with antiferromagnetic interactions,"* Phys. Rev. X **8**, 021070 (2018) [cited in page 88].

Lloyd, S., *"Universal quantum simulators,"* Science **273**, 1073 (1996) [cited in page 16].

Löw, R., Weimer, H., Krohn, U., Heidemann, R., Bendkowsky, V., Butscher, B., Büchler, H. P., and Pfau, T., *"Universal scaling in a strongly interacting Rydberg gas,"* Phys. Rev. A **80**, 033422 (2009) [cited in page 89].

Löw, R., Weimer, H., Nipper, J., Balewski, J. B., Butscher, B., Bchler, H. P., and Pfau, T., *"An experimental and theoretical guide to strongly interacting Rydberg gases,"* Journal of Physics B: Atomic, Molecular and Optical Physics **45**, 113001 (2012) [cited in page 21].

Lucas, A., *"Ising formulations of many NP problems,"* Frontiers in Physics **2**, 5 (2014) [cited in page 118].

Lukin, M. D., Fleischhauer, M., Cote, R., Duan, L. M., Jaksch, D., Cirac, J. I., and Zoller, P., *"Dipole blockade and quantum information processing in mesoscopic atomic ensembles,"* Phys. Rev. Lett. **87**, 037901 (2001) [cited in page 21].

Luther, A. and Peschel, I., *"Calculation of critical exponents in two dimensions from quantum field theory in one dimension,"* Phys. Rev. B **12**, 3908 (1975) [cited in page 144].

Magnan, E., Spontaneous decoherence in large Rydberg systems, Ph.D. thesis, Université Paris-Saclay (2018) [cited in pages 36 and 189].

Mancini, M., Pagano, G., Cappellini, G., Livi, L., Rider, M., Catani, J., Sias, C., Zoller, P., Inguscio, M., Dalmonte, M., and Fallani, L., *"Observation of chiral edge states with neutral fermions in synthetic Hall ribbons,"* Science **349**, 1510 (2015) [cited in page 157].

Mazurenko, A., Chiu, C. S., Ji, G., Parsons, M. F., Kanász-Nagy, M., Schmidt, R., Grusdt, F., Demler, E., Greif, D., and Greiner, M., *"A cold-atom Fermi–Hubbard antiferromagnet,"* Nature **545**, 462 (2017) [cited in page 18].

Ohl de Mello, D., Schäffner, D., Werkmann, J., Preuschoff, T., Kohfahl, L., Schlosser, M., and Birkl, G., *"Defect-free assembly of 2d clusters of more than 100 single-atom quantum systems,"* Phys. Rev. Lett. **122**, 203601 (2019) [cited in page 23].

Miyake, H., Siviloglou, G. A., Kennedy, C. J., Burton, W. C., and Ketterle, W., *"Realizing the harper hamiltonian with laser-assisted tunneling in optical lattices,"* Phys. Rev. Lett. **111**, 185302 (2013) [cited in page 181].

Moessner, R. and Ramirez, A. P., *"Geometrical frustration,"* Physics Today **59**, 24 (2006) [cited in page 14].

Moessner, R. and Sondhi, S. L., *"Ising models of quantum frustration,"* Phys. Rev. B **63**, 224401 (2001) [cited in page 100].

Møller, D., Madsen, L. B., and Mølmer, K., *"Quantum gates and multiparticle entanglement by Rydberg excitation blockade and adiabatic passage,"* Phys. Rev. Lett. **100**, 170504 (2008) [cited in page 126].

Moore, J. E., *"The birth of topological insulators,"* Nature **464**, 194 (2010) [cited in pages 14 and 156].

Nakamura, Y., Pashkin, Y. A., and Tsai, J. S., *"Coherent control of macroscopic quantum states in a single-cooper-pair box,"* Nature **398**, 786 (1999) [cited in page 19].

Navon, N., Nascimbène, S., Chevy, F., and Salomon, C., *"The equation of state of a low-temperature Fermi gas with tunable interactions,"* Science **328**, 729 (2010) [cited in page 18].

Nguyen, T. L., Raimond, J. M., Sayrin, C., Cortiñas, R., Cantat-Moltrecht, T., Assemat, F., Dotsenko, I., Gleyzes, S., Haroche, S., Roux, G., Jolicoeur, T., and Brune, M., *"Towards quantum simulation with circular rydberg atoms,"* Phys. Rev. X **8**, 011032 (2018) [cited in page 188].

Nogrette, F., Labuhn, H., Ravets, S., Barredo, D., Béguin, L., Vernier, A., Lahaye, T., and Browaeys, A., *"Single-atom trapping in holographic 2D arrays of microtraps with arbitrary geometries,"* Phys. Rev. X **4**, 021034 (2014) [cited in page 42].

O'Malley, P. J. J., Babbush, R., Kivlichan, I. D., Romero, J., McClean, J. R., Barends, R., Kelly, J., Roushan, P., Tranter, A., Ding, N., Campbell, B., Chen, Y., Chen, Z., Chiaro, B., Dunsworth, A., Fowler, A. G., Jeffrey, E., Lucero, E., Megrant, A., Mutus, J. Y., Neeley, M., Neill, C., Quintana, C., Sank, D., Vainsencher, A., Wenner, J., White, T. C., Coveney, P. V., Love, P. J., Neven, H., Aspuru-Guzik, A., and Martinis, J. M., *"Scalable quantum simulation of molecular energies,"* Phys. Rev. X **6**, 031007 (2016) [cited in page 19].

Omran, A., Levine, H., Keesling, A., Semeghini, G., Wang, T. T., Ebadi, S., Bernien, H., Zibrov, A. S., Pichler, H., Choi, S., Cui, J., Rossignolo, M., Rembold, P., Montangero, S., Calarco, T., Endres, M., Greiner, M., Vuletić, V., and Lukin, M. D., *"Generation and manipulation of Schrödinger cat states in Rydberg atom arrays,"* Science **365**, 570 (2019) [cited in pages 23 and 188].

Ozeri, R., Khaykovich, L., and Davidson, N., *"Long spin relaxation times in a single-beam blue-detuned optical trap,"* Phys. Rev. A **59**, R1750 (1999) [cited in page 61].

Paik, H., Schuster, D. I., Bishop, L. S., Kirchmair, G., Catelani, G., Sears, A. P., Johnson, B. R., Reagor, M. J., Frunzio, L., Glazman, L. I., Girvin, S. M., Devoret, M. H., and Schoelkopf, R. J., *"Observation of high coherence in Josephson junction qubits measured in a three-dimensional circuit QED architecture,"* Phys. Rev. Lett. **107**, 240501 (2011) [cited in page 19].

Peter, D., Müller, S., Wessel, S., and Büchler, H. P., *"Anomalous behavior of spin systems with dipolar interactions,"* Phys. Rev. Lett. **109**, 025303 (2012) [cited in page 122].

Peter, D., Yao, N. Y., Lang, N., Huber, S. D., Lukin, M. D., and Büchler, H. P., *"Topological bands with a Chern number $C = 2$ by dipolar exchange interactions,"* Phys. Rev. A **91**, 053617 (2015) [cited in page 157].

Pichler, H., Wang, S.-T., Zhou, L., Choi, S., and Lukin, M. D., *"Quantum optimization for maximum independent set using Rydberg atom arrays,"* arXiv:1808.10816 (2018) [cited in pages 118 and 186].

Pohl, T., Demler, E., and Lukin, M. D., *"Dynamical crystallization in the dipole blockade of ultracold atoms,"* Phys. Rev. Lett. **104**, 043002 (2010) [cited in page 92].

Porras, D. and Cirac, J. I., *"Effective quantum spin systems with trapped ions,"* Phys. Rev. Lett. **92**, 207901 (2004) [cited in page 19].

Pritchard, J. D., Maxwell, D., Gauguet, A., Weatherill, K. J., Jones, M. P. A., and Adams, C. S., *"Cooperative atom-light interaction in a blockaded Rydberg ensemble,"* Phys. Rev. Lett. **105**, 193603 (2010) [cited in pages 21 and 59].

Qi, X.-L. and Zhang, S.-C., *"Topological insulators and superconductors,"* Rev. Mod. Phys. **83**, 1057 (2011) [cited in page 14].

Raitzsch, U., Bendkowsky, V., Heidemann, R., Butscher, B., Löw, R., and Pfau, T., *"Echo experiments in a strongly interacting Rydberg gas,"* Phys. Rev. Lett. **100**, 013002 (2008) [cited in page 21].

Raizen, M. G., Gilligan, J. M., Bergquist, J. C., Itano, W. M., and Wineland, D. J., *"Ionic crystals in a linear Paul trap,"* Phys. Rev. A **45**, 6493 (1992) [cited in page 18].

Ramirez, A. P., Hayashi, A., Cava, R. J., Siddharthan, R., and Shastry, B. S., *"Zero-point entropy in spin ice,"* Nature **399**, 333 (1999) [cited in page 100].

Ramos, A., Moore, K., and Raithel, G., *"Measuring the Rydberg constant using circular Rydberg atoms in an intensity-modulated optical lattice,"* Phys. Rev. A **96**, 032513 (2017) [cited in page 60].

Ravets, S., Development of tools for quantum engineering using individual atoms : optical nanofibers and controlled Rydberg interactions, Ph.D. thesis, Université Paris-Saclay (2014) [cited in pages 51 and 164].

Ravets, S., Labuhn, H., Barredo, D., Beguin, L., Lahaye, T., and Browaeys, A., *"Coherent dipole-dipole coupling between two single Rydberg atoms at an electrically-tuned Förster resonance,"* Nature Physics **10**, 914 (2014) [cited in page 95].

Rechtsman, M. C., Zeuner, J. M., Plotnik, Y., Lumer, Y., Podolsky, D., Dreisow, F., Nolte, S., Segev, M., and Szameit, A., *"Photonic Floquet topological insulators,"* Nature **496**, 196 (2013) [cited in page 185].

Richerme, P., Senko, C., Korenblit, S., Smith, J., Lee, A., Islam, R., Campbell, W. C., and Monroe, C., *"Quantum catalysis of magnetic phase transitions in a quantum simulator,"* Phys. Rev. Lett. **111**, 100506 (2013) [cited in page 102].

Robicheaux, F. and Hernández, J. V., *"Many-body wave function in a dipole blockade configuration,"* Phys. Rev. A **72**, 063403 (2005) [cited in page 89].

Rondin, L., Tetienne, J.-P., Hingant, T., Roch, J.-F., Maletinsky, P., and Jacques, V., *"Magnetometry with nitrogen-vacancy defects in diamond,"* Reports on Progress in Physics **77**, 056503 (2014) [cited in page 11].

Roushan, P., Neill, C., Megrant, A., Chen, Y., Babbush, R., Barends, R., Campbell, B., Chen, Z., Chiaro, B., Dunsworth, A., Fowler, A., Jeffrey, E., Kelly, J., Lucero, E., Mutus, J., O'Malley, P. J. J., Neeley, M., Quintana, C., Sank, D., Vainsencher, A.,

Wenner, J., White, T., Kapit, E., Neven, H., and Martinis, J., *"Chiral ground-state currents of interacting photons in a synthetic magnetic field,"* Nature Phys. **13**, 146 (2017a) [cited in pages 157, 175, and 183].

Roushan, P., Neill, C., Tangpanitanon, J., Bastidas, V. M., Megrant, A., Barends, R., Chen, Y., Chen, Z., Chiaro, B., Dunsworth, A., Fowler, A., Foxen, B., Giustina, M., Jeffrey, E., Kelly, J., Lucero, E., Mutus, J., Neeley, M., Quintana, C., Sank, D., Vainsencher, A., Wenner, J., White, T., Neven, H., Angelakis, D. G., and Martinis, J., *"Spectroscopic signatures of localization with interacting photons in superconducting qubits,"* Science **358**, 1175 (2017b) [cited in page 19].

Sachdev, S., Quantum Phase Transitions, 2nd ed. (Cambridge University Press, 2011) [cited in page 14].

Sachdev, S., Sengupta, K., and Girvin, S. M., *"Mott insulators in strong electric fields,"* Phys. Rev. B **66**, 075128 (2002) [cited in page 18].

Saffman, M., *"Quantum computing with atomic qubits and Rydberg interactions: progress and challenges,"* Journal of Physics B: Atomic, Molecular and Optical Physics **49**, 202001 (2016) [cited in page 60].

Saffman, M. and Walker, T. G., *"Analysis of a quantum logic device based on dipole-dipole interactions of optically trapped Rydberg atoms,"* Phys. Rev. A **72**, 022347 (2005) [cited in pages 60 and 72].

Salathé, Y., Mondal, M., Oppliger, M., Heinsoo, J., Kurpiers, P., Potočnik, A., Mezzacapo, A., Las Heras, U., Lamata, L., Solano, E., Filipp, S., and Wallraff, A., *"Digital quantum simulation of spin models with circuit quantum electrodynamics,"* Phys. Rev. X **5**, 021027 (2015) [cited in page 19].

Schachenmayer, J., Lesanovsky, I., Micheli, A., and Daley, A. J., *"Dynamical crystal creation with polar molecules or Rydberg atoms in optical lattices,"* New Journal of Physics **12**, 103044 (2010) [cited in page 92].

Schauß, P., Cheneau, M., Endres, M., Fukuhara, T., Hild, S., Omran, A., Pohl, T., Gross, C., Kuhr, S., and Bloch, I., *"Observation of mesoscopic crystalline structures in a two-dimensional Rydberg gas,"* Nature **491**, 87 (2012) [cited in page 90].

Schauß, P., Zeiher, J., Fukuhara, T., Hild, S., Cheneau, M., Macri, T., Pohl, T., Bloch, I., and Gross, C., *"Crystallization in Ising quantum magnets,"* Science **347**, 1455 (2015) [cited in page 92].

Schlosser, N., Reymond, G., and Grangier, P., *"Collisional blockade in microscopic optical dipole traps,"* Physical Review Letters **89**, 023005 (2002) [cited in page 32].

Schlosser, N., Reymond, G., Protsenko, I., and Grangier, P., *"Sub-poissonian loading of single atoms in a microscopic dipole trap."* Nature **411**, 1024 (2001) [cited in pages 21, 28, and 32].

Schmidt-Kaler, F., Häffner, H., Riebe, M., Gulde, S., Lancaster, G. P. T., Deuschle, T., Becher, C., Roos, C. F., Eschner, J., and Blatt, R., *"Realization of the CiracZoller controlled-NOT quantum gate,"* Nature **422**, 408 (2003) [cited in page 11].

Schwarzkopf, A., Anderson, D. A., Thaicharoen, N., and Raithel, G., *"Spatial correlations between Rydberg atoms in an optical dipole trap,"* Phys. Rev. A **88**, 061406 (2013) [cited in page 89].

Shor, P. W., *"Algorithms for quantum computation: discrete logarithms and factoring,"* in Proceedings 35th Annual Symposium on Foundations of Computer Science (1994) pp. 124–134 [cited in page 12].

Šibalić, N., Pritchard, J. D., Adams, C. S., and Weatherill, K. J., *"ARC: An open-source library for calculating properties of alkali Rydberg atoms,"* Computer Physics Communications **220**, 319 (2016) [cited in page 70].

Signoles, A., Franz, T., Ferracini Alves, R., Gärttner, M., Whitlock, S., Zürn, G., and Weidemüller, M., *"Observation of glassy dynamics in a disordered quantum spin system,"* arXiv:1909.11959 (2019) [cited in page 188].

Simon, J., Bakr, W. S., Ma, R., Tai, M. E., Preiss, P. M., and Greiner, M., *"Quantum simulation of antiferromagnetic spin chains in an optical lattice,"* Nature **472**, 307 (2011) [cited in page 18].

Singer, K., Reetz-Lamour, M., Amthor, T., Marcassa, L. G., and Weidemüller, M., *"Suppression of excitation and spectral broadening induced by interactions in a cold gas of Rydberg atoms,"* Phys. Rev. Lett. **93**, 163001 (2004) [cited in page 21].

Sortais, Y. R. P., Marion, H., Tuchendler, C., Lance, A. M., Lamare, M., Fournet, P., Armellin, C., Mercier, R., Messin, G., Browaeys, A., and Grangier, P., *"Diffraction-limited optics for single-atom manipulation,"* Physical Review A **75**, 8 (2007) [cited in page 29].

Steck, D. A., *"Rubidium 87 d line data,"* (2003) [cited in page 40].

Struck, J., Ölschläger, C., Weinberg, M., Hauke, P., Simonet, J., Eckardt, A., Lewenstein, M., Sengstock, K., and Windpassinger, P., *"Tunable gauge potential for neutral and spinless particles in driven optical lattices,"* Phys. Rev. Lett. **108**, 225304 (2012) [cited in page 157].

Stuhl, B. K., Lu, H.-I., Aycock, L. M., Genkina, D., and Spielman, I. B., *"Visualizing edge states with an atomic Bose gas in the quantum Hall regime,"* Science **349**, 1514 (2015) [cited in page 157].

Su, W. P., Schrieffer, J. R., and Heeger, A. J., *"Solitons in polyacetylene,"* Phys. Rev. Lett. **42**, 1698 (1979) [cited in page 139].

Süsstrunk, R. and Huber, S. D., *"Observation of phononic helical edge states in a mechanical topological insulator,"* Science **349**, 47 (2015) [cited in page 185].

Tarruell, L., Greif, D., Uehlinger, T., Jotzu, G., and Esslinger, T., *"Creating, moving and merging Dirac points with a Fermi gas in a tunable honeycomb lattice,"* Nature **483**, 302 (2012) [cited in page 17].

Tarruell, L. and Sanchez-Palencia, L., *"Quantum simulation of the Hubbard model with ultracold fermions in optical lattices,"* Comptes Rendus Physique **19**, 365 (2018) [cited in page 17].

Tiarks, D., Baur, S., Schneider, K., Dürr, S., and Rempe, G., *"Single-photon transistor using a Förster resonance,"* Phys. Rev. Lett. **113**, 053602 (2014) [cited in page 59].

Tong, D., Farooqi, S. M., Stanojevic, J., Krishnan, S., Zhang, Y. P., Côté, R., Eyler, E. E., and Gould, P. L., *"Local blockade of Rydberg excitation in an ultracold gas,"* Phys. Rev. Lett. **93**, 063001 (2004) [cited in page 21].

Tuchendler, C., Lance, A. M., Browaeys, A., Sortais, Y. R. P., and Grangier, P., *"Energy distribution and cooling of a single atom in an optical tweezer,"* Physical Review A **78**, 033425 (2008) [cited in pages 33 and 35].

Urban, E., Johnson, T. A., Henage, T., Isenhower, L., Yavuz, D. D., Walker, T. G., and Saffman, M., *"Observation of Rydberg blockade between two atoms,"* Nature Physics **5**, 110 (2009) [cited in page 21].

Varney, C. N., Sun, K., Galitski, V., and Rigol, M., *"Kaleidoscope of exotic quantum phases in a frustrated XY model,"* Phys. Rev. Lett. **107**, 077201 (2011) [cited in page 120].

Varney, C. N., Sun, K., Rigol, M., and Galitski, V., *"Interaction effects and quantum phase transitions in topological insulators,"* Phys. Rev. B **82**, 115125 (2010) [cited in page 184].

Vigneron, K., Quantum noise of light control and quantum nondemolition measurement using cold trapped atoms., Ph.D. thesis, Université Paris Sud - Paris XI (1998) [cited in page 28].

Vitanov, N. V., Rangelov, A. A., Shore, B. W., and Bergmann, K., *"Stimulated Raman adiabatic passage in physics, chemistry, and beyond,"* Rev. Mod. Phys. **89**, 015006 (2017) [cited in page 54].

Vogt, T., Viteau, M., Zhao, J., Chotia, A., Comparat, D., and Pillet, P., *"Dipole blockade at Förster resonances in high resolution laser excitation of Rydberg states of Cesium atoms,"* Phys. Rev. Lett. **97**, 083003 (2006) [cited in page 21].

Wallraff, A., Schuster, D. I., Blais, A., Frunzio, L., Huang, R.-S., Majer, J., Kumar, S., Girvin, S. M., and Schoelkopf, R. J., *"Strong coupling of a single photon to a superconducting qubit using circuit quantum electrodynamics,"* Nature **431**, 162 (2004) [cited in page 19].

Wang, X., Dou, S., and Zhang, C., *"Zero-gap materials for future spintronics, electronics and optics,"* NPG Asia Mater **2**, 31 (2010) [cited in page 156].

Wang, Y., Zhang, X., Corcovilos, T. A., Kumar, A., and Weiss, D. S., *"Coherent addressing of individual neutral atoms in a 3D optical lattice,"* Phys. Rev. Lett. **115**, 043003 (2015) [cited in page 17].

Weber, S., de Léséleuc, S., Lienhard, V., Barredo, D., Lahaye, T., Browaeys, A., and Bchler, H. P., *"Topologically protected edge states in small Rydberg systems,"* Quantum Science and Technology **3**, 044001 (2018) [cited in pages 157, 168, and 170].

Weber, S., Tresp, C., Menke, H., Urvoy, A., Firstenberg, O., Bchler, H. P., and Hofferberth, S., *"Calculation of Rydberg interaction potentials,"* Journal of Physics B: Atomic, Molecular and Optical Physics **50**, 133001 (2017) [cited in page 95].

Weimer, H., Löw, R., Pfau, T., and Büchler, H. P., *"Quantum critical behavior in strongly interacting Rydberg gases,"* Phys. Rev. Lett. **101**, 250601 (2008) [cited in page 89].

Weimer, H., Müller, M., Lesanovsky, I., Zoller, P., and Büchler, H. P., *"A Rydberg quantum simulator,"* Nature Phys. **6**, 382 (2010) [cited in page 21].

Whitlock, S., Glaetzle, A. W., and Hannaford, P., *"Simulating quantum spin models using Rydberg-excited atomic ensembles in magnetic microtrap arrays,"* Journal of Physics B: Atomic, Molecular and Optical Physics **50**, 074001 (2017) [cited in page 188].

Wilk, T., Gaëtan, A., Evellin, C., Wolters, J., Miroshnychenko, Y., Grangier, P., and Browaeys, A., *"Entanglement of two individual neutral atoms using Rydberg blockade,"* Phys. Rev. Lett. **104**, 010502 (2010) [cited in pages 21, 59, and 150].

Xu, P., He, X., Wang, J., and Zhan, M., *"Trapping a single atom in a blue detuned optical bottle beam trap,"* Opt. Lett. **35**, 2164 (2010) [cited in page 82].

Yan, B., Moses, S., Gadway, B., Covey, J., Hazzard, K., Rey, A., Jin, D., and Ye, J., *"Observation of dipolar spin-exchange interactions with lattice-confined polar molecules,"* Nature **501**, 521 (2013) [cited in page 122].

You, J. Q. and Nori, F., *"Superconducting circuits and quantum information,"* Physics Today **58**, 42 (2005) [cited in page 19].

Younge, K. C., Knuffman, B., Anderson, S. E., and Raithel, G., *"State-dependent energy shifts of Rydberg atoms in a ponderomotive optical lattice,"* Phys. Rev. Lett. **104**, 173001 (2010) [cited in page 78].

Zhang, S., Robicheaux, F., and Saffman, M., *"Magic-wavelength optical traps for Rydberg atoms,"* Phys. Rev. A **84**, 043408 (2011) [cited in pages 61, 72, and 82].

université PARIS-SACLAY | ÉCOLE DOCTORALE Ondes et Matière (EDOM)

Titre : Physique quantique expérimentale à N corps dans des matrices d'atomes de Rydberg. Des modèles de spins à la matière topologique.

Mots clés : pinces optiques, atomes individuels, interaction dipolaire, modèles de spins, matière topologique, simulation quantique

Résumé : Des atomes individuels piégés dans des matrices de pinces optiques et excités vers des états de Rydberg forment une plateforme expérimentale performante pour la simulation quantique de problèmes à N corps, comme le confirment les récents progrès dans le domaine. Lors de cette thèse, nous avons d'abord montré la production de matrices de pinces optiques, toutes chargées par des atomes uniques dans leur état fondamental. Notre technique de piégeage a été étendue au cas des atomes de Rydberg. Ces derniers sont chassés des zones de haute intensité par la force pondéromotrice. Par conséquent, nous avons créé par holographie des zones sombres entourés de lumière, pour les confiner. Nous avons aussi étudié les corrélations entre spins dans le cas des Hamiltoniens d'Ising ou XY, en utilisant le régime d'interaction de van der Waals ou dipolaire résonnant. Lors de notre étude du modèle d'Ising, nous avons observé l'apparition de corrélations antiferromagnétiques au cours d'une variation temporelle de l'Hamiltonien, mettant en évidence une vitesse effective pour la propagation des corrélations, ainsi qu'un mécanisme caractéristique de croissance site-à-site. Pour le modèle XY, nous avons montré la préparation d'un nombre contrôlé d'excitations de spin, ainsi que la production de chaînes ferromagnétiques, ou d'un ensemble de chaînes ferromagnétiques anti-alignées deux à deux. Enfin, nous avons utilisé d'autres termes d'échange, présents dans l'interaction dipolaire, pour créer des amplitudes de saut complexe pour une particule effective. Cette utilisation a conduit à l'apparition d'un champ de jauge artificiel, dont l'effet a été mesuré sur un système minimal composé de trois atomes, et ouvre la voie à l'observation d'états de bords chiraux, caractéristiques des isolants topologiques.

Title : Experimental quantum many-body physics with arrays of Rydberg atoms. From spin models to topological matter

Keywords : optical tweezers, single atoms, dipole-dipole interaction, spin models, topological matter, quantum simulation

Abstract : Rydberg-based platforms, involving single atoms trapped in arrays of optical tweezers and excited to Rydberg states, have recently proven attractive to perform quantum simulation of many-body physics. In this thesis, we first demonstrated the generation of arrays of optical tweezers fully loaded by single ground-state atoms. The trapping technique was then extended for Rydberg atoms. The latest are repelled from high-intensity regions via the ponderomotive force, so we created holographically dark regions surrounded by light to confine them. We also studied spin-spin correlations in artificial Ising or XY magnets, engineered by using either the van der Waals or the resonant dipolar coupling between Rydberg atoms. In the Ising case, we observed the growth of antiferromagnetic correlations during a dynamical tuning of the Hamiltonian, revealing an effective velocity for the spreading of correlations, and a typical site to site build-up mechanism. In the XY case, we demonstrated the preparation of a controlled number of spin excitations, and the generation of 1D XY ferromagnets and a 2D stripy order phase (ferromagnetic chains anti-aligned with respect to each other). Finally, we used additional exchange terms of the dipole-dipole interaction to engineer complex hopping amplitudes for an effective particle. This resulted in the emergence of an artificial gauge field, characterized on a minimal three-atom system, and opens the way to the observation of chiral edge states, a signature of topological insulators.

Université Paris-Saclay
Espace Technologique / Immeuble Discovery
Route de l'Orme aux Merisiers RD 128 / 91190 Saint-Aubin, France